7th International Building Physics Conference

IBPC2018

Proceedings
SYRACUSE, NY, USA
September 23 - 26, 2018

Healthy, Intelligent and Resilient
Buildings and Urban Environments
ibpc2018.org │ #ibpc2018

A comparison of model order reduction methods for the simulation of wall heat transfer

[1]Tianfeng Hou[*], [1]Staf Roels and [1]Hans Janssen

[1]KU Leuven, Department of Civil Engineering, Building Physics Section, Kasteelpark Arenberg 40, 3001 Leuven, Belgium

[*]*Corresponding email: tianfeng.hou@kuleuven.be*

ABSTRACT

In this paper, the potential of model order reduction for simulating building performance is assessed, via a case study of modelling heat transfer through a massive masonry wall. Two model order reduction techniques – proper orthogonal decomposition and proper generalized decomposition – are investigated and compared. Moreover, to illustrate the performance of model order reduction techniques, the accuracies of the two model order reduction techniques are respectively compared with a standard finite element method. The outcomes show that both of the two model order reduction techniques are able to provide an accurate result, and the proper generalized decomposition tends to be more versatile than the proper orthogonal decomposition method.

KEYWORDS

Model order reduction, proper generalized decomposition, proper orthogonal decomposition, finite element method, heat transfer

INTRODUCTION

Today, 30% of the European building stock consists of 'historic' buildings built prior to World War II (Ribuild.eu, 2018). These buildings are typically far less energy-efficient than new buildings, and they hence account for a large share of the total energy consumption of buildings. One important measure to reduce their energy consumption is to install internal insulation. However, internal insulation is often associated with moisture damage, and much care should be taken when applying this solution. This paper is part of the EU H2020 RIBuild project, which aims at developing effective and comprehensive guidelines for internal insulation in historic buildings. Given that a multitude of scenarios and factors can be easily evaluated with numerical analyses, the use of numerical simulations for hygrothermal performance assessment tends to be the best option. However, the standard numerical methods for space and time discretization are usually very time consuming due to the high non-linearity of the equations, the multi-dimensional spatial domains and the long simulation time intervals required, in order to reduce the computation time as much as possible, an efficient solver for modelling the hygrothermal behavior of the wall is needed. Therefore, a faster surrogate model is highly desired.

Instead of using the standard numerical models, Van Gelder et al. (2014) employed statistical regression and interpolation based surrogate models (such as polynomial regression, Kriging etc.) to reduce the simulation time. However, these statistical surrogate models can only deliver static results: for the heat transfer through a wall, they may predict the yearly total heat loss, but not the temperature profile at each moment in time. Hence, to obtain the dynamic behavior with a simplifying surrogate model, model order reduction techniques as alternatives of the statistical surrogate modelling are investigated. In this paper, two model order reduction methods (proper orthogonal decomposition (POD) and proper generalized decomposition (PGD)) are

investigated and compared. The first method belongs to a family of a posteriori methods - it is built based on the preliminary results of the original time-consuming model. The second method is an a priori method which can be established by a suitable iterative process. Instead of the standard finite element method (FEM), we will use both POD and PGD to simulate the building thermal performance, exemplified through a case study of modelling the heat transfer through a massive masonry wall.

Below, first a brief introduction of POD and PGD are put forward, with focus on the potential use for the modelling of wall heat transfer. Subsequently, the calculation object and the case study with its input parameters are introduced, as that forms the central application in this study. Next, the results of using POD and PGD for simulating the wall heat transfer are presented and a discussion with respect to the interpretation of their accuracies follows. Finally, conclusions on which method is considered most optimal are formulated.

POD AND PGD FOR MODELLING WALL HEAT TRANSFER
The thermal performance of a building component can be assessed by analyzing the transfer of heat through building materials. Heat transfer is mainly related to the normal flows of heat conduction, convention, radiation and advection. Thus, assessing the thermal performance of a building component requires to get numerical simulation results of the heat transport equation based on the component geometry, the boundary conditions and the material properties. The conventional thermal simulation models are mainly based on numerical simulation methods for space and time discretization, for instance, the FEM. As mentioned before, these standard numerical methods can be very time consuming due to the high number of degrees of freedom after the spatial and temporal discretization. Therefore, in this paper we investigate two model order reduction methods (POD and PGD) which reduce the degrees of freedom of the complex system and still mimic the dynamic behavior (such as time evolution of temperatures,…).

Proper orthogonal decomposition
The POD method was first proposed by Kosambi (1943), and has been successfully applied in a variety of engineering fields, such as image processing, signal analysis, data compression and recently in building physical engineering (Tallet et al., 2017). POD is also known as Karhunen - Loeve decomposition, principal component analysis, or singular value decomposition, and the connections of these three methods are provided by Liang et al. (2002). A brief tutorial of POD can be found in (Chatterjee, 2000), a detailed introduction of its theory and related application for modelling heat transfer process are respectively presented by Liang et al. (2002) and Fic et al. (2005). The basic idea of POD is approximating a high dimensional process by its 'most relevant information'. In this paper, we extract the 'most relevant information' by making use of principal component analysis (PCA). After the PCA, the POD modes are constructed by selecting the most important k components, here $k \ll m$, where m is the number of the mesh elements. As a result, these POD modes can be used to construct a reduced model for simulating different problems (for instance, variations in the boundary conditions or material properties or longer simulation period).

Proper generalized decomposition
Despite the POD method being able to provide a reduced basis and save the computational time when simulating similar problems, this method has an important drawback: to construct a POD, 'a priori knowledge' – the snapshots of the large original model – is needed. This disadvantage in turn leads to an extra computational cost and limits its application to 'different but similar problems'. On the contrary, Ladeveze (1985) proposed a different strategy, called 'radial

approximation'. This method is based on the hypothesis that the solution of the considered problem is given by a finite sum representation:

$$u(\pmb{x}, t) = \sum_{i=1}^{N} \pmb{X}_i(x) \cdot T_i(t) \tag{1}$$

Here, u is the solution of the target problem, $\pmb{X}_i$ usually stands for the spatial parameters, T_i represents the temporal parameter. Next, injecting equation (1) into the weak formulation of the differential equation and starting from an initial point based on the related initial and boundary conditions, the solution $u(\pmb{x},t)$ can be constructed by successive iterative enrichment methods. The procedure is stopped when the convergence criteria are reached. As a result, this strategy allows to approximate the solution without any 'a priori knowledge'. Inspired by this strategy, Ammar et al. (2006) generalized this method to the multidimensional situation and named it proper generalized decomposition (PGD). A detailed tutorial of PGD is proposed by Chinesta et al. (2013), and an application of PGD for simulating thermal processes is provided by Pruliere et al. (2013) . In addition, two reviews of PGD are provided by Chinesta et al. (2010) and Berger et al. (2016), with attention for general and physical engineering applications respectively.

CALCULATION OBJECT AND CASE STUDY
For investigating the performance of POD and PGD for hygrothermal simulations, a calculation object hence needs to be formulated. Since the reference situation prior to retrofit is often a massive masonry wall, and that configuration is adopted here as calculation object. In order to judge the feasibility of internal insulation in historic buildings, the hygrothermal performances of internally insulated massive walls – heat loss, mould growth, wood rot, … – need to be investigated (Vereecken et al. 2015). To simplify the calculation complexity in this study, this paper limits that performance assessment to the transmission of heat loss through the wall. Since quantifying the heat loss requires solution of the temperature profiles of the wall, both the temperature profiles and heat losses over the entire year are taken as the targeted outputs. To do so, the thermal behavior of the wall is simulated with FEM, POD and PGD, wherein the conductive heat transfer equation is solved under the relevant interior and exterior boundary conditions. The simulation result of the FEM is taken here as the reference solution: more specifically, this reference solution is calculated by the FEM with 200 mesh elements and a fixed time step of one hour.

As mentioned before, since POD is constructed for simulating different problems, in this paper, several POD models are constructed by using snapshots of different time intervals (one year, one month, one day, half day, six hours and three hours). Except for the time interval of one year, all the other scenarios are performed 12 times: once for every month. In addition, each of the one day, half day, six hours and three hours are taken at the start of each month. In order to evaluate the performance of different model order reduction methods as a function of the number of modes, both of the POD and PGD models are calculated with 1 to 15 modes.

For the comparison case study of PGD and POD, the detailed information of the input parameters is mentioned here. For the material properties, the density, thermal capacity and conductivity of the wall are 2087 kg/m^3, 870 J/kgK and 1.07 W/mK. The boundary conditions are kept restricted to combined convection and radiation, governed by climate data of Gaasbeek (Belgium) at the exterior surface, and by the indoor air temperature as described in (EN 15026) at the interior surface. The related interior and exterior surface transfer

coefficient are $8 \, W/m^2K$ and $25 \, W/m^2K$, respectively. In relation to the component geometry, the thickness of the wall is $0.2 \, m$.

RESULTS

To compare the accuracies of PGD and different POD models, the average temperature difference between the FEM solution and different model order reduction models, as a function of the number of modes, is shown in Figure 1. For getting a more direct view of the performance of POD and PGD methods, different profiles of temperature are compared at different moments, and the result is presented in Figure 2. In addition, since in practice the cumulated heat loss is usually considered as an indicator of the thermal performance of the wall, the relative deviation of heat losses between the reference solution and different model order reduction models are shown in Figure 3.
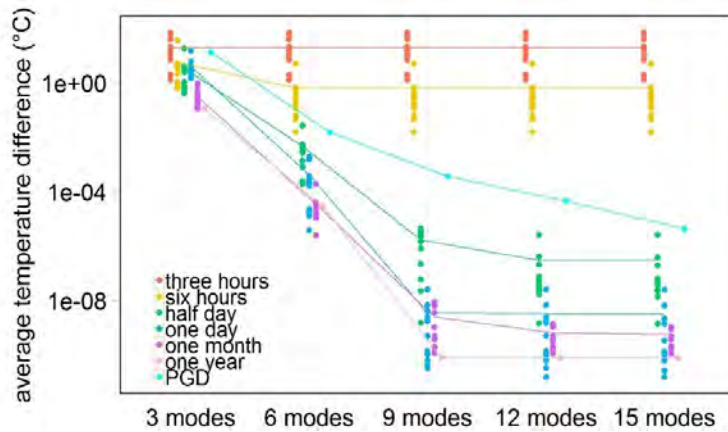

Figure 1. Average temperature differences between reference solution and different model order reduction approximations.
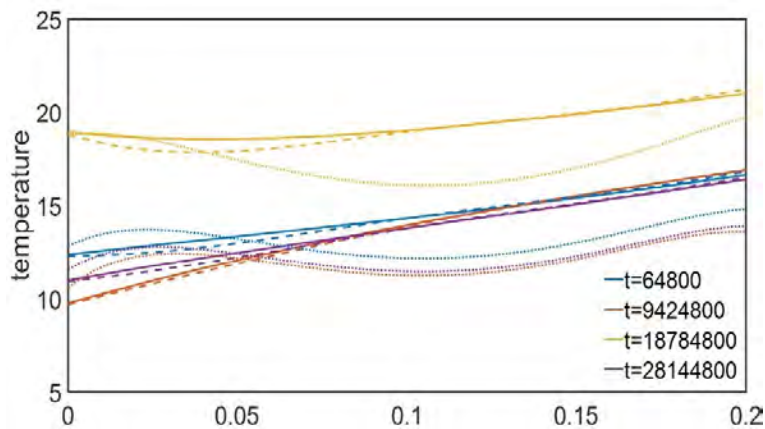

Figure 2. Temperature profiles of the reference solution and PGD solution (solid lines), POD solution constructed from 6 hours' snapshots (dashed lines) and from 3 hours' snapshots (dotted lines). All the reduced models are construed by 15 modes.
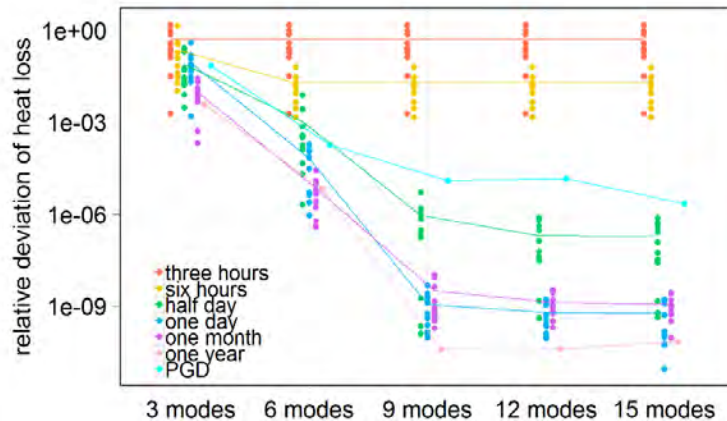
Figure 3. Relative deviation of heat loss between reference solution and different model order reduction approximations.

DISCUSSIONS

Figure 1 illustrates that, except for the POD constructed from the 3 and 6 hours' snapshots, the accuracy of the other reduced order models increases as the number of their construction modes raises. However for the POD, after 9 modes this improvement becomes negligible. In addition, one can see that the accuracy of the POD increases as the time duration of its snapshots raises. In relation to the PGD, one can see that a relatively accurate result can be reached with a sufficient number of construction modes. Figure 2 confirms the result of Figure 1, it is shown that visually there is no difference between the reference solution and PGD approximation. On the other hand, larger differences can be respectively found between the reference solution and the solution calculated by the POD with the 6 and 3 hours snapshots. Furthermore, compared with Figure 1, a very similar result can be found in Figure 3 - except for the POD constructed from the 3 and 6 hours' snapshots, the relative errors of the other reduced order models decreases as the number of their construction modes increases and these relative errors can be reached below 1% with a very limited number of modes. These findings indicate that the performance of all the model order reduction methods do not vary much for quantifying the heat loss instead of calculating the temperature profile.

In summary, combined the results of all the Figures, we can conclude that, with enough number of modes the PGD method can provide a relatively accurate result. In relation to the POD, only when the number of snapshots is really insufficient (three and six hours), an inaccurate result may be obtained. As a consequence, for using the POD method to obtain an accurate result with the smallest size of snapshot, an error estimation method is thus needed. On the other hand, since the PGD model is constructed based on a suitable iterative method, an error controller is naturally embedded in this method. Therefore, together with the advantage that the PGD model is constructed without any 'prior knowledge', this method tends to be more versatile than the POD.

CONCLUSIONS

In this paper, we investigated the performance of two model order reduction methods (POD and PGD), based on a case study of modelling heat transfer through a massive masonry wall. It is shown that, both of the two methods can provide a very accurate result. In addition, since the construction of PGD does not rely on any 'a priori information', this method tends to be more versatile than the POD and should be preferred.

ACKNOWLEDGEMENT

REFERENCES
Ammar A., Mokdad B., Chinesta F., and Keunings R. 2006. A new family of solvers for some classes of multidimensional partial differential equations encountered in kinetic theory modeling of complex fluids. Journal of non-Newtonian fluid Mechanics, 139(3), pp.153-176.

Berger J., Mendes N., Guernouti S., Woloszyn M., and Chinesta F. 2017. Review of Reduced Order Models for Heat and Moisture Transfer in Building Physics with Emphasis in PGD Approaches. Archives of Computational Methods in Engineering, 24(3), pp.655-667.

Chatterjee A. 2000. An introduction to the proper orthogonal decomposition. Current science, pp.808-817.

Chinesta F., Ammar A., and Cueto E. 2010. Recent advances and new challenges in the use of the proper generalized decomposition for solving multidimensional models. Archives of Computational methods in Engineering, 17(4), pp.327-350.

Chinesta F., Keunings R., and Leygue A. 2013. The proper generalized decomposition for advanced numerical simulations: a primer. Springer Science & Business Media.

EN B., 2007. 15026: 2007: Hygrothermal performance of building components and building elements-Assessment of moisture transfer by numerical simulation. German version DIN EN, 15026.

Fic A., Białecki R.A., and Kassab A.J. 2005. Solving transient nonlinear heat conduction problems by proper orthogonal decomposition and the finite-element method. Numerical Heat Transfer, Part B: Fundamentals, 48(2), pp.103-124.

Kosambi D.D. 2016. Statistics in function space. In DD Kosambi (pp. 115-123). Springer, New Delhi.

Ladeveze P. 1985. On a family of algorithms for structural mechanics. Comptes rendus de l'Académie des Sciences, 300(2), pp.41-44.

Liang Y.C., Lee H.P., Lim S.P., Lin W.Z., Lee K.H., and Wu C.G. 2002. Proper orthogonal decomposition and its applications—Part I: Theory. Journal of Sound and vibration, 252(3), pp.527-544.

Pruliere E., Chinesta F., Ammar A., Leygue A., and Poitou A. 2013. On the solution of the heat equation in very thin tapes. International Journal of Thermal Sciences, 65, pp.148-157.

Ribuild.eu. (2018). about RIBuild. [online] Available at: http://ribuild.eu/about.

Tallet A., Liberge E., and Inard C. 2017, February. Fast POD method to evaluate infiltration heat recovery in building walls. Building Simulation.

Van Gelder L., Das P., Janssen H., and Roels S. 2014. Comparative study of metamodelling techniques in building energy simulation: Guidelines for practitioners. Simulation Modelling Practice and Theory, 49, pp.245-257.

Vereecken E., Van Gelder L., Janssen H., and Roels S. 2015. Interior insulation for wall retrofitting–A probabilistic analysis of energy savings and hygrothermal risks. Energy and Buildings, 89, pp.231-244.

A framework for comfort assessment in buildings and districts retrofit process

Marco Arnesano[1,*], Federica Naspi[1], Livia Claudi[1] and Gian Marco Revel[1]

[1]Dipartimento di Ingegneria Industriale e Scienze Matematiche, Università Politecnica delle Marche, via Brecce Bianche, Ancona 60131, Italy

[*]*Corresponding email: m.arnesano@univpm.it*

ABSTRACT

The retrofit design of buildings and districts cannot exclude the occupants' perspective if comfortable and healthy conditions have to be obtained. For this reason, the NewTREND[1] project developed a collaborative platform for the energy efficient buildings and districts retrofit that includes the users' perspective. Three modules have been developed for thermal comfort, acoustic comfort and behavioural assessment. These modules are integrated into a Simulation and Design Hub that, after gathering data from on-site measurements, builds a simulation model of the district, calculates yearly results and exposes them to the design team through a dedicated District Information Model server and user interfaces. These modules perform deep investigations on the occupants' sensation and behaviour, based on both measured and simulated datasets and provide comparisons of comfort performances, considering different retrofit scenarios and related uncertainties. In details, the thermal comfort module performs analysis according to both predictive and adaptive models, evaluates the variability around the design conditions together with sensitivity analysis that highlights which parameters are the most critical for the retrofit design. The acoustic module provides a complete tool to predict and assess the indoor acoustic comfort, taking into account the performance of building envelope and the impact of district noise. Finally, the behavioural module empowers the building energy simulation with co-simulation capabilities that reproduces the real occupants' behaviours in relation to comfort conditions. The final goal of the framework is to support the decision-making process in selecting the optimal retrofit option that achieves the targeted energy efficiency without infringing the occupant's expectation in terms of comfort and well-being.

KEYWORDS
Thermal Comfort, Acoustic Comfort, Behavioural Modelling, Monitoring, Simulation.

INTRODUCTION
Buildings have the main goal of providing comfortable conditions for the occupants. The lower is the comfort sensation the higher will be the probability that occupants occur in non-efficient behaviours and low productivity because of the degraded well-being. Thus, maintaining the optimal thermal conditions in all occupied spaces is a key feature. On the other side buildings account for the 40% of the total energy consumption and they have to become as much efficient as possible so to use the minimum energy to provide comfortable conditions. Considering that, more than the 35% of European buildings have been built before the 60's and more than the 80% before the 90's (BPIE, 2011), they do not include materials and technologies capable of high performance or they have degraded with. In this context, the renovation and retrofit interventions are to be considered as priority to achieve the objective

---

[1] http://newtrend-project.eu/

of reducing the global energy consumption and striving to the resilience required for facing climate changes. Comfort plays an important role in buildings renovation. In fact, the recent report "Feel Good, Live Well - The UK home, health and wellbeing report"[2] points out that over 95% of homeowners and renters make some effort to look after their health and wellbeing and health and wellbeing issues in their existing homes they would like to change are in the first position. In this context, the NewTREND project proposes a Collaborative Design Platform to enable wide retrofit actions of buildings and districts, including comfort and well-being into the multicriteria assessment framework. This paper presents the platform and three tools dedicated investigate the occupants' perspective.

METHODS
The NewTREND cloud platform
The main aim of the NewTREND cloud-based platform is to support the collaborative design and to promote the dialogue between the different subjects involved in a retrofit project. In this perspective, a District Information Model (DIM) server has been developed to store data and to make them available for the designers. In parallel, a Simulation & Design Hub (SDH), creating a simulation model of the district, allows effective comparisons between retrofit options at both building and district level and guide the decision makers in choosing the best strategy. These targets are achieved using dynamic simulations (IESVE software) which provide yearly energy assessments and calculations of Key Performance Indicators (KPIs). These components are merged in a Collaborative Design Platform, which provides the access to all the embedded tools and the visualization of the results through an intuitive Graphical User Interface. Figure 1 reports a scheme of the platform.
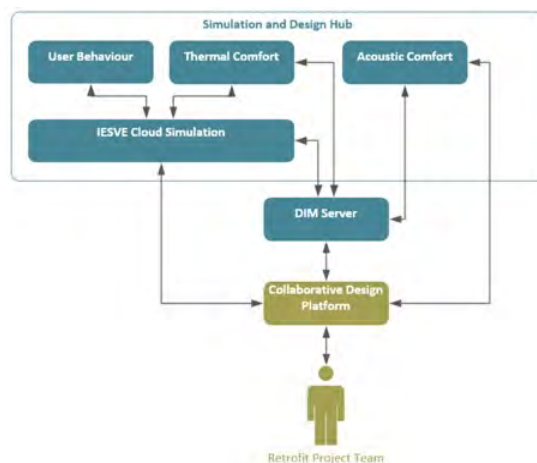

Figure 1. Scheme of the NewTREND platform.

A key improvement of this methodology concerns the inclusion of the occupants' perspective in the decision-making process. In fact, the evaluation of different retrofit scenarios is investigated considering both users' comfort (thermal and acoustic) preferences and the human-building interaction. According to this people-centred perspective, three modules have been developed. The thermal comfort and acoustic comfort modules perform a post-processing analysis on the simulation data to provide simple comfort indicators for the different design alternatives. The behavioural module includes the human component inside the simulation process since it is directly coupled with the IESVE engine.

---

[2] https://www.multicomfort.co.uk/media/1096/saint-gobain-uk-home-health-and-wellbeing-report-summary.pdf

Thermal Comfort Module

Thermal comfort is a subjective quantity which has to be measured and assessed using a statistical approach. The tool offers an evaluation of the thermal comfort conditions for each room of the studied building. The algorithms post-process the data provided by the IESVE simulation or measurements, according to the user selection both in terms of comfort model (i.e. predictive and adaptive) and season (i.e. heating, cooling). The tool displays KPIs related to the thermal comfort assessment for each investigated retrofit scenario, calculated as the percentage of occupied hours out of the optimal ranges provided by predictive and adaptive comfort models according to EN 15251 (2007). It receives the input data from the IESVE cloud energy simulation and, after the post-processing analysis, stores the results in the DIM server. In addition, this module provides a sensitivity analysis, based on Monte Carlo method, to determine which parameter has the highest impact of thermal comfort. In this way the designer has the possibility to address specific issues to be solved with the retrofit. The tool has been tested simulating a room of a monitored building to guarantee the reliability of the obtained results (Naspi et al. 2018a). After simulating the actual thermal condition, two retrofit configurations have been selected and applied. The KPIs related to the three different scenarios are illustrated and compared to investigate which solution is to be preferred.

Acoustic Comfort Module

The acoustic comfort module is composed of algorithms for the assessment of indoor acoustic comfort at building level, according to equations of EN 12354-3 (2017). The improvement of the acoustic comfort is obtained by applying building envelope interventions on the basis of the evaluation of district noise levels (through measurements - EN 16283-3 (2016) - or predictive calculation models[3]). After simulating the current building condition, the tool performs post-retrofit simulations according to the retrofit interventions selected by the user. The output of each simulation process is a specific KPI, calculated by assignment of a score according to the measured/calculated indoor sound pressure level, which allows the assessment of the indoor acoustic comfort and the comparison between the pre and post retrofit configurations. The KPI provides to the designers a clear identification of the best retrofit option on the building envelope to improve the indoor acoustic comfort. The tool, integrated in the SDH, communicates with the DIM server to receive the required input data. The investigation of the potentialities of the tool occurred following several steps. At first, an extensive data collection by acoustic measurements has been performed in a residential building, settled in Ancona (Italy), to evaluate the actual comfort condition calculating the acoustic KPI. Then, applying different retrofit scenarios, the tool simulates the post-retrofit conditions and offers a comparison of pre and post scenarios through the KPIs.

The Behavioural Module

The module consists of two behavioural functions that predict occupants' interaction with windows and electric lights in offices. The algorithms have been developed using experimental data acquired for a full year in a University building in Italy. People presence, environmental parameters and the status of the devices have been continuously recorded (10 min sampling time) in three offices equipped with sensor networks (Naspi et al. 2018a). Following the approach proposed by (Wang et al. 2016), the influence of environmental variables and time-related events on users' behaviours has been investigated. Window adjustments are driven by both indoor and outdoor temperature; while the lights are switched on and off in relation to the decreasing of the work-plane illuminance and to the users' departure, respectively. Identified the triggers, the coefficients of the equations have been

---

[3] Directive 2002/49/EC. Directive of the European Parliament and of the Council of 25 June 2002 relating to the assessment and management of environmental noise. Official J Eur Communities 2002; L189: 12-25.

tuned using regression methods. The co-simulation approach between the module and the IESVE engine allows the data exchanges during the simulation run-time. This approach offers a considerable modelling improvement since the operational schedules are dynamically defined at each time step, according to the module outputs. The integration and the predicting capabilities of the module have been tested simulating a portion of the case study. Ventilation and lighting profiles are stochastically defined; while heating and occupancy ones are set according to ASHRAE standards (2004). The results obtained using the behavioural module have been compared to those related to a standard simulation (i.e. deterministic results). Then, both of them have been evaluated in relation to the monitored data to assess which approach would have made the best predictions.

RESULTS
To demonstrate the functionalities of the tools, they have been applied to assess different retrofit scenarios to a building of the UNIVPM campus, located in Ancona (centre of Italy), and built in the seventies.
Thermal Comfort
Thermal comfort module was applied to heating season. Figure 2 shows that, before retrofit, the building is uncomfortable since the average operation is at the limit of the lowest comfort zone. This is also confirmed by the KPI, which is for more than the 60% of the time in "cold" conditions, calculated considering the category II as reference (±0.5 PMV as boundaries). The first retrofit configuration (Retrofit 1), concerning the application of envelope thermal insulation, moves the building to category II. This intervention produces only a partial improvement of the comfort conditions since the KPI is not sufficiently high. The second retrofit scenario (Retrofit 2) concerns the windows replacement and the improvement of the heating system. The design condition and its deviation reach the higher building category (±0.2 PMV). Also, the KPI shows a number of cold hours lower than the 2% of the total building operation.
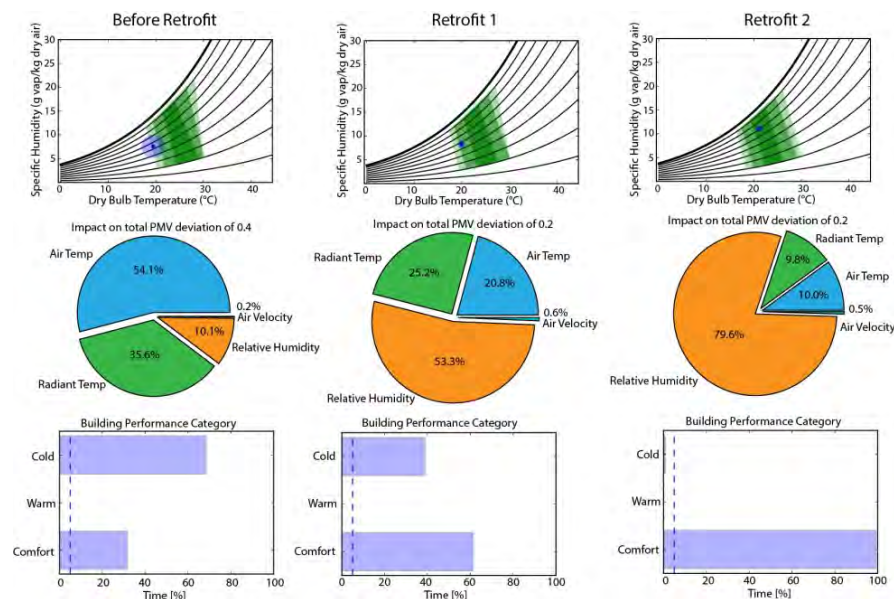

Figure 2. Results from thermal comfort analysis for heating season with predictive model.

Acoustic Comfort
The main outcomes of the acoustic comfort tool are the comparisons both between actual and retrofitted conditions and between different retrofit designs, using KPIs. Figure 3 shows the

influence of four types of interventions, with increasing impact. The first two scenarios concern only one action: the addition of an external insulation layer (case 1) and the substitution of the windows (case 2). The last two retrofit options are connected to concurrent operations: addition of an external insulation layer, substitution of windows and small elements. The key difference between case 3 and case 4 regards the features of the windows, which are much more performing in the second instance.
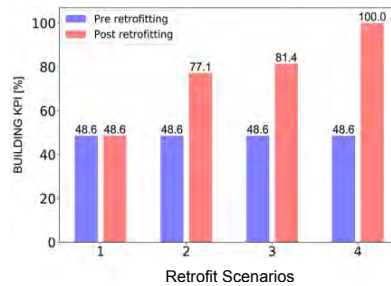

Figure 3 KPIs comparison of pre and post scenarios.

The analysis highlights that the external insulation has no impact on improving the acoustic condition while changing the type of windows provides an increase of 28.5% in the KPI value. The preferred comfort assessment is reached in case 4. In fact, combining several interventions and enhancing the features of the components, the KPI raises of 51.4%. Such assessment, clearly identifying the most effective acoustic retrofit solution, aids the users in selecting the design strategy and in avoiding time and money wastes.

Behavioural Module
The lighting and ventilation profiles obtained applying the behavioural module are compared both to standard profiles and to real users' behaviours. To perform the comparison, a sample of 14 days during the non-heating season has been selected (to avoid the influence of fixed heating profiles on the results). Figure 4 presents the lighting and ventilation profiles during two representative days. The real users' behaviours (blue dashed line) have been examined in relation to the behavioural (red solid line) and standard (grey dotted line) profiles.
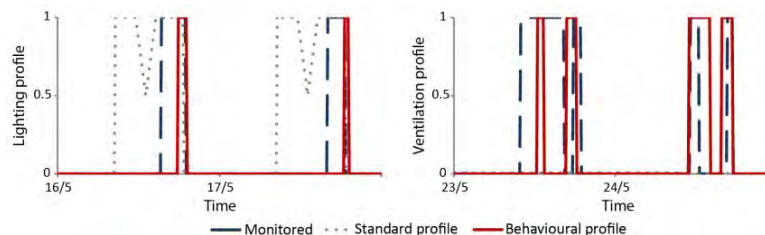

Figure 4. A two-day comparison of lighting and ventilation profiles.

Table 1 summarises the analysis for all the 14 days, reporting the percentage of time with lights on and windows open and the percentage difference (i.e. error) between simulated and real actions. The outcomes highlight that both the simulation approaches tend to overestimate the lighting use and to underestimate the window openings. However, the behavioural module minimises the discrepancy with actual data, especially for the lighting use (Δ=+5.1%), with a consequent deviation of 10% on the prediction of energy consumption, compared to standard profiles (Naspi et al. 2018b).

Table 1. Errors of Standard and Behavioural profiles in relation to the real data.

Lighting Profile	% of time lights ON	Δ% with real	Ventilation Profile	% of time windows OPEN	Δ% with real
Real	8.5	--	Real	24.9	--
Standard	42.4	+33.9	Standard	1.9	-23
Behavioural	13.6	+5.1	Behavioural	8.2	-16.7

DISCUSSIONS

The tools presented in this work are useful to support the retrofit design with deep investigations of comfort issues. Acoustic and thermal comfort modules can be a support for the selection of the optimal retrofit solution, addressing buildings pathologies. Also, the behavioural module provides a substantial empower to the simulation results since it reproduces the human-building interaction more accurately than standard profiles.

CONCLUSIONS

The paper presents the framework of the NewTREND cloud platform and, in particular, three embedded tools. The thermal comfort and acoustic comfort tools provide clear and effective evaluations between different retrofit scenarios using KPIs. The behavioural module reproduces the human-building interaction during the simulation, overwriting standard schedules. These tools, including the human component under different perspectives, support the decision-making process and aid the design team in selecting the optimal retrofit option in terms of energy efficiency and occupant's comfort expectations.

ACKNOWLEDGMENT

REFERENCES

ASHRAE. 2004. ANSI/ASHRAE Standard 90.1, Energy standard for buildings except low-rise residential buildings. Atlanta: American Society of Heating, Refrigerating, and Air-Conditioning Engineers, Inc.

BPIE. 2011. Europe's Buildings Under the Microscope. Brussel: Buildings Performance Institute Europe.

CEN. 2007. EN Standard 15251, Indoor environmental input parameters for design and assessment of energy performance of buildings addressing indoor air quality, thermal environment, lighting and acoustics. Brussels: CEN.

CEN. 2016. EN Standard 16283 part 3, Acoustics — Field measurement of sound insulation in buildings and of building elements — Façade sound insulation. Brussels: CEN.

CEN. 2017. EN Standard 12354 part 3, Building acoustics — Estimation of acoustic performance of buildings from the performance of elements —Airborne sound insulation against outdoor sound. Brussels: CEN.

Naspi F., Arnesano M., Zampetti L., Stazi F., Revel G. M., and D'Orazio M. 2018a. Experimental study on occupants' interaction with windows and lights in Mediterranean offices during the non-heating season. *Building and Environment,* 127, 221–238.

Naspi F., Arnesano M., Revel G. M., Klebow B. and Aird G. 2018b. Data-driven Behavioural Modelling for Building Energy Simulation Based on Scripted Profiles. Submitted to *BSO2018*.

Wang C., Yan D., Sun H., and Jiang Y. 2016. A generalized probabilistic formula relating occupant behavior to environmental conditions. *Building and Environment,* 95, 53–62.

A Rain Simulator to Examine Green Roof and Soil Moisture Sensor Performance

Endla S. Feustel[1,*], Yige Yang[1] and Cliff I. Davidson[1,2]

[1]Department of Civil and Environmental Engineering, Syracuse University, 151 Link Hall, Syracuse, NY 13244
[2]Center of Excellence in Environmental and Energy Systems, Syracuse University, Syracuse, NY 13244

*Corresponding email: esfeuste@syr.edu

ABSTRACT
Green roof technology plays a large role managing stormwater runoff in urban areas, where impervious surfaces cause substantial amounts of stormwater runoff to enter combined sewer systems. If the stormwater flow exceeds the capacity of treatment plants, this often results in the discharge of raw sewage into nearby bodies of water. Green roofs can reduce the occurrence of raw sewage discharge by decreasing the amount of mixed wastewater and stormwater flowing into combined sewers. Engineers and designers are looking for ways to improve the performance of green roofs and to understand parameters such as field capacity and time to onset of runoff. A better understanding of field capacity could be used to test hydrologic models that predict how much water a green roof could store under different conditions and to estimate how much runoff could be reduced.

In this project, a drip-type rain simulator is used to estimate field capacity of a plot of soil and sedum taken from the green roof on the Onondaga County Convention Center in Syracuse, NY. Three soil moisture sensors placed into the plot are used with different rain intensities to track the increase in soil water content during rain and the decrease following the end of the rain. The experimental results show that the field capacity of the Convention Center green roof is about 0.081 m^3 water / m^3 soil. This value is lower than expected and additional testing is underway. It is also shown that as rain intensity increases, time to onset of runoff decreases. With additional experiments to be conducted in Summer 2018, results of this work can be used by engineers to design and install green roofs with field capacities that complement average rain intensities and peak rain intensities and effectively reduce runoff.

KEYWORDS
Rain Simulator, Green Roof, Field Capacity, Runoff

INTRODUCTION
Green roofs play a significant role in urban stormwater management. They can store incoming precipitation, which reduces the amount of stormwater runoff flowing to combined sewers (Mentens et al. 2006). It is important to determine how much water a green roof can store during rain events in order to estimate how much runoff can be reduced. This information is important for developing improved engineered soil as well as to further advance hydrologic models like USEPA SWMM.
Rain simulators are used to produce different intensities of rain in well-controlled laboratory experiments. Operating a rain simulator with a small plot from a green roof can help

determine the performance of the green roof under various rain intensities. A drip-type rain simulator is used in these experiments to control rain intensity, drop size, and field conditions, such as slope of the roof (Bowyer-Bower and Burt, 1989).

Field capacity is an important parameter in hydrologic modeling and can be useful for simulating infiltration and evapotranspiration. The field capacity depends on soil texture, soil structure, and organic content and is measured in units of m^3water / m^3soil (Narasimhan, 2009). There are many definitions of field capacity, but for the purpose of this paper it can be described as the maximum volumetric soil water content held against the force of gravity after all excess water has been drained (Fazackerley and Lawrence, 2011). According to Veihmeyer and Hendrickson (1931), this value can be measured two days after a rain event in pervious soils.

This project utilizes soil moisture sensors that are inserted into a plot of the full depth of soil with vegetation (7.6 cm soil depth, plot area 35 cm x 58 cm) taken from the green roof on the Onondaga County Convention Center in Syracuse, NY. The plot is used with a drip-type rain simulator to determine field capacity of the green roof soil under three different rain intensities.

There are two main objectives of this project. The first is to determine the field capacity of a large, extensive green roof in a four-season climate in the Northeastern US using a rain simulator in a laboratory setting. This experimental result is compared to a theoretical value based on fundamental characteristics of the soil. The second objective is to determine how different rain intensities affect the time to onset of runoff. This research is important in preparing to use computer models to predict the hydrologic performance of this green roof in both cold and hot weather. The roof is well-instrumented to provide experimental data over a wide range of conditions for comparison with computer model results to improve our understanding of the hydrology of green roofs.

METHODS
How rain intensities were chosen

Rain event data were collected from the Convention Center green roof tipping bucket from 2015 to 2017 in order to determine the range in rain intensities to simulate. As seen in Figure 1, four mm/hr was chosen because it represents a peak rain intensity in the 50th percentile. Fourteen mm/hr was chosen because it is a
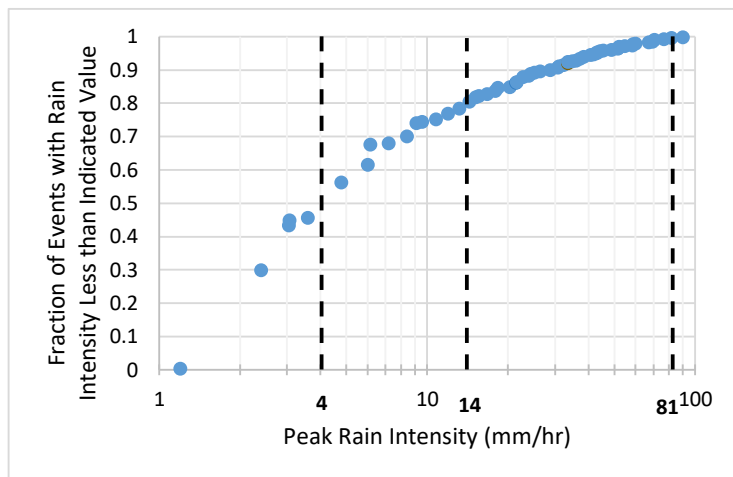

Figure 1: Fraction of rain events on the Convention Center green roof from 2015 – 2017 with peak rain intensities less than the indicated value (N=373). Each rain event has a total accumulation of 0.1 mm or greater.

relatively high peak intensity (80th percentile). Finally, an intensity of 81 mm/hr was chosen to examine the effects of extreme peak intensities (98th percentile).

Rain simulator and experimental setup
As seen in Figure 2, the rain simulator consists of a water source that feeds into a drip former box. There are small holes in the box for droplets to fall through. The plot from the green roof is placed underneath the box.

Figure 2: Drip-type rain simulator with plot from Convention Center Green Roof in Syracuse, NY

The rain simulator is calibrated directly before each experiment to ensure a constant and accurately measureable rain intensity. The first step in calibrating the rain simulator is to place a known volume of water in the drip former box and then allow additional water to flow into the box to exactly balance the droplets falling out below the box. A bucket is used to collect the droplets while the water in the box is monitored to ensure a constant volume. A specific intensity is attained by maintaining a calibrated constant volume in the drip former box. A greater water volume and thus greater height of water in the box will result in higher intensities. Smaller intensities are obtained by inserting small pieces of fish line into the holes in the bottom of the box.
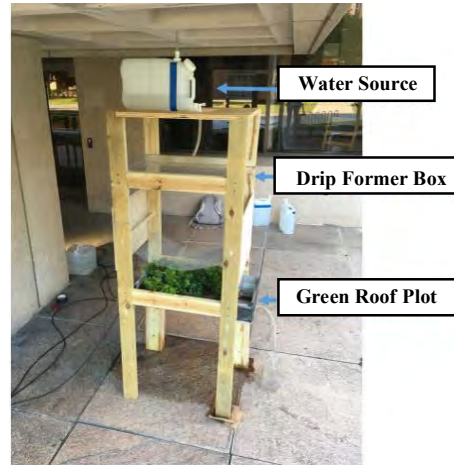
Before the green roof plot is placed under the simulated rain, three soil moisture sensors are inserted at equal depths into the side of the plot. For two experiments (reaching 4 mm/hr and 81 mm/hr intensities), Campbell Scientific 615 soil moisture sensors were used. These sensors were calibrated with one new CS655 sensor, which has a $\pm$ 3% volumetric water content accuracy with manufacturer calibration. The 14 mm/hr experiment used three CS655 sensors. After a desired rain intensity is reached, the green roof plot is placed at a fixed distance below the drip former box at a 1% slope to mimic the slope of the green roof, and volumetric water content data are collected.

As the experiment continues, it is noted when runoff occurs. The plot is kept under a constant rain intensity until runoff becomes steady and volumetric water content has reached a constant value. At this point, the rain is stopped and the soil moisture sensors continue to collect data for 48 hours so that field capacity is determined. Evapotranspiration is assumed to be negligible because the plot is left in a dark basement laboratory, where relative humidity is expected to be high, while data are being collected.

Calculation of field capacity based on soil characteristics
Dingman (2002) provides the following equation for field capacity:

$$\theta_{fc} = \phi * (\frac{|\psi_{ae}|}{340})^{\frac{1}{b}} \qquad (1)$$

where θ_{fc} is the soil field capacity, ϕ is the porosity, ψ_{ae} is the air-entry tension in cm, and b is the exponent describing the moisture characteristic curve. The data collected in the rain simulation experiments can be compared to this model.

RESULTS

Figure 3 shows volumetric soil water content measured during a period of 48 hours for three rain intensities: 4 mm/hr, 14 mm/hr, and 81 mm/hr. The point shown in the first 5-hour period represents when runoff is first observed for each experiment. During each test, the water content increases during the simulated rain event, levels out once soil is saturated and rain is stopped, then gradually decreases until the decline can be considered negligible and field capacity is measured. The results of Figure 3 show that the water content in all three experiments reaches a maximum of around 0.12 when the soil is fully saturated and that the field capacity reached is about the same for the three intensities, as shown by the dashed lines, at 48 hours.

The findings presented in Table 1 show that the field capacities reached for the three intensities range from 0.069 to 0.088, averaging 0.081. Table 1 also indicates that as rain intensity increases, time to onset of runoff decreases.

Table 1: Field Capacity and Time to Onset of Runoff for Different Rain Intensities

Rain Intensities	4 mm/hr	14 mm/hr	81 mm/hr
Field Capacity	$0.086 \frac{m^3}{m^3}$	$0.088 \frac{m^3}{m^3}$	$0.069 \frac{m^3}{m^3}$
Time to Onset of Runoff	2 hours 42 minutes	1 hour 30 minutes	14 minutes

DISCUSSION

As seen in Figure 3, there is a noticeable increase in soil water content during each simulated rain event. A greater rain intensity gives a sharper increase in water content. Figure 3 shows that after water content has reached a maximum value of 0.12, the curve remains at this value for a short time and rain is stopped. At this point, a gradual decrease in water content can be noted in the three graphs. All three plots show an initial steeper decrease directly after the rain is stopped followed by a more gradual decrease. At the time when the curve becomes less steep, percolation occurs and the water begins moving out of the large soil pores and is being replaced by air (Zotarelli, 2010). The water content curves continue to decrease as water slowly drains from the soil. After 48 hours, the drainage rate becomes negligible and field capacity is determined (Dingman, 2002). At this point, the large soil pores are filled with both air and water, and the smaller pores are still full of water (Brouwer et al. 1985). In general, green roof soil is made up of mostly large pore spaces rather than the small pore spaces that contribute to water retention at field capacity (Stovin et al. 2015). The mass median diameter of the soil particles at the Convention Center green roof is 4.0 mm, suggesting a similar size for pore spaces (Wu, 1987). The soil porosity is $0.512 \frac{m^3}{m^3}$.

The results in Table 1 show that the rain intensity does not seem to have an impact on field capacity. A particle size analysis of the green roof soil indicates the soil texture to be similar to sand, which provides parameter values used in Equation 1. From this equation, the predicted field capacity of the Convention Center green roof is 0.17. This value is also smaller than the typical value of 0.3 noted by Jarrett (2009), although roughly double the value measured in the current work. There is some uncertainty in the value generated by the equation. Further analysis of the green roof soil texture will be completed in future work.
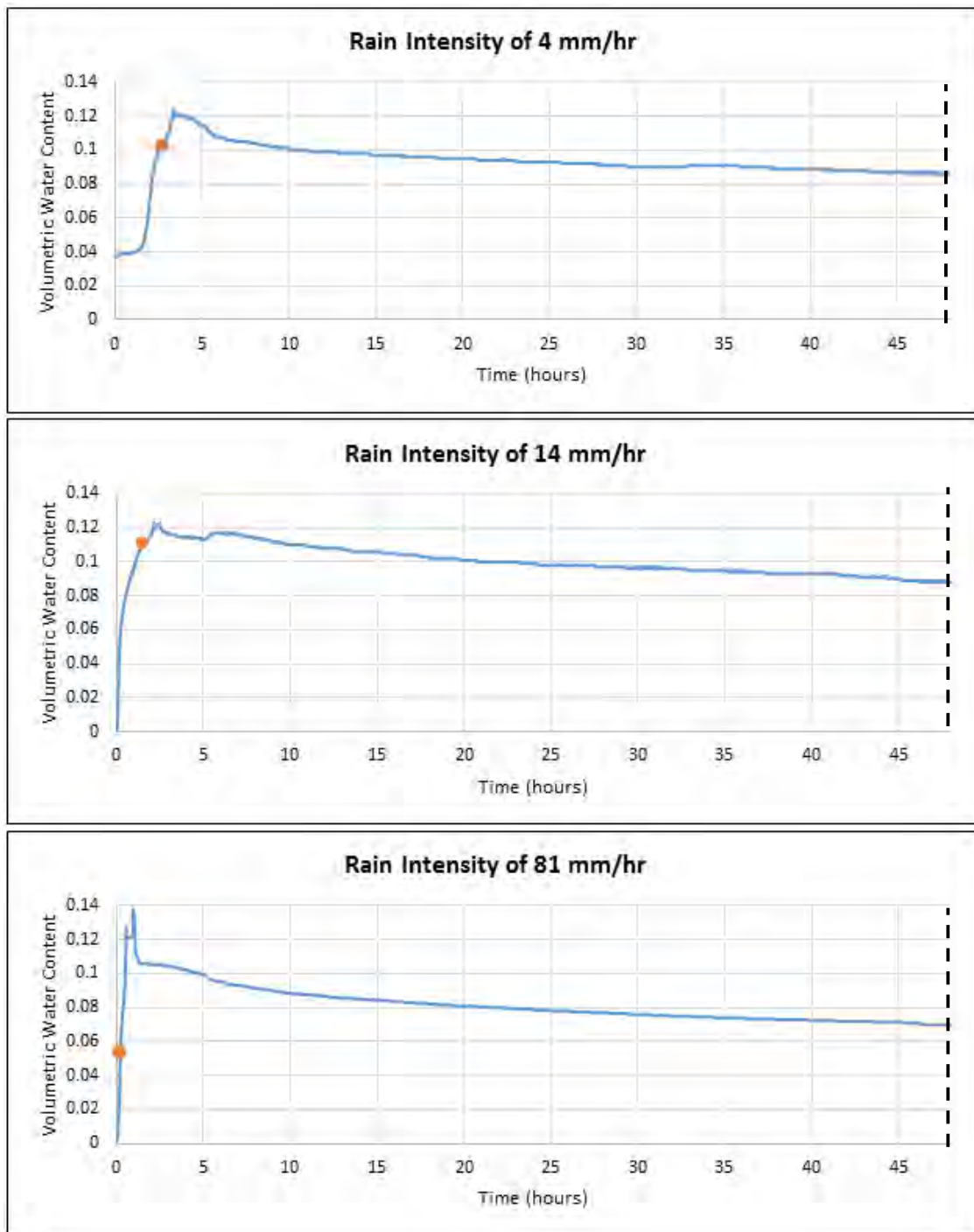
Figure 3: Volumetric Water Content vs. Time for Rain Intensities of (a) 4 mm/hr (b) 14 mm/hr, and (c) 81 mm/hr

The average field capacity of a green roof is said to be about 0.3 (Jarrett, 2009). Therefore, the field capacity measured in this project is low. Experiments are currently underway to investigate this low value.

CONCLUSIONS

A critical parameter of green roof models is the estimation of field capacity. The findings of this work indicate that the field capacity for the green roof on the Convention Center in Syracuse, NY is about 0.081. This result can be incorporated into green roof models to predict maximum soil storage capacity under various conditions. The results of this project also show that the time to onset of runoff decreases as rain intensity increases. This information will help green roof designers improve the performance of engineered soil and estimate how much runoff can be reduced. In addition, the use of a rain simulator and soil moisture sensors can be valuable for collecting data on a small scale for a green roof that does not have a monitoring system installed. This can be valuable for modeling green roof performance in a variety of climates.

ACKNOWLEDGMENT

REFERENCES

Bowyer-Bower T.A.S. and Burt T.P. 1989. Rainfall simulators for investigating soil response to rainfall. *Soil Technology,* Vol. 2, pp. 1-16.

Brouwer C., Goffeau A., and Heibloem M. 1985. Soil moisture conditions. *Introduction to Irrigation,* Food and Agriculture Organization of the United Nations.

Dingman S. Lawrence. 2002. *Physical Hydrology,* Long Grove, Illinois: Waveland Press, pp. 235.

Fazackerley S. and Lawrence R. 2011. Automatic in situ determination of field capacity using soil moisture sensors. *Irrigation and Drainage,* Vol. 61, pp. 416-424. DOI: 10.1002/ird.646

Jarrett A. 2009. Green roofs for stormwater. *Penn State Extension.* https://extension.psu.edu/green-roofs-for-stormwater.

Mentens J., Raes D., and Hermy M. 2006. Green roofs as a tool for solving the rainwater runoff problem in the urbanized 21st century? *Landscape and Urban Planning,* Vol. 77, pp. 217-226. DOI: 10.1016/j.landurbplan.2005.02.010

Narasimhan T.N. 2009. Hydrological cycle and water budgets. *Encyclopedia of Inland Waters,* pp. 714-720. DOI: 10.1016/B978-012370626-3.00010-7

Stovin V., Poe S., De-Ville S., and Berretta C. 2015. The influence of substrate and vegetation configuration on green roof hydrological performance. *Ecological Engineering,* Vol. 85, pp. 159-172. http://dx.doi.org/10.1016/j.ecoleng.2015.09.076

Veihmeyer F.J. and Hendrickson A.H. 1931. The moisture equivalent as a measure of the field capacity of soils. *Soil Science,* Vol. 32, pp. 181-194.

Wu, L. 1987. Relationship between pore size, particle size, aggregate size and water characteristics. (Unpublished master's thesis). Oregon State University, Corvallis, OR.

A Study on Natural Lighting Design Strategies for Teaching Buildings in Hot-summer and Cold-winter Zone of China—A case of the Arts and Sciences Building of Xinyang Normal University

Xinyue Yang[1], Jiehui Wang[1, *], Juanli Guo[1]

[1]School of Architecture, Tianjin University, China

[*]*Corresponding email:645896526@qq.com*

ABSTRACT
The natural lighting of buildings plays an important role in creating a comfortable indoor light environment and reducing the energy consumption of artificial lighting. Teaching buildings have special requirements for the indoor light environment. Classroom glare, corridor backlit, and low natural illumination in corridor are light pollution problems easily appear in teaching building, which cannot be ignored in the design of teaching building. Regarding the issues above, the paper took the Arts and Sciences Building of Xinyang Normal University as an example, through the architectural modeling, space forms, facade effects and other features, used VELUX simulation software to simulate the illuminance and daylighting parameters of different sunroofs and provided solutions for classroom glare and corridor lighting. Ultimately, the paper analyzed the building lighting energy saving schemes based on regional climate and environment, and found out the best balance point for the energy saving design of lighting and thermal environment, meanwhile, provided valuable and practical reference for lighting design of corridor skylights in the region.

KEYWORDS
Teaching building, Natural lighting, Design strategy, Hot-summer and Cold-winter

INTRODUCTION
The architect Ludwig Mies Van der Rohe said: "The history of architecture is the history of human struggle for light, the history of the window." The lighting discussed in the article refers to the use of direct, reflective or other aids to provide natural light to the interior of a building.

It is an important energy-saving means to optimize the design of lighting and shading for public buildings with different functions. A good architectural light environment can improve the visual comfort of indoor personnel, which also has a very important influence on people's physical and mental health. The teaching buildings have many problems in natural lighting, such as large lighting power consumption and glare which greatly reduce the quality of indoor light environment.

For the study of the top lighting of public buildings, most of them are concentrated in the skylight design for the space with large depth. It also has many research methods and design strategies on indoor glare. In specific climate such as hot-summer and cold-winter area, for the special lighting issues of teaching building including corridor skylight design, glare of side windows and corridors lack of systematic research and solutions. Computer simulation is been used to analyse the influence of inner corridor various factors on the natural lighting (Zhifang Zhang, 2011). Hao Xie summarized several design points of the public building skylight. How to put forward the corresponding design technology strategy for the special needs of education building in light environment is the key to solve the indoor natural lighting problem.

METHODS

Educational building lighting standards

Architectural lighting design standards (GB50033-2013) stipulated that the corridor lighting of the teaching building should not be lower than the standard value of the lighting level V. In this project, the illuminance of the area with roof lighting shall be 75lx, and the lighting factor shall be 0.5%.

Description of project

The comprehensive building for liberal arts and sciences to be built is in Xinyang Normal University, including the roof skylight of Building A1, the corridors of Buildings D and F, and the side windows of the classroom. The Building A1 has 12 floors, and the corridors are illuminated by both sides of the windows. To achieve the Architectural Lighting Standard, increase indoor comfort, 10-12 layers will add the skylight to meet the indoor light environment requirements through the reasonable design of natural lighting. The side windows in classrooms and corridors glare easily when it's sunny. Therefore, effective shading equipment is needed to avoid glare and create a good learning environment for students.

Figure 1. The model of Arts and Sciences Building

Specific design content

Simulation software selection and parameter setting

The solar radiation conditions are determined according to the location of the area. In the corridor lighting simulation, set the height of the reference surface to 1.5m, and the selected weather conditions for the winter solstice cloudy day. VELUX natural lighting simulation software is used to simulate the illuminance, daylighting factor and other parameters of different skylights, in order to compare their lighting effects.

Corridor skylight design

The design of the skylight is based on the building lighting standards in the area, and considering the balance of skylight lighting and heat collecting effects. Through simulation optimization, the skylight design schemes suitable for the teaching corridor of the area are analysed showed in Table 2.

Table 1. Advantages and disadvantages on skylights

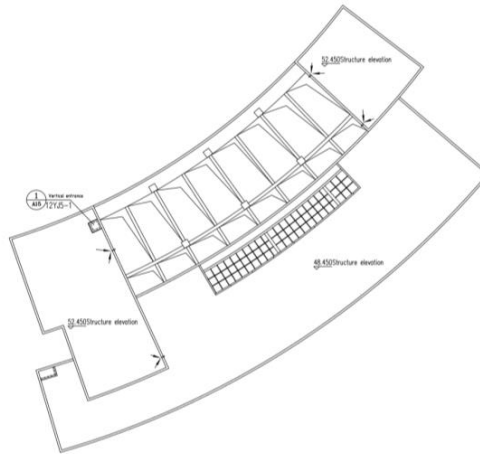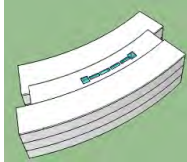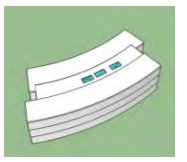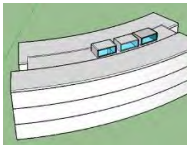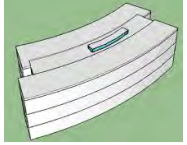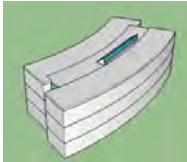| Type of top light	Advantages	Disadvanteges
Flat skylight	High lighting efficiency	Easy to glare, higher heating load
Rectangular skylight	Uniform daylighting, easy on ventilation	Complex roof structure
zigzag skylight	No glare	Low lighting efficiency in winter
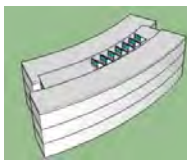
Figure 2. Position of corridor skylight

Table 2. Design of the corridor skylight.

Type of skylight	Design 1		Design 2	
	Graphic	Design parameter	Graphic	Design parameter
Flat skylight		Total area：20 ㎡ Two pieces2×2 ㎡ Four pieces1×3 ㎡ Area ratio of window to floor:1/23		Total area：24 ㎡ Three pieces2×2 ㎡ Area ratio of window to floor:1/19
Rectangular skylight		North and south Total area：52.3 ㎡ Area ratio of window to floor:1/8.8		Window all around Total area：32.42 ㎡ Area ratio of window to floor: 1/14.3
zigzag skylight		Total area：28.42 ㎡ Incline：40° Interior surface: White latex paint		Total area：24.71 ㎡ Incline：40° Interior surface: White latex paint

Corridor glare design research

Due to the climate characteristics of the hot-summer and cold-winter areas, shading facilities are required to not only cover the sun radiation in the summer, but also allow the solar radiation to enter the interior as much as possible in winter. Therefore, The selection of shade strategies should be based on the climate characteristics of the area.
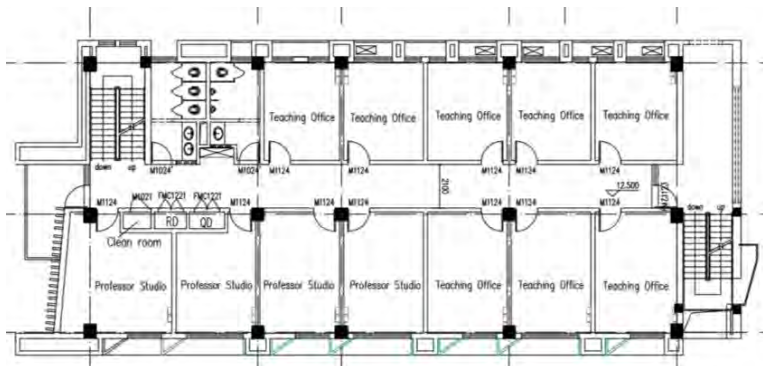
a)
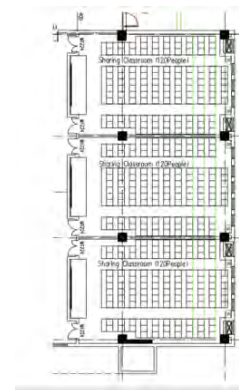
b)

Figure 3. a) Corridor plan in Building D , b) Classroom plan in Building F

RESULTS
Simulation result of corridor skylight
The VELUX simulation software was used to simulate the mentioned skylight design scheme, and the minimum illuminance during the day and daylighting factor values under different skylight forms were obtained. The simulation results are shown in the Table 3.

Table 3. Corridor skylight lighting parameters simulation results

Type of skylight		Flat skylight	Rectangular skylight	zigzag skylight
Plan 1	Minimum illuminance during the day（lx）	65.1	17.0	31.0
	Lighting factor（%）	1.1	0.2	0.6
Plan 2	Minimum illuminance during the day（lx）	84.6	13.8	21.4
	Lighting factor（%）	1.3	0.2	0.4

| a) | b) | c) |
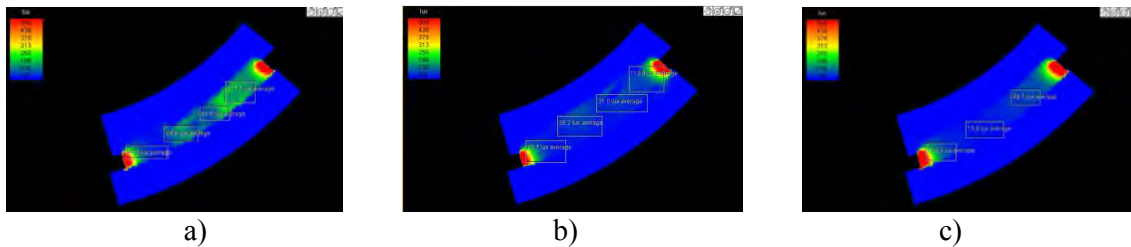
Figure 4. Illuminance during cloudy winter solstice. a) Plan 2 of Flat skylight, b) Plan 1 of zigzag skylight, c) Plan 2 of Rectangular skylight

Shading measures
After simulating the natural illumination in classrooms and corridors, it is found that the classroom relies on one side window to light has different illuminance values. The area close to side window is brighter. On the contrary, the area farther from the side windows is darker. The indoor light environment is not ideal. It is clear that corridor will generate backlight without shading measures. The simulation results are shown in the Figure 5.

| a) | b) |
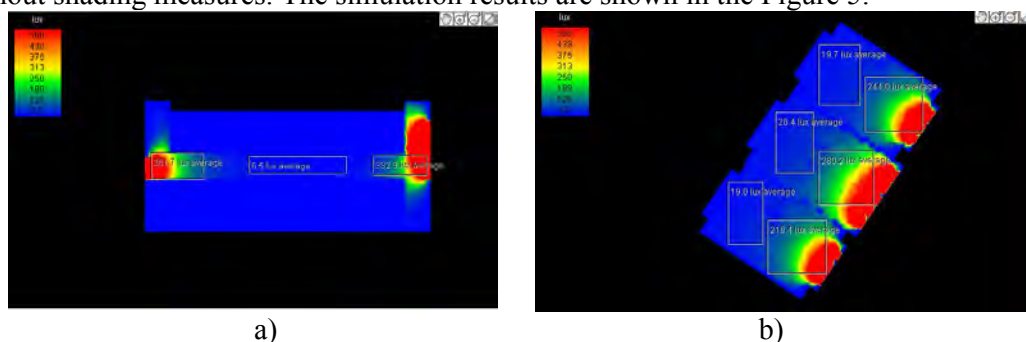
Figure 5. Illuminance during summer solstice day.a) Corridor, b) Classroom

According to the characteristics of building space, several applicable shading strategies are selected and optimized.
Higher lighting side window
It is the side window set above the sight line that can be used in corridors and classrooms to improve the illumination inside. According to *Architectural lighting design standards(GB50033-2013)*, The total area of the windows on both sides in corridors is

determined to be 6.3 ㎡, The size of each side window is 2m×1.6m, and 1.9 meters above the ground.

Reflector

It can provide more natural light for the interior space while preventing excessive direct light from entering the room which may create glare. The addition of reflectors can significantly improve the uniformity of reference surface illumination. Indoor illumination uniformity from small to large is arranged as: non-reflective plate <internal reflector <external reflector <internal and external reflector.

Outdoor reflector

Indoor reflector

a)   b)

Figure 6. a) The principle of reflector, b) Separately controled venetian blinds.

Venetian blinds

The user adjusts the appropriate blade angle according to different seasons to maximize the sunlight, so that the interior space of the classroom gets sufficient diffuse light. For buildings that do not have separate lighting windows and landscape windows, separately controlled blinds can be used to maximize the advantages of the upper and lower windows. Blinds used for outdoor shading are usually made of galvanized ste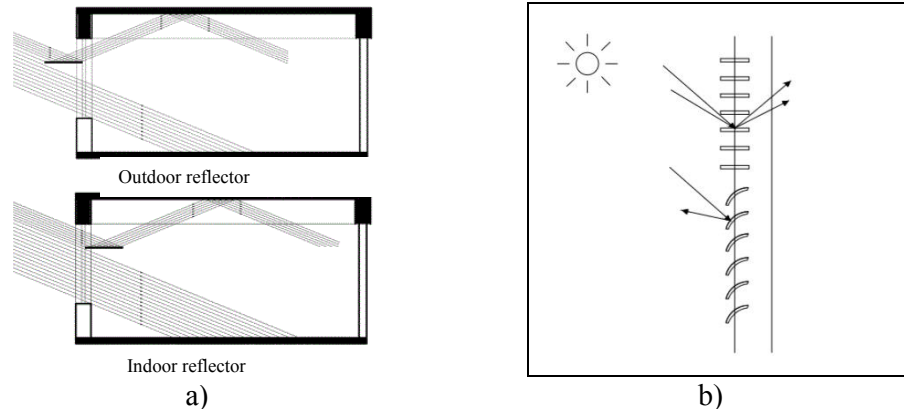el, anodized aluminum or colored aluminum and plastic (PVC). For ease of adjustment, the width of the external shading blade is usually about 100mm, and the pitch of the blade is set to 90mm (Wei Yu, 2012).

Venetian blinds are mainly horizontal and vertical. Research test findings shows venetian blinds of different rotation angles can block sunlight at different height angles and directions.

Table 4. The commonly setting method of venetian blinds

Venetian from	Rotation method
Horizontal blinds	Parallel to normal（Level 0°）
	Rotate 45° counterclockwise（Level 45°）
Vertical blinds	Parallel to normal（Vertical 0°）
	Rotate 45° counterclockwise（Vertical 45°）
	Rotate 45° clockwise（Vertical -45°）

DISCUSSIONS

From the above simulation results, it is found that when choosing plan 2 of plat skylight whose area is 24m², the natural illumination of the corridor can meet the requirements of the lighting of the whole year. Both rectangular skylight designs are unable to meet the requirements of natural light throughout the year for the three-tier walkway. However, their windows open around to avoid glaring, moreover, they are easy to open that promote natural ventilation and reduce mechanical ventilation and cooling energy consumption. The skylight area used in the two designs of the zigzag skylight is the smallest area, and the simulation

results do not meet the requirements. Due to the limitation of the skylight design position, it is difficult to increase its area. The zigzag skylight design with a window angle of 40° and interior surface of white latex paint is slightly lower than the requirement. The winter illumination may be slightly lower, but the zigzag skylight is easy to open that can improve indoor ventilation.

For some public buildings such as office and teaching buildings, the choice and design of shading measures, if the main consideration is summer shade, an outdoor reflector is generally installed to block the light with high solar elevation angle in summer and reduce building cooling load. At the same time, it reflects light to interior ceiling and enhances secondary reflections. When using a reflector to introduce light, it can also be used together with a reflective ceiling to form a light guide system.

Through the analysis of corridor skylight design and the side window shading measures of the project, the application technology of the teaching building light environment in the hot-summer and cold-winter area can be obtained and is summarized as follows.

a) The flat skylight has the best lighting effect. If the natural ventilation in the corridor is good, the skylight can be selected. The rectangular skylight and the serrated skylight can be selected to improve the natural ventilation in the corridor.
b) It is more suitable to adopt higher side lighting window and vertical blinds in order to solve the problem of backlighting in corridors. For the east side window of the corridor, it can be set with vertical blinds rotated at a certain angle to avoid direct sunlight in the morning which may generate backlighting, and to make the corridor brighter.
c) In order to solve the problem of classroom glare, you can choose high side windows, reflectors and venetian blinds.

CONCLUSIONS

Improve the natural lighting quality of teaching buildings is the key to creating a good learning environment and improving people's visual comfort. Through the rational use of auxiliary equipment for daylight and sunshade, natural light can be effectively used and controlled, which can not only achieve the purpose of energy conservation, but also can produce distinctive architectural lighting effects. The paper took the Arts and Sciences Building of Xinyang Normal University as an example, with the method of computer software simulation, analysed the lighting design strategy of the corridor in teaching building and shading measures applied to avoiding glare of the corridors and classrooms, ultimately concluded the light environment design technology strategy suitable for the teaching building in the hot-summer and cold-winter area which supported the light design of teaching building in that area.

REFERENCES

Hao Xie. 2008. Public building sunroof design strategy. *Energy Saving Technology*, 26(4), 353-357

Liuqing Pan. 2016. Optimization of light environment in typical teaching buildings, Nanjing University(China),137 pages.

Wei Yu. 2012. The study on the shading of the east and west Windows of building in hot-summer and cold-winter area, Huazhong University of Science and Technology(China), 79 pages.

William O'Brien, Konstantinos Kapsis, Andreas K. 2103. Athienitis. Manually-operated window shade patterns in office buildings: A critical review. *Building and Enviroment*, 60, 319-338

Zhifang Zhang. 2011. Study on Natural Lighting Optimization Strategy of Interior Gallery with Single Interior Gallery, Hebei University of Engineering(China), 93 pages.

Analysis of thermal bridges in insulated masonry walls: a comparison between vacuum insulated panels and expanded polystyrene

Adrian Bucur[1], Ligia Moga[1]

[1]Faculty of Civil Engineering/Technical University of Cluj-Napoca, Romania

*Corresponding emails: bucuradrian90@yahoo.com, ligia.moga@ccm.utcluj.ro

ABSTRACT
The paper presents a comparative study between the thermal performances of a couple of masonry walls with no insulation and then insulated with vacuum insulation panels and expanded polystyrene. The research purpose is to demonstrate the superior thermal performance of the vacuum insulation panels compared to common thermal insulation, in initial state and even after 25 years in service. It also provides the steps to determine the effective thermal resistance of the buildings elements insulated with vacuum insulation panels, considering both local and geometric thermal bridges. Results emphasize that even after 25 years in use, the walls insulated with vacuum insulation panels with reduced thickness possess a greater thermal performance than that of the walls insulated with expanded polystyrene with common thickness. This is one of the reasons for which this material should be improved and developed further for the future buildings envelopes.

KEYWORDS
vacuum insulation panels, thermal bridges, steady-state, effective thermal resistance

INTRODUCTION
Vacuum insulation panels are composite nano insulation materials, consisting of a nanoporous core encapsulated by a sealing envelope with multiple functions such as airproofing, waterproofing and radiation thermal transfer blocking. Their thermal conductivity in initial state is 4 mW/(mK), about 8-10 times lower than those of the common thermal insulation materials such as expanded polystyrene or mineral wool. Also, even if the envelope is damaged and the panel is filled with air, its thermal conductivity is the same as for the core material, i.e. 20 mW/mK for fumed silica, which is still approximately half of that of the expanded polystyrene.

In this paper, a comparative study is made between the thermal performances of several brick masonry walls without insulation and then thermally insulated with expanded polystyrene (EPS) and vacuum insulation panels (VIP), in different thicknesses. For each situation there are determined the effective thermal resistances, taking into account the walls thermal bridges by computing the related linear heat transfer coefficients. There are considered two types of thermal bridges given by the walls corner intersection with a concrete column (see Figure 1) and also by the walls intersection with a balcony slab (see Figure 2). At the same time, there are computed the effective thermal conductivities of the VIP, considering the local thermal bridges developed on their edges. These thermal bridges are analysed and computed in several other studies (i.e. Tenpierik and Cauberg, 2010; Sprengard and Holm, 2014).

The layers of the analysed elements may be observed in the following figures. A levelling rendering is applied on the masonry walls and then the VIP are installed. The panels are protected on their exterior side by a layer of EPS and a decorative rendering. The mounting of

the panels on the levelling layer and of the EPS on the panels is made by adhesion. The balcony slab has a width of 1.00 m and is insulated both at its inferior and superior side.
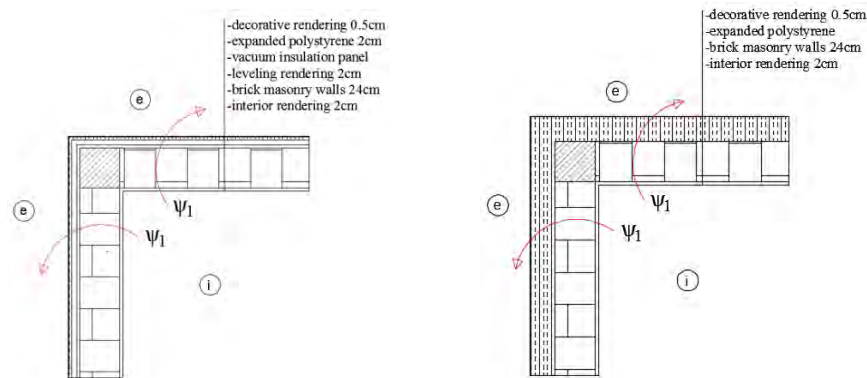

Figure 1. Wall corner intersection - i) insulated with EPS, ii) insulated with VIP
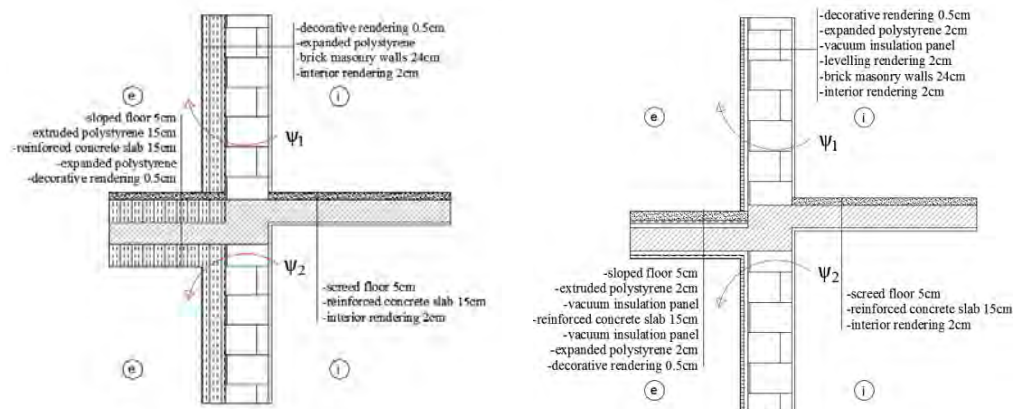

Figure 2. Balcony slab-wall intersection - i) insulated with EPS, ii) insulated with VIP

The analysis is made for the following situations: the walls and balcony slab without thermal insulation, insulated with EPS having a thickness of 10 cm, 20 cm and 30 cm and insulated with VIP of 2 cm, 3 cm and 4 cm, the latter being analysed both in initial state and also after 25 years in service. The maximum chosen thickness of the vacuum insulation panels is the highest one for the adhesion procedure. For larger thicknesses, the material requires a mounting system which develops supplementary local thermal bridges. In the case of balcony slab - exterior wall intersection where EPS is the analysed insulation, on the superior side of the exterior cantilever slab it is considered a layer of extruded polystyrene with a thickness of 15 cm.

METHODS
First of all, there is computed a mean effective thermal conductivity of the VIP. The determination considers the thermal bridges developed on the panel edges using a method from literature (Tenpierik and Cauberg, 2007).

The design value of the centre-of-panel thermal conductivity is λ_{cop}=4 mW/(mK) in initial state after production and λ_{cop}=8 mW/(mK) after 25 years in service, for the panels with envelopes consisting in metallised polymer films (MF) (Heinemann et al, 2010). The difference is given by an inherent decrease of the material thermal performance in time due to the increase of the water content and internal pressure. Two types of panel envelope are considered in analysis: MF2 having a thickness of t_f=84μm and a thermal conductivity of λ_f=0.54 W/(mK) and MF3

having a thickness of t_f =97μm and a thermal conductivity of λ_f=0.39 W/(mK) (Berge and Johansson, 2012). The panels have no gaps or seams between them, therefore their possible influence on the edge thermal bridge is not considered. Having this data, there are computed the linear thermal transfer coefficients ψ_{VIP} related to the thermal bridges developed on the panel edges. Then, there are determined the effective thermal conductivities of the VIP having the following dimensions: 300×600 mm, 600×600 mm and 600×1500 mm and an average value is calculated. The computation is made with the following formula:

$$\lambda_{VIP.eff} = \lambda_{cop} + \frac{\psi_{VIP} \times d \times P}{A} \quad [W/(mK)] \tag{1}$$

where: $\lambda_{VIP.cop}$ [*W/(mK)*] is the design value of the centre-of-panel thermal conductivity, ψ_{VIP} [*W/(mK)*] is the linear thermal transfer coefficient developed on the panel contour, d [*m*] is the panel thickness, P [*m*] is the panel perimeter and A [*m²*] is the panel area.

A next step in the analysis is the determination of the linear thermal transfer coefficients ψ related to the considered walls thermal bridges: walls corner and wall-balcony slab intersection. First of all, the unidirectional thermal resistance of the wall is determined:

$$R_{unidir} = \frac{1}{\alpha_{int}} + \sum_i \frac{d_i}{\lambda_i} + \frac{1}{\alpha_{ext}} \quad [m^2 \cdot K/W] \tag{2}$$

where: d_i [*m*] is the layer i thickness, λ_i [*W/K*] is the layer i thermal conductivity, α_{int} and α_{ext} [*W/m²K*] are the superficial heat transfer coefficients at the interior and exterior surface of the wall

Table 1. Thermal conductivities of the materials used (C107/3, 2008)

Material	λ [W/(mK)]
Brick masonry	0.55
Reinforced concrete	1.74
Renderings: interior, exterior, leveling, protection	0.93
Screed floor, sloped floor	0.93
Decorative rendering	0.7
Expanded polystyrene	0.044
Extruded polystyrene	0.04

The determination of the linear heat transfer coefficients ψ is based on a two-dimensional steady-state modelling in Therm software in accordance with EN ISO 6946:2017. The geometric models were designed according to the details presented in Figure 1 and Figure 2, for each layer being given its corresponding thermal conductivity. Also, the models were built taking into account the recommendations of the C107/3 standard which states that the cross section limits have to be placed at minimum 1.20 m relative to the central element. The interior temperature is considered T_i=20°C and the external one T_e=-18°C. The walls superficial heat transfer coefficients are α_{ext}=24 W/m²K (exterior side) and α_{int}=8 W/m²K (interior side). The limits of the cross-sectioned elements (wall, interior slab) are considered to be adiabatic. After the input data is introduced, the software generates the discretization mesh, computing the temperature and thermal flow values in each of its elements, using the Finite Element Method. The model computation is characterised by the following parameters: the maximum dimension of the grid elements is 25 mm, the maximum number of iterations is 50 and the maximum computation error is 1%. Using the program output data, the linear thermal transfer coefficients are computed with the following formula:

$$\psi = \frac{l_{therm}}{R_{therm}} - \frac{B}{R_{unidir}} \ [W/m \cdot K] \tag{3}$$

where: l_{therm} [m] is the thermal bridge length, R_{therm} [m^2K/W] is the output R-value from Therm, B [m] is the effective dimension of the linear thermal transfer coefficients ψ and R_{unidir} [m^2K/W] is the unidirectional thermal resistance

Finally, using the computed linear heat transfer coefficients, the effective thermal resistances of the walls are calculated for a 2 story building in accordance with EN ISO 10211:2017. Each level is composed of four walls having the same geometrical characteristics: two walls of 3m × 3m and two walls of 3m × 6m. Also, the two stories are separated by a reinforced concrete slab with a balcony cantilever on the building contour, having a width of 1m. The balcony slab is at an inferior level compared to the interior slab, according to the analysed details. The layers and thicknesses of the walls and slabs correspond to the ones presented before (see Figure 1 and Figure 2). The analysis is made for two inferior level walls and two superior level walls, the other four walls of the system having the same characteristics. Each wall has a corner thermal bridge for each of their lateral margins. The inferior level walls have a thermal bridge at their superior edge given by the intersection with the balcony slab. In the same way, the superior level walls have a thermal bridge at their inferior edge. The free margins (section margins) of the walls are considered to be adiabatic.

RESULTS

Table 2. Linear heat transfer coefficients ψ related to the panel edges thermal bridges. Effective thermal conductivities λ of the panels considering these thermal bridges

Panel dimensions [mm]	Envelope type	ψVIP -initial- [mW/(mK)]	ψVIP -25 years- [mW/(mK)]	λVIP.eff -initial- [mW/(mK)]	λVIP.eff -25 years- [mW/(mK)]
300 x 600 x 20	MF2	1.33	1.25	4.265	8.250
300 x 600 x 20	MF3	2.05	1.93	4.409	8.386
300 x 600 x 30	MF2	0.95	0.91	4.284	8.273
300 x 600 x 30	MF3	1.47	1.41	4.442	8.423
300 x 600 x 40	MF2	0.73	0.71	4.294	8.284
300 x 600 x 40	MF3	1.15	1.12	4.461	8.448
600 x 600 x 20	MF2	1.33	1.25	4.177	8.167
600 x 600 x 20	MF3	2.05	1.93	4.273	8.257
600 x 600 x 30	MF2	0.95	0.91	4.189	8.182
600 x 600 x 30	MF3	1.47	1.41	4.295	8.282
600 x 600 x 40	MF2	0.73	0.71	4.196	8.189
600 x 600 x 40	MF3	1.15	1.12	4.307	8.299
600 x 1500 x 20	MF2	1.33	1.25	4.124	8.117
600 x 1500 x 20	MF3	2.05	1.93	4.191	8.180
600 x 1500 x 30	MF2	0.95	0.91	4.132	8.127
600 x 1500 x 30	MF3	1.47	1.41	4.206	8.197
600 x 1500 x 40	MF2	0.73	0.71	4.137	8.133
600 x 1500 x 40	MF3	1.15	1.12	4.215	8.209

According to these results, in the following computations a mean effective thermal conductivity is considered: $\lambda_{VIP.eff.0}$ = 4.25 mW/(mK) – for initial state; $\lambda_{VIP.eff.25}$ = 8.25 mW/(mK) – after 25 years in use.
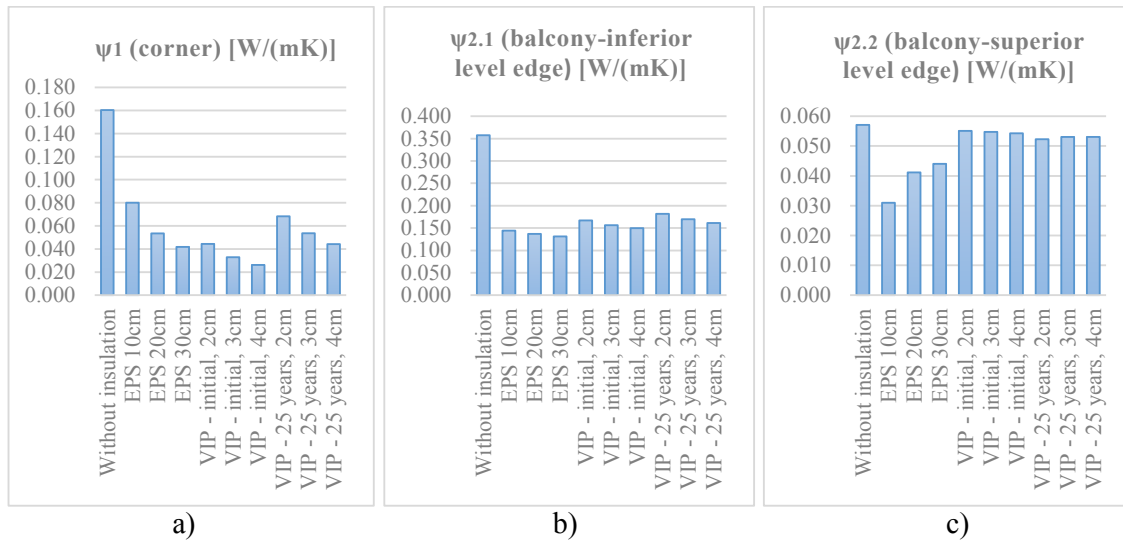
Figure 3. Linear thermal transfer coefficients of the analysed details
a) wall corner intersection, b) balcony slab-wall intersection – inferior level edge
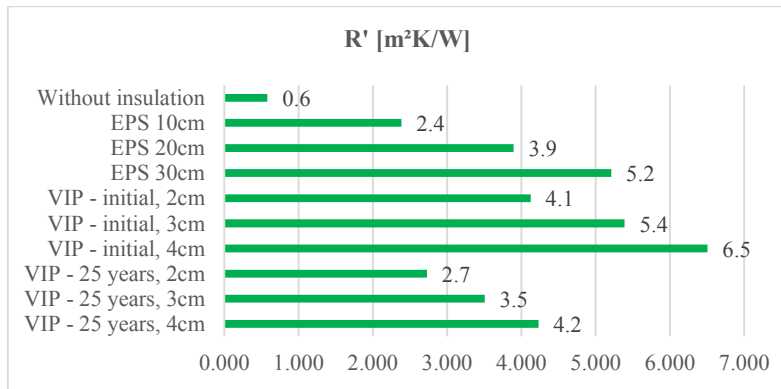c) balcony slab-wall intersection – superior level edge

Figure 4. Average effective thermal resistance of the analysed walls

DISCUSSIONS

The results regarding the thermal bridges developed on the panel contour ψ_{VIP} validate the findings from another studies (Tenpierik and Cauberg, 2007; Sprengard and Holm, 2014), for the panels having λ_{cop}=4 mW/(mK), with MF type envelope and with no gaps or seams between them. One may observe that the thermal bridges developed on the VIP edges after 25 years in service are slightly lower (between 2.60%-6.40%) than those of the new panels, a phenomenon which is more prominent as its thicknesses are lower (see Table 2). At the same time, the envelope type influence the panel thermal performance. Between two panels with same geometrical characteristics, the one with MF2 type foil has a lower linear thermal transfer coefficient with about 54-58% than the one with MF3 type foil. Another aspect revealed by the results is that the linear heat transfer coefficients related to the panels edges decrease with the increase of its thickness.

As a consequence of these local thermal bridges, the panels effective thermal conductivity is greater for those with MF3 type foil, compared to that of those with MF2 type (see Table 2). The difference raises with the increase of the panel thickness and decrease with the increase of the panel 2D dimensions: for 300×600mm – difference of 1.5-2%, for 600×600mm – difference of 1-1.5% and for 600×1500mm – difference of 0.8-1%. At the same time, the panel effective

thermal conductivity is greater than the centre-of-panel thermal conductivity with 0.124-0.461 mW/(mK) for the new panels and with 0.117-0.448 mW/(mK) after 25 years in service.

The thermal bridges of the analysed details are lowered by the use of thermal insulation (see Table 3). In most cases, the thermal bridges of the wall corner detail (ψ_1) with VIP are lower than those of the same detail with EPS. Also, the thermal bridges at the inferior level edge of the balcony detail ($\psi_{2.1}$) with VIP have similar values to those with EPS. At the same time, the thermal bridges at the superior level edge of the balcony detail ($\psi_{2.2}$) with VIP have a rather constant value, regardless of their thickness or age and they have higher values compared to the details insulated EPS.

The effective thermal resistance of the walls insulated with VIP decrease with about 35% after 25 years in use, compared to their initial state, as shown in figure 4. However, one should note that even in this situation, the thermal performance of VIP is comparable to that of the EPS, but for a reduced insulation thickness of approximately 80%. The walls insulated with the panels having a thickness of 4 cm develop an increased effective thermal resistance which recommend this solution for the higher thermal efficiency building systems.

CONCLUSIONS

One of the directions in this research field is the continuous improvement of the existing thermal insulation solutions and the development of new ones in order to increase the overall thermal performance of the buildings. In this regard, the VIP may represent a leap forward, considering its superior thermal performances.

The study reveals that even the VIP develop larger thermal bridges and their performance decrease over time, the building elements insulated with this solution have a superior effective thermal resistance compared to common solutions such as EPS. Therefore, the VIP may be a suitable replacement for the traditional insulations, especially when there is required a reduced insulation thickness.

REFERENCES

Berge A. and Johansson P. 2012 - Literature Review of High Performance Thermal Insulation. Report in building physics, Chalmers University of Technology, Gothenburg, 28 pages

C107. 2008. *C107 Standard 3-2008,* Romanian Standard for the thermotechnical computation of the buildings components

EN ISO. 2007. *EN ISO Standard 6946-2017*, Building components and building elements. Thermal resistance and thermal transmittance. Calculation methods

EN ISO. 2017. *EN ISO Standard 10211-2017*, Thermal bridges in building construction. Heat flows and surface temperatures. Detailed calculations

Heinemann U., Schwab H., Simmler H., Brunner S., Ghazi K., Bundi R., Kumaran K., Mukhopadhyaya P., Quénard D., Salée H., Noller K., Kücükpinar-Niarchos E., Stramm C., Tenpierk M., Cauberg H., Binz. A, Steinke G., Moosman A. and Erb M. 2010. Vacuum Insulation Panel Properties & Building Applications, ECBCS Annex 39 Project Summary Report, 32 pages

Sprengard, C., Holm, A. H. 2014. Numerical examination of thermal bridging effects at the edges of vacuum-insulation-panels (VIP) in various constructions. *Energy and Buildings*, Vol. 85, pp. 638-643

Tenpierik M. and Cauberg H. 2007. Analytical Models for Calculating Thermal Bridge Effects Caused by Thin High Barrier Envelopes around Vacuum Insulation Panels, *Journal of Building Physics*, Vol. 30, No. 3, pp. 185-215

PCM-to-Air Heat Exchangers for Free Cooling Applications

Mohamed Dardir[1,*], Mohamed El Mankibi[2], Fariborz Haghighat[1]

[1]Department of Building, Civil and Environmental Engineering, Concordia University, Montreal, Canada
[2]Ecole Nationale des Travaux Publics de l'Etat (ENTPE), Lyon, France
*Corresponding email: mo_m@encs.concordia.ca

ABSTRACT
Applications of PCM-to-air heat exchangers (PAHXs) were discussed in literature for free cooling application due to their latent thermal storage abilities. This paper aims to justify the generalization of a numerical model of PAHX and to compare the thermal performance of two different configurations of PAHX system. A generalized numerical model is developed and validated based on general apparent heat capacity method. The validation results show good agreement of the generalized approach in terms of averaged error with the experimental data. Model potential and limitations are discussed, and further recommendations are proposed to improve model accuracy. The paper ensures the significant potential of a PAHX ventilated façade configuration in free cooling applications.

KEYWORDS
Latent thermal storage, PCM-to-air heat exchangers, phase change materials, free cooling.

INTRODUCTION
The general awareness of using latent heat thermal energy storage (LHTES) systems has been growing widely due to their increased storage capacity, system efficiency and durability. Phase Change Materials (PCMs) are being used in building applications due to their latent thermal storage abilities. One of the efficient passive cooling concepts is utilizing night cold energy to be re-supplied at hot period of the next day; this needs involving a thermal storage process. Integrating this free cooling concept with a LHTES system can provide an acceptable indoor environment for building occupants. Applications of PCM-to-air heat exchangers (PAHXs) have been widely discussed in literature for free cooling applications. Those applications can be classified into two main configurations: system equipment as a part of ventilation systems, and ventilated facades as improved building envelopes. Both types involve convective heat transfer process between air and PCM.

It can be inferred from literature of integrated PAHX ventilation system configuration that maintaining supplied air temperature that achieves indoor thermal comfort is a current system limitation. Several studies reported that insufficient difference between phase change temperature (PCT) range and inlet temperature during charging affects system storage abilities and overall thermal performance (De Gracia et al. 2015; Waqas and Kumar, 2011). Using a hybrid system of PAHX and a direct evaporative cooling unit, Panchabikesan et al. (2017) experimentally found that the hybrid system increased the cooling potential by reducing the inlet air temperature during PCM solidification. Some studies confirmed the potential of using multiple PCMs in free cooling systems to satisfy workability under high inlet temperatures (Mosaffa et al. 2013). Regarding long-term applications, applying same PCM affects the annual system performance due to changing of ambient temperature profiles in various seasons, consequently, standalone PAHX system cannot maintain indoor thermal comfort all year-round; thermal management is required in such cases (Osterman et al. 2015). On the

other hand, PAHX ventilated envelope configuration showed some achievements in free cooling applications, De Gracia et al. (2013) showed that direct free cooling had a high potential in reducing the cooling loads, however, insufficient difference between night temperature and PCT during solidification results in low system energy storage. Some other studies assured the system cooling potential when combined with night ventilation strategy (Jaworski, 2014; Evola et al. 2014, El-Sawi, et al 2013).

It can be inferred from the literature that PAHX ventilated façade configuration has lower performance than the ventilation system configuration. This paper investigates the performance of the two configurations of PAHXs. By monitoring system outlet air temperature, the current work investigates PAHX system parameters of both configurations that achieve same thermal performance. The main goal of this paper is the justification of a general numerical model of PAHX to be used efficiently in both configurations by designers and building developers. Also, this paper investigates the effect of numerical model generalization on the overall PAHX thermal behavior.

METHODS
In this study, a generalized numerical model for PAHX is proposed and validated based on developments of an earlier version of the model. The model proposes an energy balance approach over number of control volumes to represent the system three media of heat transfer: air flow, encapsulation material and PCM. Full model nodal discretization and heat balance equations are described in detail in (Stathopoulos et al. 2016). Expression of latent heat storage during the phase change of the PCM is achieved by monitoring the change of heat capacity (c_p) values over the temperature range for each control volume. This apparent c_p method assumes fixed rate of heating/cooling during the latent heat transfer process. An earlier version of the numerical model was proposed by Stathopoulos et al. (2016) based on an improved apparent c_p method that proposes multiple values of c_p due to different heating/cooling rates. This method is based on measurements data using Differential Scanning Calorimetry (DSC). Using a developed version of model, this study is performing a comparison between general apparent c_p model and improved apparent c_p model proposed by Stathopoulos et al. (2016) to test the thermal performance of the two configurations of PAHXs: integrated ventilation system configuration, and ventilated envelope configuration.

Model potential and limitations
The model has good potential in terms of predicting the outlet air temperature due to the accurate evolution of c_p values over temperature. PCM thermal conductivity, density and volume are interpolated over temperature through phase change range. The model can auto-generate air density value according to air temperature. However, the early version of model discussed by Stathopoulos et al. (2017; 2016) showed some limitations in terms of its dependency on experimental data. Inlet air temperature and volume flow rate were represented to model every time step; these values were obtained from experimental data. Also, both cooling and heating curves for c_p were determined based on different cooling/heating rates of DSC measurements. Although these procedures provided better model accuracy, the dependency on experimental data obstructed the model applicability for broad investigations instead of single case study. Moreover, the model used a fixed input value for convective heat transfer coefficient, h. As mentioned by authors, the model also neglected the natural convection inside PCM, and long-wave radiation heat transfer between PCM plates. In this paper, further developments are made in terms of generalization of the model to be applicable for broad investigations. Also, the developed model promotes the applications of different PAHX configurations.

Justification of general apparent heat capacity method

Heat capacity value is a key factor in model accuracy. Stathopoulos et al. (2017) proposed the improved apparent c_p model using the experimentally obtained values of c_p, shown in figure 1-a, as model input. They also divided the system to three consequent parts (inlet, middle and outlet) assigning different cooling/heating curve for each part. Towards model generalization, the c_p values are reconsidered as average values for each curve maintaining the same approach of multiple curves for c_p, as presented in figure 1-b. In this case, an average value of c_p is introduced for each curve. Moreover, this approach still requires knowledge and access to the measured values of c_p to calculate the average values. Towards tackling the model limitation of obstructing the broad applications, current model developments assume having two curves for heating and cooling, as shown in figure 1-c. This approach assumes one fixed rate for cooling/heating along the system, which is the original assumption of apparent heat capacity method. This assumption was previously discussed by Stathopoulos et al. (2017) and was claimed to have less accuracy than the improved apparent c_p method due to the differences in heat transfer rate along the PCM plate. Despite the expected less accuracy, this approach can be beneficial to formulate a platform for system designers based on data sheets of c_p cooling and heating curves provided by PCM suppliers. In this paper, investigations for the general apparent c_p approach will be conducted to justify its acceptability and validity with experimental data.
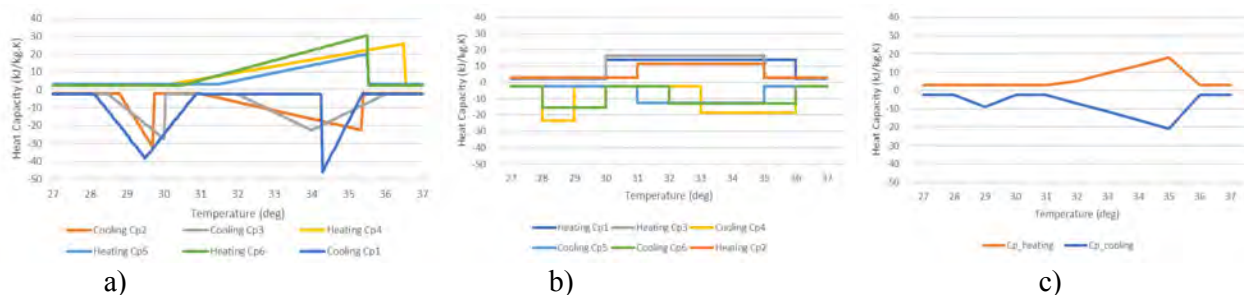

Figure 1. Heat capacity heating and cooling curves for PCM Microtek 37D a) improved apparent c_p method, b) c_p average values, c) general apparent c_p method

Experimental installation

The experimental investigation of PAHX ventilation system type (configuration 1) was illustrated in-detail in (Stathopoulos et al. 2016). A flat plated encapsulation of 16 aluminum PCM plates were investigated under various airflow rates. Microtek 37D paraffin was used as PCM (melting temperature 37.0°C and latent heat of 230 kJ/kg). The total dimensions of the heat exchanger were 1.05m in length, 0.75m in width and 0.25m in height; it contained 31.8kg of PCM. Airflow and air temperature were actively regulated and controlled to the desired velocity and temperature. Inlet temperature varied from around 44.0°C during melting phase and 26.0°C during solidification phase. The available experimental data are for around 15 hours (1.0 hour introductory – 9.0 hours for melting – 5.0 hours for solidification). Sensors were installed within the heat exchanger to measure: PCM and encapsulation surface temperatures in three locations (inlet, mid, and outlet parts), inlet and outlet air temperatures, and airflow rate.

RESULTS

Figure 2 presents the results of the validation for different numerical models with the experimental results. The results show the evolution of system outlet air temperature under volume airflow rate of around 300 m³/h during both melting (discharging) and solidification

(charging). There are three presented numerical models based on the different c_p values discussed earlier: 1- the improved apparent c_p model tested by Stathopoulos et al. (2016) with experimentally obtained values of c_p, 2- the model that is based on developed average values of c_p, and 3- the generalized apparent c_p model that is based on simplified c_p values. The results show that considering an average value for each c_p curve is very close to the improved apparent c_p model. The generalized apparent c_p model shows some discrepancy with the original model and experimental results due to the simplified approach of c_p. For investigating the discrepancy level of the generalized model, a percent error test is performed for both improved and generalized apparent c_p models. Figure 3-a shows the percentage of error of both models compared to experimental data. The results show that both models exceed 10% of error percentage with the experimental data only at the start of each phase changing. Otherwise, the error for both models remains below 10% with the experimental data. In terms of the average error, improved apparent c_p model shows average errors of 3.2% and 3.7% during melting and solidification respectively with the experimental data. While the general apparent c_p model shows average errors of 3.9% and 4.6% during melting and solidification respectively with the experimental results. In comparison with the improved model, the generalized apparent c_p model shows up to 7% of percent error.
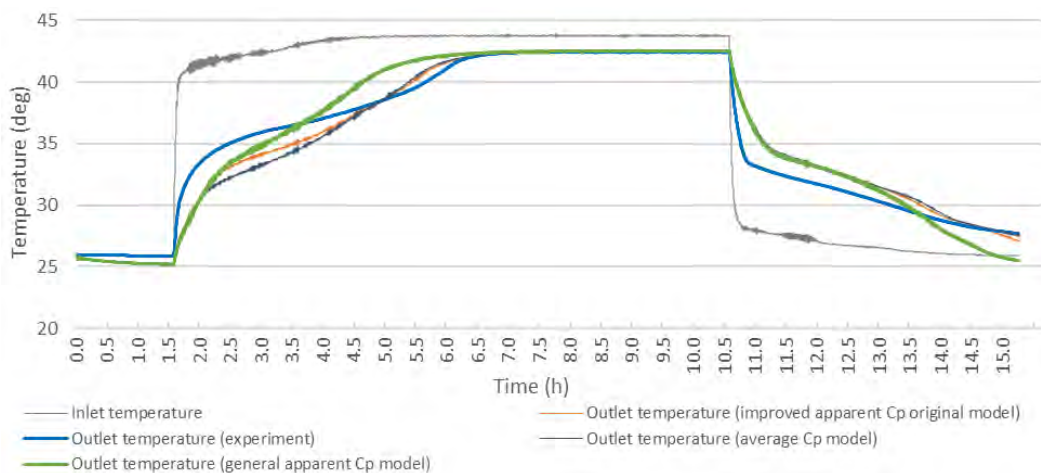

Figure 2. Validation of different models with experimental data

Comparison to ventilated envelope configuration
Using the generalized apparent c_p model, a comparison between the previous investigated PAHX ventilation system unit (configuration 1) and a ventilated envelope PAHX type (configuration 2), shown in figure 4, is held to monitor the thermal performance of the two configurations. In both configurations, inlet air temperature is fixed to two values: 44.0°C during melting and 26.0°C during solidification. Airflow rate is fixed to 300 m³/h. RUBITHERM RT35 is used as a storage medium with thermal properties mentioned in table 1. Two curves for heating and cooling for c_p values are applied and presented at figure 5. The total PCM volume is 0.052 m³. PAHX ventilated façade configuration variables are mentioned in figure 4, with total PCM volume of 0.064 m³. It is worth mentioning that the objective of this investigation is the comparison between the two configurations and not obtaining the best thermal performance of the system. The results, shown in figure 3-b, prove that with almost the same volume of PCM, both configurations show significant conformity with values of outlet air temperature profile.
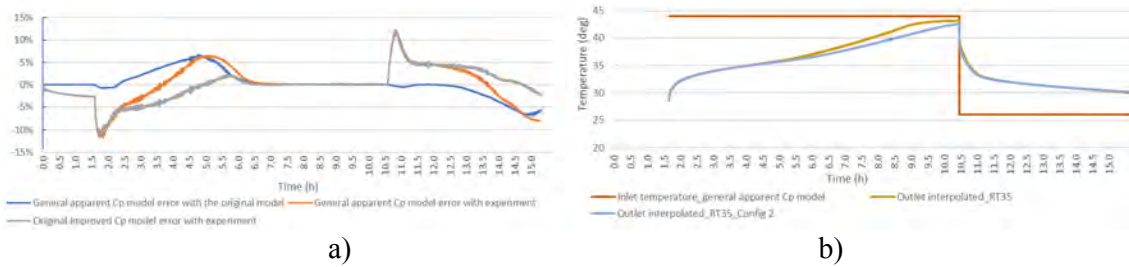
a)   b)

Figure 3. a) Percent error analysis of original and generalized models b) Outlet air temperature of PAHX different configurations

Table 1. Thermal properties of PCM RUBITHERM RT35

Melting range	Solidification range	Heat Storage Capacity	Specific heat capacity	Density	Thermal conductivity	Volume expansion
29-36 °C	36-31 °C	160 kJ/kg	2.0 kJ/kg.K	0.86 *solid* / 0.77 *liquid*	0.2 W/m.K	12.5%

A complementary study is conducted to test the indoor thermal performance of a ventilated façade PAHX type with the given configuration using TRNSYS. A standalone test unit of volume $27.0m^3$ (3.0*3.0*3.0) is proposed with a northern window of $1.0m^2$ and a heavy construction of stone walls (0.3m thick) and concrete roof slabs (0.25m thick). Two systems are compared: the PAHX ventilated façade system, and a conventional ventilation system with the same airflow and inlet temperature as the numerical model. The results show that 4.6% of the cooling loads can be saved during 5.0 hours of PAHX system operation.
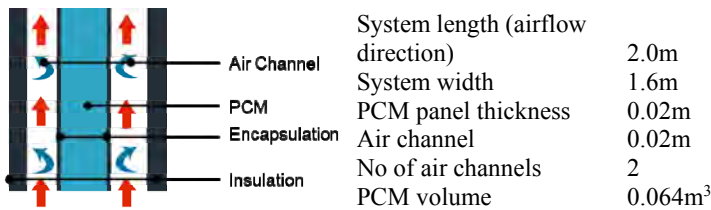

System length (airflow direction)	2.0m
System width	1.6m
PCM panel thickness	0.02m
Air channel	0.02m
No of air channels	2
PCM volume	$0.064m^3$

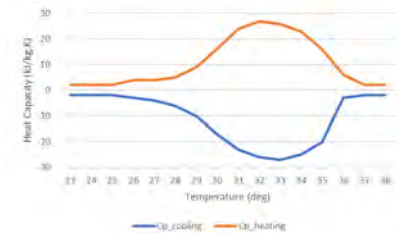Figure 4. Ventilated envelope PAHX configuration   Figure 5. RT35 apparent c_p curves

DISCUSSIONS

With the validation of the general apparent c_p model, the discrepancy at the end of each phase change process is noticed. It means that with the simplified c_p approach the system tends to consume its storage capacity faster than the actual behavior. Accordingly, it can be noticed from the percent error analysis that the general apparent c_p model shows up to 10% as a level of discrepancy, and 3.9% and 4.6% as average errors during melting and solidification respectively with the experimental data due to consideration of system storage capacity. However, one of the advantages of the general model is its in-dependence of the spatial time constrains. Time step, discretization length and investigation duration can be adapted to desired conditions. Regarding general model limitations, the model still uses a fixed input value for convective heat transfer coefficient. Also, the natural convection inside PCM during melting and liquid phase is still neglected. It is expected that model accuracy can be enhanced when heat transfer coefficient is calculated according to airflow conditions. Also, it can be inferred from the results of comparison between the two configurations of PAHX system that the governing parameter in determining PAHX thermal performance is the volume of PCM. Both configurations have almost the same PCM volume and, as reported in results, the both outlet temperature profiles show the same behavior with great level of consistency, especially during solidification process. PAHX ventilated façade configuration shows promising

potential for free cooling applications; it is recommended to improve the model by developing the convective and radiative heat transfer boundaries.

CONCLUSIONS

A generalized numerical model of PCM-to-air heat exchangers is developed and validated in this paper based on general apparent heat capacity method. A simplified approach for implementing heat capacity cooling and heating curves is presented and validated with experimental data. The general approach showed some discrepancies with experimental data. Using a percent error test, the average error of the general model was 3.9% and 4.6% during melting and solidification processes respectively. Referring to its ability of broad applications, the developed general model is very beneficial to building designers due to its in-dependence from experimental data as model inputs. Using the developed general model, a comparative analysis between PAHX ventilation system configuration and a ventilated envelope PAHX configuration is conducted. The study proved that PAHX ventilated façade type has promising potential for free cooling applications.

ACKNOWLEDGEMENT

REFERENCES

De Gracia, A. et al., 2013. Experimental study of a ventilated facade with PCM during winter period. Energy and Buildings, Issue 58, pp. 324-332.

El-Sawi, A., Haghighat, F., Akbari, H., 2013, Centralized latent heat thermal energy storage system: model development and validation, Energy and Buildings 65, 260-271

Evola, G., Marletta, L. & Sicurella, F., 2014. Simulation of a ventilated cavity to enhance the effectiveness of PCM wallboards for summer thermal comfort in buildings. Energy and Buildings, Volume 70, pp. 480-489.

Jaworski, M., 2014. Thermal performance of building element containing phase change material (PCM) integrated with ventilation system – An experimental study. Applied Thermal Engineering, 70(1), pp. 665-674.

Mosaffa, A., Ferreira, C. I., Talati, F. & Rosen, M., 2013. Thermal performance of a multiple PCM thermal storage unit for free cooling. Energy Conversion and Management, Issue 67, pp. 1-7.

Osterman, E., Butala, V. & Stritih, U., 2015. PCM thermal storage system for 'free' heating and cooling of buildings. Energy and Buildings, Issue 106, pp. 125-133.

Panchabikesan, K. et al., 2017. Effect of direct evaporative cooling during the charging process of phase change material-based storage system for building free cooling application - A real time experimental investigation. Energy and Buildings, Volume 152, pp. 250-263.

Stathopoulos, N. et al., 2016. Air–PCM heat exchanger for peak load management: Experimental and simulation. Solar Energy, Issue 132, pp. 453-466.

Stathopoulos, N., El Mankibi, M. & Santamouris, M., 2017. Numerical calibration and experimental validation of a PCM-Air heat exchanger model. Applied Thermal Engineering, Issue 114, pp. 1064-1072.

Waqas, A. & Kumar, S., 2011. Thermal performance of latent heat storage for free cooling of buildings in a dry and hot climate: An experimental study. Energy and Buildings, Issue 43, pp. 2621-2630.

Assessment of the BIPV potential at the city of Prague and their effect on the built environment

Nikolaos Skandalos[1,*], Jan Tywoniak[1,2], Kamil Stanek[1,2], Lenka Maierova[1,2]

[1]University Centre for Energy Efficient Buildings, Czech Technical University in Prague Třinecká 1024, 273 43 Buštěhrad, Czech Republic

[2]Faculty of Civil Engineering, Czech Technical University in Prague, Thákurova 7, 166 29 Prague 6, Czech Republic

[*]*Corresponding email: Nikolaos.Skandalos@cvut.cz*

ABSTRACT
This work highlights the BIPV potential in two urban areas with different characteristics at the city of Prague. Representative building blocks were selected and CitySim software tool was used for the assessment of the hourly irradiation profiles on each surface over one year period. Considering appropriate irradiation thresholds, suitable surfaces were then quantified. Integration criteria are discussed and suitable BIPV applications are proposed considering not only energy performance but also their impact on the quality of built environment. Results indicated that only 5.5% of the total area can be used in Vinohrady and 13.7% in Jizni Mesto contributing on average by 32% and 31% on the hourly electricity demand respectively.

KEYWORDS
Building-integrated photovoltaics, solar potential, architecture, load matching

INTRODUCTION
The building sector is the major consumer of energy, accounting for around 40% of the worldwide consumption (UNEP, 2012). On the road towards Low or Zero Energy Buildings, renewable energy harvesting becomes compulsory and thus photovoltaic systems are expected to be the main technology to generate on-site electricity. PV systems have great potential to be used in the city context through various BIPV products (Shukla et al., 2017). Rooftop PVs are so far considered to be the most common application since it provides the best annual energy harvesting. However, due to significant decrease in prices and technological improvements in PV industry, building facades now represent good potential especially for high-rise buildings. Successful integration of PVs into a building requires both technical and architectural knowledge.

In this context, a suitable procedure is needed to assess the solar potential and propose PV concepts based on the characteristics and cultural aspects of the location. This paper aims to analyse the PV potential of two locations within the city of Prague. Considering the solar availability and shadings for the surrounding buildings, the available area for installation is determined and suitable PV applications are proposed considering all the constraints imposed form the locations and building morphologies. Finally, suitable index is used to investigate the interaction between on-site generation and building's electricity demand on hourly basis.

METHODS
Location characteristics
Two urban areas in the city of Prague with different characteristics were selected and used for analysis and comparison. A representative building block, constitute of residential buildings,

was selected for each location as presented in Fig.1. Case one, Vinohrady, is within a high dense area of the city centre with considerable architectural and cultural value. Houses built around 1900 are characterized by sloped roofs in different shapes and heights. Case two, Jizni Mesto, is a suburban area built in 1970es. Prefabricated high rise buildings are characterized by simple shape, flat roofs and big vertical facades with balconies on South and West orientation.
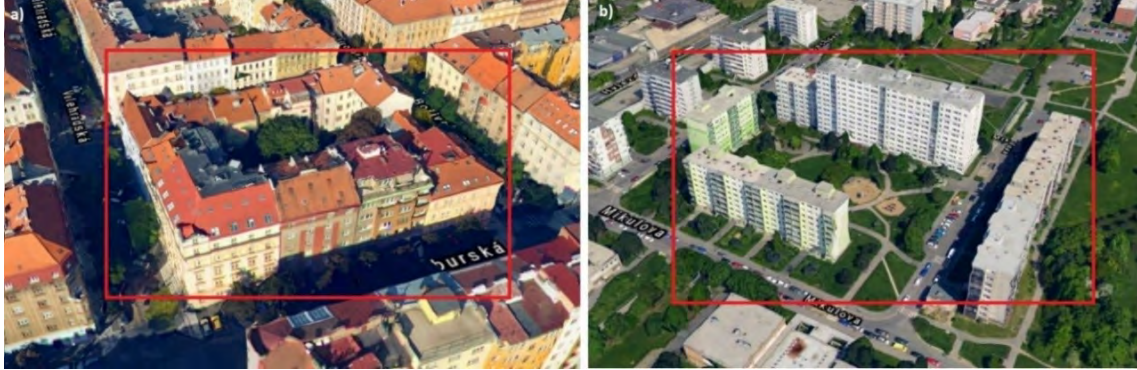

Figure 1. Aerial view of the selected locations in a) Vinohrady and b) Jizni Mesto.

Solar PV potential
Appropriate 3D models for each building block were prepared based on the geometry of the buildings, including dimensions and shape of the roof superstructures (dormer, chimney, etc.). Building surfaces were divided according the floor level, excluding areas that for some reason cannot be considered for PV integration (e.g. north facade). Radiation on building surfaces is commonly influenced by the near environment and thus were the heights of the surrounding buildings, trees and elements in each direction were considered in the model for the evaluation of shading. Afterwards, the 3D model was imported to CitySim Pro, an urban energy modelling tool developed at LESO-PB/EPFL, for further analysis. Incoming solar radiation was calculated in hourly values, according to the type of the building surface and the climate data collected by a nearby meteo station. For each building surface was defined by its area, orientation and tilt angle. Finally, percentage of solar obstruction were calculated as the ratio of the solar radiation within the surrounding context to the one without the surrounding obstacles. Hourly values were solar weighted, annual shading index (SI) was derived according to Eq.1, where $F_{sh,i}$ is the hourly shading factor of each building surface, G_i is the hourly and G_t the annual solar radiation respectively.

$$SI = \frac{\sum_{i=1}^{N=8760} F_{sh} G_i}{G_t} \tag{1}$$

Once the radiation values on each surface are available, they can be analyzed to assess the PV potential. For this purpose, an irradiation threshold was used indicating the minimum amount of annual radiation required for PV system to be beneficial. Such thresholds are somewhat arbitrary; conservative value of 800 kWh/m^2 annually is proposed by many authors (Li et al., 2015), while others define it as a percentage of the horizontal insolation (Vulkan et al., 2018). Considering the technological progress and enormous decline of PV costs within last decade, approximately 58% according to (Maturi et al., 2017), lower values such as 650 kWh/m^2 (Kanters et al., 2014) are still reasonable. To this end, PV potential calculated as the relative fraction (percentage) of the roofs and facades of the buildings that can be used for PV integration. Based on the area of the suitable surfaces a simple model was applied to quantify the annual energy output (E_{PV}) of each building block according to Eq.2:

$$E_{PV} = \eta * PR * \sum_{i=1}^{n_{threshold}} (I_i * A_i) \tag{2}$$

,where η is the PV conversion efficiency, *PR* is the performance ratio representing all system losses (mismatch, inverter..), $n_{threshold}$ is the number of surfaces exceeding irradiation threshold, I_i is the cumulative insolation (kWh/m^2.year) and A_i the relative area (m^2) of surface *i*.

Afterwards, data for the annual electricity consumption of representative buildings in each location, were collected and analyzed in hourly basis according to the occupants (REMODECE, 2008) and typical user profiles (Staněk, 2012). Based on the peak loads and the selection criteria that apply in each location, PV systems were sized properly, while load match index (Voss et al., 2010) was used as indicator of the hourly self-consumption of the PV generated energy.

BIPV integration criteria

It is evident that excessive use of PV systems can often have an adverse effect on the build environment and thus criteria and recommendations about dimensioning and positioning are needed. In order to select an appropriate BIPV application, both technical, architectural and economical aspects should be included. In case of Jizni Mesto, there is no limitations arising from the near environment and thus several scenarios and PV technologies can be considered (Fig.2). High performance modules can be installed on flat roof of the buildings horizontally to camouflage the installation or tilted to optimize performance. On vertical facades, PV modules should be grouped together in an ordered way creating unique textures (e.g. horizontal stripes). In this context, ceramic panels or solar glazing in various colours (Jolissaint et al., 2017) could be a solution, providing good durability and aesthetic quality. Finally, complementary building elements such as windows and existing balconies are well suited to support PV integration representing good compromise in terms of energy performance and aesthetics. In addition, optimized semi-transparent PV elements could be used as shading devices to increase indoor thermal comfort by mitigation of overheating during summer, but still to provide daylighting and to make use of passive heating during winter (Skandalos et al., 2018).

Figure 2. Examples of architecturally integrated PV systems in the two building blocks: (1) PV balconies. Source: Etsprojects; (2) Coloured PV-façade. Source: Swissinso; (3) Roof-added PVs. Source: Cromwellsolar; (4) PV tiles. Source: Tradeford; (5) PV shutter and PV blinds. Source: COLT international, Solargaps; (6) PV terrace. Source: (López and Frontini, 2014).

On the other hand, BIPV integration in the sensitive built environment such as Vinohrady district, is a more challenging task. Applicability of conventional PV modules in buildings with strong architectural or cultural value is limited. Since the full integration and imperceptibility of the technical elements from the public domain is the most important criteria for the acceptance of the BIPV within the historical context (Munari Probst and Roecker, 2015), small scale highly innovative PV products are needed. Suitable surfaces are limited to the sloped roof, flat terraces and vertical facades facing to the courtyard. Based on the geometry of each surface, BIPV applications such as solar glazing or PV tiles, balustrades and PV shutters (Fig.2) constitute effective practices of integration in the building envelope providing a balanced solution between technical and architectural standards as defined in (Frontini et al., 2012).

RESULTS & DISCUSSION
Solar PV potential
Results from solar analysis in both locations are presented in form of annual irradiation colour map (Fig.3). As expected, best solar resources were observed for sloped roofs facing south (Vinohrady), exceeding the 1200kWh/m^2 annually. However, different roof typologies were recognised and thus solar potential varies according to its slope and orientation. Relative results for the flat roofs of Jizni Mesto were slightly lower (around 10%), but still exceed the irradiation thresholds. Conversely, facades in both locations found to receive significantly lower level of irradiation, especially the ones on East and West façade. This is also explained from the increased shading factors. Average solar obstruction can reach up to 57% for a building in Vinohrady (high density) and 22% in Jizni Mesto respectively. Consequently, only a small portion of the total building area can be considered as suitable for PV integration. Percentages for buildings in each location vary between 5-18% in Vinohrady and 15-27% in Jizni Mesto respectively.
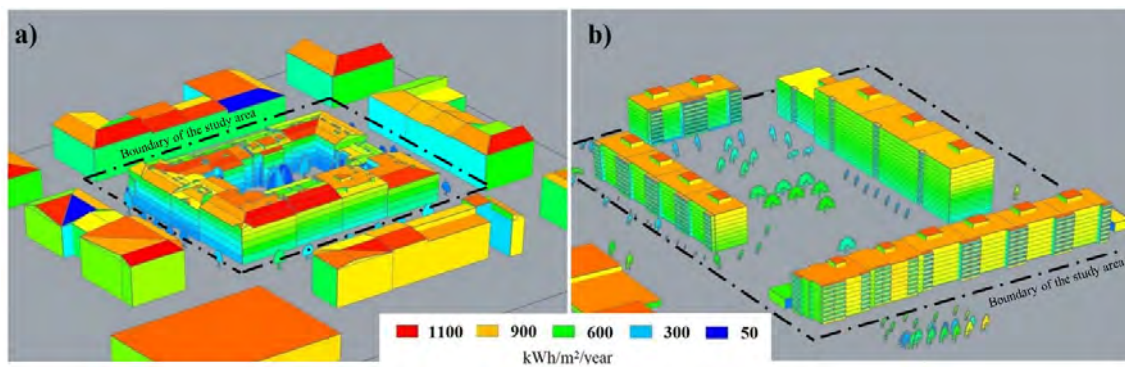
Figure 3. Annual solar irradiation map for each building block in a) Vinohrady and b) Jizni Mesto.

With respect to the hourly irradiation profiles, maximum PV potential in each location was calculated and presented in Fig.4. PV modules were assumed to be installed at the same plane with the building surface considering typical values for the conversion efficiency (η) according to the BIPV application (η=15% for roofs and η=8% for facades/balconies/glazing). For Vinohrady, annual PV generation could be up to 440MWh with peak generation in July (62 MWh). However, 58% of that energy is related to the building surfaces facing streets and thus could not be considered according to the criteria discussed in previous section (Fig.4a). Similar results for the Jizni Mesto revealed 2.7 times higher PV potential (1100 MWh/annually) with relative contribution from roof, façades and balconies by 49%, 45% and 6% respectively (Fig. 4b).
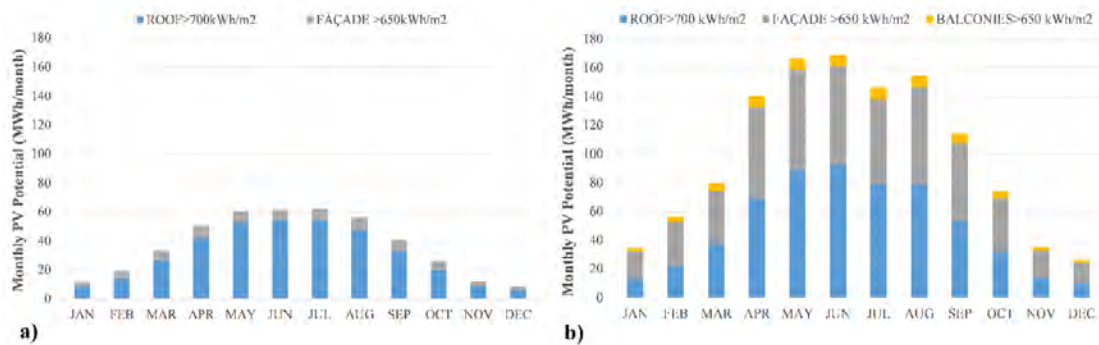
Figure 4: Monthly PV potential for the building block in a) Vinohrady and b) Jizni Mesto based on the selected irradiation thresholds.

System evaluation

Hourly peak loads were calculated and used as indicator, together with the criteria discussed in previous section, to size properly the PV systems in each building. Consequently, suitable PV systems were considered and results regarding the interaction between electricity consumption and generation are presented in Fig.5 for both locations. Despite the PV potential in Vinohrady, available space is limited to only 5.5% of the total building area due to the integration criteria applied. It is obvious that the generated energy is not enough to cover the loads of the building block (Fig.5a). However, almost all the generated PV energy can locally be used within the building block and it is enough to compensate on average by 38% (max value of 49% per building) the hourly electricity demand. In case of Jizni Mesto, there is no such limitations and thus 19% of the area can be used according to the irradiation thresholds. In that case, PV generation is enough to cover the electricity demand during the summer period, but also leads to excess of energy for 35% of the PV operation time (hourly). Therefore, better interaction between generated and consumed electricity is needed to increase the self-consumption of the buildings providing more efficient performance. If maximum load matching is taken into account, integration will be limited to only 13.7% of the total building area leading to lower PV generation (Fig.5b). Alternatively, excess of energy can be used for cooling purposes since peak production coincides with peak cooling demand. Analytical results, regarding maximum load match index (hourly intervals) between the buildings in Jizni Mesto found to be 43%.

CONCLUSIONS

Two representative building blocks, with different characteristics and level of preservation in the urban context of Prague, were selected and analysed for their hourly solar radiation per unit area according to the local weather data. As expected, most of the potential is intrinsically related to roofs, while façades suffer more the shadowing effect caused by the surroundings. According to the integration criteria and energy consumption applied in each location, suitable PV systems were proposed. Only small part of the building area can be used, varying from 5.5% for Vinohrady and 13.7% for Jizni Mesto. Interaction between electricity demand and consumption revealed that proposed PV systems could compensate on average by 32% the hourly energy demand in Vinohrady and by 31% in Jizni Mesto. It is evident that even in areas with sensitive built environment adoption of solar energy is still possible for balancing local electricity needs. Further work is needed to assess the indirect effect (thermal, daylighting) of the proposed solutions. Also economic assessment based on the actual market conditions (BIPV prices, installation costs and electricity tariffs) will also reveal the profitability of the proposed solutions.
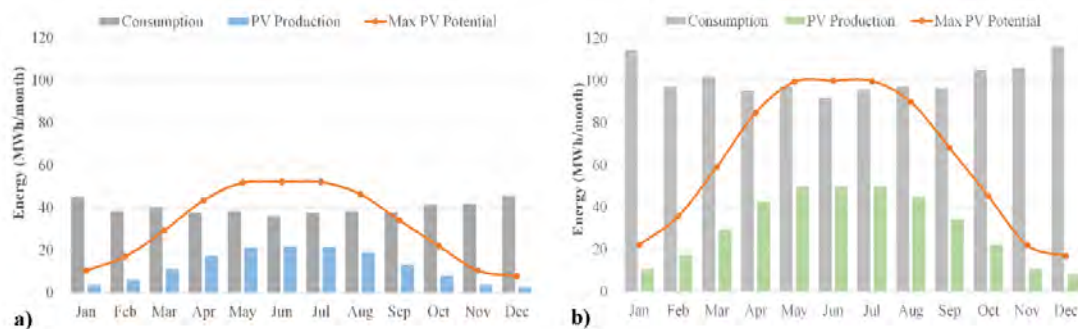
Figure 5: Annual electricity consumption and generation of the proposed PV system together with maximum potential according to irradiation threshold (800kWh/m^2 year) based on monthly data for a) Vinohrady and b) Jizni Mesto.

ACKNOWLEDGEMENT

REFERENCES

Frontini F., Manfren M. & Tagliabue L.C. 2012. A Case Study of Solar Technologies Adoption: Criteria for BIPV Integration in Sensitive Built Environment. *Energy Procedia,* 30**,** 1006-1015.

Jolissaint N., Hanbali R., Hadorn J.C. & Schuler A. 2017. Colored solar façades for buildings. *Energy Procedia,* 122**,** 175-180.

Kanters J., Wall M. & Dubois M.C. 2014. Typical Values for Active Solar Energy in Urban Planning. *Energy Procedia,* 48**,** 1607-1616.

Li, D., Liu G. & Liao S. 2015. Solar potential in urban residential buildings. *Solar Energy,* 111**,** 225-235.

Lopez C.S.P. & Frontini F. 2014. Energy Efficiency and Renewable Solar Energy Integration in Heritage Historic Buildings. *Energy Procedia,* 48**,** 1493-1502.

Maturi L., Adami J., Lovati M., Tilli F. & Moser D. 2017. BIPV Affordability. *33rd European Photovoltaic Solar Energy Conference and Exhibition.* Amsterdam, the Netherlands.

Munari Probst M.C. & Roecker C. 2015. Solar Energy Promotion & Urban Context Protection : Leso-qsv (quality- Site-visibility) Method. *31th PLEA Conference*, Bologna, Italy.

REMODECE 2008. Residential Monitoring to Decrease Energy Use and Carbon Emissions in Europe. *Annual electricity use in the Czech Republic.* Available at: http://remodece.isr.uc.pt.

Shukla A.K., Sudhakar K. & Baredar P. 2017. Recent advancement in BIPV product technologies: A review. *Energy and Buildings,* 140**,** 188-195.

Skandalos N., Karamanis D., Peng J. & Yang H. 2018. Overall energy assessment and integration optimization process of semitransparent PV glazing technologies. *Progress in Photovoltaics: Research and Applications,* 26**,** 473-490.

Stanek, K. 2012. Photovoltaics for buildings, Grada for the Department of Building Structures at the Faculty of Civil Engineering of the Czech Technical University in Prague.

UNEP 2012. Building Design and Construction: Forging Resource Efficiency and Sustainable Development.

Voss K., Sartori I., Napolitano A., Geier S., Gonzalves H., Hall M., Heiselberg P., Widen J., Candanedo J.A., Musall E., Karlsson B. & Torcellin P. 2010. Load Mathing and Grid Interaction of Net Zero Energy Buildings. *EuroSun Conference.* Graz, Austria.

Vulkan A., Kloog I., Dorman M. & Erell E. 2018. Modeling the potential for PV installation in residential buildings in dense urban areas. *Energy and Buildings,* 169**,** 97-109.

Bio-inspired outdoor systems for enhancing citizens thermal comfort in public spaces by learning from nature

Marta Chafer[1,2], Cristina Piselli[2,*], Anna Laura Pisello[2,3], Ilaria Pigliautile[2], Gabriel Perez[1], Luisa F. Cabeza[1]

[1]GREiA Research Group, INSPIRES Research Centre, University of Lleida, Lleida, Spain
[2]CIRIAF - Interuniversity Research Centre, Perugia, Italy
[3]Department of Engineering, University of Perugia, Perugia, Italy

Corresponding email: piselli@crbnet.it

ABSTRACT

In the last decades a variety of high-energy efficient solutions for building envelopes were developed and tested for enhancing indoor thermal comfort and improving indoor environmental quality of private spaces by learning from nature. To this aim, adaptive solutions, conceived thanks to green and bio inspiration, were designed and constructed in various climate conditions and for a variety of building uses. Given the huge population flow toward urban areas, well-being conditions in the public spaces of such dense built environment are being compromised, also due to anthropogenic actions responsible for massive environmental pollution, local overheating, urban heat island, etc. Moreover, this process is exacerbated by temporary phenomena such as heat waves. Therefore, outdoor spaces are becoming increasingly less comfortable and even dangerous for citizens, especially if they are affected by general energy poverty, with no chance for active systems management for air conditioning, or health vulnerability. In this view, this study concerns the first concept for the development of a simple and adaptive nature-inspired solution for outdoor thermal comfort enhancement and local overheating mitigation for pedestrians. The system will be evaluated in terms of the cradle-to-cradle approach and the initial performance assessment is carried out via thermal-energy dynamic simulation. The final purpose will be to design outdoor "alive" shading system to be applied in open public spaces, with evident physical and social benefits.

KEYWORDS

Bio-inspired solutions; Biomimetics; Biophilic cities; Outdoor thermal comfort; Thermal-energy dynamic simulation.

INTRODUCTION

Nowadays, a topic with increasing relevance is how an exterior space affects physical, physiological, and psychological well-being. The achievement of comfortable outdoor spaces and microclimate in urban environments is, indeed, fundamental since those spaces are where social activities happen, people gather/socialise, but also connect the indoors with nature (sun/green spaces). Architects and designers were inspired by nature since long before the term biomimicry (biometics or bio-inspired architecture) was introduced. In the past, architecture featured ornamental design influenced by nature, and this tendency was accentuated by turn-of-the century Catalan Modernism (Spain) or Art Nouveau (Belgium) as examples. Nowadays, a methodological approach to assess innovation was developed through merging bio-inspiration and sustainability based on the reintegration of basic bio-inspired principles into material systems of humankind (Horn et al. 2018). Biomimetics is a rapidly growing discipline in engineering, and an emerging design field in architecture. In

biomimetics, solutions are obtained by emulating strategies, mechanisms, and principles found in nature (Badarnah 2017). Therefore, the study of green infrastructures providing benefits not only in terms of outdoor thermal comfort, but also for the built environment located in their close proximity may represent a further mitigation and wellbeing opportunity.

In this context, plants have also the capability to transform global solar radiation that reaches their surfaces into biomass, oxygen, air humidity, etc. (Pacheco-Torgal et al. 2015). Furthermore, biophilic spaces, those that learn from nature and emulate natural systems, must be considered for the development of cities. In fact, a biophilic city is a city in which residents are actively involved in experiencing nature (Beatley & Newman 2013). Moreover, biophilic urbanism can complement urban greening efforts to enable a holistic approach, which is conducive to comprehensive, intentional, and strategic urban greening (Revee et al. 2015). Different studies about outdoor thermal comfort showed that the sun sensation coming from solar radiation has the most significant influence on human thermal sensation in outdoor spaces (Yang et al. 2013). On the other hand, pedestrians usually inclined to green areas within the urban environment. This increase of vegetation, combined to other solutions, showed the most significant impact in summer overheating mitigation and urban resilience to anthropogenic climate change (Piselli et al. 2018).

Within this background, there is a lack of information about how greenery shading systems can influence outdoor thermal comfort in the inter-building space. Therefore, the purpose of this work is to study a simple and adaptive system of bio-inspired architecture connected to the building for the improvement of thermal comfort in the outdoor inter-building space. Therefore, this strategy is able to mitigate the build environment and the urban heat island phenomenon (UHI) as bottom-up approach. The other aim of the paper is to simulate the outdoor thermal comfort with greenery, since there are no previous studies concerning that. Moreover, the selected materials are meant to produce the minimum impact in terms of cradle-to-cradle vision.

METHODS
Description of the concept
The design was created with different spaces that can provide thermal comfort to outdoor users (Figure 1). Two main objectives were pursued: (i) to reduce the incidence of the direct solar radiation to achieve higher visual comfort, and (ii) to mitigate surface temperatures of the connected buildings and the air temperature in the inter-building space to achieve thermal comfort. In fact, the system did not seek to create a stand-alone piece at the outdoor. On the contrary, the intervention tried to strengthen the key assets of surrounding buildings, creating an extension of the existing buildings that it may be.

Figure 1. The shading system proposed.

The shading system was composed of two interwoven systems of ropes running freely between the two buildings. The ropes connected on the middle creating a bench where people

could sit. The new three-dimensional surfaces created shadings of varying densities that reconfigure the original outdoor space into a more confined and enclosed space. The confined space changed constantly with shadows produced by the rope and greenery systems (using deciduous plants) depending on the season since the solar irradiance is different for each one. Thus, the inter-building space became an ever-changing stage that responded to the movement of the visitor, the changing patterns of light through the day, and the outdoor thermal comfort depending on the season. The selected specie, i.e. Boston Ivy (Parthenocissus Tricuspidata), is a deciduous specie well adapted to the Mediterranean Continental climate.

The performance of the system was simulated in this study to demonstrate its potential in sites requiring context-specific real-time responses. The system was modelled under the case study climate context of Lleida, Spain, with Continental-Mediterranean weather conditions, i.e. Csa (warm temperate, dry and hot summer) zone according to Köppen-Geiger climate classification (Kottek et al. 2006). To improve the efficacy of the proposed system in terms of cradle-to-cradle, the materials selected for the prototype corresponded to: (i) Wood structure to support the shadow shading system. This wood structure includes a bench integrated in the basement structure with a substrate for the climbing plants that will grow on it. (ii) Ropes made of natural fibres for the shading system. (iii) Climbing deciduous plants.

Thermal-energy dynamic simulation
For the system modelling and thermal-energy assessment, EnergyPlus v8.1 simulation engine (Crawley et al. 2000) with DesignBuilder v4.7 graphical interface (DesignBuilder software Ltd, 2016) were selected. The following steps were followed in the simulation process:
- Building geometry modelling based on the designed drawings and technical specifications.
- Characterization of the architectural elements and their thermal properties.
- Proposed shading system modelling and characterization: the rope-based shading system with greenery was modelled as a solid obstacle, characterized by rope properties. This configuration was considered an acceptable approximation due to the unavailability in the software of a model for stand-alone green infrastructures implemented in outdoor areas, i.e. not integrated in the building envelope.
- Run of hourly simulations for the hottest week in summer (i.e. July 15th to July 23rd), with the more regular outside temperatures along the season.
- Analysis and comparison of the performance of different scenarios for the outdoor shading system in terms of thermal conditions under the shading and external surface temperatures of the shaded buildings.

The statistical weather file of the city of Lleida from the EnergyPlus database (U.S. DOE BTO, 2016) was used for triggering the model in the calculations. Different scenarios were defined for the proposed system in order to evaluate the impact of shading percentage of the system, i.e. the amount of vegetation growth on the rope-based system. To this aim, the different scenarios were modelled by varying the transmittance capability of the solid obstacle. Therefore, the studied scenarios (Figure 2) were those proposed by Ng et al. (2012):
- Covered 0%: Without greenery, i.e. solar radiation transmittance equal to 1.
- Covered 33%: With greenery covering 33% of the structure, i.e. solar radiation transmittance equal to 0.67.
- Covered 67%: With greenery covering 67% of the structure, i.e. solar radiation transmittance equal to 0.33.
- Covered 100%: With greenery covering 100% of the structure, i.e. solar radiation transmittance equal to 0.

The purpose of the numerical simulation was to study the influence on the surface temperatures of the buildings connected and shaded by the system (east and west walls were selected since are those which receive more solar radiation in summer) and to study the variation of temperatures below the system depending on the coverage. To this aim, the inter-building area below the shading system was modelled as an internal thermal zone, characterized by thin air layer envelope and high air infiltration and ventilation to approximate outdoor conditions to the best.

a)   b)

b)   d)
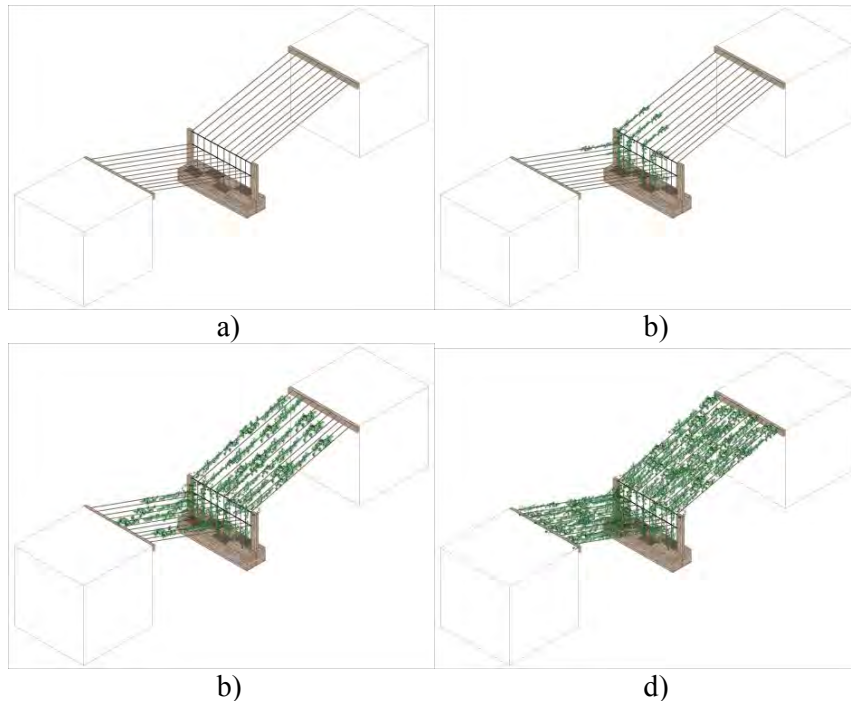
Figure 2. The four different scenarios of the shading system. a) Without greenery, b) With greenery covering 33%, c) With greenery covering 66%, d) With greenery covering 100%.

RESULTS AND DISCUSSION

As the external wall surface concerns (Figure 3), significant differences were observed between the four scenarios. More in detail, the maximum variation in the surface wall temperatures was found in the west facade, since among the considered orientations it is the one that receives the highest solar radiation in summer (Pérez et al. 2017). The peak temperatures showed significant variation depending on the shading scenario, while the minimum temperatures were similar.

Figure 3. Daily variation of west facade temperature.

In particular, a difference of 16ºC was found between the scenario without shadow (i.e. Covered 0%) and the one totally Covered (i.e. Covered 100%), where the surface temperatures reached 54ºC and 38ºC, respectively. Concerning the scenarios Covered 33% and Covered 67%, the maximum surface temperature reached 48ºC and 42ºC, respectively. These results highlight that the external temperatures of the walls of existing buildings can be reduced thanks to the implementation of the prop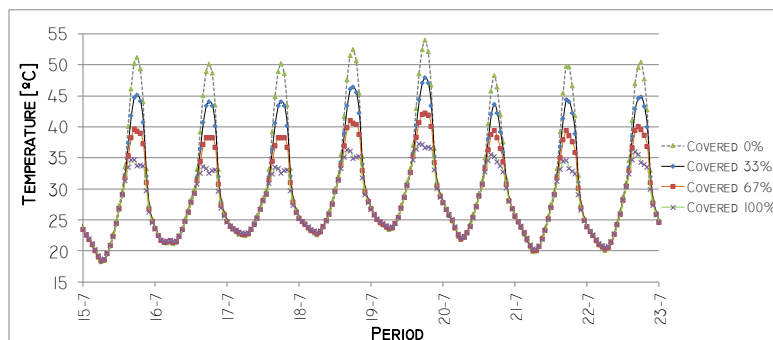osed shading system. Accordingly, this is expected to be associated to a significant decrease in the indoor ambient temperature.

On the other hand, in the east facade, a difference of 7ºC was found between the scenario Covered 0% and the Covered 100% (with peak temperatures up to 43ºC and 36ºC, respectively). In this facade, each day shows two peaks, the first following the solar incidence and the second one corresponding to the maximum outside air temperature. As expected, the solar incidence has a stronger influence when no shadowing system is used (wall temperatures reaching up to 39ºC), while with the system this temperature decreases up to 22.5ºC. When the solar incidence decreases, the outside temperature effect is very strong, but in this case all scenarios reach similar temperatures (around 34-35.5ºC).
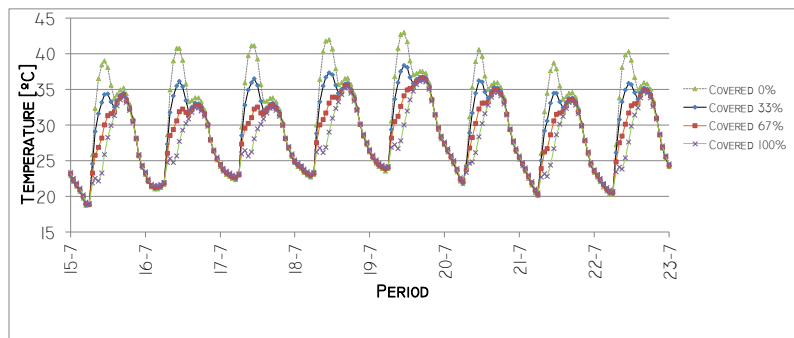
Figure 4. Daily variation of east facade temperature.

Regarding the air temperature in the inter-building space, i.e. under the shading system, the maximum temperatures ranged from 33ºC for the Covered 100% scenario, to 34ºC for the Covered 67%, to 36ºC for the Covered 33%, up to 38ºC for the system without greenery, i.e. Covered 0%. Therefore, the shading effect associated to the implementation of the greenery was able to provide an outdoor air temperature reduction up to 5ºC.
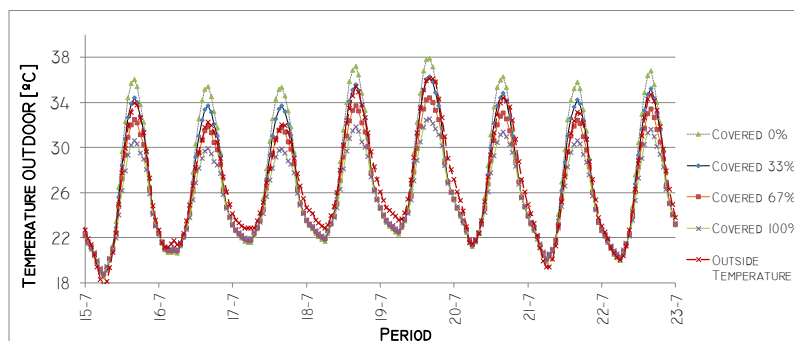
Figure 5. Daily ambient temperature under the shading system.

CONCLUSIONS AND FUTURE DEVELOPMENTS
This study presented the concept of a simple and adaptive bio-inspired vegetated shading system for inter-building spaces. The purpose of the study was to analyse the effect of varying the greening percentage on the shading system on the air temperature of the inter-building

area covered by the system and the connected buildings surfaces, through numerical modelling tools usually considered for indoor thermal-energy dynamic simulation. Simulations showed, as expected, that both the wall surface temperature and the air temperature under the shading system decreased when percentage of covering due to the greenery increased. Therefore, the theory of the benefits of a greenery system in summer is confirmed also for inter-building spaces. Since this study was carried out via numerical simulation, more exhaustive experimental research is needed to confirm these results. Therefore, reliable data will be available for architects, urban planners and engineers on the implementation of new concepts inspired by nature for both indoors and outdoors well-being.

ACKNOWLEDGEMENTS

REFERENCES

Badarnah L. 2017. Form Follows Environment: Biomimetic Approaches to Building Envelope Design for Environmental Adaptation. *Buildings* 7 (2), 40.

Beatley T. and Newman P. 2013. Biophilic cities are sustainable, resilient cities. *Sustainability (Switzerland)*, 5, 3328–3345.

Crawley D.B, Pedersen C.O, Lawrie L.K, and Winkelmann F.C. 2000. Energy plus: Energy simulation program, ASHRAE Journal, 42, 49–56.

DesignBuilder software Ltd. 2016. DesignBuilder software. https://www.designbuilder.co.uk/ (accessed March 22, 2018).

Horn R., Dahy H., Gantner J., Speck O., Leistner P. 2018 Bio-Inspired Sustainability Assessment for Building Product Development: Concept and Case Study. *Sustainability*, *10* (1), 130.

Kottek M., Grieser J., Beck C., Rudolf B., Rubel F. 2006 World map of the Köppen-Geiger climate classification updated, *Meteorol. Zeitschrift*. 15, 259–263.

Ng E., Chen L., Wang Y., Yuan C. 2012. A study on the cooling effects of greening in a high-density city: An experience from Hong Kong. *Building and Environment*, 47, 256–271.

Pérez G., Coma J., Sol S., Cabeza L.F. 2017. Green facade for energy savings in buildings: The influence of leaf area index and facade orientation on the shadow effect. *Applied Energy*, 187, 424–437.

Piselli C., Castaldo V., Pigliautile I., Pisello A.L., Cotana F. 2018. Outdoor comfort conditions in urban areas: on citizens' perspective about microclimate mitigation of urban transit areas. *Sustainable Cities and Society*, 39 16–36.

Reeve A. C., Desha C., Hargreaves D. 2015. Biophilic urbanism: contributions to holistic urban greening for urban renewal. *Smart and Sustainable Built Environment,* 4(2), pp. 215-233

U.S. Department of Energy's (DOE) Building Technologies Office (BTO). 2016. EnergyPlus - Weather Data. https://energyplus.net/weather (accessed March 22, 2018).

Yang W., Wong N.H., Jusuf S.K. 2013. Thermal comfort in outdoor urban spaces in Singapore. *Building and Environment*, 59, 426–435.

Pacheco-Torgal, F., Labrincha, J.A., Diamanti, M.V., Yu, C.-P., Lee, H.K. 2015. Biotechnologies and biomimetics for civil engineering. Springer.

Building Information Modeling (BIM) Implementation for Sustainability Analysis: A Mega Airport Project Case Study

Basak Keskin[1*], and Baris Salman[2]

[1]Syracuse University, Syracuse
[2] Syracuse University, Syracuse

*Corresponding email: bkeskin@syr.edu

ABSTRACT

It has been generally perceived that decision-making processes for implementing sustainable solutions to building elements should be in design and pre-construction phases. This perception hinders the transformation of current non-sustainable buildings into sustainable ones. It has been realized that retrofitting existing buildings can be more beneficial in terms of time and cost compared to new construction. This study aims to show that implementation of Building Information Modeling (BIM) for energy analysis improves the retrofit planning process. This study explains that in practice, BIM tools provide significant opportunities for creation of Building Energy Modeling (BEM); and the outputs of BEM analysis can be readily used in selection of energy efficiency measures. The case study approach is used in this study. Accordingly, 3D energy models of the Istanbul Grand Airport Project have been created. A heuristic optimization depicts a clear picture of why it is necessary to incentivize transforming BIM to BEM for decision-making processes of retrofitting. Correspondingly, the study findings show that BIM implementations can provide cost and time savings for energy analysis practices.

KEYWORDS

Building Information Modeling, Building Energy Modeling, retrofitting, heuristic model

INTRODUCTION

Energy analysis tools are integral to the process of identifying and implementing building energy savings measures (Evan, 2003). Such tools have many uses; typically, they are used for design of new building or renovation of existing ones with detailed design analysis (Sanquist & Ryan, 2012; Evan, 2003). Appropriate utilization of building energy analysis tools leads to accurate and cost-effective energy analyses, which depict the total energy use and savings opportunities. The origins of building energy software trace back to the 1970s. Before then, energy analysis was managed by hand at significant cost and time. According to Evan (2003), in the 1980s, the first-generation of simulation-based analysis and design tools emerged. From late 90s until now, rapid proliferation of tools targeted at a broader spectrum of users and the advent of web-based tools. Through web and literature searches, commonly used whole building energy simulation software tools in North America are compiled: TREAT, Sefaira Architecture, EnergyPlus, Pleiades+COMFIE, Autodesk Insight 360, EDAPT, TRNSYS, eQuest, TRACE 700, REM/Design, Open Studio, EDGE Excellence In Design, Design Builder, HA (Carrier).

Moreover, the opportunities can be magnified using recent innovations in energy management tools that provide greater access to energy use data as well as analytics and increased intelligence to optimize systems (Woo & Gleason, 2014). Additionally, typical processes of whole Building Energy Model (BEM) generation are subjective, labor intensive, time

intensive, and error prone (O'Donnell, et al., 2013). At this point, it is clear that integrating BIM and BEM generates value in terms of time, cost, and quality since BIM-based building energy models are capable of collecting and also rapidly processing real-time energy performance data. This also provides more accurate and detailed input and output for energy simulation process.

Using the aforementioned energy analysis tools for retrofitting with an optimized investment budget appears to be a viable investment tool. Such procedures can provide substantial savings in terms of energy use, energy cost, and carbon emissions. (Camlibel & Otay, 2011) Not all facility managers, building owners, and other related parties have the ability to access and use a sophisticated optimization software. There are cases in which fast and cost-efficient processes are needed. Heuristic approach can be used to calculate energy, energy cost, and CO_2 savings per invested amount for different energy efficiency measures (EEMs) (retrofit alternatives). Heuristic approach includes the following steps: calculating energy, energy cost, CO_2 savings per investment for each EEM; showing budget amount by drawing a vertical line along the budget amount; selecting EEM with the highest value of saving per USD on the left side of the vertical line; subtracting the selected EEM's investment amount from the given budget; drawing a new vertical line along the new value of the budget amount (Camlibel & Otay, 2011). This process is repeated until the budget no longer supports any other EEM. Thus, the BIM-BEM integration can improve heuristic optimization and selection of energy efficiency measures by providing fast and more accurate input data.

This study shares the energy analysis approach applied to Istanbul Grand Airport Project BIM models. The project encompasses four phases, which includes six runways, three terminals, and an annual 200 million passenger capacity. The first phase of the construction started in 2015. It was planned to make the airport operational in the first half of 2018. This timeline shows that the energy analysis results address the potential future rework that may target to meet or exceed performance guidelines set by building rating systems (e.g., ISI's Envision and the Middle East's ESTIDAMA which include energy efficiency of building envelopes, day-lighting performance, and embodied energy as the crucial part of their evaluation.)

In the literature, it is generally discussed that BIM-based energy modelling utilization leads to sustainable design, and provides easy access to energy analysis results in the early design process. However, to the authors' knowledge, there are no case studies showing that BIM can contribute to sustainability, not only in the design phase, but also throughout the life cycle of the building. Essentially, this study tries to fill the gap in the literature, via proposing BEM generation, by the use of BIM to accelerate the energy retrofitting decision making process.

METHODOLOGY
The case study shows the energy analysis procedure used for Istanbul Grand Airport (IGA) Project BIM models. These models are composed of architectural and structural Revit models. As one of the world's largest aviation projects, the IGA Project encompasses a terminal building with a total floor area of 950,000 m^2, and pier buildings with a total floor area of 320,000 m^2. The methodology used in the case study enables a holistic approach on the magnitude of future energy consumption of IGA project. In this respective order, the methodology contains a selection of the most suitable digital tools, an optimization of BIM models, and generation of an energy analysis.

According to Stumpf, Kim, & Jenicek (2009), the energy modeling process can be divided into two sub-processes. The first sub-process is a macro-level energy analysis, which focuses

on comparing building size, shape, and orientation. The second sub-process is a micro-level energy analysis, which considers building details such as wall penetrations and building system details. An energy analysis framework is obtained through the methodology presented below (See Figure 1). It contains data coming from both macro and micro level energy analysis processes.
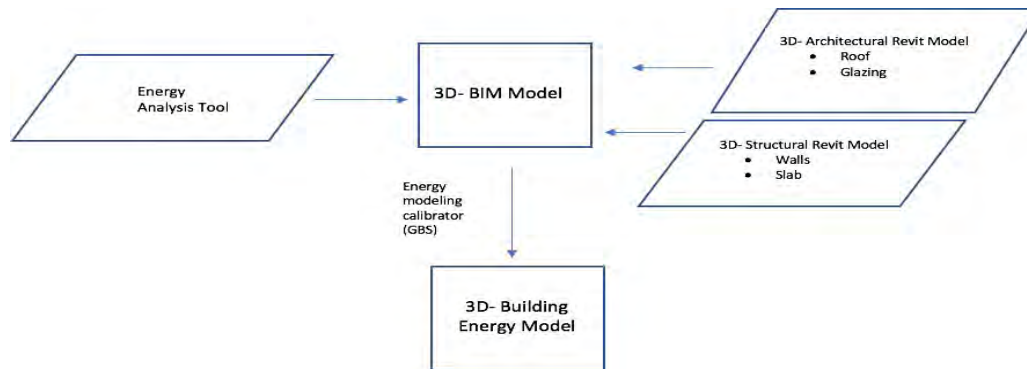
Figure 1: Energy Analysis Process Framework

At the first step of the methodology, the digital tool Insight 360 is chosen for this case study. This tool works as an add-in to Autodesk Revit and integrates existing workflows such as Revit Energy Analysis and Lighting Analysis for Revit. Insight 360 also allows visualization of solar radiation on mass or building element surfaces. Solar analysis includes a new automated workflow for understanding photovoltaic (PV) energy production. Insight 360 also provides a comparison of design scenarios to track performance of the building lifecycle, as well as, measuring the performance against Architecture 2030 and ASHRAE 90.1 benchmarks. The energy analysis results presented in this case study are limited. In essence, only visualization of solar radiation and energy production results are provided.

At the second step, optimization of BIM models, which is mainly dividing and simplifying architectural and structural Revit models, is conducted. Smaller models were extracted out of one master model (See Figure 2). Main purpose of this optimization, which requires discarding some architectural and structural elements, is to achieve the most appropriate model size and complexity for Insight 360, so that the tool can process data smoothly. Such tools have limited capabilities in terms of model size and complexity, making the model shown in Figure 2 infeasible to be analyzed as a whole. Accordingly, five different models with the most basic features (Kim & Anderson, 2011) (See Table 1) were obtained via taking reference of high level zoning plan given in Figure 3. However, it is important to keep in mind that, the number of sub-models should be kept to a minimum. Also, all sub-models should have a fully closed geometry to generate energy analytical models. Overall, the purpose is to eliminate issues including missing elements, elements that are not set to room bounding, gaps in geometry, in-place families, small spaces and surfaces, and columns that cause surfaces to be omitted from the energy model.

Table 1. List of sub-models

Sub-Models
Terminal 1 (all levels)
Terminal 2 + Terminal 3 (all levels)
Pier 1 – Pier 2 (all levels)
Pier 3- Pier 4 (all levels)
Pier 5 (all levels)

Figure 2: Master Model of the Project

Figure 3: High Level Zoning of the Project

Furthermore, the master model is at its real-world coordinates having high accuracy in level and shape to ensure sustaining maximum accuracy in total volume of energy analytical model. As the third step, energy analysis is conducted; and for that purpose, **Generate** command (in Revit 2017) or **Generate Insight** command (Revit 2016) in **Analyze** ribbon (see Figure 4) is used. The process begins with creation of energy analytical model, followed by transmission of the model to the cloud-based Green Building Studio (GBS) server to obtain the results of energy analysis.

Figure 4: Analyze Command in Revit 2016

RESULTS & DISCUSSIONS

Visualization of solar radiation and energy production results are provided below for each sub-model developed through optimization. The results demonstrate significant total potential in solar energy generation due to the geographic coordinates of the structures, when the retrofitting solutions are applied correctly.

However, the BIM tools used in this study for energy analysis are still under development. Accordingly, it is a significant challenge to optimize models to have accurate flow of data between systems. Since, BIM modeling software market is greatly dominated by only a few companies (e.g. Autodesk Revit), sustainability practitioners are depending upon a limited extend of energy analysis plug-ins; which may otherwise result in compatibility issues.
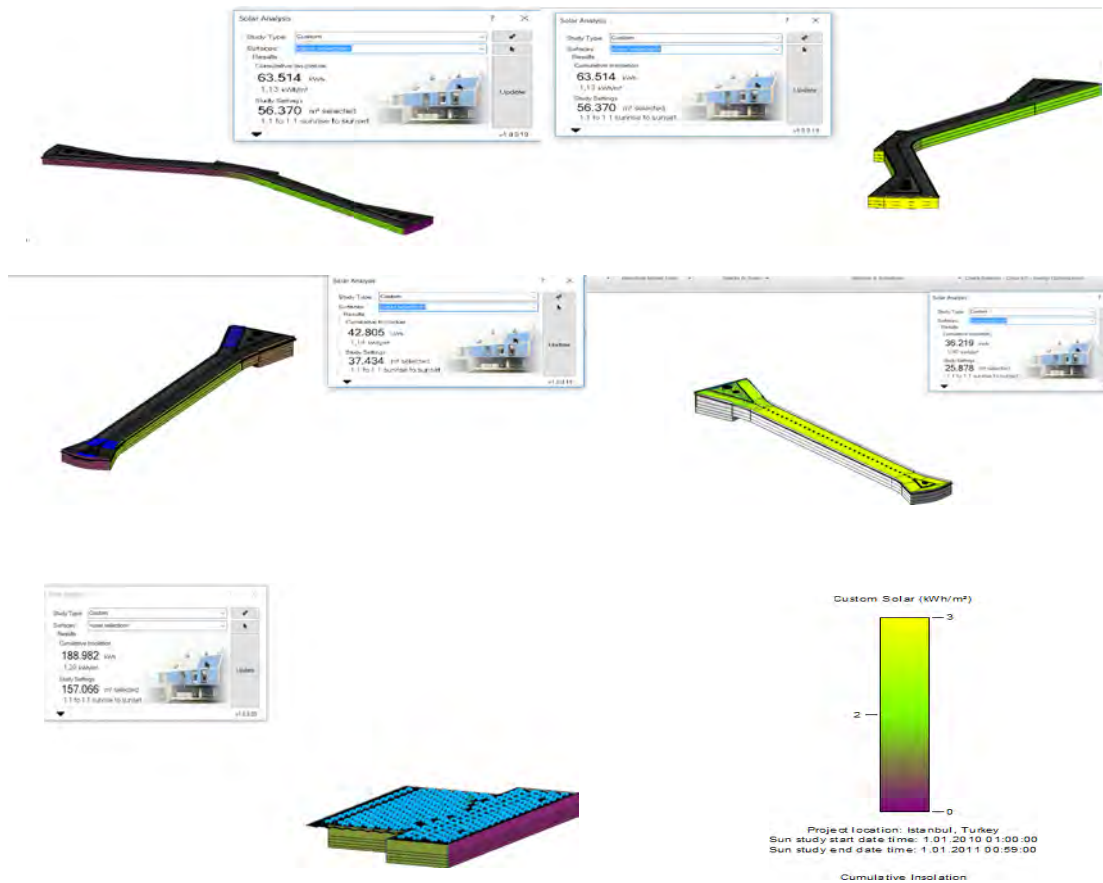
Figure 5: Solar Energy Results for Pier 1-2, Pier 3-4, Pier 5, Pier 5 Roof, Terminal Building, Custom Solar Scale on Energy Units (kWh) per Unit Area (m²)

Another problem about this BIM application is associated with the lack of guidelines and standardized workflows for right data retrieval from BIM models. Correspondingly, commercial BIM software technology market should further be evolved; and preparation of detailed BIM guidelines should be encouraged to improve the effectiveness of building retrofitting plans.

Retrofitting of existing buildings, as an evolving field of research, represents vast possibilities in increasing the energy efficiency of buildings. Façade design plays a crucial role in the retrofit of a building, and can offer additional benefits by incorporating possibilities of energy production (Bigaila, Hachem-Vermette, El-Sayed, & Athienitis, 2016).

Correspondingly, building-integrated photovoltaic (BIPV) glazing can be suggested as a retrofit solution for this case study. This is a new approach in which PV modules are integrated into the building envelope materials and components. As such, the PV system is not an added component, but rather a part of the essential building envelope. The electricity generated by the BIPV system can be stored in batteries so that the system can be used as an off-grid system. Alternatively, the system can be interfaced with the utility grid and the electricity generated can be sold back to the grid (Verboon & Laufs, 2013).

BIM implementation in the project gives many opportunities in terms of providing easy access to all project data (or one can say "big data") – including 3D models at various levels of detail (LODs), 2D drawings, and all supplemental documents- from a single digital platform. Besides,

BIM also allows fast modification or update on data whenever needed while greatly eliminating waste in terms of time and money. As a summary, following points can be listed as benefits of BIM for sustainability;

- Energy modeling (detailed analysis of energy needs of the structure and analysis of renewable energy options such as solar energy),
- Building orientation (providing best building orientation option that leads to minimum energy cost),
- Reducing wasted time and resources for energy analysis (allowing rapid modifications in many design parameters),
- Access to current data for unit energy costs and weather via an internet server.

CONCLUSIONS

Building energy modeling tools provide an efficient, simple method in predicting the energy use of new and existing buildings. Via a decent optimization procedure and project defaults assumptions, energy analysis of all Terminal and Pier Buildings are conducted. Consequently, Autodesk Insight 360 provides annual and monthly data – both in energy units and in monetary units- of total energy consumption of the analyzed buildings. Annual and monthly monetary and energy equivalents of space heating, space cooling, area lighting, hot water supplies can also be generated graphically, which can enable the users to foresee energy consumption levels of airport buildings in future studies. However, in the context of this paper, solar analysis results are presented to articulate the simplicity in extracting data for retrofitting decision-making process. Since the tool aids in conducting iterative process by means of fast data-input, the facility owners can acknowledge the potential in PV energy production at the operational stage of the airport.

REFERENCES

Abdalla, J. A., & Law, H. K. (2014). A Framework for Building Energy Model to Support Energy Performance Rating and Simulation. *Computing in Civil and Building Engineering.*

Bigaila, E., Hachem-Vermette, C., El-Sayed, M., & Athienitis, A. K. (2016). Solar Energy Potential For Commercial Building Facade Retrofit. *IBPSA eSim 2016.* Hamilton: International Building Performance Simulation Association.

Camlibel, M. E., & Otay, E. N. (2011). *An Integrated Optimization Model Towards Energy Efficiency For Existing Buildings - A Case Study For Bogazici University Kilyos Campus.* Istanbul: Bogazici University.

Evan, M. (2003). Inter-comparison of North American residential energy analysis tools. 865-880.

Kim, H., & Anderson, K. (2011). Energy Simulation System Using BIM (Building Information Modeling).

O'Donnell, J. T., Maile, T., Rose, C., Mrazović, N., Morrissey, E., Regnier, C. . . . Bazjanac, V. (2013). *Transforming BIM to BEM: Generation of Building Geometry for the NASA Ames Sustainability Base BIM.* California: Lawrence Berkeley National Laboratory.

Sanquist, T. F., & Ryan, E. M. (2012). Validation of building energy modeling tools under idealized and realistic conditions. *Energy and Buildings,* 375-382.

Stumpf, A., Kim, H., & Jenicek, E. (2009). Early Design Energy Analysis Using BIMS (Building Information Models). *Construction Research Congress.* ASCE.

Verboon, E., & Laufs, W. (2013). Innovative Façade Design and Products. In t. C. Engineers, *Curtain Wall Systems* (pp. 154-194). Reston: American Society of Civil Engineers.

Woo, J.-H., & Gleason, B. (2014). Building Energy Benchmarking with Building Information Modeling and Wireless Sensor Technologies for Building Retrofits. *Computing in Civil and Building Engineering.*

Chemical Analysis of Precipitation and Stormwater Runoff from a Large Green Roof

Kimberly Fitzgerald[1*], Alexander Johnson[1] and Cliff I. Davidson[1,2]

[1]Department of Civil and Environmental Engineering, Syracuse, NY 13244
[2]Center of Excellence in Environmental and Energy Systems, Syracuse, NY 13244

[*]*kafit100@syr.edu*

ABSTRACT
The growth medium of a green roof is likely to affect the chemistry of the rainwater passing through it, which may impact the receiving waters. Currently only limited data exist on the changes in rain chemistry caused by green roofs. The objectives of this project are to determine the differences in concentration of several contaminants in rain and in runoff from a green roof in downtown Syracuse, NY, and to explore reasons for the observed differences. A few samples were collected in 2014 and 2016, but most of the data are from 2017. Collection of precipitation uses funnels, while collection of runoff takes place using a drainpipe that connects to several roof drains. Both types of samples are analyzed by ion chromatography for chloride, sulfate, and nitrate. Preliminary tests show that chloride concentrations in the green roof runoff are generally greater than or equal to those in precipitation. Sulfate in the runoff is greatly enhanced compared with precipitation. Nitrate concentrations do not show a clear pattern. Engineered soil greatly influences the chemistry of the incoming rain, and additional research is needed to better understand this chemistry.

KEYWORDS
Green Roof, Stormwater, Ion Chromatography, Precipitation Chemistry, Runoff Chemistry

INTRODUCTION
Widespread urbanization has shown an increase in impermeable surfaces where there was once soil and plants to absorb the precipitation. The lack of area for infiltration can lead to flooding, and in cities with combined sewers, it can lead to combined sewer overflow where raw sewage enters the receiving waters. To reduce flooding and discharge of untreated sewage, green infrastructure such as green roofs can be installed to delay and store rain runoff.

Previous work has shown that rainwater flowing through the growth medium of a green roof (engineered soil) can experience changes in chemistry. For example, Vijayaraghavan et al. (2012) report higher concentrations of nitrate, phosphate, and sulfate in runoff compared to the incident rain using green roof test plots in Singapore. The plots incorporated growth medium with the trade name "universal garden soil" and were planted with sedum. Czemiel Berndtsson (2010) presents a literature review of green roof studies, some of which include chemical analysis of runoff. The data show that levels of nitrogen and phosphorus species in green roof runoff by different authors are quite variable, in part due to different roof characteristics.

The primary objective of this project is to compare the concentrations of chloride (Cl^-), sulfate (SO_4^{2-}), and nitrate (NO_3^-) in fresh precipitation and in rainwater that has passed through a large, extensive green roof. A second objective is to explore the reasons for these changes. Chemicals such as sulfate and nitrate, which contribute to acid deposition, are especially

important. Excess nitrogen in the runoff can have an adverse effect on the receiving waters by enhancing algae growth and eutrophication. The roof used in this study is on the Onondaga County Convention Center (OnCenter) in Syracuse, NY.

METHODS
The green roof, installed in 2011, is 0.56 hectares with growth medium 7.6 cm deep planted with six types of sedum. There are 25 roof drains, and samples are collected from a pipe connected to eight of these drains. Precipitation is collected on the roof of the Biological Research Laboratories on the Syracuse University campus, about 1.6 km east of the green roof. Sample bottles are secured in a wooden frame with funnels. Field blanks are obtained at each location. All samples are analyzed for chloride, sulfate, and nitrate using an ion chromatograph (IC). No fertilizer or other chemicals have been added to the roof since it was installed in 2011, although characteristics of the growth medium have undoubtedly changed over time. Only limited chemistry data from runoff were obtained prior to 2017.

RESULTS
Figure 1. a, b, c shows average net concentrations for Cl^-, SO_4^{2-}, and NO_3^- in the precipitation and green roof runoff. Each bar represents a separate rain event from 2014 to 2017.

DISCUSSION
Figure 1a shows that chloride concentrations in the runoff are usually equal to or greater than concentrations in the incoming rain. In storms 4/15/2017 and 7/20/2017, the opposite is observed, but the number of samples in these storms is small. The reason for the high chloride concentration in runoff on 6/4/2017 is unknown. This concentration is not likely due to contamination, as all three samples of runoff show similar high concentrations.

Sulfate concentrations shown in Figure 1b are consistently significantly higher in the runoff than in the precipitation. The data support the green roof being a source of sulfate. Investigations of the source of this sulfate are underway.

The nitrate concentrations from the runoff represented in Figure 1c show no dominant pattern when compared to the rain concentrations. About half of the rain events have runoff concentrations greater than precipitation, while the other half of the runoff concentrations are less than the those in precipitation.

The highest nitrate concentration in runoff occurs on .8/3-4/2017. The precipitation data shown in the graph is an average of five samples, one from an event on 8/3 and four from an event on 8/4. The storm on 8/3 had a nitrate concentration of 5.7 mg/L, while the storm on 8/4 had a concentration of 1.4 mg/L. The first storm had an intensity of 15.6 mm/hr and lasted for 10 minutes, a brief but intense cloudburst. In contrast, the second storm the next day had an intensity of 2.4 mm/hr and lasted two hours. The differences in concentrations in the precipitation from these storms is notable.

No runoff from the green roof occurred during the cloudburst on 8/3, as the total rainfall was only 2.6 mm. However, runoff occurred the next day when the total rainfall reached 4.6 mm. The concentration in the runoff averaged 5.0 mg/L, much greater than the concentration in the rain on that day. The runoff on 8/4 most likely included some of the high concentration rain on 8/3. Hence one cannot conclude that the nitrate in the growth medium was responsible for the elevated levels in runoff on 8/4.
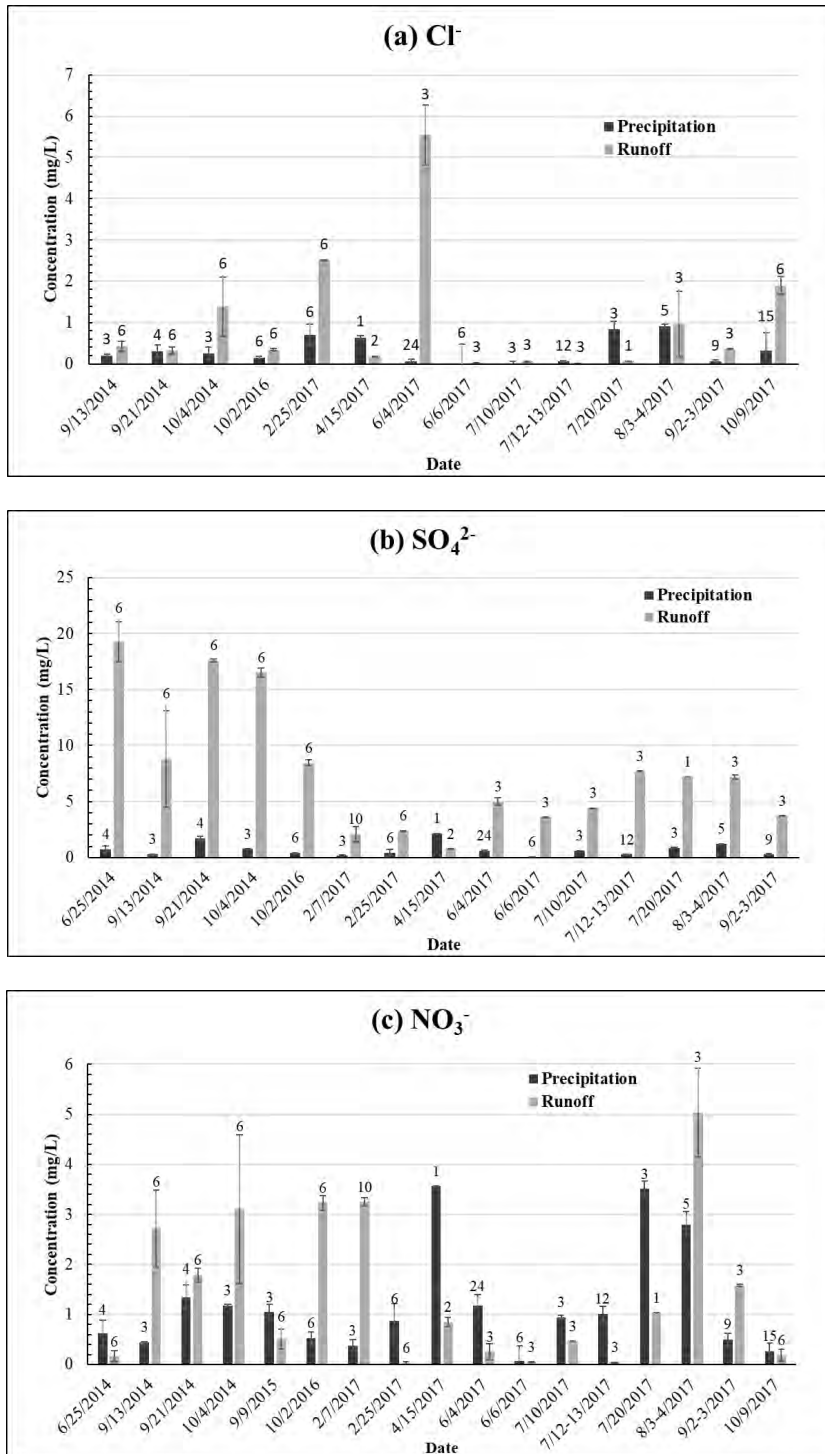
Figure 1. Average concentrations of chloride, sulfate, and nitrate, measured in precipitation and green roof runoff from selected storms. Error bars show one standard deviation from the mean. Each bar represents the average of the indicated number of samples, ranging from 1 to 24.

Johnson and Davidson (2017) note that fertilizer was applied to the green roof at the time of its installation in 2011. It is not known whether the nitrate concentrations in Figure 1c were influenced by this fertilizer. However, it is of interest that events on 6/25/14, 9/9/15, and many events in 2017 had runoff nitrate levels less than those in incoming rain. Rowe (2011) reports high nutrient concentrations in green roofs that have been fertilized. Age of green roof and vegetation type can factor in to the leeching of nitrate into the runoff (Czemiel Berndtsson, 2010).

Comparing patterns for the three analytes in Figure 1 shows that the storm on 4/15/2017 is unique in that concentrations in precipitation exceeded those in runoff for all three analytes. Further investigation of this event is underway.

Data collection is continuing and will expand to include other chemicals in future work. Arrangements are also being made to sample a nearby traditional roof as a control.

CONCLUSIONS
Concentrations of chloride, sulfate, and nitrate in fresh precipitation and runoff from a green roof in several events show a number of patterns. Concentrations of chloride in the runoff are generally equal to or greater than levels in the incoming rain. The same is true for sulfate. However, concentrations of nitrate showed more complex results: nitrate levels in runoff exceeded levels in rain for roughly half of the events, while the opposite was observed for the other half. One especially intense storm produced the highest levels of nitrate in rain observed throughout the study; runoff from a storm the next day most likely included some of the previous day's rainwater and showed similarly high concentrations. Chemical analysis of rain and runoff will continue in future work.

ACKNOWLEDGMENT

REFERENCES
Czemiel Berndtsson, J. (2010). Green roof performance towards management of runoff water quantity and quality: A review. *Ecological Engineering, 36*(4), 351–360. https://doi.org/10.1016/J.ECOLENG.2009.12.014

Johnson, Alex J. and Cliff I. Davidson, Chemistry of stormwater runoff from a large green roof in Syracuse, NY, Poster Presentation. *Proceedings, Third International Conference on Sustainable Infrastructure*, New York City, NY, October 26-28, 2017.

Rowe, D. B. (2011). Green roofs as a means of pollution abatement. *Environmental Pollution*, 159(8–9), 2100–2110. https://doi.org/10.1016/j.envpol.2010.10.029

Vijayaraghavan, K., Joshi, U. M., & Balasubramanian, R. (2012). A field study to evaluate runoff quality from green roofs. *Water Research, 46*(4), 1337–1345. https://doi.org/10.1016/J.WATRES.2011.12.050

Computational Evaluation of the Thermal Performance of Underground Bunkers: The Case of Albania

Rudina Breçani[1,*] and Sokol Dervishi[1, 2]

[1] Epoka University, Faculty of Architecture, Tirana, Albania
[2] Vienna University of Technology, Institute of Architecture Science, Vienna, Austria

*Corresponding email: rbrecani12@epoka.edu.al

ABSTRACT

The present paper studies the thermal and energy performance and potential adaptive reuse of the lost underground bunkers of Kukës, Albania. The approach is exemplified using a 150-m long cross-section of the underground network selected for the parametric computational simulations. Data regarding local climate, design typology, and building materials is used to generate a finite-element simulation model of the underground tunnels. Different scenarios including insulation of the outer walls, occupancy patterns, and ventilation regimes are tested. The results show that indoor air temperature ranges from 15-18°C during winter and 23- 28°C during summer. During January, the temperatures are higher by 3-5 °C in comparison to the same structure and scenarios located above ground, whilst during July they are 5-8 °C lower. Insulation does not affect the heat flux through the outer walls. The average energy consumption oscillates around 55 KWh.m^{-2}.a^{-1} for base case and 98-230 KWh.m^{-2}.a^{-1} for design scenarios. The results establish the same building consumes 44-145% more energy when located above ground as opposed to underground.

KEYWORDS

Thermal performance simulation, scenarios, energy, underground nuclear bunker, adaptive reuse

INTRODUCTION

a)   b)
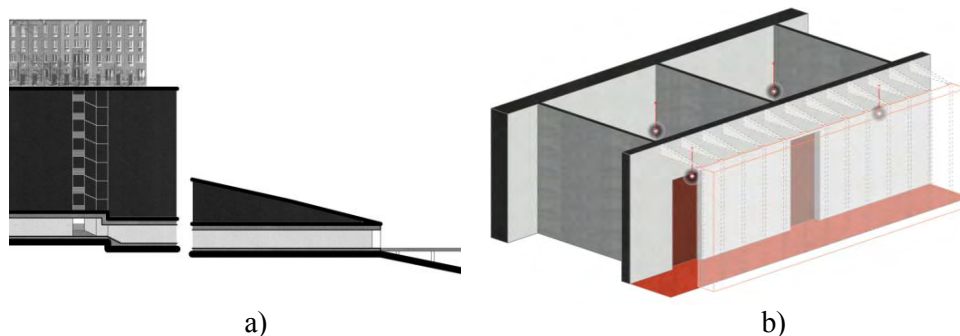
Figure 1. a) Partial section of the underground network of tunnels for Kukës, b) Close-up partial axonometric drawing of the inner construction of the tunnels.

Whilst above ground thermal comfort can be reached only via additional services, earth sheltered buildings are known for their temperature stability (Kajtar et al. 2015) and they gain benefit from the soil's quasi-stationary temperature to achieve energy conservation (Alkaff et al. 2016). Because of the high thermal inertia of the soil, the temperature fluctuations at the

surface of the ground are diminished as the depth of the ground increases (Florides and Kalogirou, 2005): the temperature of the soil changes with amplitude of 0.6 °C in the depth of 8 m and 0.2 °C in the depth of 10 m (Kajtar et al. 2015). After the depth reaches more than 20 m, the temperature becomes practically constant (Popiel et al. 2001). Popiel has concluded with the formula shown in Equation 1, where x is the depth below the ground surface, T is the temperature, k is the heat conductivity of the ground, and q the heat flux, that the heat flux of the soil is practically constant (2001). Florides depicts that due to the solar radiation and soil's relative capacity there is a 5-hour time lag a day regarding temperature distribution (2005). This explains why after reaching a specific depth the soil's temperature is always higher than the air temperature during winter and lower during summer.

$$q = -k\frac{\partial T}{\partial x}$$ (1) (Popiel et al. 2001)

This knowledge has been practiced since ancient times: Samos, Greece, Cappadoccia in Turkey, and the Hypogeum belong to the 6th century BC, 1900-1200 BC, and 4000 BC respectively (Nývlt et al. 2016; Debertolis et al. 2015). Living underground has become today a widely spread trend in countries such as China, Japan, and Korea where residents find comfort from the increasingly high economic pressure of living in apartments. In these countries, underground urban planning is a field study of its own (Zhao et al. 2016; Li et al. 2016) and some insist it should be an integral part of any National Regulation Plan (Tan et al., 2018). The studies on the computational evaluation of either thermal or energy performance for such spaces are fewer in number. Zhu has carried out thermal simulations on a sample of atrium plan earth sheltered buildings concluding that the buildings constitute a step forward towards low energy building design (Zhu and Tong, 2017). Another thermal performance simulation and evaluation study has been carried out by Ip, but the building in question has only one wall in contact with the earth (Ip and Miller, 2009). Tan has investigated the thermal comfort conditions in underground spaces in four major Chinese cities characterized by different climate conditions in order to assess the influence of the specific climatic variables (Tan et al. 2018). Tan however also recognizes his study as only qualitative and evaluates a building energy modeling would provide more solid data since qualitative analyzes often depend on real life restrictions (Tan et al. 2018).

In Albania, a special kind of underground shelters can be observed: nuclear bunker tunnels. A similar design typology is the subway, but it differs in many ways such as scenario, and traffic network which greatly influence the thermal and energy performance of the construction. The tunnels of Kukës are part of the ex-secret military establishments of Albania. This network is 2400 m long and composed of 30 galleries. Each gallery is composed of a corridor with a row of rooms on one side; an outer concrete shell envelops rooms and corridors, whilst the indoor walls were built with bricks. The tunnels have corridors which are 270 cm high and 120 cm wide, and rooms of an average of 3.4x3.4m. The network is located from 319 m to 336 m above the sea level (the different levels are connected by staircases), whilst the ground level of the city of Kukës is located 350 m above the sea level (Poliba, 2017; Municipality of Kukës, 1973). The outer walls of the tunnels are composed of 40 cm thick reinforced concrete. The inner walls are composed of bricks and amount to 27 cm thickness. These capillaries, which were constructed in several cities during the communist period and never used to fulfill the purpose for which they were built (refuge in case of war), constitute a large underground network of concrete leftover space. Therefore, the question on the efficiency with which they can fulfill their original purpose i.e. that of sheltering, comes out naturally. This study assesses the thermal performance and evaluates the adaptive reuse efficiency of the underground shelters via computational simulation modelling using the case study of the

tunnel network found in the city of Kukës as a starting point. Whereas previous studies have provided significant insight on different topics related to underground structures, there is a lack of quantitative studies providing close examination of thermal performance and energy consumption evaluation. Thermal and energy performance evaluation has not been explored yet on this typology of shelter in Albania or elsewhere, and the number of similar studies worldwide is limited. Furthermore, this paper suggests and tests alternatives for low energy consumption adaptive reuse functions appropriate for the design typology, and space quality of the tunnels.

METHODS

Initial simulation models were generated based on collected geometry and construction data. Assumptions were made based on in situ observations and historical documents. The simulations are conducted with Design Builder, a software tool used to perform building energy, lighting, and comfort performance. The software has been developed to simplify the process of building, modelling, and simulation for maximum productivity allowing users to rapidly compare the function and performance of building designs, different scenarios, and deliver results quickly. Meteonorm software was used to generate the local weather file for the city of Kukës. A 150 m tunnel section that serves as an extension of the existing hospital of the city, directly connected to it by its basement, is used for the simulations. A digital performance simulation model of the underground tunnel section is generated including the modelling, occupancy patterns, air humidity, and ventilation regimes. A set of five sample scenarios are established for the parametric study. The first scenario (S1) corresponds to the existing conditions. A second scenario (S2) is defined involving thermal insulation. Three additional scenarios (S3-S5) address the thermal performance of different potential reuse activities: laboratory (S3), hospital (S4), and museum (S5). Two simultaneous sets of simulations for scenarios S3-S5 are conducted to verify energy reduction potential of underground buildings with comparison to above ground buildings: S3-S5 when the building is located at 325 m above the sea level (the actual level of the tunnels), and S3.2-S5.2 when the building is located at 350 m above the sea level (the level of the city). Table 1 illustrates the data on scenarios S3-S5 and S3.2-S5.2. The thermal transmittance of the materials is as follows: 0.27, and 0.29 for inner and outer walls respectively, whilst without insulation these values are 1.42, and 2.31.

Table 1. Data pertaining to chosen scenarios for the study of activity impact on the underground tunnels' thermal load.

Code	Activity	Schedule	Density (people/m²)	Gain (W/m²)	Radiant fraction	Heating (20ºC)	Cooling (20ºC)
S3; S3.2	Laboratory	12/24 h	0.11	8.73	0.2	20	23
S4; S4.2	Hospital	24/24 h	0.10	3.58	0.2	18	25
S5; S5.2	Museum	varying	0.15	3.50	0.2	20	24

RESULTS

a)   b)
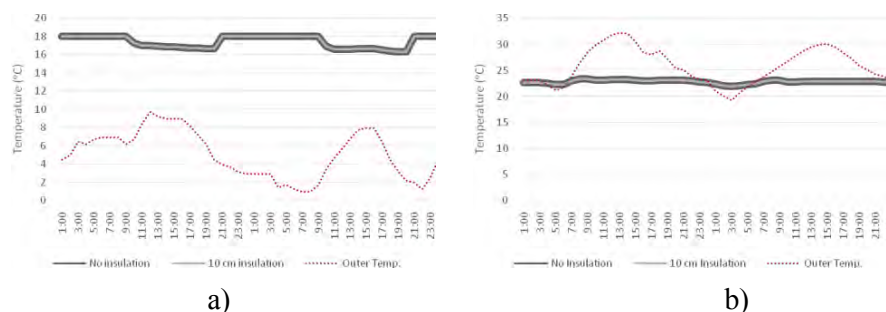
Figure 2. Simulated indoor temperatures (whole building) for S1 (base case without insulation) and S2 (base case with insulation) together with the external temperature data from the weather file. a) 15th and 16th of January, 2016, b) 15th and 16th of July, 2016.

a)   b)
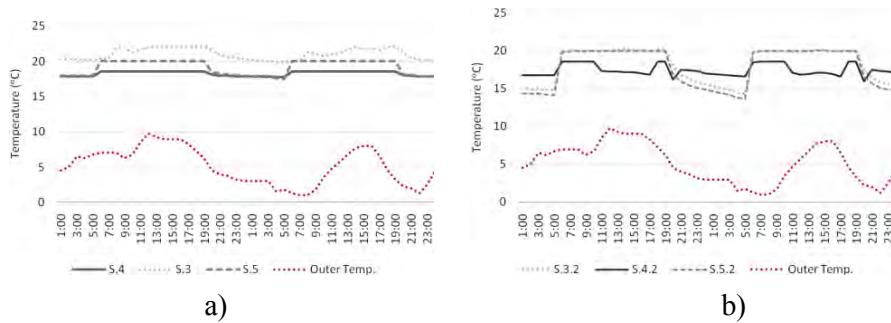
Figure 3. Comparison of the simulated indoor temperatures (whole building) of the scenarios together with the external temperature data from the weather file for the 15th and 16th of January, 2016, a) S3-S5 (underground), b) S3.2-S5.2 (above ground).

a)   b)
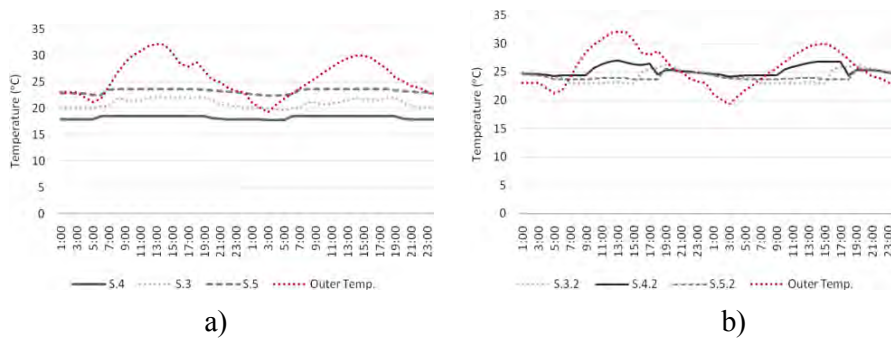
Figure 4. Comparison of the simulated indoor temperatures (whole building) of the scenarios together with the external temperature data from the weather file for the 15th and 16th of July, 2016, a) S3-S5 (underground), b) S3.2-S5.2 (above ground).

a)   b)
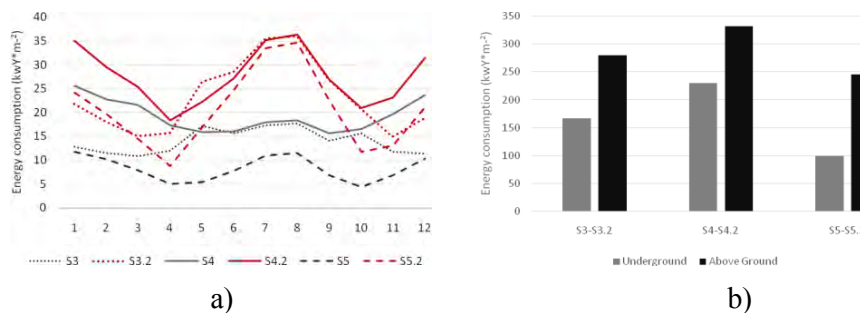
Figure 5. a) Comparison of simulated monthly energy demand (kWh.m^{-2}) for S3-S5 and S3.2-S5.2, b) Simulated annual energy demand (kWh.m^{-2}.a^{-1}) for S1-S5.

Figure 2 illustrates the thermal performance of base case scenarios with and without insulation, S1-S2. Figures 3 and 4 provide an overview of the thermal performance in the selected scenarios (S3-S5; S3.2-S5.2) based on two reference days in January and July. Figure

1356

5 summarizes comparative information regarding undergrounds' monthly energy use for the selected activities (S3-S5; S3.2-S5.2), as well as yearly overall energy consumption for S1-S5.

DISCUSSIONS

After comparing the theoretical background presented in the *Introduction* section and the results from the graphs in the *Results* section, conclusions are as follows:

i. The theoretical background assesses the heat flux of the soil in the depth where the tunnels are located, 25 m underground, is almost constant and allows the spaces enveloped in it to remain cool during summer and warm during winter. This fact is proven by the graphs shown in Figure 2 where the graph lines for 10 cm and no thermal insulation temperature performance are overlapping, thus demonstrating the effect of thermal insulation on the thermal performance of the building is negligible. During January, the time lag phenomenon described in the *Introduction* can be observed: the temperature alternates between the earth and the ground, when above ground the temperatures are high, they are lower underground and vice versa. The time lag is of approximately 10 hours. However, this phenomenon cannot be observed during July because the temperatures are constantly high and do not vary.

ii. Figures 3a and 4a compare the temperature performance of scenarios S3-S5 during two days in January and July. During January, all temperatures show an increment during the day, and cooling down after 18:00. The hospital's temperatures are more constant and 2-3℃ lower. The laboratory's and museum's temperatures vary considerably during the 12/24 hours of activity, most likely due to the nature of the activities held which require more physical interaction and movement from the people involved. During July, the temperature variation lines are considerably more constant and closer in value to one another. The average temperatures during July are 23.1℃, 24.2℃, and 23.3℃ for S3, S4, and S5 respectively. The average temperatures during January are 21℃, 18.3℃, and 19.1℃ for S3, S4, and S5 respectively. Figures 3b and 4b compare the temperature performance of the activity scenarios when located above ground: S3.2-S5.2. During January, the temperatures are lower by 3-5℃ in comparison to the same scenarios located underground, whilst during July they are 5-8℃ higher.

iii. The performance of the three scenarios regarding energy consumption varies. The average energy consumption per month is 14, 19.2, and 8.24 kWh m-2.a-1 for S3, S4, and S5 respectively. Regarding yearly energy consumption, the hospital's energy consumption results are 38% higher than the laboratory's, and 135% higher than the museum's. The results establish the same building consumes 44-145% more energy when located above ground as opposed to underground.

CONCLUSIONS

The case study of underground shelters poses an invitation for different research topics, however, the majority of information on them is provided by theoretical or qualitative studies. This paper is preoccupied with providing quantitative data on underground spaces, specifically nuclear shelters situated in the city of Kukës, Albania. The focus is on indoor thermal performance and energy consumption evaluation conducted via simulation software in order to assess the feasibility of adaptive reuse. Using the example of thermal simulation of a tunnel section, we explore the process and the recent results from the data collection. Hence, a building simulation model can be applied toward the assessment of the buildings'

performance and prediction of the consequences of alternative options for its renovation, reuse, and adaptation. Different scenarios are tested in order to assess the thermal performance of adaptive reuse alternatives for activities of 12/24 h, 24/24 h, and indefinite occupancy hours such as laboratories, hospital extensions, and museums respectively. The study concludes that a preferable scenario for adaptive reuse would be an activity held only 12/24 h, resulting in less energy consumption. In the present specific case, the 150 m section rooms can be proficiently repurposed as laboratory sectors that could serve to the hospital situated above ground. Although simulation and evaluation through software may face limitations due to the inability to make comparison with real life situations, the study represents an effective and well documented first step towards energy efficiency and possible adaptive reuse of abandoned underground or earth sheltered bunkers.

ACKNOWLEDGEMENT

REFERENCES

Alkaff, Saqaff A., Sim, S. C., and Ervina Efzan, M. N. 1993. A review of underground building towards thermal energy efficiency and sustainable development. In: *Renewable and Sustainable Energy Reviews*, Vol. 60, pp. 692-713.

Debertolis, P., Coimbra, F., and Eneix L. 2015. Archaeoacoustic Analysis of the Ħal Saflieni Hypogeum in Malta. In: *Journal of Anthropology and Archaeology*, Vol. 3, pp. 59-79.

Florides, G., and Kalogirou, S. 2004. Measurements of Ground Temperature at Various Depths. In: *Proceedings of the SET 2004, 3rd International Conference on Sustainable Energy Technologies on CD-ROM*, Nottingham.

Ip K. and Miller A. 2009. A. Thermal behaviour of an earth-sheltered autonomous building-The Brighton Earthship. In: *Renewable Energy,* Vol. 34, pp. 2037-43.

Kajtar L, Nyers J, and Szabo J. 2015. Dynamic thermal dimensioning of underground spaces. In: *Energy*, Vol. 87, pp. 361-8.

Li., X., Xu, H., Li, C., Sun, L., and Wang R. 2016. Study on the Demand and Driving Factors of Urban Underground Space Use. In: *Tunneling and Underground Space Technology*, Vol. 55, pp. 52-8.

Municipality of Kukës. 1973. General Urban Plan for the New City of Kukes. 1:2000.

Nývlt V, Musílek J, Čejka J, and Stopka O. 2016. The Study of Derinkuyu Underground City in Cappadocia Located in Pyroclastic Rock Materials. In: *Procedia Engineering*, Vol. 161, pp. 2253-58.

Polytechnic University of Bari. 2017. *Notes on the Underground Tunnels of Kukës*.

Popiel, C. O., Wojtkowiak, J., and Biernacka, B. 2001. Measures of Temperature Distribution in Ground. In: Experimental Thermal and Fluid Science, Vol. 25, pp. 301-309.

Tan Z, Roberts AC, Christopoulos GI, Kwok KW, Car J, Li XZ, et al. 2018. Working in underground spaces: Architectural parameters, perceptions and thermal comfort measurements. In: *Tunneling and Underground Space Technology*, Vol. 71, pp. 428-39.

Zhao, J., Peng, F., Wang, T., Zhang, X., and Jiang B. 2016. Advances in Master Planning of Urban Underground Space (UUS) in China. In: *Tunneling and Underground Space Technology*, Vol. 55, pp. 290-307.

Zhu J and Tong L. 2017. Experimental study on the thermal performance of underground cave dwellings with coupled Yaokang. In: *Renewable Energy*, Vol. 108, pp. 156-68.

Criteria for identifying failure optimization algorithms in building energy optimization and case studies

Binghui Si[1] and Xing Shi[1,*]

[1]School of Architecture, Southeast University, Nanjing, China

[*]*Corresponding email: shixing_seu@163.com*

ABSTRACT

Optimization algorithms plays a vital role in the Building Energy Optimization (BEO) technique. Although many algorithms are currently used in BEO, it is difficult to find an algorithm that performs well for all optimization problems. Some algorithms may fail in some cases. This study specifically focuses on failure algorithms in BEO and the possible causes. Several criteria are proposed for identifying failure algorithms. Four optimization problems based on the DOE small and large office buildings are developed. Three commonly used algorithms in BEO, namely, Pattern Search (PS) algorithm, Genetic Algorithm (GA) and Particle Swarm Optimization (PSO) algorithm, are applied to the four problems to investigate possible reasons for their failure. Results indicate that the effectiveness of the three selected algorithms is highly dependent on the optimization problems to be addressed. Besides, the control parameter setting of the PS algorithm appears to be a significant factor that may cause the algorithm to lose effectiveness. However, it does not seem to be the main reason for the failure of the GA and PSO algorithm. In General, the results gained from this study can deepen our understanding of optimization algorithms used in BEO. Besides, understanding the reasons why optimization algorithms are ineffective can help architects, engineers, and consultants select the appropriate optimization algorithms and set their parameters to achieve a better BEO design that is less vulnerable to failure.

KEYWORDS

Building energy optimization; failure optimization algorithm; cause of failure; algorithm parameter setting

INTRODUCTION

Building Energy Optimization (BEO) is a booming technique that combines building energy simulation engines with optimization engines. Unlike the conventional "trial-and-error" design methodology, which requires designers to manually adjust the design based on their experience and limited simulations, the BEO technique can automatically generate and simulate new designs utilizing optimization algorithms and performance simulation software and finally achieve the best design based on the predefined design objectives (Si et al. 2016). Therefore, optimization algorithms plays a crucial role in the application of the BEO technique.

As shown in some important review works (Machairas et al. 2014; Shi et al. 2016), a quite number of algorithms can be used in BEO, for example, the evolutionary algorithms, direct search algorithms, hybrid algorithms, etc. However, there is in fact no universal algorithm that applies to all optimization problems, which means an algorithm may fail under certain circumstances. Thus, finding the causes for their failure and exploring the circumstances under which an algorithm may become fail can significantly help designers to choose an appropriate algorithm among the available options and help them avoid failure algorithms.

The objective of this research is to study failure optimization algorithms used in BEO and possible failure reasons. The first research task is to develop a set of criteria to recognize whether an optimization algorithm fails for a BEO problem. Then four optimization problems are developed using the DOE small and large office buildings. Three optimization algorithms are selected to investigate the possible factors that may cause them to fail for the four optimization problems.

METHODS
Criteria for identifying failure algorithms
Before defining a failure algorithm, we need to distinguish two concepts: a failure algorithm and a failure optimization run. For a specific optimization problem, an optimization algorithm fails on an optimization run does not mean it fails for the optimization problem. The reasons are stochastic optimization algorithms (e.g., GA, PSO, etc.) usually involve random operators in their optimization processes, which will result in different optimization runs when they are run repeatedly. In this case, one specific optimization run cannot reflect the performance of the algorithm. Users need to repeat the optimization test as many times as possible and then analyse all optimization runs. However, for a determined optimization algorithm, it usually has a unique optimization run which can fully reflect the performance behaviour of the algorithm when all relevant parameters and the initial solution remain unchanged. Therefore, in this study, we firstly proposed two criteria, which are the most concerned issues for designers when using optimization techniques, to identify a failure optimization run. Then the failure rate criterion was used to identify a failure algorithm. Note that this paper is particularly focuses on single-objective algorithms because about 60% of the building optimization studies used the single-objective approach (Nguyen et al. 2014). Multi-objective optimization algorithms are not covered.

In general, a successful optimization run should find the optimal solution within the desired accuracy level using a limited amount of time. It requires two criteria that should be met simultaneously, one of which is the quality of the optimal solution obtained in the optimization run should be high enough to meet the users' requirements, and the other is the computing time cannot exceed the time limit. An optimization run that violates any of the above two criteria is considered failure. In this study, to measure the quality of the optimal solution, Equation 1 can be used to calculate the relative distance between the optimal solution found in an optimization run and the true optimum of the optimization problem.

$$\delta = \frac{|f(X') - f(X^*)|}{f(X^*)} \times 100\% \tag{1}$$

where $f(X')$ is the objective value of the optimal solution found in an optimization run, and $f(X^*)$ is the objective value of the true optimum, which in some cases can be obtained through brute-force search. If the value of δ is larger than that of δ^* which is the acceptable accuracy level defined by the designer, then the optimization run is considered failure.

To define a failure optimization algorithm for a given problem, the algorithm needs to repeat the optimization process several times and then those failure runs need to be isolated to calculate the failure rate, which in essence, is the ratio of failure optimization runs to the total runs. Equation 2 provides a formula.

$$\beta = \frac{N_{failure}}{N_{total}} \times 100\% \tag{2}$$

where $N_{failure}$ is the number of failure runs and N_{total} is the total number of runs driven by the algorithm. According to the Low Probability Event (LPE) principle (Mcclelland et al. 1993), which is an important theorem in probability and commonly applied in practical projects and mathematical statistics, an LPE is considered will not occur in the actual environment. In practice, the value of 0.01, 0.05 or 0.1 are commonly used for an LPE which can be denoted by β^*. Users can also set other values according to their specific conditions. Consequently, in this study, an algorithm is considered failure for a given optimization problem when $\beta > \beta^*$.

Description of the standard optimization problem

Table 1. Specifications of optimization variables.

Design variables	Symbol	Unit	Step size	Range	Initial value
Building long axis azimuth	x_1	°	5	[0,180]	90
Cooling set-point temperature	x_2	°C	0.05	[22,29]	24
Heating set-point temperature	x_3	°C	0.05	[15,22]	21
Roof insulation conductivity	x_4	W/m·K	0.001	[0.03,0.06]	0.049
Roof insulation thickness	x_5	m	0.002	[0.01,0.15]	0.126
South wall insulation conductivity	x_6	W/m·K	0.001	[0.03,0.06]	0.049
East wall insulation conductivity	x_7	W/m·K	0.001	[0.03,0.06]	0.049
North wall insulation conductivity	x_8	W/m·K	0.001	[0.03,0.06]	0.049
West wall insulation conductivity	x_9	W/m·K	0.001	[0.03,0.06]	0.049
South wall insulation thickness	x_{10}	m	0.002	[0.01,0.15]	0.036
East wall insulation thickness	x_{11}	m	0.002	[0.01,0.15]	0.036
North wall insulation thickness	x_{12}	m	0.002	[0.01,0.15]	0.036
West wall insulation thickness	x_{13}	m	0.002	[0.01,0.15]	0.036
South window upper position	x_{14}	m	0.02	[1,2.7]	2.5
East window upper position	x_{15}	m	0.02	[1,2.7]	2.5
North window upper position	x_{16}	m	0.02	[1,2.7]	2.5
West window upper position	x_{17}	m	0.02	[1,2.7]	2.5
South window U-value	x_{18}	W/m^{2}K	0.05	[1,7]	3.25
East window U-value	x_{19}	W/m^{2}K	0.05	[1,7]	3.25
North window U-value	x_{20}	W/m^{2}K	0.05	[1,7]	3.25
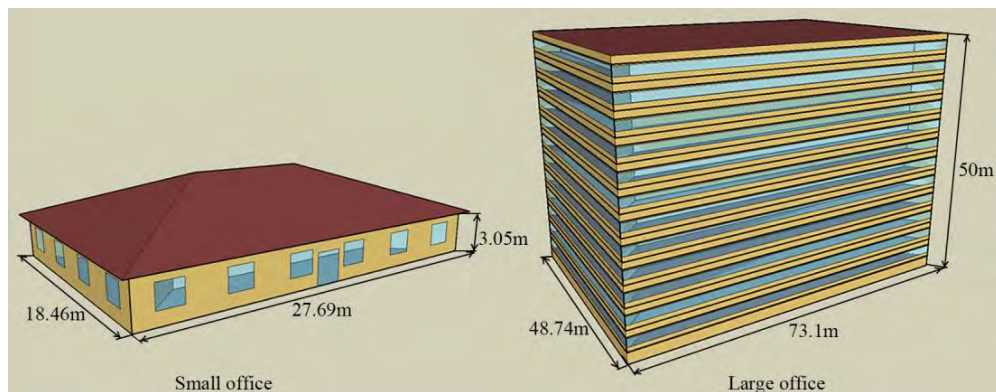
Figure. 1 Perspective views of the DOE small and large office buildings.

In this study, four optimization problems with 10 and 20 optimization variables respectively were developed following the models of the DOE small and large office buildings (Deru et al. 2011) in Baltimore, USA. They were all designed to minimize the annual energy consumption of the case buildings. Figure 1 shows the architectural schematic views of the buildings. They

all have one core thermal zone and four perimeter thermal zones on each floor. Table 1 lists the optimization variables involved in the optimization problems as well as their initial values, step sizes and range of variations. Specifically, the value for the lower window position is fixed at 0.9 m, and the windows in the same facade are of equal area. Besides, the first ten variables were used for optimization problems with 10 design variables.

RESULTS

In this section, three commonly used optimization algorithms in BEO, namely, Pattern Search (PS) algorithm, Genetic Algorithm (GA) and Particle Swarm Optimization (PSO) algorithm were assessed to find out possible factors that may can cause the algorithms to fail. As shown in Table 2, four algorithm parameter settings for each algorithm are randomly generated to investigate their impacts on the effectiveness of the selected algorithms. Readers are referred to the manual book (Wetter M, 2011) for more information of the working strategies and the original development of each algorithm. Based on the two criteria proposed above about a failure optimization run, two evaluation approaches are accessible: (1) assessing the quality of the optimal solution obtained when the computing time is restricted; (2) assessing the computing time consumed when the optimization run finds the desired solution. In this study, we chosen the first approach. The maximum number of simulations for each optimization run was restricted at 300, and each optimization process was repeated 10 times to calculate the failure rate. These numbers were chosen to strike a balance between what is preferred and what is practical in terms of computing time. Specifically, the true optimum of the four optimization problems were obtained by brute-force search and were listed in Table 3. Besides, the desired accuracy level δ^* of optimal solutions was set at 1%, and the acceptable maximum failure rate β^* was 10%.

Table 2. Algorithm control parameter settings for each algorithm.

Algorithms	Parameters	Test 1	Test 2	Test 3	Test 4
PS	Expansion factor	2	3	4	5
	Contraction factor	0.2	0.4	0.6	0.8
GA	Population size	10	15	20	30
	Number of generations	30	20	15	10
	Elite count	1	2	3	4
	Crossover fraction	0.2	0.4	0.6	0.8
	Mutation rate	0.05	0.1	0.15	0.2
PSO	Population size	10	15	20	30
	Maximum number of iterations	30	20	15	10
	acceleration const 1 (local best influence)	2	3	2	3
	acceleration const 2 (global best influence)	2	2	3	3
	Initial inertia weight	0.9	0.8	0.7	0.6
	Final inertia weight	0.4	0.3	0.2	0.1

For each optimization problem, the quality variation of the optimal solution obtained by each algorithm in each test were illustrated in Figure 2. As shown, each algorithm has 4 consecutive boxplots, corresponding to the 4 tests listed in Table 2. It is noted that all optimization runs used the same initial solution listed in Table 1 to avoid the influence of different initial solutions on the evaluation results.

As shown in Figure 2, for each optimization problem, the average quality of optimal solutions found by the PS algorithm changes violently between different tests, which means the performance of the algorithm is sensitive to its parameter settings. It is further verified when the PS algorithm was use to solve Problem 1, in which it succeed in Test 1 but failed in Tests

2-4. Therefore, inappropriate parameter settings of the PS algorithm may cause it to fail. However, for the same optimization problem, the average quality of optimal solutions searched by the GA and PSO algorithm appears to be more stable between different tests. Thus, the effectiveness of the two algorithms are less sensitive to their parameter settings. Although GA and PSO algorithm failed in all four tests for Problem 1, 2 and 4, we cannot conclude if different parameter settings will cause the two algorithm to lose effective.
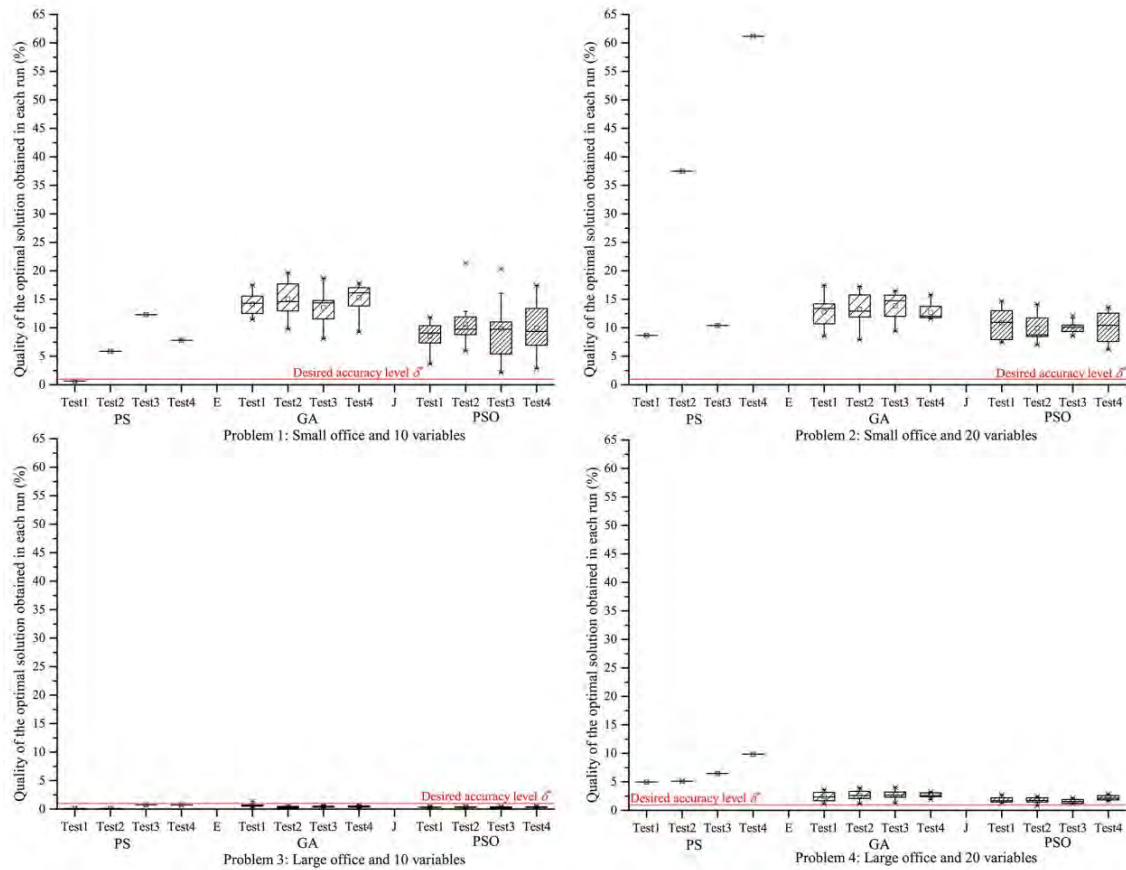

Figure. 2 Quality variability of the optimal solutions obtained by each algorithm in each test with different algorithm parameter settings.

Table 3. True optimum of each optimization problem and failure rate of each algorithm for each test.

Index	Optimization problems	True optimum (kW·h/m^{2}a)	Algorithms	Failure rate			
				Test 1	Test 2	Test 3	Test 4
Problem 1	Small office and 10 variables	95.532	PS	0	100%	100%	100%
			GA	100%	100%	100%	100%
			PSO	100%	100%	100%	100%
Problem 2	Small office and 20 variables	134.741	PS	100%	100%	100%	100%
			GA	100%	100%	100%	100%
			PSO	100%	100%	100%	100%
Problem 3	Large office and 10 variables	96.066	PS	0	0	0	0
			GA	10%	0	0	0
			PSO	0	0	0	0
Problem 4	Large office and 20 variables	125.355	PS	100%	100%	100%	100%
			GA	100%	100%	100%	100%
			PSO	100%	90%	100%	100%

Table 3 gives the calculated failure rate of the trial optimizations (each statistic relating 10 repeated optimization runs). It shows that for Problem 1, the PS algorithm performed well for Test 1with a failure rate of 0, but failed for Tests 2-4 with a failure rate of 100%. The quality of the optimal solutions obtained by GA and PSO in the four tests were all beyond the desired accuracy level of Problem 1, and therefore, their failure rates were all 100%. For Problems 3 and 4, all the three algorithms failed to find desired solutions in all tests with a failure rate larger than the acceptable maximum failure rate (i.e., 10%). However, when applying the three algorithms to Problem 2, all of them could consistently find desired optimal solutions with a failure rate of no more than 10% even when they used different parameter settings. Thus, the effectiveness of the three selected algorithms highly depends on the optimization problems solved. In this study, some properties involved in the Problems 1, 2 and 4 seem to dominate the failure of the three selected algorithms.

CONCLUSIONS
Optimization algorithms play a critical role in determining the effectiveness and efficiency of BEO techniques. In this study, the criteria for helping users to detect failure optimization algorithms used for BEO problems are proposed. Four optimization problems were developed to find out possible factors that may cause three commonly used algorithms to fail. The numerical results demonstrate the following failure mechanisms of the selected algorithms: (1) algorithm control parameter setting is an important factor that may cause the PS algorithm to fail but it does not seem to be a key factor that may cause the failure of the GA and PSO algorithm. (2) Some inherent properties of optimization problems may cause the three algorithms to fail because their performance appeared to be highly dependent on the optimization problems addressed. Future research is required to examine the impacts of different properties involved in a BEO problem on the performance behaviour of different optimization algorithms.

ACKNOWLEDGEMENT

REFERENCES
Si B., Tian Z., Jin X., Zhou X., Tang P. and Shi X. 2016. Performance indices and evaluation of algorithms in building energy efficient design optimization. Energy, 114, 100-112.
Machairas V., Tsangrassoulis A. and Axarli K. 2014. Algorithms for optimization of building design: A review. *Renewable & Sustainable Energy Reviews*, 31(2), 101-112.
Shi X., Tian Z., Chen W., Si B. and Jin X. 2016. A review on building energy efficient design optimization from the perspective of architects. Renewable and Sustainable Energy Reviews, 65, 872-84.
Nguyen A.T., Reiter S. and Rigo P. 2014. A review on simulation-based optimization methods applied to building performance analysis. *Applied Energy*, 113, 1043-1058.
Mcclelland G.H., Schulze W.D., and Coursey D.L. 1993. Insurance for Low-Probability Hazards: A Bimodal Response to Unlikely Events. Making Decisions About Liability And Insurance, Springer Netherlands.
Deru M., Field K., Studer D., Benne K., Griffith B., Torcellini P., Liu B., Halverson M., Winiarski D., Rosenberg M. and Yazdanian M. 2011. US Department of Energy commercial reference building models of the national building stock.
Wetter M. 2011. GenOpt® Generic Optimization Program User Manual Version3.1.0. Lawrence Berkeley National Laboratory.

Effects of Gaseous Pollution and Thermal Conditions on the Corrosion Rates of Copper and Silver in Data Centre Environment: A Literature Review

Rui Zhang[1, *], Roger Schmidt[1], Jeremy Gilbert[2] and Jensen Zhang[1]

[1]Syracuse University, Syracuse
[2]Clemson University, South Carolina
[*]*rzhang20@syr.edu, rrschmid@syr.edu, jlgilbe@clemson.edu, jszhang@syr.edu*

ABSTRACT
The objectives of the present review are to: 1) summarize the existing knowledge on the mechanisms of the corrosion, identify and analyze the major factors affecting the corrosion of copper and silver; 2) compare various measurement techniques for the study of atmospheric corrosion and models of corrosion; 3) identify knowledge gaps for atmospheric corrosion; 4) recommend "realistic worst case" pollution levels for laboratory testing of humidity and temperature effects on corrosion and assessment of datacom equipment reliability in data centers. This review focuses on the five pollutants: SO_2, NO_2, H_2S, O_3 and Cl_2. Results of the review include: the pollution levels and thermal environmental conditions in data centers; fundamental mechanisms of corrosion; current knowledge of the major factors affecting the corrosion rates of copper and silver; the techniques (QCM, Coulometric Reduction, SEM, XPS, FTIR and EIS) for the measurement of corrosion levels. It was found that the "realistic worst-case" concentrations for H_2S, NO_2, SO_2, Cl_2 and O_3 are 10 ppb, 80 ppb, 40 ppb, 2 ppb and 60 ppb, respectively. Different levels and combinations of contaminants, temperature, relative humidity and air velocity cause different corrosion on the metal. Chloride, Nitrogen dioxide and Sulfur dioxide are the common corrosive gases for the datacom equipment. Hydrogen sulfides and ozone are very important gaseous contamination in data center environment. Each of them alone can damage the equipment, and their synergistic effects with the other compounds and humidity can cause significantly more damages, but a mechanistic model is lacking for predicting the synergistic effects and better design of the thermal environment to ensure equipment reliability while improve the energy efficiency through the use of outdoor air for free cooling.

KEYWORDS
Atmospheric corrosion, copper, silver, SO_2, NO_2, H_2S, O_3 and Cl_2

INTRODUCTION
Data centers have the highest energy usage intensity among all building types and consume increasingly more energy due to the significant increase in the number of data centers worldwide. In an effort to reduce energy consumption, an increasing number of data centers have adopted air-side economizers to enable "free-cooling". However, gaseous and particulate contaminants can enter data center when using air-side economizers, which may cause environment-related IT and Datacom equipment failures. Due to lack of data on the severity of the corrosion effects under realistic concentration levels and thermal environmental condition, gaseous contamination limits for the reliable operation of electronic equipment cannot be specified presently in terms of the concentration of gaseous contaminants in the air. ITEs can operate in a wide range of thermal environmental conditions including relative humidity levels up to 80% according to the current standards (ASHRAE, 2012c). There is clearly a need to determine the allowable gaseous concentration limits for the data center environment, especially under higher relative humidity conditions.

The objectives of the present review are to summarize the existing knowledge about the mechanisms of the corrosion, compare various measurement techniques for the study of atmospheric corrosion, identify knowledge gaps for atmospheric corrosion and recommend the "realistic worst case" pollutant levels and thermal environmental conditions for corrosion testing and assessment for data center applications.

MECHANISM OF ATMOSPHERIC CORROSION

Atmospheric corrosion is one kind of electrochemical corrosion. It occurs at the metal-solution interface with the creation of cathodic and anodic sides of the metal surface. The anode and cathode reactions in atmospheric corrosion are shown in Equation (1) and (2):

$$Me \rightarrow Me^{n+} + ne^- \quad \text{(anode reaction, metal dissolution)} \tag{1}$$

$$\frac{1}{2}O_2 + H^+ + 2e^- \rightarrow OH^- \text{(cathode reaction, oxygen reduction)} \tag{2}$$
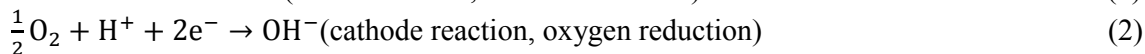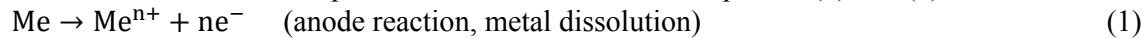
Figure 1 shows various processes involved in the atmospheric corrosion of copper based on the existing finding from the literature (T. Aastrup, 2000).
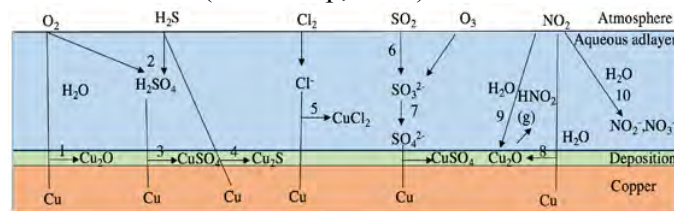

Figure 1 A schematic description of the atmospheric corrosion of copper

In the case of corrosion of ITEs, because the air is strictly controlled to have a dew point lower than the surface temperature of ITEs components to avoid apparent condensation, the aqueous layer above is likely to be only a thin layer or multi-layer of H_2O molecules adsorbed on the surface. Without the presence of contaminants, O_2 can diffuse into the aqueous layer and react with the pure copper to form a layer of copper oxide, a deposition layer that would protect the copper from corrosion. However, the gaseous pollutants, if present, can be dissolved into the adsorbed water molecules and react with O_2 to form H_2SO_4, which then reacts with copper to form copper sulfates. H_2S can also react directly with copper and O_2 to form copper sulfides (Processes 1 through 4 above).

When chlorine dissolves in the aqueous adsorption layer (adlayer), it resolves to the chloride ions. And these ions can react with the copper, which causes the copper dissolves into the liquid regime. Sulfur dioxide react with ozone in the liquid regime and ozone oxidizes the sulfur dioxide to H_2SO_4. Then H_2SO_4 combines with copper to generate the $CuSO_4$. NO_2 dissolves in the liquid regime and create HNO_2. And it has a reaction between HNO_2 and Cu to get the products of Cu_2O and HNO_2(gas). NO_2 also generates NO_2^- and NO_3^- after dissolving in the liquid. (Processes 5 to 10 above). While the reaction processes can be identified qualitatively, data are lacking on the reaction rate constants for the various processes identified above, and the synergistic effects of the various compounds under different relative humidity and temperature conditions cannot be readily determined from the existing literature.

FACTORS AFFECTING THE CORROSION RATES OF COPPER AND SILVER
Relative humidity

Primary, secondary and tertiary values of Critical Relative Humidity have been defined as the values of relative humidity below which no corrosion of the metal in question takes place, at which corrosion occurs rapidly, and above which further acceleration of corrosion can be

observed (if exists). The primary value of critical RH for uncorroded metals seems to be virtually independent of type of metals, which depends on the type of pollutants and moisture content (and hence the temperature for the given relative humidity level) in the atmosphere (Vernon, 1935). But the secondary and tertiary (if exists) values vary quite widely, depending on the presence and levels of gaseous pollutants and their potential synergistic effects as well as the metal type (Syed, 2006).

Air temperature

For a given moisture content (or specific humidity) in the moist air mixture, an increase in temperature reduces the level of relative humidity, resulting less water molecules being adsorbed on the material surface, and hence leads to a less amount of soluble pollutant's deposition on the surface and would likely reduce the corrosion effect (Mohan, 1991). However, on the other hand, a higher temperature tends to increase the reactivity of the ionization processes involved in the corrosion, and hence could enhance the corrosion effect (Franey, 1985) Therefore, the tradeoff between these two opposite effects needs to be evaluated for specific pollutant or pollutant mixture.

Sulfur dioxide

Sulfur dioxide is the most common corrosive gas for the Datacom equipment. Combustion of all fossil fuels can form the sulfur dioxide. Copper exposed to 80% RH, and 200 ppb SO_2 for approximately 1000 minutes formed copper sulfite, probably as a $CuSO_3$-xH_2O-like species, and cuprous (Cu_2O-like) oxide as major corrosion products (T. Aastrup, 2000). Similar results were also obtained by Erikson (1993).

Nitrogen Dioxide

Nitrogen dioxide source is the high-temperature combustion and biomass burning. Natural phenomenon like lightening also forms NO_2. According to Eriksson (1993), NO_2 has very small corrosive effects alone even in the ppm range. Muller (1991) also found that nitrogen dioxide had little influence on the corrosion rate of silver. The data reviewed above indicates that the NO_2 alone is not a significant factor for corrosion, but it can accelerate corrosion through synergistic effect with SO_2. Data on its possible synergistic effect with other gases of interests such as O_3, H_2S, and Cl_2 under different humidity and temperature conditions are lacking.

Hydrogen sulfide

Hydrogen sulfides is the most important gaseous contamination in the data center. It can cause the serious corrosion on the circuit board. Hydrogen sulfide is formed by the fossil fuel processing and combustion and natural processes (decay of vegetation in soils and wetlands, excess sulfur emission from vegetation and the like). There are two common modes of hardware which will be damaged if they are exposed to the sulfur-bearing gases (H_2S, SO_2): printed circuit boards (PCBs) and miniature surface-mount technology (SMT) resistors. Trana (2003) found that after the copper was exposed in this condition, copper sulfide was formed. Exposure to a higher concentration of H_2S resulted in a faster and larger increase of the thickness of Cu_2S, as expected. The data also show that there appears to be a maximum thickness of Cu_2S of 8-10 um, beyond which further increase of exposure time had little impact on the thickness. It is possible that at this thickness, the Cu_2S layer became a significant resistance to the diffusion of ions between the adsorbed moisture layer and the pure copper, and hence slowed down the electrochemical process that was responsible for the corrosion. It is noted that even at 10 ppb (the proposed realistic worst-case level), 0.1 um of corrosion layer was measured after 3 days of exposure (T.T.M.Trana, 2003).

Ozone

Natural and anthropogenic electrical discharge is the source of the ozone. It can increase the corrosive effect for the copper and silver (T. Aastrup, 2000). Ozone also enhanced the copper sulphadation when copper was exposed in SO_2 with ozone (T. E. Graedel, 11 May 1984).

Chloride

Chloride has limited corrosive ability to copper or silver. But it has a large influence on these metals when it combines with the hydrogen sulfide. In the study by Muller (1991), the copper and silver were exposed to 1.9 ppb of Cl_2 at 22°C and 50 $\pm$ 5% RH for one month. The results show that chloride alone had mild corrosion effect, similar to that of SO_2 tested, but significantly weaker than that of H_2S. Data are lacking on the synergistic effects of Cl_2 with other gasses, and for different RH and temperature conditions. When copper is exposed in H_2S, Cl_2 and NO_2, the role of Cl_2 is to remove the Cu_2O then other pollutants can attack Cu directly(Abbott,1988).

Synergistic effect

Figure 2 shows the corrosion thickness as a function of pollutant exposure amount (concentration times duration) found by previous researchers. The combined effects of different pollutants and relative humidity are very complex, and not yet well understood. Data is especially lacking under field concentration levels which are typically much lower than those used in the laboratory studies.
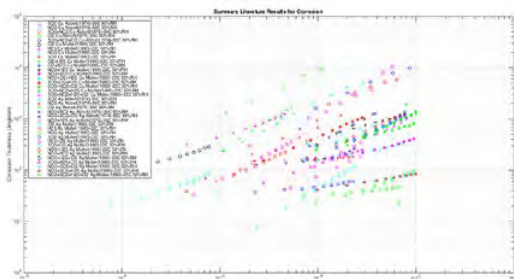

Figure 2 Summary Literature Corrosion Results

Chloride, Nitrogen dioxide and Sulfur dioxide are the common corrosive gases for the Datacom equipment. Each of them alone can cause only a small amount of corrosion on the metallic surfaces, even though some corrosion products can be detected on the surfaces of the materials. However, their co-existence can cause significant corrosion to ITEs due to synergistic effects among them Muller (1991). Cl_2, H_2S, NO_2 and SO_2 can all cause significant damages to silver surface. But for coppers, H_2S and Cl_2 can cause the most damage. Hydrogen sulfides and ozone are very important gaseous contamination in data center environment. Each of them alone can damage the equipment, and their synergistic effects with the other compounds can cause even more damages (T. Aastrup, 2000). The catalytic mechanism can increase the reaction speed but cannot produce additional products. It is necessary to consider the synergistic effect to assess the risk of ITE failure in a polluted environment. Such studies are lacking and need to be pursued in order to develop a reliable method for failure predictions.

MODELING OF ATMOSPHERIC CORROSION

In the data center, gaseous contaminations can include SO_2, H_2S, NO_2, Cl_2, and H_2S. They can corrode the metallic materials and damage the circuit boards, connectors and various other electronic components. From the multi-regime perspective on atmospheric corrosion chemistry (Graedel, 1996), six regimes can be identified (Figure 3-1): G (gas), I (interface), L (liquid), D (deposition layer), E (electrode regime) and S (solid). Study of different layers requires knowledge of different science fields: gas layer – atmospheric chemistry; interface layer – convective and diffusive mass transfer and interface thermodynamics; liquid layer – freshwater, marine, and brine chemistry; deposition layer – colloid chemistry, surface science, and mineralogy; electrodic layer – electrochemistry; and solid layer – solid-state chemistry.

In this model, for the gas regime, pollutant gases by convection or detrainment from interface

get into this regime. Then some of the gases deposit on the interface. Some species have chemical interaction with each other. When they arrive at the interface, some of them will volatilize into the gas regime and some enter into the liquid regime. In the interface regime, there are some chemical transformations among different
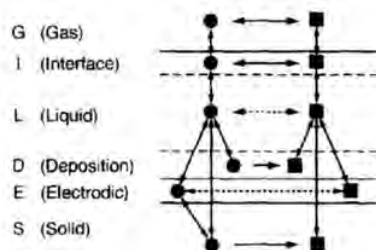
species. In the liquid regime, the species not only can reach the deposition regime but also can directly reach the electrodic regime and the solid regime. Chemical transformation can take place at each regime. For the species in the solid regime, they react with species which come from the liquid regime and electrodic regime. The electrodic regime is where electrochemical reaction takes place. Copper loses its electrons and becomes the copper ions which get into the electrodic regime. Oxygen which is in the liquid regime reacts with the copper ions to generate the depositions. The circle and square symbols represent different species. When the corrosion products are generated over the surface, they will become more resistant to the corrosion process. The research of T.T.M.Tran (2003) shows that Cu_2S is an important resistance of diffusion of the ions between the liquid regime and the solid regime.

Figure 3 A schematic representation of the six regimes

MEASUREMENT TECHNIQUES

In order to analyze the corrosion, there are many techniques for monitoring the mass change and for analyzing the geography of surface and surface compositions. Quartz crystal microbalance (QCM) is a technique to detect the mass change of the materials using the piezoelectric effect. In scanning electron microscopy (SEM), the information of topography and composition on the surface can be gained. X-ray photoelectron spectroscopy (XPS) is for the solid surface. It can be applied for the oxide thickness measurements. It can identify all elements except for hydrogen. In Fourier transform infrared spectroscopy (FTIR), it is useful for identifying the "chemical family" of a substance. An electrochemical impedance spectroscopy (EIS) is very useful for detecting the atmospheric corrosion. It measures the corrosion rate by estimating the polarization resistance, which is based on the theory of AC impedance. This technique is useful on high resistance materials and non-destructive. Coulometric Reduction is an electrochemical-based technique. This technique measures the thickness of the film by monitoring the quantity of electricity which is forming during the chemical reaction between the electrolyte and the corrosion products.

RECOMMADATION FOR THE "REALISTIC WORST-CASE CONCENTRATION LEVELS"

Table 1. Summary of Pollutant Concentrations and Recommended Limits by IEC (2002), Telcordia (2006), ISA(1985) and One Manufacturer's Internal Standards

Gas	H_2S		SO_2		Cl_2		NO_2		O_3	
	Max	Min	Max	Min	Max	Min	Max	Min	Max	Min
Measurement (ppb)	8310008	0.101	87	0	0.58	0	152	0	174	0
Limits (ppb)	40	2	50	10	35	1	700	50	123	2

Table 1 shows the measurement data of outdoor pollutant levels and the concentration limits recommended for IT equipment protection against corrosion. The current guideline gives the recommended temperature and relative humidity envelope: the dew point is from -9 °C to 15 °C; The dry-bulb temperature is from 18 °C to 27 °C and the relative humidity is less than 60%. We propose the following as the "realistic worst- case concentration levels" for the MFG testing (Table 2)

Table 2. Proposed "Realistic Worst Case" Concentrations for Mixed Flow Gas (MFG) Testing

Pollutant	H_2S	NO_2	SO_2	Cl_2	O_3
Concentration (ppb)	10	80	40	2	60

The values in the table are consistent with the guideline limits for G2 (moderate) levels of corrosion per the ANSI/ISA Standard 71.04-2013.

SUMMARY AND CONCLUSIONS

It was found that the "realistic worst-case" concentrations for H_2S, NO_2, SO_2, Cl_2 and O_3 are 10 ppb, 80 ppb, 40 ppb, 2 ppb and 60 ppb, respectively. Chloride, Nitrogen dioxide and Sulfur dioxide are the common corrosive gases for the datacom equipment. Hydrogen sulfides and ozone are very important gaseous contamination in data center environment. But the lack of knowledge is about the synergistic effect at different thermal environmental conditions. There is lacking for a mechanistic model to predict the synergistic effects combing with various thermal environment.

REFFERENCES

Abbott, W. H. (1988). The Development and Performance Characteristics of Mixed Flowing Gas Test Environment. *IEEE Transactions on Components, Hybrids, and Manufacturing Technology VOL. 11. NO. 1. MARCH 198R*, Vol. 11, No. 1, 22-35.

ASHRAE. (2012c). *Thermal Guidelines for Data Processing Environment, 4ed.* ASHRAE.

Chris, M. (1991). Multiple Contaminant Gas Effects on Electronic Equipment Corrosion. *Corrosion - Houston*, 47(2), 146-151.

D.W.Rice, P. E. (1981). Atmospheric Corrosion of Copper and Silver. *Journal of Electrochamical Society*, Vol. 128, No. 2, 275-284.

J. P. Franey, G. W. (1985). The Corrosion of Silver by Atmospheric Sulfurous Gases. *Corrosion Science*, Vol. 25, No. 2, 133-143.

L.Mariaca, D. l. (2008). Interaction of Copper and NO2: Effect of Joint Presence of SO2, Relative Humidity and Temperature. *Journal of Physics and Chmistry of Solids*, 895-904.

P. S. Mohan, M. S. (1991). Corrosion of Metals in Sulphur Dioxide Atmosphere - A Laboratory Study. *Key Engineering Materials*, 179-184.

Peter Eriksson, L.-G. J. (1993). Initial Stages of Copper Corrosion in Humid Air Containing SO2 and NO2. *Journal of the Electrochemical Society*, Vol. 140, No. 1.

R.Wiesinger, I. C. (2013). Influence of Relative Humidity and Ozone on Atmospheric Silver Corrosion. *Corrosion Science*, 69-76.

S. Feliu, L. M. (2003). Effect of NO2 and/or SO2 Atmospheric Contaminants and Relative Humidity on Copper Corrosion. *Rev. Metal. Madrid*, 279-288.

Syed, S. (2006). Atmospheric Corrosion of Materials. *Emirates Journal for Enginerring Research*, 1-24.

T. Aastrup, M. W. (2000). In Situ Studies of the Initial Atmospheric Corrosion of Copper Influence of Humidity, Sulfur Dioxide, Ozone and Nitrogen Dioxide. *Journal of the Electrochemical Society*, 147(7), 2543-2551.

T. E. Graedel, J. P. (11 May 1984). Ozone- and Photon-Enhanced Atmospheric Sulfidation of Copper. *Science*, Vol. 224, Issue 4649, 599-601.

T.T.M.Trana, C. F. (2003). The atmospheric corrosion of copper by hydrogen sulphide in underground conditions. *Corrosion Science*, Volume 45, Issue 12, 2787-2802.

Vernon, W. H. (1935). A Laboratory Study of the Atmospheric Corrosion of Metals.

Elaboration of the decision space for an optimization of building retrofit

Yannis Merlet[1,*], Simon Rouchier[1] Arnaud Jay[2] and Monika Woloszyn[1]

[1]Univ. Grenoble Alpes, Univ. Savoie Mont Blanc, CNRS, LOCIE, 73000 Chambéry, France
[2]Univ Grenoble Alpes, CEA, LITEN, DTS, INES, F-38000 Grenoble, France

[*]*Corresponding email: yannis.merlet@univ-smb.fr*

ABSTRACT
Multiobjective optimization is widely used in building physics but it has to face construction and regulation constraints to elaborate feasible solutions. This paper investigate how to integrate constraints in genetic optimization carried out with NSGA2 algorithm: it studies the implementation of constraints in the decision space and its impact on convergence speed and diversity in the optimization. The study was carried out on a 8 appartments building with three objective function to optimize: energy demand, comfort of the tenants and economic cost. As a result, convergence speed was improved and expert knowledge was included inside the decision space in a comprehensive way.

KEYWORDS
Multiobjective optimization, retrofit, building stocks, decision space

INTRODUCTION
In France, new buildings represent 1% of constructions each year. Decreasing the energy demand of the entire building stock will only be achieved if existing building are refurbished. On this topic social housing tenants have specific constraints and opportunities, and build their refurbishment strategies based on expert judgment. Experts try to balance constraints such as environmental impact, energy consumption, comfort of tenants to end up on a good solution and it is not possible to confirm that they are objectively the best solutions. Multiobjective optimization is an appropriate approach to efficiently suggest optimal solutions, so the expert could focus on picking a solution in the optimal ones. This work has been carried out in the scope of Reha-Parcs project which aim to apply multi-objective optimization on building stocks constituted of approximately 100 buildings owned by the same entity. Optimal solutions may then feed a decision-making tool for managers to pick the best one according to subjective needs like local policy, and funding.

Multi-objective optimization has been carried out on the design stage of new buildings to improve the shape and windows with respect to the energy demand and comfort (Tuhus-Dubrow and Krarti 2010; Diakaki, Grigoroudis, and Kolokotsa 2013) . Other work addresses the optimization of HVAC Systems in addition to the building envelope (Machairas, Tsangrassoulis, and Axarli 2014).

In multi-objective optimization, the formulation of the problem has a significant role in the success of the process, in order to get solutions that fit with construction and regulation constraints. The implementation of these constraints is mostly done at the optimization level by a penalty function (Coello Coello 2002). This approach limits the number of valid individuals in the population and consequently limits the diversity of the solutions. This seems to imply more generations to be computed in order to achieve the same diversity. This can be

time consuming depending on the computational cost of the evaluation function, especially on multiple buildings, as it limited previous works (Rivallain 2013)

A novel approach is to integrate constraints directly into the decision space, and this is the main focus in this paper. The aim of the study is to determine the impact of the integration of constraints in the decision space in term of convergence speed and diversity of the optimization.

METHODS
Optimization involve multiple parts: in this section will be detailed the evaluation function used to affect a fitness value to each retrofit strategy, the algorithm that has been chosen to carry out the optimization and the decision space of the optimization.

To evaluate the energy efficiency of a retrofit strategy, a test building has been modelled. This building is constituted of 4 floors and 8 apartments. Each apartment is 65m2 large and is 2,3m high. In the model, each of those apartments is a thermal zone. The building is modelled in Modelica language using models issued from the *BuildSysPro* library, developed by EDF (Plessis et al. 2014). The model features an ideal heating generator and will be upgraded in future work with realistic systems. A TMY file is used to simulate the weather of the city of Nice (France). The objective function of the simulation are the energy needs of the building and summer comfort of the inhabitants that is presented in degrees.hours above an adaptive comfort temperature. The adaptive comfort model chosen is the revised standard 55 of ASHRAE (De Dear and Brager, 2002).
The last objective function is the economic cost of retrofit strategies. It is calculated with expert data provided in Reha-Parcs project: material price is a function of its thickness, then labour time cost is included and added to it.

First of all, the choice of an appropriate algorithm has been made with respect to the discrete nature of the problem: in order to keep only possible strategies. Indeed we had to comply with commercial solutions (eg. insulation is available for only selected thickness). In a discrete decision space, genetic programming suits better to the problem (Evins 2013). Moreover, genetic algorithm are widely used in building physics, especially NSGA2 (Deb et al. 2000) as it has proven to be both stable and efficient. In this paper, we used the implementation of NSGA2 provided in Python library DEAP (Fortin et al. 2012). The parameters used are the following:

Table 1: Settings of NSGA2 algorithm

Number of individuals	96
Number of generations	50
Probability of crossing	0,8
Probability of mutation	0,2

Those parameters were selected after a literature study (Rosenthal and Borschbach). They enable to have a good exploration of the decision space with mutation while the convergence speed towards Pareto front is not slowed down. The number of individuals has been selected to be 96 for a good diversity and to suit the 48 cores available for parallel computation.

In this paper, the main focus is on the decision space. In our case, the decision space is constituted of a series of retrofit possibilities. Those retrofit possibilities are considered for the

envelope: outer walls, top floor ceiling, bottom floor and windows. The comparison is made between a decision space that includes every retrofit possibility broken down into elementary tasks and a decision space composed of aggregated task for walls and windows operations. Both of them are described below.

Standard decision Space

The outer vertical walls, ceiling and floor have the same structure, which is 20cm of reinforced concrete. Vertical walls, ceiling and floor are independent from each other in the optimization. The insulation proposed features one of the following component:

Table 2: Insulation possibilities for outer walls in the optimization

Insulation material	Commercially available thickness (in cm)
Polyurethane	2, 4, 6, 8, 10, 12, 14, 16, 18, 20
Glasswool	6, 8, 10, 12, 14, 16, 18, 20
Polystyrene	6, 8, 10, 12, 14, 16

Another parameter of the optimization is the windows: the U coefficient for each type of window is the value that changes. Commercially available windows used in refurbishment in France where again provided by expert data within Reha-Parcs project, and are as follow:

Table 3: windows possibilities in the optimization

Windows U values	0.8, 1, 1.2, 1.4, 2

As a result, this decision space provides 109760 possibilities of retrofit that could be applied on the building.

Constrained decision Space

The second decision space differs from the first one as windows and outer vertical walls are combined: in this problem, one gene of each individual corresponds to a facade solution which includes one type of window and one type of insulation of the vertical walls.

In order to fit construction constraints, some solutions are not possible: these solutions involve high performance wall with low performance windows or high performance windows with low performance walls. In this problem, 22 combination are forbidden. Should an individual propose on a forbidden solution, it will be mutated until it is an allowed combination. In this way, optimization avoids a costly evaluation function but can slow the convergence of the optimization. Constraints slightly reduce the decision space to 92512 possibilities offered to elaborate retrofit strategies.

RESULTS

In order to benchmark convergence speed of the optimization, we chose the Hypervolume criteria (Zitzler et al. 2002). Hypervolume is computed with a reference point chosen outside the objective space of both optimizations: depending on the shape of pareto front, the reference point can be selected from Nadir point to 150% of the values of Nadir point (Ishibuchi et al. 2017). Here, according to Ishibuchi and the shape of our Pareto fronts, the reference point should be between 120% and 150% of Nadir point's values. Whatever the value for the reference point results remain identical, hence figures for a reference point at 130% of Nadir point will be presented. Same reference point has been selected for both of hypervolumes computation.
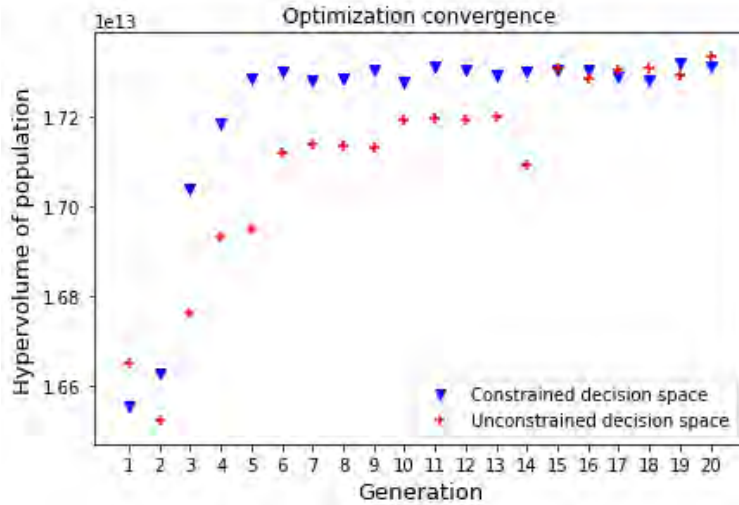
Figure 1: Convergence performance of each decision space

This figure show a quickest convergence of the optimization when carried out with the constrained decision space. With this decision space, the best Pareto front is reached from generation 6 while with the first and unconstrained decision space, best solutions are found at generation 15. Moreover, the figure shows that with the unconstrained decision space, optimization does not reach global optimum before generation 15, while constrained decision space does reach it as soon as generation 5.

Pursuing the optimization until 50th generation shows that hypervolume does not vary significantly after generation 15, that is why only the first 20 generations are showed in Figure 1. It decreases for some generations due to mutations of individuals and get back to prior levels after two generations of selection.

Figure 2: Pairwise plotting of last generation of optimization

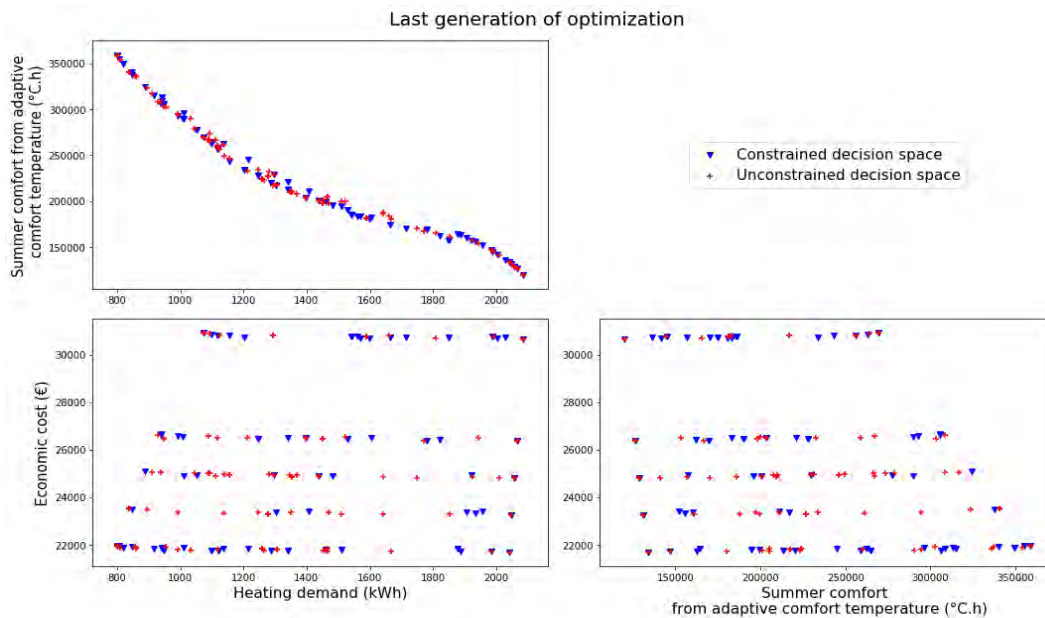Diversity of individuals is ensured with NSGA2's selection process. The diversity of proposed solutions can be checked by plotting Pareto fronts: Figure 2 shows Pareto fronts for all of the 3 objectives. A wide spread of the solution can be noticed and can sometimes be counter-intuitive regarding the performance of some of them. However, NSGA2 tends to keep only strictly non dominated solutions since it is an elitist algorithm.

DISCUSSIONS

Results support the integration of constraints in the decision space on a test case rather small with a decision space composed of around 100 000 possible combinations. It shows that optimization could be stopped 7 generations earlier with the same results if constraints are implemented in decision space, saving in our case 672 thermal simulations, which are the more costly part of the optimization calculation-wise.

This approach avoid implementing constraints by penalty function or by "death penalty" (Coello Coello 2002), but still enable to incorporate expert knowledge in the optimization problem. Moreover, it shows that adding expert knowledge in the algorithm can speed up the elaboration of retrofit strategies on this multi-family dwellings. Those results are promising since regulation and new construction solutions brought to market are generating more and more constraints, and we can implement them in a comprehensive way. Indeed it will help bringing multi-objective optimization to engineering by keeping the link between optimization constraints and practical solutions. In addition as a minor side effect, implementing constraints in the decision space saves time in post-processing to pick possible solutions and preventively clears out unrealistic solutions.

As optimization problem are quite specific, further studies will have to determine whether the impact is the same with more complex problems. First of all, the combinatorial will get bigger with the implementation of new possible retrofit tasks in the decision space. Secondly, the aim is to turn building model into a small building stock model of around 15 buildings with different shape and construction type. Finally, the application of such constraints should be verified with more than 3 objectives as NSGA2 algorithm is less efficient with more objectives (Campos Ciro et al. 2016).

CONCLUSIONS

This paper presents a method to integrate constraints in a problem of multi-objective optimization of building retrofit. A case test was studied in order to compare the performances of this approach: as a result, 25% less evaluation were needed during the optimization process in order to converge to Pareto front of optimal solutions. Some solutions proposed by the algorithm can be counter intuitive because of its performance on one objective but are still non-dominated on other objective, which illustrates that diversity is kept in the set of possible solutions.

Multi-objective optimization is a growing field when it comes to retrofitting buildings, and will get more important to develop strategies for energy conservation for buildings and building stocks. That is why we handled constraints here with a simple description that keeps the link between the decision space and the actual construction work. This method would be appropriate for an integration in an engineering tool featuring interactive decision-aid for the elaboration of optimal retrofit strategies developped by (Delhomme et al. 2017). This tool will enable designers to parse through optimal solutions for energy retrofit and to save time on

defining building stock-wide retrofit strategies and spend more time on non objective criteria such as the acceptability by users and urban integration of retrofit strategies.

REFERENCES
Campos Ciro, Guillermo, Frédéric Dugardin, Farouk Yalaoui, and Russell Kelly. 2016. "A NSGA-II and NSGA-III Comparison for Solving an Open Shop Scheduling Problem with Resource Constraints." Elsevier: 1272–77.

Coello Coello, Carlos A. 2002. "Theoretical and Numerical Constraint-Handling Techniques Used with Evolutionary Algorithms: A Survey of the State of the Art." *Computer Methods in Applied Mechanics and Engineering* 191 (11–12): 1245–87.

Dear, Richard J. De, and Gail S. Brager. 2002. "Thermal Comfort in Naturally Ventilated Buildings: Revisions to ASHRAE Standard 55." *Energy and Buildings* 34 (6): 549–61.

Deb, Kalyanmoy, Samir Agrawal, Amrit Pratap, and T. Meyarivan. 2000. "A Fast Elitist Non-Dominated Sorting Genetic Algorithm for Multi-Objective Optimization: NSGA-II." In *Proceedings of 6th International Conference on Parallel Problem Solving from Nature*

Delhomme, Benjamin, Franck Taillandier, Irène Abi-Zeid, Rallou Thomopoulos, Cédric Baudrit, and Laurent Mora. 2017. "Designing an Argumentative Decision-Aiding Tool for Urban Planning,"

Diakaki, Christina, Evangelos Grigoroudis, and Dionyssia Kolokotsa. 2013. "Performance Study of a Multi-Objective Mathematical Programming Modelling Approach for Energy Decision-Making in Buildings." *Energy* 59 (September): 534–42.

Evins, Ralph. 2013. "A Review of Computational Optimisation Methods Applied to Sustainable Building Design." *Renewable and Sustainable Energy Reviews* 22: 230–45.

Fortin, Félix-Antoine, François-Michel De Rainville, Marc-André Gardner, Marc Parizeau, and Christian Gagné. 2012. "DEAP : Evolutionary Algorithms Made Easy." *Journal of Machine Learning Research* 13: 2171–75.

Ishibuchi, Hisao, Ryo Imada, Yu Setoguchi, and Yusuke Nojima. 2017. "Reference Point Specification in Hypervolume Calculation for Fair Comparison and Efficient Search." In *Proceedings of the Genetic and Evolutionary Computation Conference on - GECCO '17*, 585–92. New York, New York, USA: ACM Press.

Machairas, Vasileios, Aris Tsangrassoulis, and Kleo Axarli. 2014. "Algorithms for Optimization of Building Design: A Review." *Renewable and Sustainable Energy Reviews* 31 (March): 101–12.

Plessis, Gilles, Aurelie Kaemmerlen, and Amy Lindsay. 2014. "BuildSysPro: A Modelica Library for Modelling Buildings and Energy Systems," 1161–69.

Rivallain, Mathieu. Étude de l'aide à la décision par optimisation multicritère des programmes de réhabilitation énergétique séquentielle des bâtiments existants.Université Paris-Est, 2013.

Rosenthal, Susanne, and Markus Borschbach. n.d. "Impact of Population Size, Selection and Multi-Parent Recombination within a Customized NSGA-II and a Landscape Analysis for Biochemical Optimization."

Tuhus-Dubrow, Daniel, and Moncef Krarti. 2010. "Genetic-Algorithm Based Approach to Optimize Building Envelope Design for Residential Buildings." *Building and Environment* 45 (7): 1574–81.

Zitzler, Eckart, Lothar Thiele, Marco Laumanns, Carlos M Fonseca, Viviane Grunert, and Da Fonseca. 2002. "Performance Assessment of Multiobjective Optimizers: An Analysis and Review."

Energy Flow through the Onondaga County Convention Center Green Roof in Syracuse, NY

Alyssa Pizzi[1,*] and Cliff I. Davidson[1,2]

[1]Department of Civil and Environmental Engineering, Syracuse University, 151 Link Hall, Syracuse, NY 13210
[2]Center of Excellence in Environmental and Energy Systems, Syracuse University, Syracuse, NY 13210

[*]*Corresponding email: ampizzi@syr.edu*

ABSTRACT

Buildings in the Northeast U.S. with large interior open spaces and high ceilings require substantial amounts of energy to heat and cool the spaces. The objectives of this experiment are to model the heat flux across different layers of a green roof and to estimate the thermal resistance of the layers. The project will examine conditions in winter and summer, considering air temperature and snow cover on the roof. The scope of this study includes measurements of the transfer of energy through the green roof on the Onondaga County Convention Center in Syracuse, NY. The methods include collection of data from Campbell Scientific temperature probes at six heights through the roof layers, ranging from the Convention Center ceiling to the ambient air above the roof. The temperature data are stored in CR-1000 data loggers. Under certain conditions, the green roof is expected to be an effective barrier to energy flow across the roof. The implications of this work are a better understanding of how green roofs function as a barrier to energy loss from the building in winter and a barrier to energy gain from direct sunlight in the summer. This, in turn, can assist designers of green roofs in a variety of climates.

KEYWORDS

Green Roof, Energy Flow, Heating and Cooling, R-values

INTRODUCTION

Green roofs are sometimes used to reduce the amount of flooding and combined sewer overflow in a city caused by lack of surface area where rainwater can infiltrate into the soil. However, they can also have other benefits, such as reducing the heat loss during winter and reducing heat gain in summer, leading to reductions in energy used for heating and cooling.

For example, Jaffal et al. (2012) report a 6% reduction in annual energy demand in a simulation study with a single-family house when a green roof is added. Another simulation study by Zhang et al. (2017) shows the potential temperature reduction of the external surface of a building and subsequent energy savings with a green roof. Dahanayake and Chow (2018) have determined that green roofs and green walls reduce the surface temperature of buildings, therefore controlling the cooling load to maintain indoor temperatures.

The overall goal of this study is to determine the heat flux through the Onondaga County Convention Center green roof in different seasons, and to calculate the thermal

resistance of the roof layers. Previous work on heat flux through this roof was based on a smaller dataset and produced preliminary findings for 2014-15 (Squier and Davidson, 2016).

This study looks at temperatures in different layers of the Onondaga County Convention Center green roof from December 2016 through February 2018. Heat flux was calculated for December 2016 until June 2017. Times in winter were chosen when there was sufficient snowpack to insulate the surface from variable air temperature, creating quasi steady state conditions in which the thermal resistance (R-values) were calculated.

METHODS

During construction of the roof, Campbell Scientific T109 temperature probes were placed in 4 roof layers (A, B, C, G); this was accomplished at 5 widely separated stations on the roof. Three more probes were affixed to the ceiling below at Y (**Figure 1**).
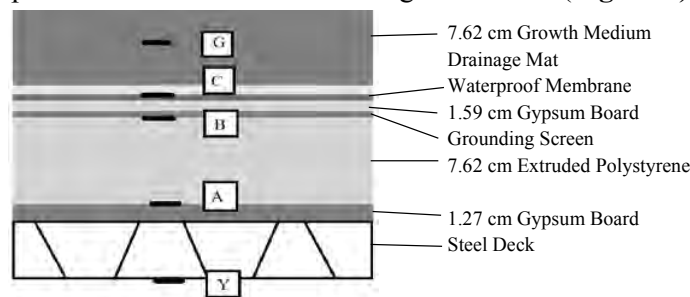
Figure 1: Layers of the roof and locations of the temperature sensors.

Because of possible malfunctioning probes, duplicate temperature sensors were placed in a number of roof layers. When analyzing the temperature data, some values from probes at stations 3 and 4 were flagged due to inconsistent temperatures for short time periods; the problematic data represent only a small fraction of the data from these sensors. Nevertheless, it was decided to exclude values from stations 3 and 4 in calculating average temperatures and R-values. Thus, data from only stations 1, 2, and 5 were used in the current study.

R-values were calculated over a period of high snow depth, 400-600 mm, which occurred over March 15-19, 2017 (**Figure 2**).
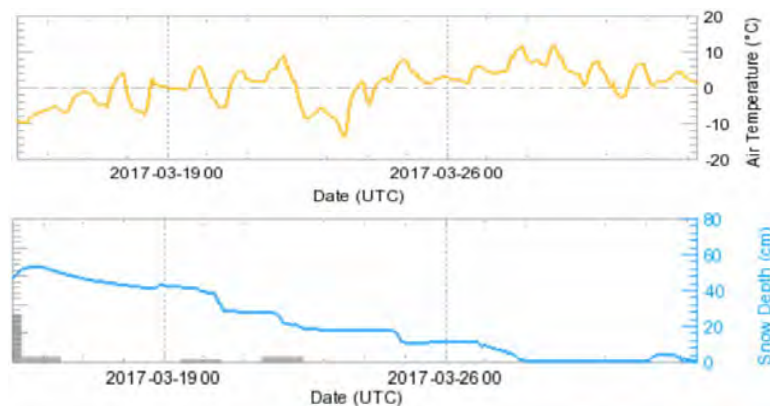
Figure 2: Air Temperature and Snow Depth as reported by the National Weather Service. The y-axis on the left side of both graphs corresponds to March 15, 2017.

The snow depth on the roof was assumed to be the same as the data collected by the National Weather Service station in Dewitt, NY, 4.1 km from the test site. This snow depth is consistent with the height of snow used by Squier and Davidson (2016) to calculate the R-values.

Fourier's equation was used for the steady state calculation of flux and resistance:

$$q = \frac{1}{R}\Delta T \qquad (1)$$

where q is heat flux through the layers (W m^{-2}), R is the thermal resistance of the layers between the sensors (m^2 K W^{-1}), and ΔT is the difference in temperatures (degrees K) between the layers of the roof, calculated using the data from the temperature sensors. The R-values reported by the manufacturer are in **Table 1**. Additionally, the values calculated by Squier and Davidson (2016) based on limited data are in **Table 2.**

Table 1: Layers of the roof and their respective thickness and thermal resistance values as reported by the manufacturer.

Layer	Thickness (cm)	Material R-Values (m^2 K W^{-1})
Growth Medium	3.81	0.211
Drainage Mat	0.63	n/a
Waterproof Membrane	0.12	0.028
Gypsum Board 2	1.59	0.118
Grounding Screen	0.102	0
Extruded Polystyrene Insulation	7.62	2.64
Gypsum Board 1	1.27	0.079

Table 2: R-values calculated by Squier and Davidson (2016) at stations 1, 3, 4, and 5 from February 1-14, 2015.

	5	1	4	3
B-C (Gypsum Board 2)	0.245	0.170	0.180	0.268
C-G (Waterproof Membrane and Growth Medium)	0.216	0.306	0.218	0.241
Overall, A-G	3.100	3.116	3.038	3.149

RESULTS AND DISCUSSION

Using Fourier's equation, the R-values across the roof layers for March 15-19, 2017 are given in **Table 3**. Based on the difference in temperature between layers B and C in both **Table 2** and **Table 3,** the R-values at station 5 are higher than the R-values at station 1. Conversely, over C-G, values at station 5 are less than the values at station 1. Values for stations 3 and 4 as presented by Squier and Davidson (2016) could not be compared for March 2017 due to malfunctioning sensors. It should be noted that station 2 reported average values in between the values of stations 1 and 5 in **Table 3**.

Table 3: R-values calculated at stations 1, 2, and 5 from March 15-19, 2017.

	5	1	2
B-C	0.246	0.139	0.174
C-G	0.214	0.327	0.278
Overall, A-G	3.100	3.106	3.092

The relationships between R-values shown in **Tables 2 and 3** are consistent. The values across different stations may be explained by the placement of sensors within the layers at each station. It is possible that some sensors rest slightly higher or lower than others at different stations, which would account for these deviations.

Figure 3 shows the temperature data for the G layer at the three stations used in this experiment from December 1, 2016 until March 31, 2017. The effect of the mid-March snowpack was to insulate the soil so that the temperature of the G layer hovered around 0° C throughout the period, despite wide variations in air temperature as shown in **Figure 2**.
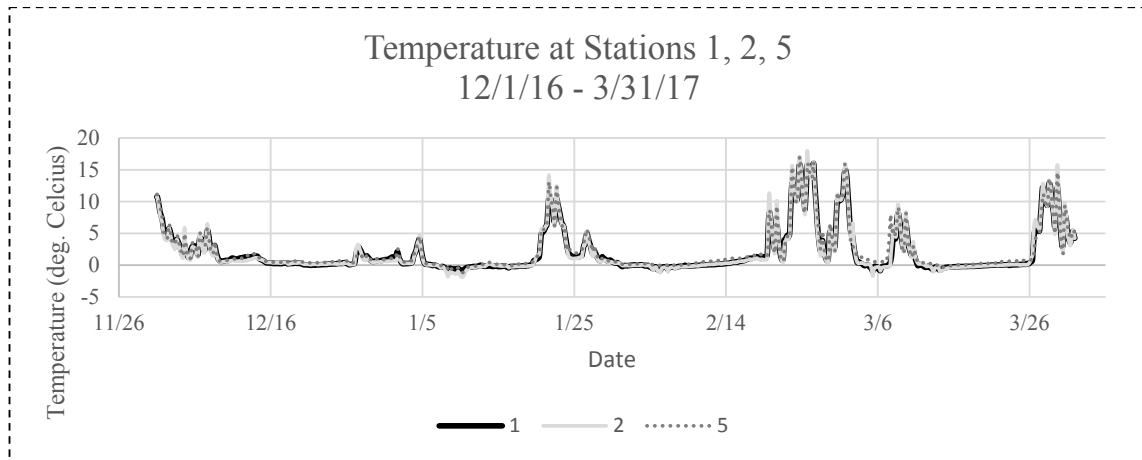
Figure 3: G-layer temperatures from three stations during Dec. 1, 2016 - March 31, 2017.

Figure 4 shows the temperatures in the different layers of the roof during 20 days of typical weather in the summer. Values shown are the averages at stations 1, 2, and 5. The temperatures at sensors G, C, and B follow the curve of the air temperature and frequently exceed the air temperature due to direct sunlight reaching the roof. The peaks at G, C, and B occur slightly later each day than the peak in air temperature, due to the time for heat conduction through the roof. Temperatures at A and Y are much lower than the air temperature and the other sensors in the roof because the Center is air conditioned. The greatest difference in temperature between adjacent sensors occurs between A and B.
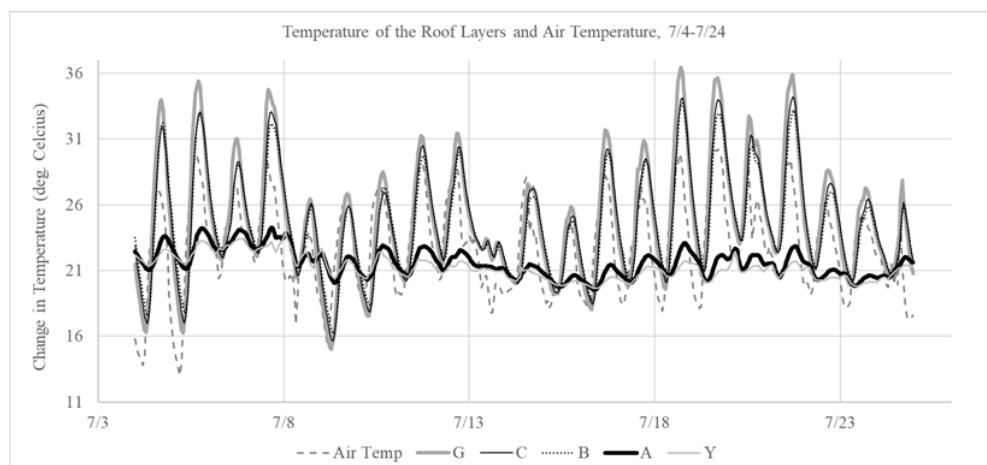

Figure 4: Temperature of each layer of the roof during July 4-24, 2017

Figure 5 shows the temperatures in the different layers of the roof during a 20-day period with typical winter weather. According to the National Weather Service there was no snow until January 24. There was significant snowpack (~100 mm) from January 24-27. From January 28-29, there is no snow on the roof, which corresponds to the small increase in temperature in the roof layers on January 28. Finally, there is significant snowpack again from January 31-February 9. The temperatures at Y and A reflect the heated interior of the building. The greatest difference in temperature between adjacent sensors again occurs over the insulation layer from sensor A to sensor B. Sensor G is closest to the air, followed by sensors C and B. The temperature at B is higher than at C, which is higher than at G, consistent with distance from the heated interior. Around January 23, there is an increase in air temperature, and the temperatures at sensors G, C, and B increase and are nearly the same over this period.
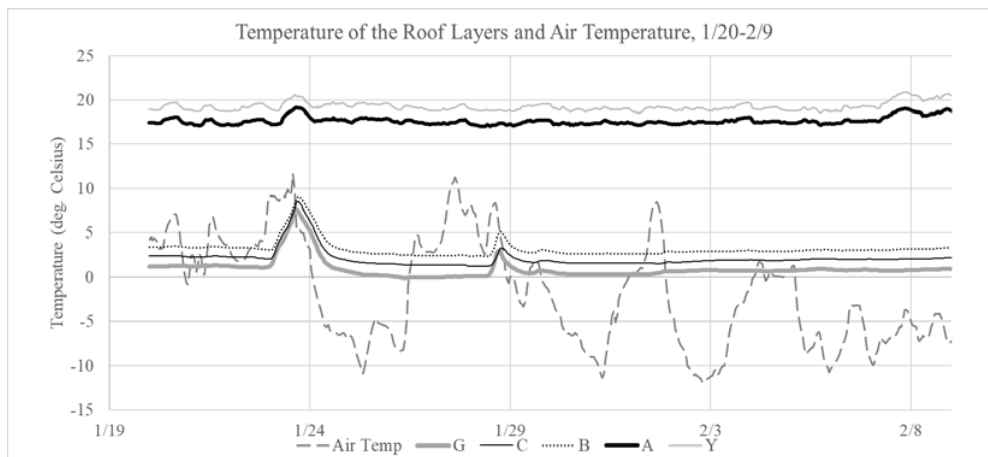
Figure 5: Temperature of each layer of the roof during January 20 - February 9, 2018.

The heat flux from A to B shows the transfer of energy across the insulation layer. **Figure 6** shows this heat flux over six months. During the winter months, there is generally a positive flux of heat escaping the building through the roof. During the summer months, the flux is negative, indicating heat entering the building. The heat flux from March 15-19 (shown by dashed lines) is positive as expected, and this time period corresponds to the period of high snowpack on the roof, as shown in Figure 2.
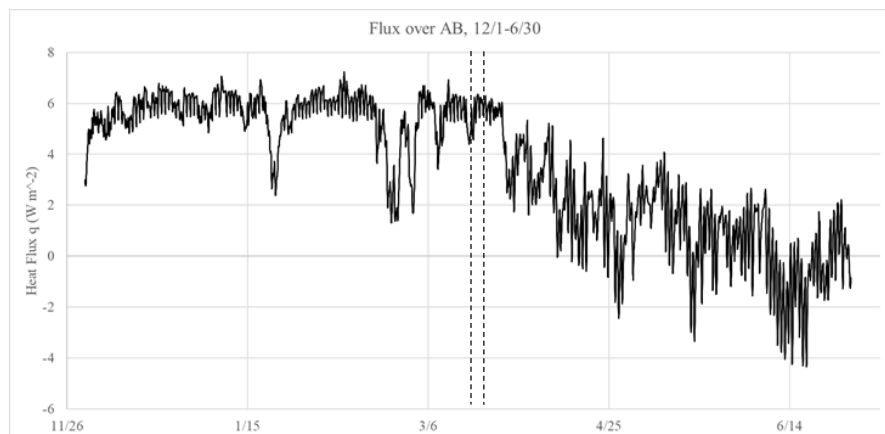
Figure 6: The heat flux through the insulation layer during Dec. 1, 2016 - June 30, 2017.

CONCLUSION

Temperatures have been measured from December 2016 to February 2018 in layers of a green roof on the Onondaga County Convention Center. The inside temperature at the ceiling, and temperatures in the lowest roof layers below the insulation, remain around 20° C in both winter and summer. The greatest difference in temperature between adjacent sensors occurs across the insulation layer (A to B). The temperatures at the top of the insulation (B), at the upper gypsum board (C), and in the growth medium (G) are closer to the air temperature. During the winter, and when there is significant snowpack on the roof, the temperature in these upper layers remains at $0\text{-}5^\circ$ C despite much colder air temperatures. The insulation layer provides the main barrier to heat escaping the building during cold conditions. During the summer, the temperatures in the top layers of the roof tend to be higher than the air temperature, due to the impact of direct sunlight impinging on the roof surface.

The calculated R-values of the green roof are consistent with previously calculated R-values based on limited data. The values from stations 1, 2, and 5 show distinct differences that may be due to the precise placement of the sensors within the various roof layers. For example, the R-values overall from A to G are nearly identical at all three stations, but the R-values between sensors B and C at stations 1 and 2 are much smaller than at station 5. This indicates that sensors B and C are probably closer together at stations 1 and 2 than originally thought, providing more information on the build of the roof. Additional data collection and analysis is underway, both at the green roof and at a traditional roof nearby.

ACKNOWLEDGMENT

REFERENCES

Dahanayake K.C. and Chow C.L. 2018. Comparing reduction of building cooling load through green roofs and green walls by EnergyPlus simulations, *Building Simulation*, Vol. 11, pp. 421-434.

Jaffal I., Ouldboukhitine S.E., Belarbi R. 2011. A comprehensive study of the impact of green roofs on building energy performance, *Renewable Energy*, Vol. 43, pp 157-164.

Squier M. and Davidson C. 2016. Heat flux and seasonal thermal performance of an extensive green roof, *Building and Environment*, Vol. 107, pp. 235-244

Zhang L., Jin M., Liu J., and Zhang L. 2017. Simulated study on the potential of building energy saving using the green roof, *Procedia Engineering*, Vol. 205, pp. 1469-1476.

Estimating time constants for over 10,000 residential buildings in North America: towards a statistical characterization of thermal dynamics

Camille John[1, *], Charalampos Vallianos[2], José Candanedo[1, 2] and Andreas Athienitis[1]

[1]Concordia University, 1515 St. Catherine W., Montreal, QC, H3G 2W1, Canada
[2]CanmetENERGY-Varennes, 1615 Lionel-Boulet Blvd., Varennes, QC, J3X 1S6, Canada

*Corresponding email: camille.john@mail.concordia.ca

ABSTRACT
Understanding the dynamic response of a building is essential in the design of sustainable energy-efficient buildings. Using data from over 10,000 smart thermostats, this study identifies patterns in the dynamic thermal response of residential buildings in Canada and the United States (US). The data set consists of one year of measurements recorded at 5-minute intervals for the indoor and outdoor air temperature as well as HVAC equipment run times.

This study focuses on identifying effective values of time constants for the houses by applying the following procedure. First, periods complying with the following basic criteria are identified: a) the house is under free-floating conditions (i.e. when the HVAC system is switched off) for more than three hours and b) the outdoor temperature remains approximately constant (the outdoor temperature change is smaller than or equal to 2°C). Second, for each identified period, time constant values are determined by tracking the temperature responses of the house. These values are determined assuming the characteristic exponential decay of a first-order resistance-capacitance (RC) thermal model. Finally, a statistical analysis is applied to identify a typical range of effective time constant values according to month.

Consequently, calculations show significant differences between estimated values for the summer and winter months, which may be attributed to occupant behaviour. In winter, the majority of time constants range from 15 to 55 hours. In summer, most of time constants vary between less than 1 hour and 18 hours due to occupants opening windows. In addition, the dependence of the time constant on the age of the home is investigated.

KEYWORDS
Time constant estimation; pattern recognition; dynamic thermal response; residential building; statistical analysis.

INTRODUCTION
In support of sustainable development and energy efficiency, effective energy management in buildings is increasingly recognized as a priority. In Canada and the US, the building sector accounts for approximately 28% and 40% of the national energy consumption, respectively. The residential sector is a major contributor to the energy use of both the Canadian and American building sectors, making up 62% and 53% of their total energy consumption, respectively. Moreover, in both countries, more than 40% of the total energy demand in a residential building is used to heat and cool the occupied spaces (Office of Energy Efficiency, 2016; U.S. Energy Information Administration, 2009, 2018).

With the increased adoption of the Internet-of-Things (IoT) such as smart thermostats, numerous homeowners are outfitting their residences with home automation and data acquisition systems. A recent study predicted that, by 2025, IoT applications would offer a potential economic impact of $200-300 billion a year in relation to the residential sector (Manyika et al., 2015). In the building and urban environment, big data sources are becoming increasingly more prominent and the release of certain anonymized data sets for data science could progressively become the norm. As a result, the building industry will face a critical dilemma: how will performance data from potentially thousands—or even millions—of buildings be reasonably integrated into design and energy management? This unprecedented level of access to raw data will promote the potential of machine learning, visual analytics, and data-driven statistical modelling techniques in estimating the building's dynamic thermal response (Miller, Nagy, & Schlueter, 2017). Grey-box model approaches use operational data from numerous real buildings to calibrate a simplified physical model, in the effort of providing good approximation of a building's thermal response (Vivian, Zarrella, Emmi, & De Carli, 2017).

In this study, the operational data of real homes are analyzed to recognize patterns in their dynamic thermal response. This paper focuses on proposing a method of estimating the typical thermal time constant values for residential buildings located in Canada and the US. The estimation is based on temperature measurements and equipment runtimes acquired from smart thermostats. When limited information is available, the knowledge provided in this paper can: i) assist in the generation of simple grey-box models that could guide the preliminary design of new residential buildings (Vivian et al., 2017), and ii) assist in the development and adoption of effective load management strategies for existing buildings.

METHODOLOGY
Data Collection
Ecobee, a Canadian home automation company, has established the Donate Your Data (DYD) program for its smart thermostat users to donate measured time series data to science. The meta-data from this program are user-reported, anonymized and include details such as the geographic location, age of home, total floor area, style of home, and number of occupants. Recorded at 5-minute intervals, the Ecobee thermostats collect measurements for temperature, humidity, occupancy detection, and HVAC equipment runtimes. For the building time constant estimation, over 10,000 residential buildings were monitored between March 2016 and February 2017. The Ecobee smart thermostats control the HVAC system based on the indoor control temperature, which is an average temperature of the building based on readings from the thermostat and any additional remote sensors present.

Building Time Constant Estimation
Diurnal and seasonal variations in outdoor temperature, solar energy and occupant behaviour account for the main thermal losses and gains between the building and its surroundings. The time constant is a measure that characterizes a building's ability to retain heat. With no influence from a heating or cooling system, theoretically, the thermal time constant provides an indication of how fast the building will take to achieve a new thermal equilibrium in response to changes in its internal and external thermal conditions. As demonstrated in Figure 1, the time constant can be found by applying a step input to the building and then recording the time the building takes to realize 63.2% of the final value in the step change (Equation 1).

The first step in estimating the time constant of a building is the identification of suitable time periods for analysis. In this study, these analysis periods are selected according to following

basic criteria: a) the house is under free-floating conditions (i.e. when the HVAC system is switched off) for more than three hours, and b) the outdoor temperature remains approximately constant (the outdoor temperature change is smaller than or equal to 2°C).

The measured time series data for HVAC equipment runtimes and the outdoor temperature are used to determine if the criteria are met during each analysis period.
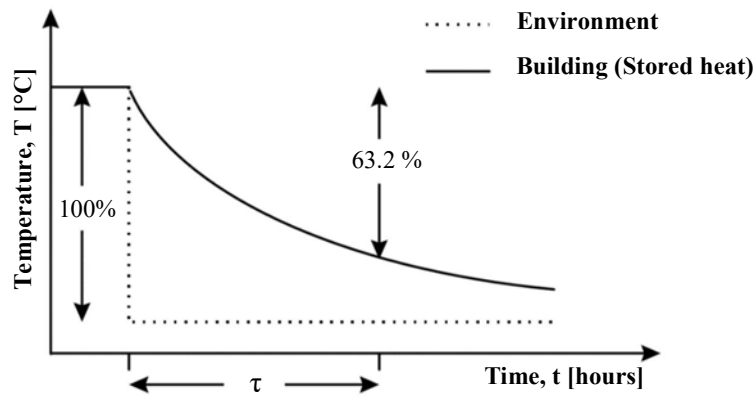

Figure 1: The time constant, τ, is the time needed for the building to realize 63% of the final value of an applied step change.

The second step is the determination of a time constant for each identified analysis period by treating the thermal space of every home as a first-order resistance-capacitance (RC) model (Vivian et al., 2017). While this is a relatively simple model, it provides a useful characterization of the dynamic behaviour of the house. Assuming the characteristic exponential decay of a first order system:

$$T(t) = T_f + \left(T_i - T_f\right)e^{-t/\tau_{bldg}} \tag{1}$$

where t represents time elapsed in hours, T_i represents the initial indoor temperature, T_f represents the long-term final temperature of the indoor space in free-floating conditions, and τ_{bldg} represents the estimated time constant value.

Considering plausible physical constraints and using the least squares method, the following parameters of a regression function are calculated according to Equation 1 and the recorded indoor temperature measurements $T(t)$: a) the long-term final indoor temperature b) the change in indoor temperature $(T_i\text{-}T_f)$, and c) the time constant value to be estimated. The time constant values were estimated with the use of the programming language Python. Next, these estimated values are then filtered, retaining only those whose corresponding R-squared values are 0.7 or higher. The R-squared value of 0.7 was visually determined to be the minimum acceptable value representing an accurate fit of the regression line to the observed data.

Identification of Typical Building Time Constant Values

In the previous step, multiple time constants are found for each building and organized according to month for analysis purposes. For each residence, a monthly average of the estimated time constant values can be obtained by weighing these estimated values by their corresponding R-squared values from the previous step. Statistical learning methods, particularly visual analytics, are then used to identify typical time constant values among the weighted averages. Histograms, kernel density estimations (KDE) (a method to estimate frequency distributions), and other statistical analysis tools are used to identify patterns in the

distribution of time constant averages. Furthermore, possible correlations between the time constant averages and the age of the home have been investigated.

RESULTS

Figure 2 and 3 show typical results obtained for the time constants for the months of August and February, respectively. The time constants are plotted versus the age of the home.
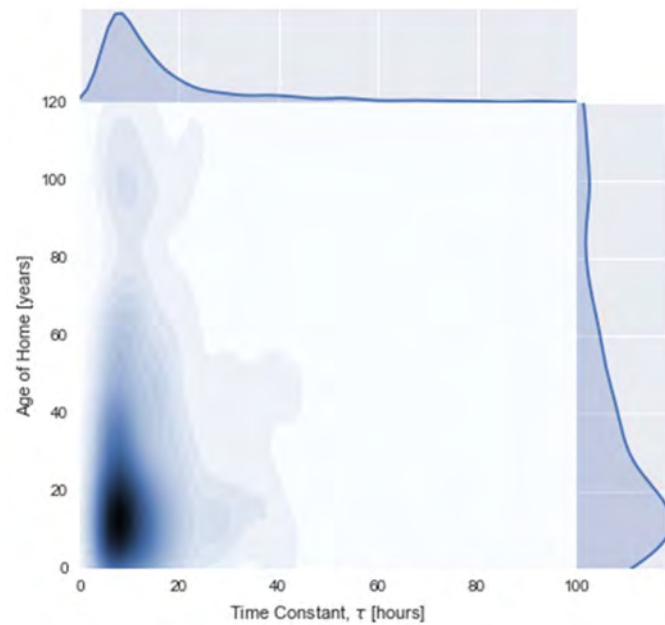

Figure 2: For August 2016, KDEs representing the building age distribution (right), time constant distribution (top), and their relationship to each other (center).
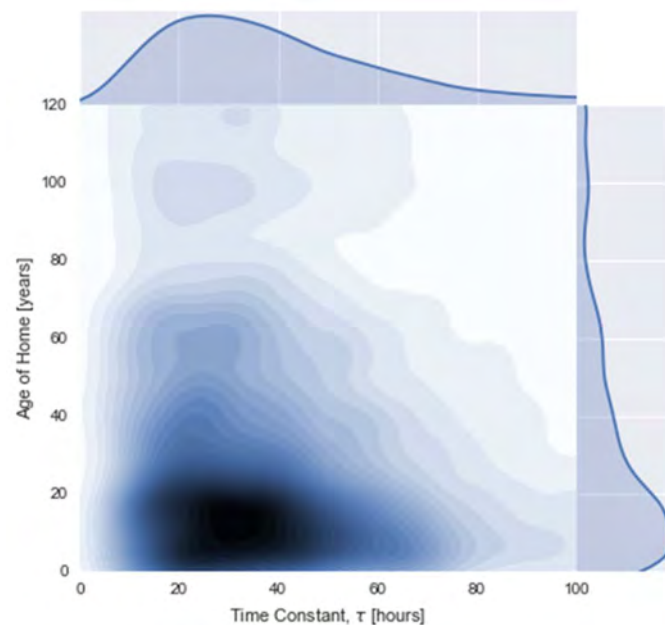

Figure 3: For February 2017, KDEs representing the building age distribution (right), time constant distribution (top), and their relationship to each other (center).

The patterns observed in August and February are very similar to time constant distributions seen throughout the rest of the warmer months and colder months, respectively. For the warmer months, specifically June through September, most of time constants fall within a range of less than 1 hour to 18 hours as seen in Figure 2. The colder months, meaning October through May, have most of their time constants varying between approximately 15 to 55 hours as demonstrated in Figure 3. As seen in both Figure 2 and Figure 3, the greater part of the buildings observed are between 0 and 35 years old.

DISCUSSION
Comparing Figure 2 and Figure 3, the warmer and colder months show significant differences between their resulting time constant averages; for the same group of homes, the warmer months have time constants that are much lower in value. The occurrence of different time constants for one building at different times of the year is an interesting phenomenon. In principle, the time constant should only depend on the materials and physical configuration of the house, which should not be expected to change. This decrease in value for the time constant averages may be linked to occupant behaviour. During the warmer months, it is reasonable to expect occupants to have their windows open and leave them open for longer periods of time due to more favorable weather conditions; open windows decrease a building's ability to resist changes in external thermal conditions thus reducing the effective resistance. Moreover, there is also a trend observed shared by both the warmer and colder months: the variance of time constants narrows with an increase in the age of home. The broad range of values for younger buildings and the narrow range of low values for older buildings suggest the introduction of a larger variety of construction methods and materials—some more energy efficient than others—over the last 120 years.

Understanding a building's natural dynamic thermal response is crucial to the design of heating, ventilation, and air conditioning (HVAC) systems, the maintenance of a comfortable environment for occupants, and the management of their electrical load profile (Palensky & Dietrich, 2011). In future studies, the proposed method will be extended to a larger data set of approximately 27,000 smart thermostats in North America to examine the relationship of the time constant to other variables. The variables to be considered include type of home (e.g. semi-detached, row house, condominium), geographical location and floor area. Considering that the age of home is user-reported, it would be interesting to see if the relationship observed between the time constant and the age of home persists in a larger sample of homes. Other considerations taken into account to select the periods of interest will include the effects of weather conditions, solar gains and occupancy which are currently not being tracked.

As we seek increasingly low-energy solutions for buildings, HVAC systems are being designed as more responsive to changes in a building's internal (e.g. occupants, appliances) and external thermal conditions (e.g. temperature, humidity, solar gain). The most commonly used software tools for building performance simulation (e.g. EnergyPlus or TRNSYS) require extensive computational power and a large number of assumptions about the building's geometry, its characteristic physical properties, its environment and its occupancy (Zawada, 2017). In addition, many of these inputs end up being assumptions based on the experience and intuition of professional experts. As a result, simple, reliable building models (e.g. grey-box models) have been receiving more attention of late, because there is often a need to model building performance when the required inputs are limited (e.g. only age, location and building type) and the energy modelers are less experienced. When limited building information is available, the knowledge acquired from this study will be used to facilitate preliminary estimations of dynamic parameters (such as RC values) in the rapid generation of control-oriented models.

CONCLUSIONS

This study presents a statistical methodology for the identification of typical time constant values of residential buildings for the heating, cooling and intermediate shoulder seasons (i.e. when houses are typically in passive mode with open windows). Preliminary results for different times of the year have been presented. Based on a simple physical model and measurement data from smart thermostats in North America, the proposed method for making preliminary estimations of the time constant offers benefits for researchers, home automation companies, utilities and homeowners who seek to reduce energy costs while maintaining occupant comfort The advantages include facilitating the creation of simpler models for testing and control scenarios, providing a better understanding of consumer behaviour and needs, and promoting energy conservation and efficiency. A major result of the present study is the observation that time constants vary seasonally: from less than 1 hour to 18 hours during summer, to 15 to 55 hours during winter. This result is most likely due to open windows that directly couple the interior of a house to the exterior environment through a high effective thermal conductance. Future studies will focus on extending the proposed method to a larger data set and examining the relationship of the time constant values to other variables including type of home, geographical location and floor area.

REFERENCES

Manyika, J., Chui, M., Bisson, P., Woetzel, J., Dobbs, R., Bughin, J., & Aharon, D. (2015). The Internet of Things: Mapping the value beyond the hype. *McKinsey Global Institute*.

Miller, C., Nagy, Z., & Schlueter, A. (2017). A review of unsupervised statistical learning and visual analytics techniques applied to performance analysis of non-residential buildings. *Renewable and Sustainable Energy Reviews*, 1–13.

Office of Energy Efficiency. (2016). *Energy Use Data Handbook*. Ottawa, ON. Retrieved from http://oee.nrcan.gc.ca/corporate/statistics/neud/dpa/data_e/downloads/handbook/pdf/201 3/HB2013e.pdf

Palensky, P., & Dietrich, D. (2011). Demand side management: Demand response, intelligent energy systems, and smart loads. *IEEE Transactions on Industrial Informatics*, *7*(3), 381– 388.

U.S. Energy Information Administration. (2009). *Residential Energy Consumption Survey*. Washington, DC. Retrieved from https://www.eia.gov/consumption/residential/data/2009 /index.php?view=consumption

U.S. Energy Information Administration. (2018). *Februray 2018 Monthly Energy Review*. Washington, DC. Retrieved from https://www.eia.gov/totalenergy/data/monthly/pdf/mer.pdf

Vivian, J., Zarrella, A., Emmi, G., & De Carli, M. (2017). An evaluation of the suitability of lumped-capacitance models in calculating energy needs and thermal behaviour of buildings. *Energy and Buildings*, *150*, 447–465.

Zawada, B. (2017). Experimental determination of parameters in models of indoor air temperature response to reduction in supplied energy. *Journal of Building Physics*, *40*(4), 346–371.

Experimental Investigation of the Impact of PCM Containment on Indoor Temperature Variations

Iva Rešetar[1*], Norbert, Palz[1]

[1]Berlin University of the Arts, Institute for Architecture and Urban Planning

*Corresponding email: i.resetar@udk-berlin.de

ABSTRACT

In view of growing concerns on climate change and temperature extremes, there is a need to explore novel methods that provide thermal comfort in architecture. Latent heat thermal energy storage with phase change materials (PCM) has been widely researched in last decades in the field of energy technology and proved beneficial for reduction and shifting of the thermal loads and improving the overall thermal storage capacity of building components. Although a variety of PCM containments have been investigated for indoor cooling applications, the examples of exposed, design-oriented macro-encapsulations are rare.

This paper presents a study of visible, suspended ceiling encapsulations for passive cooling, made of glass and novel bio-based PCM. The aim is to provide an overview of correlations between basic containment geometries and their thermal behavior that serves as a base for the further design of custom-made PCM macro-encapsulations. An experimental set-up of test boxes is developed for thermal cycling and a comparative analysis of the thermal performance of varied PCM encapsulation geometries. The study concludes that the containments with the large exchange surface and the small thickness offer an optimal material distribution for the temperature reduction in the box. Based on experimental results, suggestions are made on further formal strategies for the design of cooling elements for local thermal regulation.

KEYWORDS
Phase change materials, passive cooling, containment geometry, thermal cycling, glass macro-encapsulation

INTRODUCTION

Contemporary buildings increasingly rely on centralized mechanical systems for the indoor climate control, due to the low thermal inertia and high energy gains in buildings. A promising renewable energy alternative that could decrease the dependency on high-energy consuming technologies and improve the thermal stability of buildings is the latent thermal energy storage with PCM (Kośny, 2015; Zalba et al., 2003).

Current advancements in materials science and the growing interest of designers in a material-driven performance are opening a possibility for architectural elements to take a more active role in managing thermal environments (Addington and Schodek 2005; Bechtold and Weaver 2017). PCM belong to the novel class of property-changing materials with an inherent capacity for thermoregulation, as they can dynamically exchange the energy with surroundings while changing the phase at a desirable temperature. Although the primary goal of the implementation of PCM is to achieve energy savings in buildings, PCM present yet unrealized potential for architectural design and an opportunity for new design methodologies based on their thermodynamic behavior.

PCM are substances capable to absorb, store and release a large amount of energy in the form of latent heat during melting and solidification at a certain, predictable temperature. PCM act as latent thermal energy storage due to their large phase change enthalpy or latent heat of fusion. Unlike the sensible heat storage, where the added heat results in the temperature increase of the storage medium, the latent heat storage medium remains at almost constant temperature throughout the solid-liquid phase transition. The added heat is gradually absorbed by the material till the melting is complete and released when the surrounding temperature drops, and the material starts to solidify (Mehling and Cabeza, 2008). In that way, PCM operate in thermal cycles responding to local temperature fluctuations and can be used repeatedly without material degradation.

In passive or free cooling applications, PCM takes advantage of diurnal temperature differences, releasing the coldness stored during the night when, during the day, the indoor temperature rises above the comfort zone (Raj and Velraj, 2010). Currently available PCM products for passive cooling span from micro-encapsulations integrated in different building materials to macro-encapsulated elements placed behind the suspended ceiling. However, for PCM to function efficiently and regenerate during the night, a direct contact with the cold air (heat sink) is of advantage. This study therefore proposes visible suspended glass encapsulations that support recharging of the PCM by night ventilation. Since PCM has a low thermal conductivity, the containment geometry plays an important role for managing the heat transfer between the PCM and surroundings. Thus, coupling the basic encapsulation geometries with their thermal behavior in this paper aims to widen the range of PCM encapsulations and outline their use within the design realm.

METHODS
To evaluate the impact of varied PCM encapsulations on the indoor temperature, an experimental set-up for thermal cycling with test boxes was developed. Previous experiments that used test boxes to access the thermal performance of the composite PCM wall are described in literature (Kuznik and Virgone, 2009). Similarly, in this study two identical boxes – a test box containing the PCM sample and an empty reference box – were placed next to each other in a controlled indoor environment and exposed to thermal excitation. Boxes were made of plywood 18mm, covered with 30mm insulation panels, with the glazed front that allowed irradiation by two halogen 750W lamps placed in the front (Fig. 1).
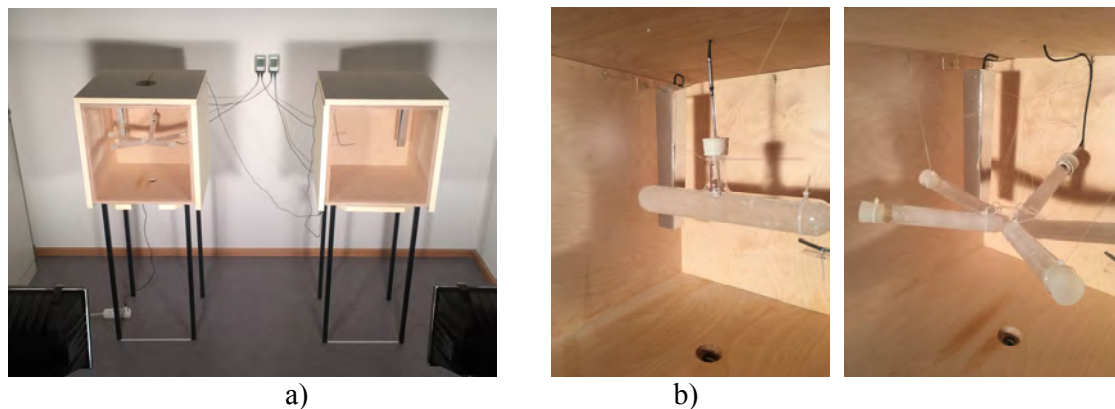

a)   b)

Figure 1. Experimental set-up for thermal cycling. a) Test boxes, b) Tubular encapsulations.

The temperature differences were observed during two subsequent heating (3h) and cooling (6h) cycles of total duration of 18h. During heating cycle, the temperature in the boxes

oscillated from 17∘C to 30∘C, with a resulting heat rate slightly above of the average due to the direct solar irradiation of buildings in the summer. The cooling cycle corresponded to the effect of night cooling needed for the PCM regeneration. The instrumental set-up consisted of two 176T2 dataloggers with four Pt-100 glass-coated probes of the class A precision, measuring air, PCM and the room temperature in the interval of 1 minute. Thermal camera was attached at the bottom of the box, capturing surface temperatures every 30 minutes. A reflective shield protected air probes from the direct irradiation. Before commencing measurements, several calibration cycles with different positions of probes were done and showed no temperature gradients in the box, and the temperature differences within tolerance values (0.2∘C).

Table 1. Physical properties of bio-based PCM from the data sheet of the producer.

Property	Values
Melting / crystallization temperature	21∘C / 19∘C
Latent heat	190 KJ/kg
Specific heat capacity solid / liquid	2.1 kJ/(kg·°C) / 2.3 kJ/(kg·°C)
Thermal conductivity solid / liquid	0.18 W/(m·°C) / 0.15 W/(m·°C)
Density solid / liquid	891 kg/m3 / 850 kg/m3

The material used in the study belongs to the novel bio-based category of PCM, with a low melting temperature suitable for indoor applications (Tab. 1). The choice of the containment geometries was made according to the standard typologies described in the literature (Mehling and Cabeza, 2008; VDI, 2016). A total volume of 500ml of PCM was used in each measurement, either in a single containment or divided into five smaller units of 100ml. Encapsulations were made of borosilicate or soda-lime glass of approx. thickness 2mm in following formats: spherical containments used standard laboratory 500ml and 100ml glass flasks; multiple tubular used standard 100ml test tubes; 500ml tube was produced by lampworking technique; flat container was produced by modifying a standard petri dish ∅ 180mm.

A=336.18cm² thk=10.5cm	A=612.61cm² thk=6.4cm	A=534.07cm² thk=5cm	A=836.40cm² thk=3cm	A=604.92cm² thk=3cm
a)	b)	c)	d)	e)
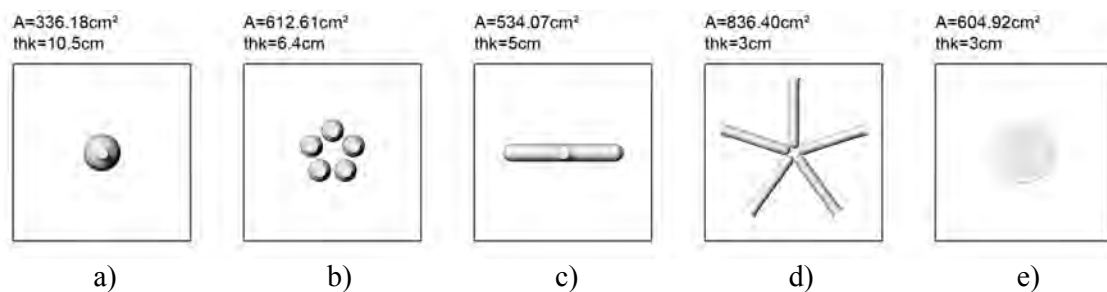
Figure 2. Ground plan of the box with containment geometries showing surface area and max. thickness. a) Sphere 500ml, b) Multiple spheres 5x100ml, c) Tube 500ml, d) Multiple tubes 5x100ml, e) Flat plate containment 500ml.

RESULTS

The graphs show a characteristic latent heat thermal storage effect with a temperature plateau during the melting phase of the material (Fig. 3). All encapsulations except the 500ml spherical and flat containments allowed the full melting of the PCM. The multiple tubular geometry caused the biggest temperature differences between the test boxes (Tab. 2 and Fig. 3) and allowed the largest portion of the material to recharge during the cooling cycle in comparison to other containments (Fig. 4).

Tables and illustrations

Table 2. Temperature differences in boxes in relation to geometry.

Encapsulation geometry	Values 1st/2nd cycle
a) Sphere 500ml	1.15∘C / 1.13∘C
b) Multiple spheres 5x100ml	1.64∘C / 1.62∘C
c) Tube 500ml	1.51∘C / 1.48∘C
d) Multiple tubes 5x100ml	2.04∘C / 2.03∘C
e) Flat containment 500ml	1.41∘C / 1.50∘C

a)

b)

c)

d)

e)
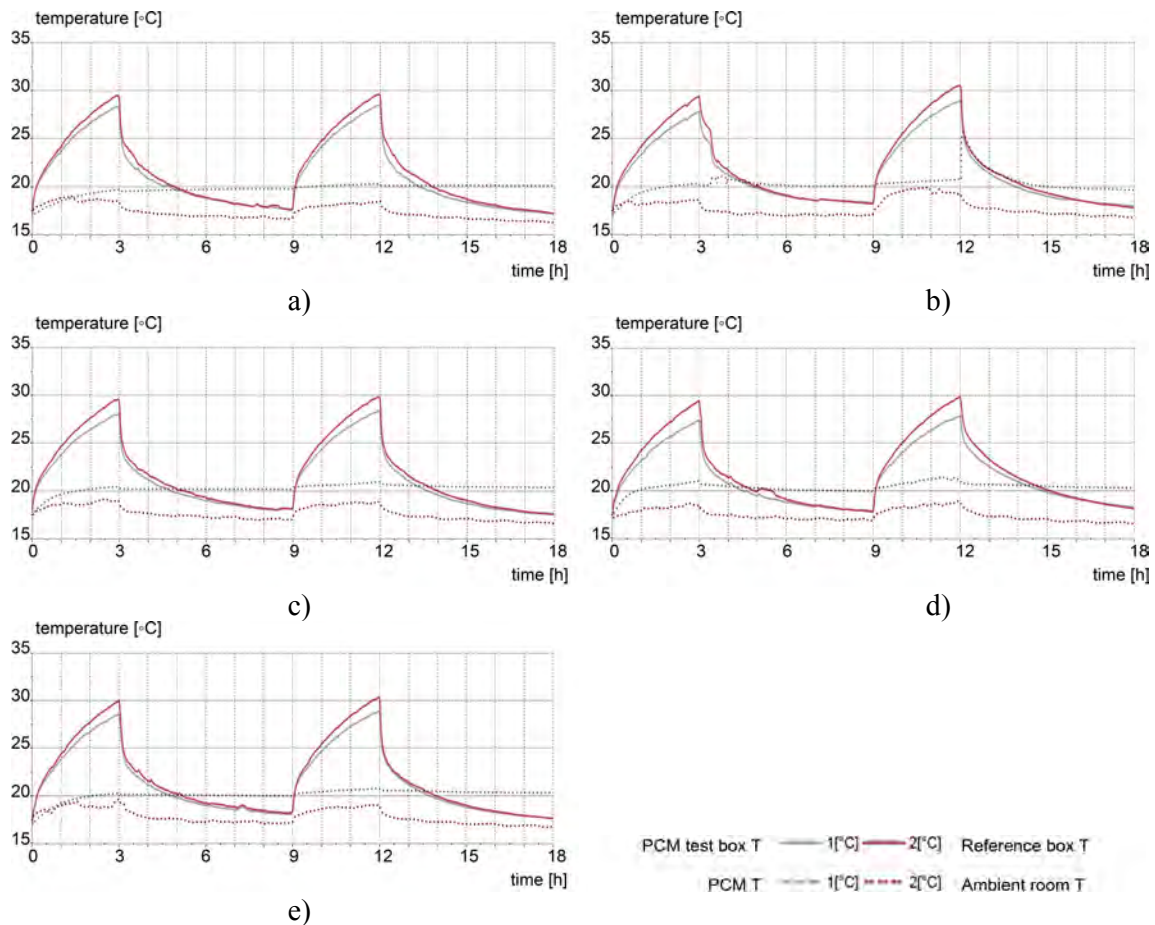
Figure 3. Impact of PCM on temperature reduction in the box. a) Spherical containment, b) Multiple spherical containment, c) Tubular containment, d) Multiple tubular containment, e) Flat plate containment.

DISCUSSIONS

Multiple containments improved the cooling effect of the single ones by 40%. The results point out to benefits of increasing and differentiating surfaces that enclose a certain volume. Although the exhibited differences of the cooling potential between PCM containments are small, it is expected that they gain on importance in the design of larger ceiling systems. Measurements in real conditions with actual thermal loads, building materials and occupant behaviour are, however, necessary to validate these findings. Regarding the orientation of encapsulations, the experiments assumed the horizontal position of tubes and flat containers optimal for the uniform temperature distribution and steadily moving melting fronts (Khan et. al, 2016).
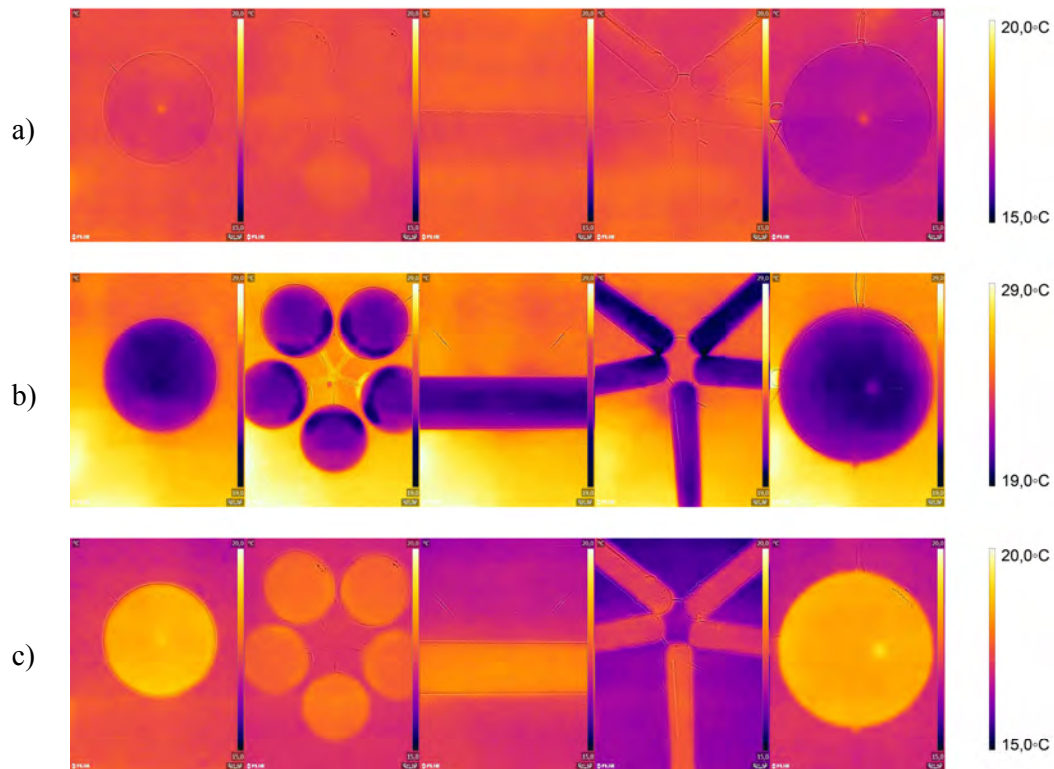
Figure 4. Thermographic images showing surface temperature at the beginning and the end of the heating and cooling cycle: a) 0h, b) 3h, c)12h.
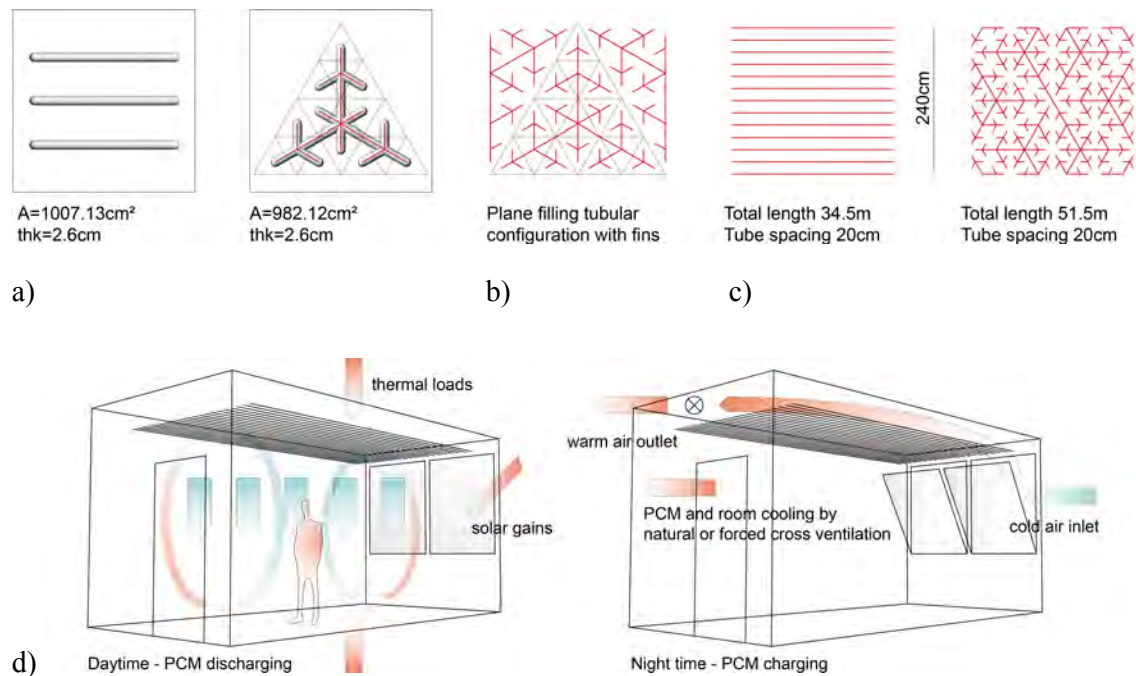
Figure 5. a) Linear and plane filling tubular elements of 2.6cm thickness and 500ml volume in the test box, b) Plane filling configuration principle, c) Difference between linear and plane filling patterns in material distribution in larger space, d) Diagram of the operating principle of the PCM cooling ceiling made of suspended glass elements.

A further increase of the surface area of tubular encapsulations could be achieved by introducing elements with fins (Fig. 5a), and by formal strategies for connecting elements into larger systems, such as plane or space filling tree configurations (Fig. 5b). Compared to linear configurations (VDI, 2016), these branching structures could provide a large and uniform material distribution with an increased element spacing (Fig. 5c) necessary for recharging the material during the night by convection and conduction (Fig. 5d).

CONCLUSIONS

This work presented investigation of thermal performance of spherical, tubular and flat plate glass encapsulations containing novel bio-based PCM. An experimental set-up of the test box was developed for the comparative analyses of the impact of the encapsulation geometry on the indoor temperature in the test box. Single and multiple units of an equal volume, but varying surface and thickness were tested, and the effect of the increased surface and reduced thickness on temperature reduction was observed. Temperature measurements reflected the differences in the volume-surface ratio of containments and showed the biggest reduction of 2◦C in the box with multiple tubular PCM encapsulations. The paper concludes that new design and recharging opportunities for cooling ceilings could be afforded by the exposed glass encapsulations and suggests further formal strategies for increasing the surface area while keeping the thickness, volume and spacing of the encapsulation elements at optimum. These findings on cooling effects of glass encapsulations can inform the concept phase of the design of more elaborate custom-made ceiling elements for local thermal regulation.

ACKNOWLEDGEMENT

REFERENCES

Addington M. and Schodek D. 2005. *Smart Materials and Technologies for Architecture and Design Professions*. Oxford: Elsevier Architectural Press.

Bechthold M. and Weaver J. C. 2017. Materials science and architecture. *Nature Reviews Materials*. Vol. 2, pp. 1-20.

Mehling H. and Cabeza L. 2008. *Heat and cold storage with PCM: An up to date introduction into basics and applications.* Berlin: Springer.

Khan Z.; Khan Z.; Ghafoor A. 2016. A review of performance enhancement of PCM based latent heat storage system within the context of materials, thermal stability and compatibility, *Energy Conversion and Management*, 115, pp. 132–158.

Kośny, J. 2015: *PCM-Enhanced Building Components: An Application of Phase Change Materials in Building Envelopes and Internal Structures*. Springer International Publishing.

Kuznik F. and Virgone J. 2009. Experimental Investigation of Wallboard Containing Phase Change Material: Data for Validation of Numerical Modeling. *Energy and Buildings*, 41 (5), pp. 561-570.

Raj V. A. A. and Velraj R. 2010. Review on free cooling of buildings using phase change materials. *Renewable and Sustainable Energy Reviews*, 14, pp. 2819–2829

VDI. 2016. *VDI Standard 2164*, PCM energy storage systems in building services. Düsseldorf: Verein Deutscher Ingenieure.

Zalba, B.; Marın, J.M.; Cabeza F.L.; Mehling. H. 2003. Review on thermal energy storage with phase change materials, heat transfer analysis and applications. *Applied Thermal Engineering*, 23, pp. 251–283.

Hygrothermal modelling of building enclosures: reference year design for moisture accumulation and condensation risk assessment

Michele Libralato[1,*], Giovanni Murano[2], Onorio Saro[1], Alessandra De Angelis[1] and Vincenzo Corrado[2].

[1]Università degli Studi di Udine / Universitât dal Friûl, Italy
[2] Politecnico di Torino, Italy

[*]*Corresponding email: Libralato.michele.1@spes.uniud.it*

ABSTRACT

Interstitial condensation and water accumulation risk in building envelopes could be assessed with methods and models based on moisture migration through porous media coupled to heat transfer. One of the difficulties in evaluating the boundary conditions for the heat and mass transfer model is the choice of an appropriate weather file. The most advanced models, described by the standard EN 15026:2007, require the hourly values of rain, wind, radiation, temperature and relative humidity to compute the water content in the porous materials.

In this contribution, the method described by the standard EN ISO 15927-4:2005, typically used to design Moisture Reference Years (MRY), has been extended to the design of 34 typologies of representative weather files. The generation criteria have been based on the assumption that the simulation results are influenced by rain deposition on the considered wall. The procedure has been followed considering 5 different wall exposures that lead to different MRY. The years of the climate of Turin (Italy) between 2002 and 2016 have been considered for the generation of the reference years.

Finally, the annual mean moisture contents for two common wall types have been calculated using the obtained MRY and compared to the annual mean moisture contents obtained with the measured weather data, and the effects of the selection of the weather parameters is presented.

KEYWORDS

Building enclosures, condensation risk assessment, moisture accumulation, reference year, weather file, Moisture Reference Years.

INTRODUCTION

The building envelope design process requires the risk assessment for condensation and moisture accumulation of all the enclosures and their intersections to avoid mould growth conditions and material damage due to prolonged moisture exposure. Up to now, several evaluation methods, simplified and advanced, have been developed. The simplified and most used methods are based on stationary models, they consider monthly mean weather data and are not intended to simulate the real phenomena of the heat and moisture transfer (for example the Dew-Point method or the Glaser method). When more accurate methods are needed (and a simulation of the real physical phenomena is required) it is possible to use advanced models. These models are based on transient state heat, air and moisture transfer equations and require a deep knowledge of the material properties, with weather data files that have to include additional hourly normal rain, wind and solar radiation descriptions.

The standard EN 15026:2007 describes the commonly accepted models used for the advanced moisture accumulation and interstitial condensation risk assessment and refers to the EN ISO 15927-4:2005 for the boundary conditions; this standard describes a method intended to produce hourly data for assessing the annual energy use for heating and cooling. In this paper,

following the previous works of the authors (for example Riva et al. 2010, Riva et al. 2012 and Murano et al. 2016), a modification to the standard method of reference years generation is presented. It has to be noted that the methodology produces reference years and not extreme weather years. Reference years could be used only for moisture accumulation and interstitial condensation risk assessment; if water condensation in building components is not acceptable, even for short periods, other methods are available for the generation of extreme weather years. Various approaches have been investigated in the literature. Cornick et al. (2003) have selected Reference Years using a Moisture Index approach developed for Moisture Management of Exterior Wall Systems (MMEWS). The index comprises wetting function and drying function. In this approach wet and dry years are defined as those years that deviate more than one standard deviation from the mean value on long-term. MEWS is a building-independent method. The wet year is defined as the year with highest moisture index, the dry year as the year with lowest moisture index, and the average year as the year closest to the mean Moisture Index. MEWS can be assembled for problems such as long-term performance or limit-state design. There isn't a definitive method for selecting MRY's but different sets of MRYs should be produced to evaluate different problems.

Salonvaara et al. (2010) have developed a new method that provides an approach for selecting the most critical years in terms of hygrothermal performance. Performance data is analysed using various methods to provide a ranking of the weather years in terms of severity. Damage functions (time of wetness, mould growth index, and maximum moisture content) are used to quantify the moisture related performance of the building envelope. The analysis has included 30 years of hourly weather data for 12 locations in the U.S. and Canada.

Schönerl and Zirkelbach (2016) for the selection of the months of the reference years for the hygrothermal assessment (HRY) have used median, mean, minimum, maximum value, the 25%, and the 75% quartile of air temperature and normal rain. The results of HRY was compared with the standard methodology of EN ISO 15927-4 and with measured data on long-term. The simulations have shown that the mean water content based on the HRY was slightly higher than the one based on the measured data.

Considering the effect of climatic variability on the performance of the building envelope, Zhou et al. (2016) have developed a Climatic Index that considered wind-driven rain load and potential evaporation. This index was suitable for the evaluation of the level of moisture damage risk of wall assemblies where typical moisture problems are mainly caused by rainwater uptake or ingress. The combination of Climatic Index and RHT Index has allowed the creation of MRYs that have 10% level of failure.
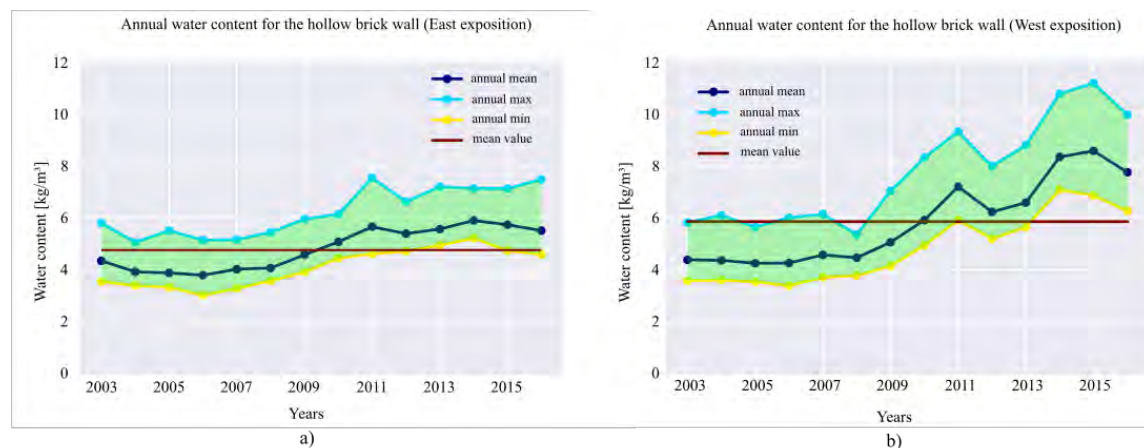

Figure 1. Annual mean water contents of the hollow brick wall for the measured weather files simulations for the East exposition (a) and the West exposition (b).

METHOD

The EN 15026 (European Committee for Standardization, 2007) refers to EN ISO 15927-4:2005 (International Organization for Standardization, 2005) for the creation of Moisture Reference Years. This method is intended for the creation of typical meteorological years and it is based on the Finkelstein-Schafer (FS) statistic method (Finkelstein and Schafer, 1971). In this research some modifications are introduced to extend the procedure to moisture migration related applications. From the observation that the total moisture content of a simulated wall depends also on the exposure of the wall itself (Figure 1) other rain related climate parameters (normal rain, driving rain) are alternatively considered to select the representative months of the reference year from the historical measured data, in addition to the standard ones (temperature, relative humidity, irradiation, wind speed). Then, the validity of the reference years generated for every combination is evaluated on two wall build-ups with a comparison in terms of the moisture contents against the historical years. The revised procedure for the generation of reference years is shown below. Let p be the generic measured parameter of the historical years required for the hygrothermal simulations. First, from at least 10 years of hourly values of p, for every day i, the daily mean $\overline{p_i}$ is calculated; then, for each calendar month (m), the values $\overline{p_i}$ are ordered in ascending order and 12 arrays for the whole data set are obtained. The cumulative distribution function $\Phi(p,m,i)$, associated to every $\overline{p_i}$ over all the years in the data set, is calculated using the Eq. (1), with i the considered day in the month, from 1 to N, and N the sum of the number of days in any calendar month, $K(i)$ is the position ("rank") in the ordered list of $\overline{p_i}$ of the month m;

$$\Phi(p,m,i) = \frac{K(\overline{p_i})}{N+1} \tag{1}$$

For each year y of the data set, the cumulative distribution function of the daily means within each calendar month (using Eq. (2)), $F(p,y,m,i)$, is obtained by sorting all the values for the month m and the year y, in increasing order. 12 arrays are obtained for every year. $J(i)$ is the "rank" of the value of the daily mean $\overline{p_i}$ for the month m and the year y, n is the number of days in the month m;

$$F(p,y,m,i) = \frac{J(\overline{p_i})}{n+1} \tag{2}$$

For each calendar month, for each year of the data set, the Finkelstein-Schafer statistic, $F_S(p,y,m)$, is calculated using Eq. (3):

$$F_S(p,y,m) = \sum_{i=1}^{n} |F(p,y,m,i) - \Phi(p,y,m,i)| \tag{3}$$

For each calendar month with the same m from all the years, the rank R is calculated for each value. Differently from the standard method, in this work the ranking is performed ordering the values ascending by the F_s, calculated from the multiyear record for the parameters selected among temperature (T), solar irradiance (I) and relative humidity (RHU) the driving rain (RDW obtained from the wind normal to the considered wall direction and from normal rain RIH), the wind speed (WS) and the normal rain (RIH); for each calendar month and for each year, the separated ranks (R) are summed for the climate parameters selected for the formation of MRY (the parameter selection used in this work is shown in Table I) and the total ranking $R_{tot}(y,m)$ is obtained; the month with the lowest $R_{tot}(y,m)$ is selected as the "best" month to be included in the Moisture Reference Years;
 Once the months are selected, the weather file is completed substituting the unrealistic leaps between the values of adjacent months with a linear interpolation.

The validation of the proposed MRYs is carried out by comparing the hygrothermal behaviour of building components simulated with the new MRY, with the behaviour obtained with the weather conditions over the long term from the measured weather file. 34 MRYs weather files have been generated with 16 different criteria. The historic weather data series, from 2002 to 2016, are provided by the Regional Agency for the Protection of the Environment (ARPA) of the Piedmont Region (Italy).

The evaluation of the obtained reference years has been performed comparing the hygrothermal simulation results of two different building envelopes, a hollow brick wall and a timber wall. The simulations have been performed with the software WUFI Pro, based on the model presented in Künzel et al. (1996). The comparison is held evaluating the monthly mean moisture content and comparing it to the one evaluated with the historical data set.

Table I: Climate parameters selected for the formation of MRY.

ID	ISO	1	2	3	4	5	6	7	8	9	10	11	12	13	14	15	16	17	18	19	20	21	22	23	24	25	26	27	28	29	30	31	32	33	34
T	x	x	x	x	x	x	x	x	x					x	x	x	x											x		x	x		x		
I	x	x	x	x	x													x	x	x	x								x	x				x	
RHU	x	x	x	x	x	x	x	x	x	x	x	x		x	x										x					x	x	x			
WV	x																												x						
RIH																														x	x	x	x	x	x
RDW (South)		x				x				x				x				x				x													
RDW (East)			x				x				x				x				x				x												
RDW (North)				x				x				x				x				x				x											
RDW (West)					x				x				x				x				x				x										

T=Air temperature, *RHU*=Relative humidity, *I*=Solar irradiance, *RDW*=Rain deposition on vertical wall, *MRY*=Moisture Reference Years, *WS*=Wind speed, *WD*=Wind direction, *RIH*=Rainfall intensity on a horizontal surface

RESULTS

The reference years from number 1 to number 24 have been simulated considering the design orientation (for example the reference year 1, designed considering the rain deposition on vertical wall facing South has been used for the simulation of the wall build-up facing South), while the reference years from number 25 to 34 have been used for the simulations for the five expositions considered (since normal rain has a general effect on all the expositions). The walls passed the moisture accumulation assessment and the condensation risk assessment for every MRY considered and for the historical data set. For this reason the annual mean results (Figure 1) have been compared in terms of relative standard deviation from the annual mean values obtained by the measured weather data (Figure 2). The Timber wall results show better representative MRY, with lower values of the relative standard deviation, with respect to the Hollow brick wall results.

Water content relative standard deviation for the Timber wall — Relative standard deviation [-]

Water content relative standard deviation for the Hollow brick wall — Relative standard deviation [-]

X-axis categories: 1-4,29 | 5-8,30 | 9-12,31 | 13-16,32 | 17-20,33 | 21-24,34 | 25 | 26 | 27 | 28 | 29 | 30 | 31 | 32 | 33 | 34 | ISO

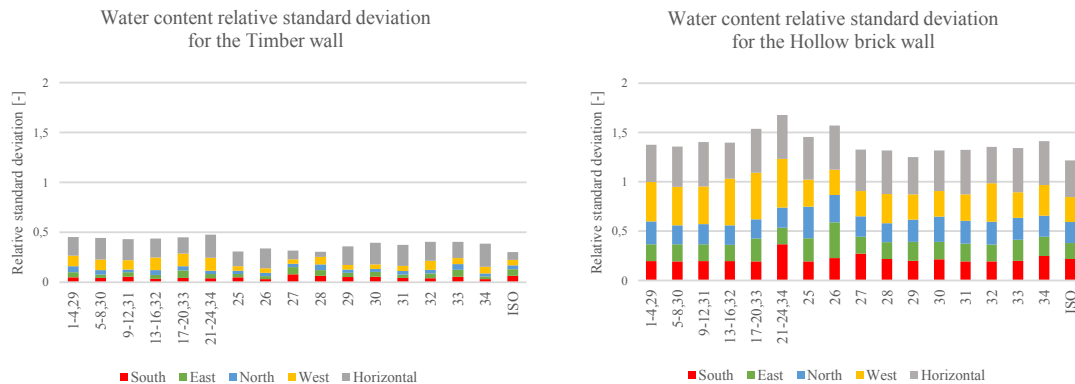Legend: ■ South ■ East ■ North ■ West ■ Horizontal

Figure 2. Relative standard deviations of the moisture contents between the simulation of the historical years and every reference year described in Table 1.

The results present exposition specific trends. For the Timber wall, the ID 34 (based on *RIH*) better represents the South, East and North expositions, while the West exposition is better described by the ID 25 (based on *RHU*) and the Horizontal by the ID 28 (based on *I*). The ID ISO and the ID 28 are the reference years better representing the walls in the five directions. The Hollow brick wall shows different exposition specific trends: the South facing exposition is better represented by the ID 34 (based on *T* and *RHI*), the East and West by the ID ISO, the North by the ID 7 (based on *T, RHU, RDW*) and the Horizontal by the ID 32 (based on *T* and *RHI*). From Figure 2 it is also possible to observe some overall results. The ID from 1 to 24, considering *RDW* are generally less representative for the most rain exposed directions (West and Horizontal). Exclusively *RDW* based years (21-24) are less representative than ID from 29 to 34, based also on *RIH*. For the Timber wall the ID from 25 to 28 and the ID ISO (not based on *RIH* or *RDW*) are better performing than the *RIH* based ones, while for the Hollow brick wall, their behaviour is similar.

DISCUSSION

The relative standard deviations of the Timber wall are lower than the Hollow brick wall. This difference is due to the different hygrothermal properties of the materials. The Hollow brick wall external layer has higher liquid transport coefficient values than the Timber wall, which has also higher moisture storage function values, and that could lead in faster responses to the rainfall (larger water content variations), with larger differences from the historical data set results.

The moisture reference years depending on rain deposition on vertical wall (obtained from wind speed, direction and normal rain) led to less representative years than the ones generated by the standard method. This result could be related to the features of the climate of Turin (Italy), whose rains are brief and quickly dried afterwards. On the other hand, one of the reasons could also be the fact that the external material layers do not respond instantly to the transient hourly rainfall excitations (slower than the heat excitations) and that the total water content of the wall is more influenced by the long term mean values of the environmental excitations, which is also been discussed in Libralato et al. (2017).

CONCLUSIONS

In this study, 34 moisture reference years (MRY, to be used for hygrothermal analysis of building structures) have been generated from a data set of measured weather files from the year 2002 to the 2016, in the city of Turin (Italy). Each MRY has been generated selecting the months from the historical data set, with a modified EN ISO 15927-4:2005 method, based on the rain deposition on vertical walls with different expositions. From the simulation of two wall types to all the 34 MRY, it has been observed that an orientation differentiation does not lead to more representative MRY for the two considered building structures in the considered climate.

The results suggest that, when the use of a single MRY is preferred, the MRYs obtained with the standard procedure EN ISO 15927-4:2005 better reproduce the results obtained with the simulation of the measured weather files and that is could be used, not only for the energy consumption simulations, but also for the moisture migration in building envelopes simulations. Considering exposition and material specific applications, that could benefit from the use of more than one MRYs, other generation methods presented in this work could be taken in consideration, depending on the building material properties and on the wall orientation.

Further work will be carried out to establish if this approach could be extended to critical weather data design for moisture accumulation risk assessments and if the proposed MRY generation method could be used proficiently for other applications, like energy simulations in

which the efficiency of the components of the systems depends on moisture related environmental conditions, such as evaporative towers (De Angelis et al. 2013), evaporative cooling systems for industrial buildings (De Angelis et al. 2017a), shopping malls (De Angelis et al. 2017b) and other heat recovery systems (Chinese et al. 2017).

REFERENCES

Chinese D, Santin M. and Saro O. 2017. Water-energy and GHG nexus assessment of alternative heat recovery options in industry: A case study on electric steelmaking in Europe. *Energy*, *141*, 2670–2687.

Cornick S, Djebbar R, and Alan Dalgliesh W. 2003. Selecting moisture reference years using a Moisture Index approach. *Building and Environment*, *38*(12), 1367–1379.

De Angelis A, Saro O and Truant M. 2017a. Evaporative cooling systems to improve internal comfort in industrial buildings. In *Energy Procedia* (Vol. 126, pp. 313–320).

De Angelis A. Chinese D and Saro, O. 2017b. Free-cooling potential in shopping mall buildings with plants equipped by dry-coolers boosted with evaporative pads. *International Journal of Heat and Technology*, *35*(4).

De Angelis A, Saro O, Lorenzoni G, D'Elia S, and Medici M. 2013. Simplified Models for Assessing Heat and Mass Transfer in Evaporative Towers. *Synthesis Lectures in Engineering,* Morgan & Claypool Publishers.

Finkelstein J. M. and Schafer R.E, Improved goodness-of-fit tests. 1971. Biometrika, Volume 58, Issue 3, Pages 641–645

Künzel H. M, and Kiessl K. 1996. Calculation of heat and moisture transfer in exposed building components. *International Journal of Heat and Mass Transfer*.

Libralato M, Saro O, De Angelis A and Spinazzè S. 2017. Comparison between Glaser method and Heat, Air and Moisture transient model for moisture migration in building envelopes. *Proceedings of the 12th International enviBUILD 2017 Conference*, Vienna.

Murano G, Corrado V, and Dirutigliano D. 2016. The new Italian Climatic Data and their Effect in the Calculation of the Energy Performance of Buildings. In *Energy Procedia* (Vol. 101, pp. 153–160).

Riva G, Murano G, Corrado V, Baggio P, and Antonacci G. 2012. Aggiornamento parametri climatici nazionali e zonizzazione del clima nazionale ai fini della certificazione estiva. September 2012, *ENEA, Ministero dello Sviluppo Economico*.

Riva G, Murano G, Corrado V, Baggio V, and Antonacci G. Definizione degli anni tipo climatici delle province di alcune regioni italiane (Emilia Romagna - Friuli Venezia Giulia – Liguria – Lombardia – Piemonte Toscana – Trentino Alto Adige Valle D'Aosta – Veneto); *ENEA, Ministero Dello Sviluppo Economico*, 2010, pp 347.

Salonvaara M, Sedlbauer K, Holm A, and Pazera M. Effect of selected weather year for hygrothermal analyses. In: *Buildings XI, thermal performance of the exterior envelopes of whole buildings XI, CD-ROM proceedings*, Clearwater Beach, Florida. Atlanta: ASHRAE; 2010.

Schöne T and Zirkelbach D. 2016. Development of hygrothermal reference years for Germany, *Proceedings of Central European Symposium on Buildings Physics (CESBP)*.

Zhou X, Derome D, and Carmeliet J. 2016. Robust moisture reference year methodology for hygrothermal simulations. *Building and Environment*, *110*, 23–35.

Hygrothermal performance of historic massive wall: when is 2D simulation necessary?

7th International Building Physics Conference, IBPC2018

Dario Bottino Leone[1,2*], Marco Larcher[1], Alexandra Troi[1] and John Grunewald[2]

[1]Eurac research, Italy
[2]Technical University of Dresden, Germany

*Corresponding email: dario.bottino@eurac.edu

ABSTRACT

Hygrothermal analysis of historical building envelopes is crucial in ensuring their durability and enhancing their performances. The use of hygrothermal dynamic simulation is the most effective approach to predict moisture related damages or risk of mould growth on ancient masonry envelopes. However, simulating the hygrothermal behaviour of a historic wall composed by stones or bricks and mortar joints, with a detailed two-dimensional (2D) model, is typically a complex and time-consuming process. For this reason, in numerical models, composite walls are often simplified with a one-dimensional (1D) layer, neglecting the mortar joints. An oversimplified numerical model could affect the evaluation of a retrofit intervention and lead to inadequate design choices. This study evaluates when the description of a historic wall as a 1D homogenous layer leads to an acceptable level of accuracy and when it is necessary the use of a more precise 2D model. We quantified the error by comparing 1D and 2D simulations of different massive walls in three Italian climate conditions. We examined a possible retrofit intervention with different internal insulation systems considering vapor tight, vapor retardant and capillary active solutions. Although simplified 1D models are reliable for thermal parameters, we have identified a different behavior regarding the hygric parameters. Whereas for a capillary active insulation system the 1D and 2D simulations show a reasonable agreement, the 1D approximation is no longer acceptable in the case of vapour closed insulation systems as it leads to large deviations. Knowing when it is possible to implement a simplified 1D model and quantifying the introduced error will support architects and energy consultants in the design process. It will guide them in the choice of the most suitable model depending on their specific requirements.

KEYWORDS

Hygrothermal simulation, Interior insulation, Performance evaluation, Moisture related issues, Historic stonewall.

INTRODUCTION

Historic buildings are highly energy-consuming parts of the city center, and their energy consumption provokes large CO_2 emissions due to the low performances of their thermal envelopes. A possible strategy to reduce this impact is to decrease the thermal transmittance of the outer walls. In the case of aesthetically valuable historic buildings, interior insulation has proven to be a reliable solution, but dynamic hygrothermal simulations are needed to avoid possible hygrothermal risks. In fact, the change of the original thermal and moisture balance could lead to a higher moisture accumulation into the wall [1] with a consequent spalling and cracking due to hygric expansion and contraction or frost-thaw cycles, or visual deterioration due to salt efflorescence [2]. A thorough understanding of the moisture transport is also primary to make an accurate choice of the correct inner insulation system. It is common practice, while performing a hygrothermal simulation, to simplify the historical wall as a homogeneous stone or brick layer. This simplification gives the user the possibility to have quicker results, but has the effect of

neglecting mortar joints, which could play a significant role in terms of moisture storage and transport; the resultant deviations are investigated in this paper. A previous study [3] analyzed the impact of the mortar joints for a massive brick wall exposed to real climate conditions showing that they have a negligible impact and concluding that typically the approximation to a homogenous brick layer is allowed. In the present work, we extend previous analysis considering a broader range of variants and situations. We analyze a historic wall that is retrofitted with the application of different types of internal insulation, we consider several materials for the composition of the historic wall, ranging from stone to bricks, and finally we examine different climates zones.

METHODS DESCRIPTION

Hygrothermal simulation tool

In order to perform a full hygrothermal assessment, the commercial software Delphin 6.0.16 is employed. We considered a full hygrothermal simulation, which includes heat transport, liquid convective transport and vapor diffusion [4].

Boundary condition: Outdoor

In this study we focus on Italian climate; in particular we selected three locations to consider North, Middle and South latitudes and cover different climate zones. The hourly climate data files were generated with Meteonorm 7.0. They include hourly data of temperature, relative humidity, direct and diffuse short wave radiation, long wave radiation, wind direction, wind velocity, and rain. In Table 1, we summarize the main characteristics of the three selected climates, Udine, Ancona and Messina for a North-facing wall.

	Annual Wind Driven Rain [l/m²]	Annual Global Radiation [kWh/m²]	Winter T average [°C]	Summer T average [°C]	Winter RH average [%]	Summer RH average [%]
Udine	44.29	326.54	4.72	23.95	71.95	66.86
Ancona	31.53	344.76	6.51	23.22	72.69	69.24
Messina	50.14	358.08	10.07	24.75	72.22	68.49

**Table 1.** Environmental conditions highlights. Annual radiation is calculated on the wall.

The thermal resistance of the exterior surface was set to 0.04 m²K/W. The absorption coefficient for short wave radiation was set to 0.6 and the emissivity for long wave radiation exchange to 0.9. The rain exposure coefficient was set at 1.00 assuming no sheltering, since worst-case scenarios were assessed.

Boundary condition: Indoor

The interior climate was calculated based on external daily temperature data, according to the adaptive indoor climate model presented in the standard UNI EN 15026 [5]. The selected temperature range is between 20 and 25°C, while relative humidity varies between 35 and 65% following the recommendation of the WTA leaflet 6.2 [6]. The thermal resistance of the interior surface was set to 0.125 m²K/W.

Historical wall characterization

The construction technique chosen for the reference hygrothermal model is a traditional core masonry wall. It is a widely used technology of the ancient Italian buildings [7]. The materials for the simulations are chosen among the most commonly spread over the Italian context. Four different stones are selected: granite, limestone, sandstone and tuff. The brick masonry, generally widespread in the Center-North of the country, is also included in this study. The mortar and the plaster chosen for the reference wall are a Lime Cement Mortar and an historical Lime Plaster; their hygric characterization parameters, as for the other materials, are selected from Delphin Material Database 6.0. In Figure 1 and Table 2, we report the main hygrothermal characteristics of the chosen materials.
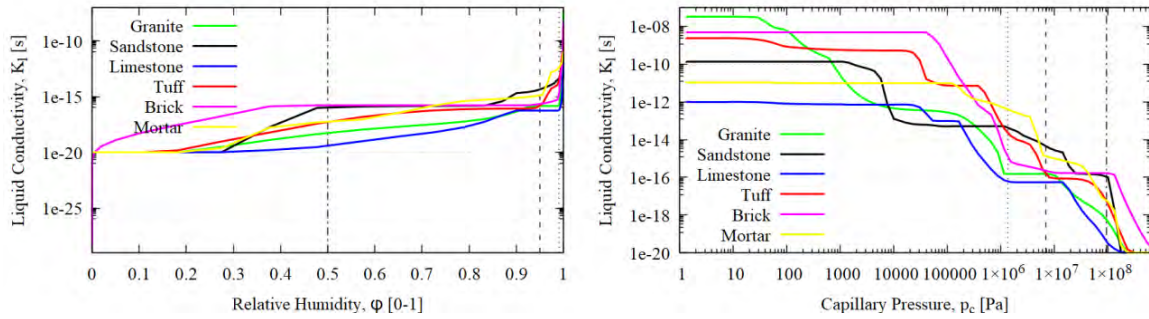
Figure 1. Liquid water conductivity, K_l, as a function of the relative humidity (left) and as a function of the capillary pressure, p_C (right). The three vertical dashed lines are drawn at the relative humilities 0.50, 0.95 and 0.99 in both graphs.

The 2D model includes irregular mortar joints of maximum 20 mm thickness. In figure 2 we show the full 2D description used in Delphin as well as the 1D approximated model.
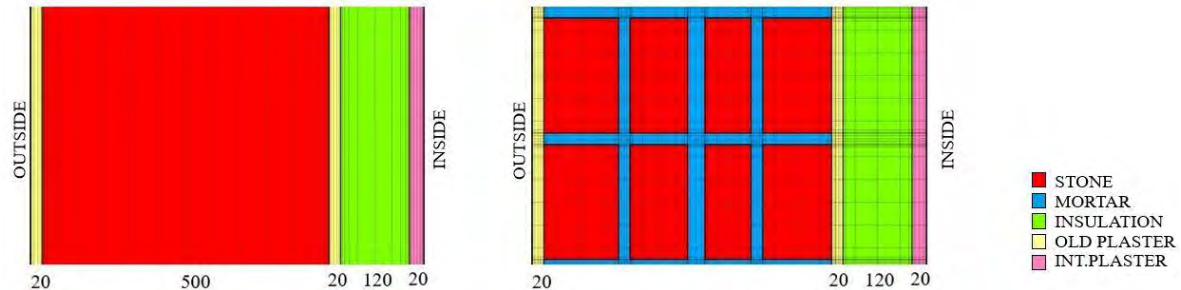
Figure 2. Schematic of the 1D and 2D models (elevation view of the section) of the historical wall section, with dimensions (mm).

Insulation systems

Three kind of insulation systems were investigated in this paper, classified by their vapor permeability: Vapor Barrier (VB), Vapor Retardant (VR), Vapor Open (VO). The thickness of each insulation layer is set to 120 mm. The VB insulation system consist of a mineral wool insulation layer plus a low permeability vapor barrier on its inner side. Two 12.5 mm gypsum board are used as surface coatings. As VR insulation system, we chose an extruded Polystyrene board installed with 20 mm of glue and a surface coating of 20 mm lime plaster. The VO insulation system is composed by a Calcium Silicate board, with 20 mm glue to attach it to the existing plaster, plus a surface coating of 20 mm lime plaster. The most relevant hygrothermal parameters of the insulation material are summarized in Table 2.

Materials	ρ [Kg/m³]	C_p [J/KgK]	θ_{eff} [m³/m³]	λ_{dry} [W/mK]	μ_{dry} [-]	A_w [Kg/m²s$^{1/2}$]
Mineral Wool	67	840	0.9	0.04	1	-
Extruded Polystyrene	35	1500	0.9	0.027	225	8e-06
Calcium Silicate	270	1158	0.9	0.069	3.8	1.114
Granite	2453	702	0.054	1.71	53.8	0.085
Limestone	2440	850	0.127	2.3	140	0.003
Sandstone	1967	264	0.12	0.95	106.9	0.012
Tuff	1450	925	0.299	0.48	10.4	0.098
Brick	1788	800	0.24	0.81	28.3	0.031
Lime Mortar	1878	758	0.223	0.8	36.9	0.036
Lime Plaster	1800	850	0.285	0.82	12	0.127

Table 2. Hygrothermal proprieties of the chosen materials. Density (ρ), Specific Heat capacity (C_p), Theta effective (θ_{eff}), thermal transmittance (λ_{dry}), vapor resistance (μ_{dry}), and water absorption coefficient (A_w).

Investigated outputs

The choice of the output to analyze in this assessment is based on the prescriptions of the WTA leaflet 6.5 [6]. The analysis of frost damages is neglected, since in the studied locations temperatures barely go under zero. Moreover, this study had shown a good correspondence of surface temperature and relative humidity values between 2D and 1D simulations, so the mold germination risk is not strongly influenced by this simplification. Therefore, the most interesting outputs to discuss, as proposed in WTA leaflet 6.5 [6], are relative humidity and temperature behind insulation, averaged on the first 10mm behind the insulation layer.

Error calculation

Outputs are evaluated on an hourly basis, in particular we compare the results of 1D and 2D simulations. The deviation between the two simulations is evaluated calculating the absolute error. In particular, for a given quantity X (that can be either the temperature, T, or the relative humidity behind the insulation, φ) we define the absolute error as

$$\Delta X(t) = |X_{2D}(t) - X_{1D}(t)| \tag{1}$$

where $X_{2D}(t)$ and $X_{1D}(t)$ represent the parameter X calculated as a function of time in the 2D and in the 1D simulation respectively. Then we define the absolute mean error, $\langle \Delta X \rangle$, as the time average of $\Delta X(t)$ over the last year of simulation and the maximum absolute error, ΔX_{max} as the maximum over the all simulation.

RESULTS

The thermal analysis shows a high correspondence of the simulation results between 2D and 1D case. In particular for the calculation of the temperature behind the insulation we get the following typical errors: $\langle \Delta T \rangle = 0.12\,°C$ and $\Delta T_{max} = 1.4\,°C$. Contrariwise, more deviations exist for the hygric behavior reaching mean absolute errors up to 7% for the relative humidity behind the insulation. Figures 3, 4 and 5 show the average relative humidity behind the insulation in the simulations of Udine for each case: Vapor Barrier, Vapor Retardant and Vapor Open insulation systems. A similar behavior is observed also for the simulation performed in Messina and Ancona.
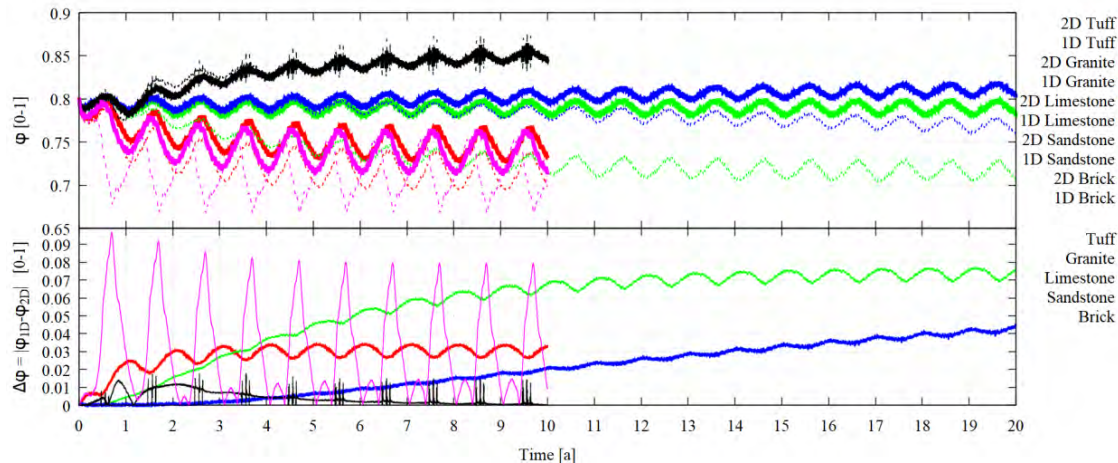
Figure 3. Relative humidity behind the insulation, φ, as a function of time (top panel) and corresponding absolute error, $\langle \Delta\varphi \rangle$, (bottom panel) for Vapor Barrier insulation system and for the climate of Udine. The different colors refer to different materials composing the historic wall.
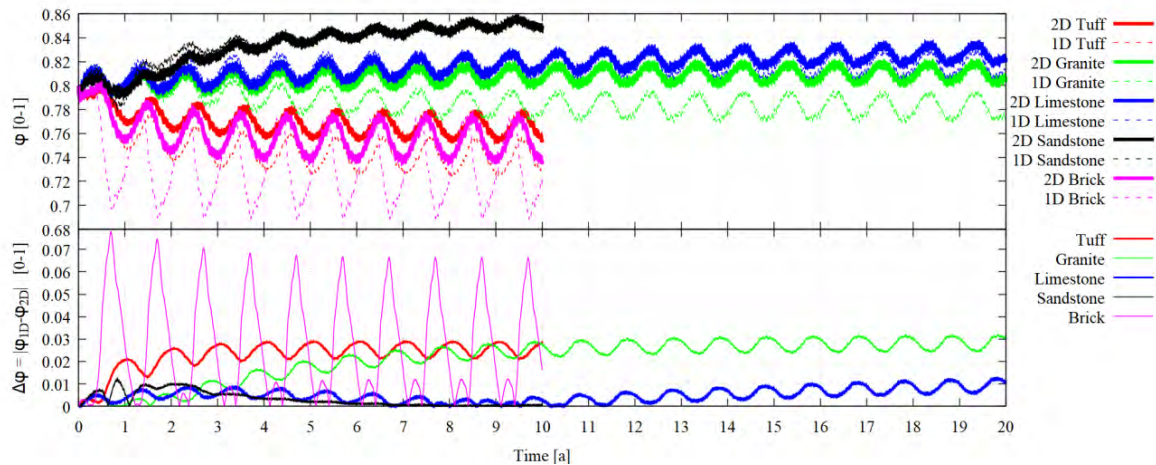
**Figure 4.** Same as Figure 3 but for Vapor Retardant insulation systems.
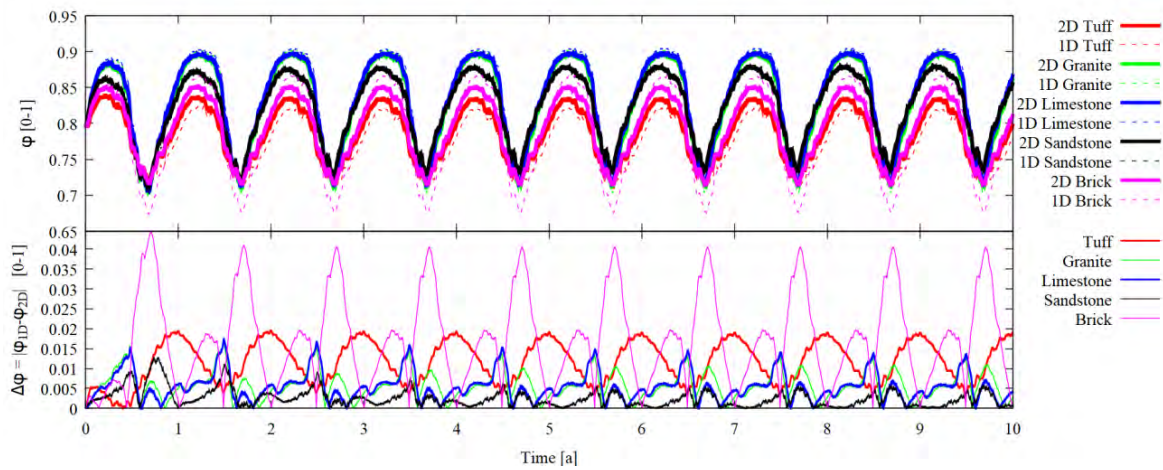
Figure 5. Same as Figure 3 but for Vapor Open Insulation system.

DISCUSSIONS

Figures 3, 4 and 5 show that depending on the insulation type and on the material that forms the historic wall we can get very different absolute errors between 1D and 2D simulations. For instance when considering the sandstone wall we always get very small errors, while the largest mean absolute errors are observed for the case of granite. Also in the case of the limestone wall we get significant deviations. In the specific case of the limestone wall with a vapor tight insulation system, the situation is particularly critical since the 1D and the 2D simulation have different behaviors. The 2D simulation reaches a quasi-stationary behavior, while the relative humidity in the 1D simulation keeps decreasing over the years. For the brick masonry wall we observe peaks up to 9% deviation. For the vapor open insulation system, we typically get small deviations while the largest errors are found in the case of vapor tight solutions. Conversely, we observe that the climate does not play a crucial role in the determination of the behavior of the absolute error. We only observe a small correlation between the quantity of wind driven rain that reaches the façade and the absolute error. In order to get a closer insight on the correlation between the observed error and the parameters varied in the simulations we represent in Figure 6 and 7 the distributions of the absolute mean error using box plots. In Figure 6 the absolute mean error distributions are grouped depending on the insulation type, while in Figure 7 according to the material of the historic wall.
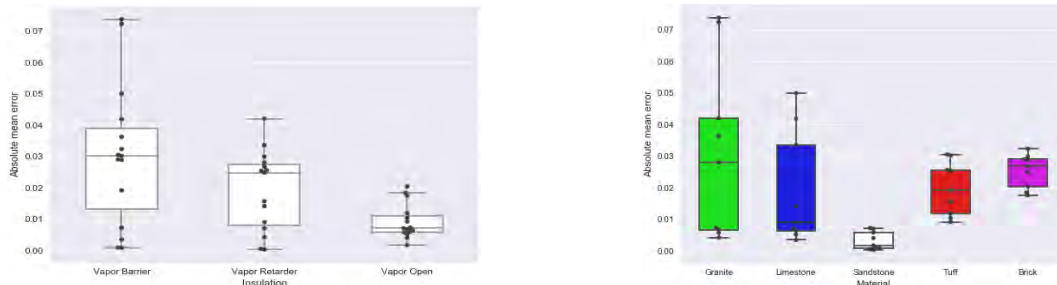
Figures 6-7. Absolute mean error: Insulation system dependency, Material dependency.

Fig.6 confirms that vapour tight insulation systems lead to higher errors. In particular, decreasing the vapour tightness of the insulation system, we observe smaller mean absolute errors. For vapour open insulation systems the mean absolute error $\langle\Delta\varphi\rangle$ is, for almost all the cases, smaller than 2%, while for vapour barrier insulation system we get errors of up to 7%. When using a vapour retardant solution we get an intermediate behaviour. The use of a vapour tight system on the internal side of the construction strongly reduces the interaction of the wall with the internal environment and therefore the behaviour of the wall is mainly determined by the interaction with the exterior climate. This interaction strongly depends on the way in which the wall is modelled, thus a detailed description of the wall becomes more relevant in this situation. Fig.7 confirms that the material forming the wall plays a significant role in the determination of the mean absolute error. In particular, we observe smaller errors for materials that have a liquid water conductivity close to the one of the mortar in the range 80 – 99%. These observations strongly suggest that the approximation of a masonry wall to a homogenous brick or stone layer has to be used with caution, especially when looking at hygric properties of the wall.

CONCLUSIONS

This study analyzed the effect of simplifying an historical wall with a homogeneous layer in hygrothermal assessments, comparing the results of a 1D approximated simulation with those of a detailed 2D simulation. Three Italian climates and five materials were investigated, in combination with three internal insulation systems: a Vapor Barrier, a Vapor Retardant and a Vapor Open one. Results had shown a high correspondence in thermal behavior. Contrariwise, higher deviations are found in hygric results, especially in vapor tight and retardant insulation systems, which are influenced by a moisture accumulation process. Regarding the historic wall composition, those materials that have a similar liquid water conductivity to the mortar in the relative humidity range of the simulation, lead to smaller deviations. Our results show that representing an historic wall with a homogenous 1D layer could be in some situations an oversimplified model. We identified the situations that lead to larger errors in the framework of the parameters that we varied. However, further investigation are needed to develop a systematic approach for the identification of those situations.

REFERENCES

[1] Vereecken E., Van Gelder L., Jannsen H., 2015. Interior insulation for wall retrofitting – A probabilistic analysis of energy savings and hygrothermal risks.
[2] Janssen H., Derluyn H., Carmeliet J., 2012. Moisture transfer through mortar joints: a sharp-front analysis.
[3] Vereecken E., Roels S., 2013. Hygric performance of a massive masonry wall: How do the mortar joints influence the moisture flux?
[4] Sontag L., Nicolai A., Vogelsang S., 2013. Validierung der Solverimplementierung des hygrothermischen Simulationsprogramms DELPHIN.
[5]UNI/EN15026,2008.Hygrothermal performance of building components and building elements.
[6] WTA, 2014. Leaflet 6.2 and 6.5, Simulation of heat and moisture transfer. Interior insulation.
[7] Pascucci M., Lucchi E. 2D-Higrothermal simulation of historical solid walls.

Innovative composite materials with enhanced acoustic, thermal, and optical performance for urban pavements: experimental characterization

Verronica Lucia Castaldo[1], Claudia Fabiani[2,*], Anna Laura Pisello[3] and Franco Cotana[4]

[1]CIRIAF-Interuniversity Research Center, Department of Engineering, University of Perugia, Via G. Duranti 63, 06125, Perugia, Italy, castaldo@crbnet.it

[2]CIRIAF-Interuniversity Research Center, Department of Engineering, University of Perugia, Via G. Duranti 63, 06125, Perugia, Italy, fabiani@crbnet.it

[3]Department of Engineering, University of Perugia, Via G. Duranti 93, 06125, Perugia, Italy, anna.pisello@unipg.it

[4] Department of Engineering, University of Perugia, Via G. Duranti 93, 06125, Perugia, Italy, cotana@crbnet.it

Corresponding email: fabiani@crbnet.it

ABSTRACT

Over the last decades, the implementation of innovative multifunctional materials for urban surfaces has produced a variety of paving solutions characterized by self-cleaning, self-healing, electricity conductive, solar reflective, sound absorbent properties and so on. Therefore, a key challenge is nowadays represented by the need for combining multi-physics properties in a single material or system for flooring. The present work concerns the development of a new outdoor paving application with enhanced acoustic, thermal, and optical performance. To this aim, eleven concrete mix-designs were tested. The composites were characterized by different aggregate size, material and additives. The aggregates included in the composite consist of (i) natural stones with different grain sizes, (ii) expanded clay aggregates, and (iii) glass fragments. Acoustic, thermal, and optical measurements were performed for each sample. Additionally, a dedicated in-field monitoring campaign was carried out to characterize the albedo under summer boundary conditions. Finally, the thermal behaviour of the samples was tested in an environmental chamber using controlled boundary conditions in terms of temperature, humidity, and radiation. The results demonstrate that bigger grain size presents the best acoustic performance in terms of absorption capability, i.e. absorption coefficient of about 0.9 and 0.8 at 1000 Hz and 500 Hz, respectively. Moreover, the thermal-optical lab and field tests confirm previous literature results demonstrating that the mix-design with the smaller grain size has the best reflectivity potential.

KEYWORDS
Paving materials; Optimized mix-design; Thermal-optical performance; Acoustic properties.

INTRODUCTION
Urban environments are often affected by microclimate phenomena such as Urban Heat Island (UHI), a local condition that can significantly harm the health and the quality of life of citizens. In particular, the UHI consists of a significant increase in temperature in the urban area compared to the surrounding rural areas (Vardoulakis, Karamanis, Fotiadi, & Mihalakakou, 2013). Such phenomenon is generally influenced by the thermal and radiative properties of the typical urban surface materials (i.e. asphalt, cement) where the absorption of solar radiation prevails over its reflection (Taha, 2008). Moreover, the human action and the buildings operation strongly contribute to the overheating of urban areas. Such contribution is (i) direct, through traffic, industrial activities and HVAC systems, and (ii) indirect, though the alteration

of the radiative properties of the atmosphere due to the high levels of associated pollution (Pisello, 2017). Over the last few decades, many techniques have been proposed for the mitigation of such phenomenon. Among the main ones there is the use of permeable surfaces in urban environment, consisting of gravels or vegetation able to generate surface cooling by means of evapotranspiration. Furthermore, "cool" materials represent another suitable solution for reducing high urban temperatures (Santamouris, Synnefa, & Karlessi, 2011). These materials are characterized by a high solar reflectance and thermal emissivity that avoids overheating of the surfaces and the air near them. The benefits achievable when installing a cool material over urban paved surfaces can be summarized as follows (Rosso et al., 2017): (i) mitigation of the urban overheating thanks to the capability to reflect most of the incoming incident solar radiation and (ii) consequent reduction of CO_2 emissions emitted in the environment. Another issue typical of urban environments relates to the high noise levels in cities and is referred to as Urban Noise Island (UNI), where depending on the road and tires characteristics and of course on the vehicles' speed, the prominent noise peak very frequently is found at 1000 Hz but it may also be shifted within the range 630-2000 Hz (Sandberg 2003). It is generated by the combination of the different and multiple sources of noise (such as traffic, industrial activities, etc.) that generate sound pollution in urbanized environments (Asdrubali et al., 2015). The study of this phenomenon, which depends on both the generation and propagation of sound, involves the environmental analysis of the external and internal sources at building level, of the control actions on the source, on the propagation path and on the receptor, as well as on the analysis of the response of the human ear to sound stress. In this case, the main mitigation techniques consist of passive type protections that act on the propagation path or on the receptor. In this sense, to reduce the problem of urban noise it is possible also to act on the shape of the buildings, i.e. mainly on the acoustic requirements of the façade (i.e. acoustic insulation). Based on the framed background, the present research work deals with the development, characterization and optimization of concrete-based materials with high-thermal and acoustic performance for urban paving applications. The aim is therefore to implement innovative materials able to mitigate both the UHI and UNI when installed over urban pavements. To this purpose, an extensive experimental laboratory and field campaign was carried out and different mix design where tested and compared in terms of their coupled thermal-acoustic behavior.

MATERIALS AND METHODS

Five different components were selected and used to produce advanced concrete mix designs with enhanced acoustic and visual performance to be used as urban pavements: sand (i.e. fine grains, 0-4 mm), pebbles (i.e. medium grains, 2-5.6 mm), chippings (i.e. large grains, 4-12.5 mm), glass fragments (4-12.5 mm) and expanded clay spheres (2-5 mm). These components were alternatively treated with titanium dioxide to maximize their capability to reflect solar radiation. The samples had a diameter of 10 cm and 2.9 cm and a thickness of 6.5 cm for the laboratory acoustic tests (i.e. for the evaluation of the acoustic absorption).

Starting from the first basic paving mix-design (i.e. traditional paving recipe chippings-based), additional samples were prepared, by varying (i) type of aggregate (sand, pebbles, chippings, expanded clay spheres, and glass fragments), (ii) TiO_2 treatment, and (iii) kind of additive (i.e. dynamon floor 20 and bt02) in the case of the pebble mix design.

Thermal-optical in-lab experimental analysis

Firstly, spectrophotometric measurements were carried out to investigate the reflectance capability of the different evaluated samples. The experimental campaign was performed by using a Shimadzu UV-VIS-NIR spectrophotometer equipped with a double-radius optical system over time and integrating sphere. Moreover, the calculation of the spectral solar reflectance in the range 300-2500 nm was carried out according to the ASTM E903-12

Standard Test Method (American Society for Testing and Materials, 2010b). Secondly, the thermal emissivity of the samples was measured by means of a portable emissometer according to the ASTM C1371 Standard Test Method (American Society for Testing and Materials, 2010a). Finally, a DM340SR (ATT) climatic chamber was used to test the thermal behavior of the samples within controlled dynamic conditions in terms of temperature, humidity and solar radiation (Fabiani & Pisello, 2017).

Acoustic in-lab experimental analysis
In order to characterize the acoustic properties of the selected materials, the impedance tube was used. To this aim, a Brüel & Kjær Kundt's tube with all the related equipment and accessories was used. The measurements were carried out according to the classic standardized procedures in materials analysis in the lab (Asdrubali et al., 2015). The test procedure involved at least three measurements for each sample to obtain an acceptable result reliability. Finally, the comparison between the absorption coefficients of the different samples was made considering the average value of the measurements carried out for each sample.

Albedo field monitoring
After the preliminary in-lab experimental campaign, the albedo of the samples was monitored in-field by means of a dedicated double pyranometer or albedometer, an instrument able to measure both the incident solar radiation and the one reflected from the surface between 300 and 2500 nm. The experimental measurement campaign was carried out according to the ASTM E1918-06 international standard (2006). The experimental campaign was performed in the period from 10 July to 10 August 2017 to characterize its reflectance potential when the climatic forcing to the boundary and the meteorological conditions vary. To this end, after the measurement of black and white reference samples (Akbari, Levinson, & Stern, 2008) the different samples were monitored on typical summer days.

RESULTS
Thermal Emissivity and Solar Reflectance
In this section, the results of the testing of the thermal-optical properties of the samples are presented. In particular, Figure 1 shows the trend of the solar reflectance of fine sand, mortar and pebbles concrete mix designs, and the obtained solar reflectance (SR), emissivity (ε) and solar reflectance index (SRI). It is clear how the solar reflectance increases as the grain size decreases. In fact, as can be seen by comparing the pure mortar with the mix designs produced by introducing the same amount of sand or pebbles, the sample with fine sand shows the greatest solar reflectance, followed by pebbles and the traditional mortar. In terms of thermal emissivity, the values are generally high, i.e. varying from to 0.91 (mortar) to 0.99 (fine sand).
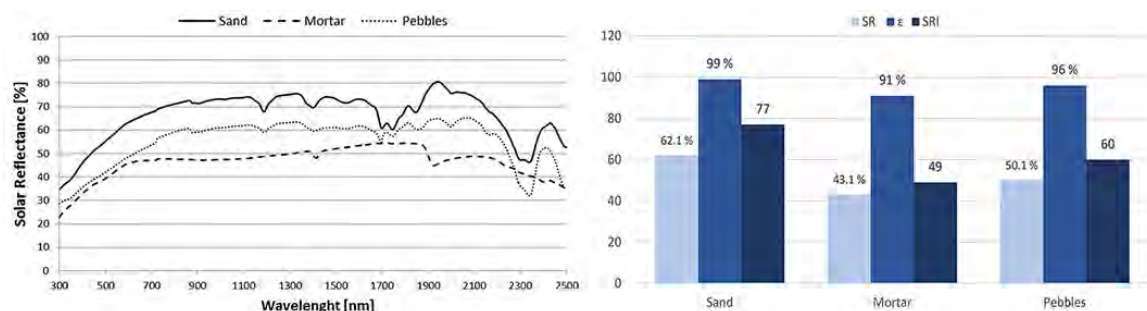

Figure 1. Solar reflectance profiles in the range 300-2500 nm, SR, ε and SRI of the samples.

Dynamic controlled environment: climatic chamber

This section summarizes the results of the tests carried out in the climatic chamber. The purpose of the tests was to investigate and compare the thermal behavior of the samples under the same controlled dynamic environmental conditions, i.e. a typical summer day in the Rome climate zone taken from the TMY (Typical Metereological Year). Therefore, the surface temperatures of the upper and lower face of the samples was measured with varying air temperature, relative humidity, and incident solar radiation.

Figure 2 shows how the samples containing fine sand present the best surface thermal behaviour, followed by the mortar and the pebbles mix design with the Dynamon 20 additive, which possess the highest thermal inertia due to their highest density and the samples with TiO_2 and glass fragments, which are capable to reflect the highest amount of the incoming radiation (an average direct radiation on the horizontal surface of 820 W/m^2 was imposed through the halogen lamp according to data from the TMY). On the other hand, expanded clay sphere and pebbles samples with bt02 or without any additive, which are characterized by a larger grain size and lower densities, show the worst performance in terms of surface temperature, reaching up to 68°C.
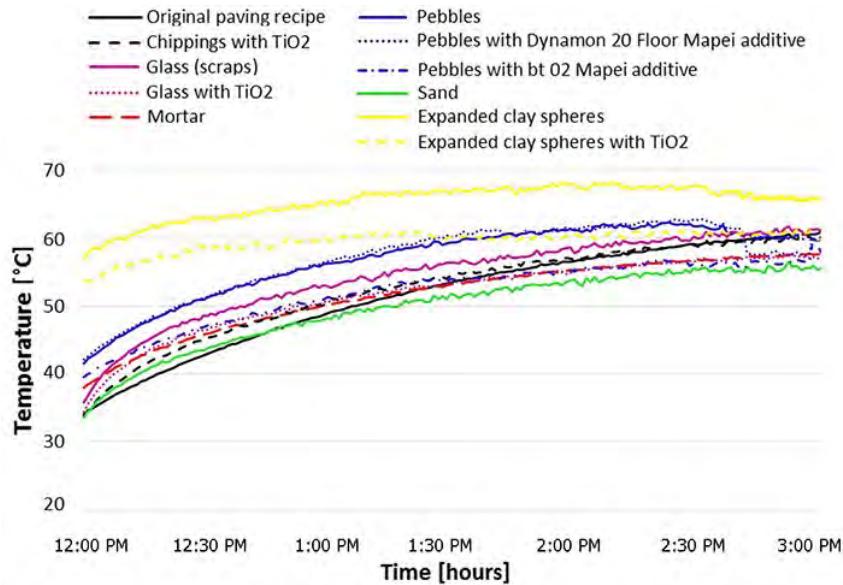

Figure 2. Average temperatures of the upper (left) and lower (right) surface of the samples.

Albedo in-field measurements

Table 2 shows the albedo values measured in the field during typical summer days (July 2017) for the different samples of paving material produced. It is evident how the paving recipe characterized by the presence of glass fragments and TiO_2 treatment present a greater albedo than all the other samples, followed by the expanded clay spheres with TiO_2 treatment. The paving samples produced using the original recipe with chippings included, and the one characterized by the presence of pebbles are those with lower potential in terms of albedo. These results are consistent with previous studies showing that albedo increases with decreasing grain size.

Table 2: Albedo test results.

Sample	Traditional asphalt	Original paving recipe	Expanded clay spheres+ TiO₂	Glass fragments + TiO₂	Pebbles
Albedo (12-3PM)	~7	37.9	40.8	44.4	36.8

Acoustic absorption coefficient

Figure 3 shows the trend of the acoustic absorption coefficient for the various samples tested with respect to the original paving recipe. The sample of the original pavement recipe is not very absorbent. In fact, the maximum absorption coefficient is equal to 0.2 at 450 Hz. As for the mortar sample, this has a maximum absorption coefficient equal to 0.2 at 600 and 1300/1400 Hz. As regarding the samples with aggregates of different grain sizes, the sand has a maximum absorption coefficient of 0.2 at 400 Hz, and then remains almost constant (<0.1) at the other frequencies. The sample with pebbles, on the other hand, presents a bell-shape absorption coefficient with a positive peak of 0.85 just before 600 Hz and a negative peak of less than 0.2 at about 1600 Hz. The clay sphere sample is characterized by a high absorption coefficient, with a peak of 0.9 at 600 Hz. As for the mix design with chippings and TiO_2, a maximum absorption of 0.3 between 500 and 600 Hz is reached. Subsequently, the absorption capacity decreases at about 0.1 between 800 and 1200 Hz, then decreasing again. By adding the bt02 additive, the aforesaid sample becomes very absorbent, with a maximum absorption coefficient of 0.9 at 500 Hz. By adding a different type of additive ("Dynamon"), the absorption coefficient reaches a value of almost 0.8 at 500 Hz. The sample produced using expanded clay spheres and TiO_2 has a very high absorption capacity, up to a maximum value of 0.8 at 500 Hz. The sample with glass fragments, on the other hand, has a low absorption capacity, with a maximum of less than 0.2 at 450 Hz. By adding the TiO_2 to the present recipe, the absorption coefficient increases slightly to 0.25 at 600 Hz and then decreases at the other frequencies.

Based on such results, the mix-design showing the highest absorption coefficient is that with pebbles, with and without additives, and the expanded clay spheres one, with and without TiO2. All the other samples examined show absorption coefficient peaks ranging from about 0.2 to 0.3. On the other hand, samples with pebbles and expanded clay spheres reach peaks of almost 0.9 with respect to the traditional paving recipe which almost does not reach 0.2. It is also possible to notice that all the tested samples have an absorption coefficient peak between 400 and 600 Hz.
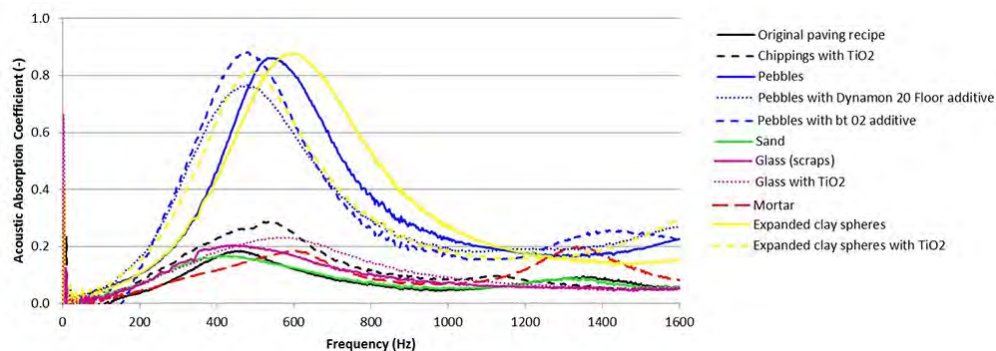

Figure 3. Comparison among the acoustic absorption coefficients of the tested samples.

CONCLUSIONS

The present work aimed at developing and experimentally characterize the thermal and acoustic performance of composite materials for external urban paving. To this purpose, samples of different materials were produced, with varying mix design, particle size, and components (i.e. natural gravel, glass fragment, expanded clay). Results from the experimental campaign allowed to identify the best recipe for urban paving application depending on the need to optimize the performance in terms of solar reflectance, thermal emissivity, albedo, surface temperature and/or absorption and sound insulation potentiality. In general, it was found that to optimize the thermo-optical performance of the paving it is necessary to reduce the grains size of the aggregates as much as possible. In fact, the solar reflectance increases as the particle size of these components decreases. As far as the albedo is concerned, the tests demonstrated that to

improve the performance of the original paving mix it is appropriate to integrate glass fragments and TiO_2 (40% enhancement of the albedo compared to the traditional base-case paving recipe). As for the optimization of the acoustic behavior, it was shown that the best absorption performances are achieved by the samples in loose configuration, due to the interstitial voids that increase the amount of sound energy dissipated by the interaction between the solid matrix and the air molecules. Furthermore, it was possible to notice how the two different configurations (i.e. low density and high density mix design) work properly at different frequencies. Therefore, to maximize the acoustic performance of urban paving materials it is necessary to select materials that work well at low frequencies. In this view, the best materials in terms of acoustic absorption potential are those ones with expanded clay balls, which allow an improvement up to 0.6 (300%) compared to the original paving.

ACKNOWLEDGEMENT

REFERENCES

Akbari, H., Levinson, R., & Stern, S. (2008). Procedure for measuring the solar reflectance of flat or curved roofing assemblies. *Solar Energy*, *82*(7), 648–655. https://doi.org/10.1016/J.SOLENER.2008.01.001

American Society for Testing and Materials. (2010a). ASTM C1371-04a, Standard Test Method for Determination of Emittance ofMaterials Near Room Temperature Using Portable Emissometers. West Conshohocken, PA, USA.

American Society for Testing and Materials. (2010b). ASTM E903-96, Standard Test Method for Solar Absorptance, Reflectance, andTransmittance of Materials Using Integrating Spheres. West Conshohocken, PA, USA.

Asdrubali, F., Cotana, F., Pisello, A. L., Mencarelli, N., D'Alessandro, F., & Schiavoni, S. (2015). Acoustic properties of stone aggregates used in cool roofs. In *22nd International Congress on Sound and Vibration, ICSV 2015*.

Fabiani, C., & Pisello, A. L. (2017). Coupling controlled environmental forcing and Transient Plane Source method: an innovative thermal characterization procedure for building insulation materials. *Applied Thermal Engineering*, *In Press*. https://doi.org/10.1016/j.applthermaleng.2017.10.155.

Pisello, A. L. (2017). State of the art on the development of cool coatings for buildings and cities. *Solar Energy*. https://doi.org/10.1016/j.solener.2017.01.068

Rosso, F., Pisello, A. L., Castaldo, V. L., Fabiani, C., Cotana, F., Ferrero, M., & Jin, W. (2017). New cool concrete for building envelopes and urban paving: Optics-energy and thermal assessment in dynamic conditions. *Energy and Buildings*, *151*. https://doi.org/10.1016/j.enbuild.2017.06.051

Sandberg, U. (2003). The Multi-Coincidence Peak around 1000 Hz in Tyre/Road Noise Spectra. Euronoise Conference. Naples.

Santamouris, M., Synnefa, A., & Karlessi, T. (2011). Using advanced cool materials in the urban built environment to mitigate heat islands and improve thermal comfort conditions. *Solar Energy*. https://doi.org/10.1016/j.solener.2010.12.023

Taha, H. (2008). Meso-urban meteorological and photochemical modeling of heat island mitigation. *Atmospheric Environment*. https://doi.org/10.1016/j.atmosenv.2008.06.036

Vardoulakis, E., Karamanis, D., Fotiadi, A., & Mihalakakou, G. (2013). The urban heat island effect in a small Mediterranean city of high summer temperatures and cooling energy demands. *Solar Energy*, *94*, 128–144. https://doi.org/10.1016/j.solener.2013.04.016

Intrinsic Evaporative Cooling with Natural Ventilation and Shading for Adaptive Thermal Comfort in Tropical Buildings

Lokko, Mae-ling.[1,*] and Alexandra Rempel[2]

[1]School of Architecture, Rensselaer Polytechnic Institute, Troy NY 12180, USA
[2]Environmental Studies Program, University of Oregon, Eugene OR 97403, USA

*Corresponding email: lokkom2@rpi.edu

ABSTRACT

Hygroscopic materials, including earth- and plant-based materials used in tropical vernacular architecture, often sorb significant moisture from the atmosphere during humid nighttime hours; evaporation the following day then provides a pronounced cooling effect, particularly in semi-arid regions. While such intrinsic evaporative cooling is also active in wet-tropical climates, it cannot maintain indoor comfort, and vernacular structures are highly open to facilitate air movement. Recently, new hygroscopic materials have been developed from coconut agricultural wastes that show great potential for intrinsic evaporative cooling and indoor humidity control in contemporary tropical buildings. As expected, however, they must be combined with additional cooling strategies to maintain thermal comfort. This investigation explores the integration of intrinsic evaporative cooling with natural ventilation and shading to determine the extent to which indoor thermal comfort, as evaluated by the ASHRAE 55 adaptive thermal comfort standard, may be maintained in the representative wet-tropical climate of Ghana, West Africa.

KEYWORDS

intrinsic evaporative cooling, hygroscopic, agrowaste, natural ventilation, passive cooling

## INTRODUCTION

Hygroscopic materials, including adobes, grasses, fibers, and leaves used widely in tropical vernacular buildings can sorb significant moisture from the atmosphere during humid nighttime hours; evaporation the following day can then offset appreciable solar gains. This phenomenon, termed intrinsic evaporative cooling, has recently been characterized in diverse earth materials and semi-arid climates (Rempel 2016) as well as in agrowaste fibers and fiberboards in humid and subtropical climates (Lokko 2016). Intrinsic evaporative cooling in itself, however, cannot maintain indoor comfort in humid tropical climates (Lokko 2016). While moisture sorption by hygroscopic agrofiber envelope materials has previously been shown to lower indoor humidity to as little as 70% of outdoor daytime levels (Lokko 2016), indoor operative temperatures remained outside adaptive thermal comfort standards (ASHRAE 2017) and higher than outdoor conditions. The present study addresses these comfort issues by incorporating the effects of shading and natural ventilation, using window operation strategies common in tropical cities like Accra, Ghana, and evaluating results in light of the adaptive comfort standard (ACS) to reflect the relaxation of thermal expectations and higher levels of perceived control observed in naturally ventilated buildings (Brager 1998). Following natural ventilation strategies used in vernacular and contemporary buildings, which facilitate air movement through occupied zones, this work studies the impact of shading and natural ventilation on two scales of window openings. While the ACS applies to sedentary activity and may not account for the changing thermal preferences of tropical building inhabitants who have become accustomed to air-conditioning, it is used here to reflect the broad thermal adaptation typical of people living in the tropics.

METHODS

A simple gabled rectangular building with multiple window and shading configurations was
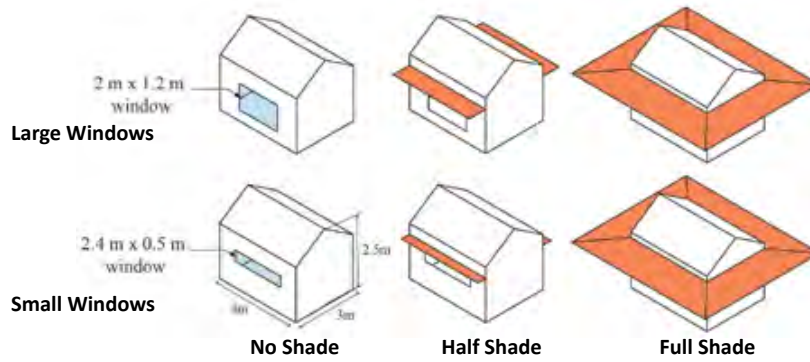
Figure 1. Study building dimensions, window configurations, and shading elements.

modeled in EnergyPlus 8.7, using Euclid 0.9.3 for geometry input (Fig. 1). Oriented along the east-west axis, the roof and walls were simulated as hygroscopically-active coconut fiberboard assemblies surrounding a tiled concrete floor in contact with the ground. Internal gains assumed a single occupant, with a sensible heat fraction of 0.3, activity level of 90-120 W/person when occupied, and 5pm-9am residential occupancy. To understand heat, air, and moisture transfer patterns, the EnergyPlus Heat and Moisture Transfer (HAMT) algorithm was used to simulate the effects of evaporation from, and condensation onto, building materials following established procedures (Rempel 2016). Infiltration and natural ventilation were simulated with airflow networks, allowing EnergyPlus to calculate wind pressure coefficients from the orientations of wall and roof surfaces with respect to wind speed and direction. Infiltration, active in all models, was governed by an air mass flow coefficient of 0.001 kg/s at reference conditions of 20°C with a cross-crack pressure difference of 1 atm, for wall and roof assemblies, and 0.01 kg/s at the same reference conditions for window perimeters, reflecting typical construction practices. Natural ventilation, in turn, assumed openable areas equal to the window areas specified (Fig. 1), with discharge coefficients estimated conservatively at 0.65. To reveal the effect of natural ventilation on indoor operative temperatures, independent of shading, models possessing either small or large windows (Fig. 1) were simulated with a baseline condition of closed windows (i.e. with infiltration only) and with two predominant ventilation control practices found in Ghana in the hottest months: one with windows open only during the day, and one with windows open both day and night. Natural ventilation was anticipated to improve thermal comfort in three ways: first, by removing warm indoor air and replacing it with cooler outdoor air; second, by cooling thermal mass; and third, by increasing indoor air velocity, thereby accelerating evaporation of moisture from skin and effectively expanding the thermal comfort zone. Because of this, building indoor operative temperatures (°C) and air velocities (m/s) were compared to adaptive comfort boundaries in each case. All simulations used the SWERA weather file for Accra, Ghana, and results were reported for one representative week in March, the warmest month of the year.

Table 1. EnergyPlus Model Parameters

| Construction	Material	Density (kg/m³)	Thickness (m)	k (W/m-K)	c (J/kg-K)
Exterior Floor	Heavyweight concrete	2240	0.1016	1.95	900
	Ceramic tile	1920	0.0127	1.59	1260
Coconut Wall	Coconut Fiberboard	1100	0.00952	0.36	4379
Coconut Roof	Coconut Fiberboard	1100	0.00952	0.36	4379
	Coconut Fiber mat	155	0.00318	0.03	4102
Window Glazing	Clear uncoated glass	-	0.003	0.90	0

RESULTS

Intrinsic evaporative cooling. Typical outdoor air temperatures in Accra, Ghana in March, the warmest month of the year, fluctuate from the high 20's to low 30's Celsius, while outdoor relative humidity typically rises above 80% overnight but falls to ~60% at mid-day (Fig. 2a). Sorption of moisture from humid nighttime air by hygroscopic coconut fiber materials is evident in latent heat transfer into wall and roof surfaces, shown by negative values. Evaporation from these surfaces, in turn, which provides cooling, is shown by positive latent heat flux values, resulting in an average daytime evaporative cooling effect of ~50 W/m² for wall and ~15 W/m² for roof surfaces. While this process effectively diminished indoor relative humidity compared to outdoor levels (Fig. 2a), indoor temperatures remained uncomfortably high (e.g. Figs. 3a, c).
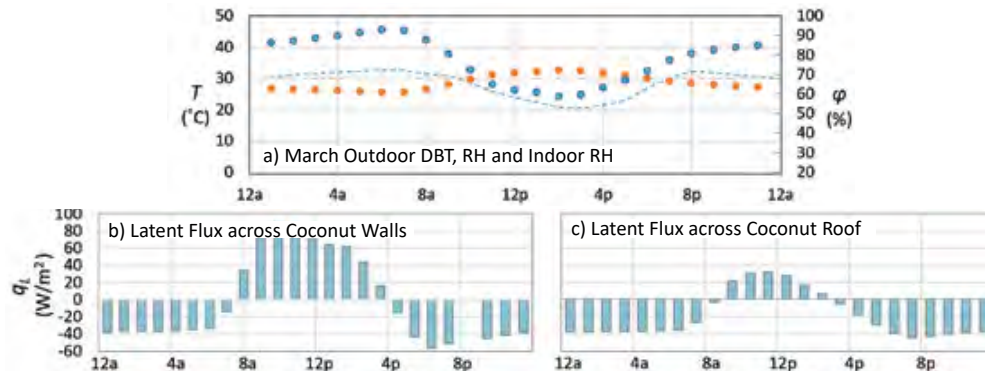
Figure 2. Intrinsic evaporative cooling in the study building, showing a) March outdoor air temperatures (orange dots) and relative humidities (blue dots) and indoor relative humidity (blue dashes), as well as latent heat fluxes across b) coconut fiberboard walls and c) roof surfaces.

Natural ventilation. Without natural ventilation, i.e. with only infiltration to exchange indoor and outdoor air, indoor operative temperatures reached ~40°C at mid-day, with small-windowed models remaining only slightly cooler than the large-windowed counterparts (Figs. 3a,c). This shows the importance of heat transfer through the lightweight, relatively conductive coconut envelope panels, which contributed more than window solar transmission or infiltration to total heat gain. At the same time, this envelope allowed "No Vent" models to cool to near-outdoor temperatures each night, such that near-comfortable conditions were predicted during most occupied hours (6pm-8am). Adding daytime ventilation (8am-8pm) diminished daytime operative temperatures dramatically, lowering peak values by about 6°C in the days shown (Fig. 4) and bringing 2-4 additional hours per day into the adaptive comfort zone, easily encompassing the occupied hours. Night operative temperatures dropped as well, though less extensively, reaching minima ~1-2°C lower than observed in "No Vent" models. This drop was associated with lower mass surface temperatures, showing that the limited mass provided (0.5cm ceramic tile over a 10cm concrete floor) was able both to sustain higher nighttime temperatures when ventilation was eliminated, and to facilitate additional cooling when it was permitted, even during the day. Adding night ventilation, i.e. opening windows for 24h daily, did not noticeably affect indoor operative temperatures in either small- or large-windowed models (Figs. 3a, c). This was unexpected, given the massive floor, but closer inspection revealed several explanations. First, March nighttime winds are typically low in Accra (≤3 m/s in >90% of hours), compared to daytime values of 4-6 m/s, diminishing night ventilation' effectiveness. Second, infiltration exchanged sufficient air at night in the "12h Vent" model that open windows added only modest air exchange. Third, consistent with the previous two points, the mass floor did not become appreciably cooler in the "24h Vent" models, showing that the additional air exchange was not enough to lower floor mass temperatures to an extent relevant to thermal comfort.
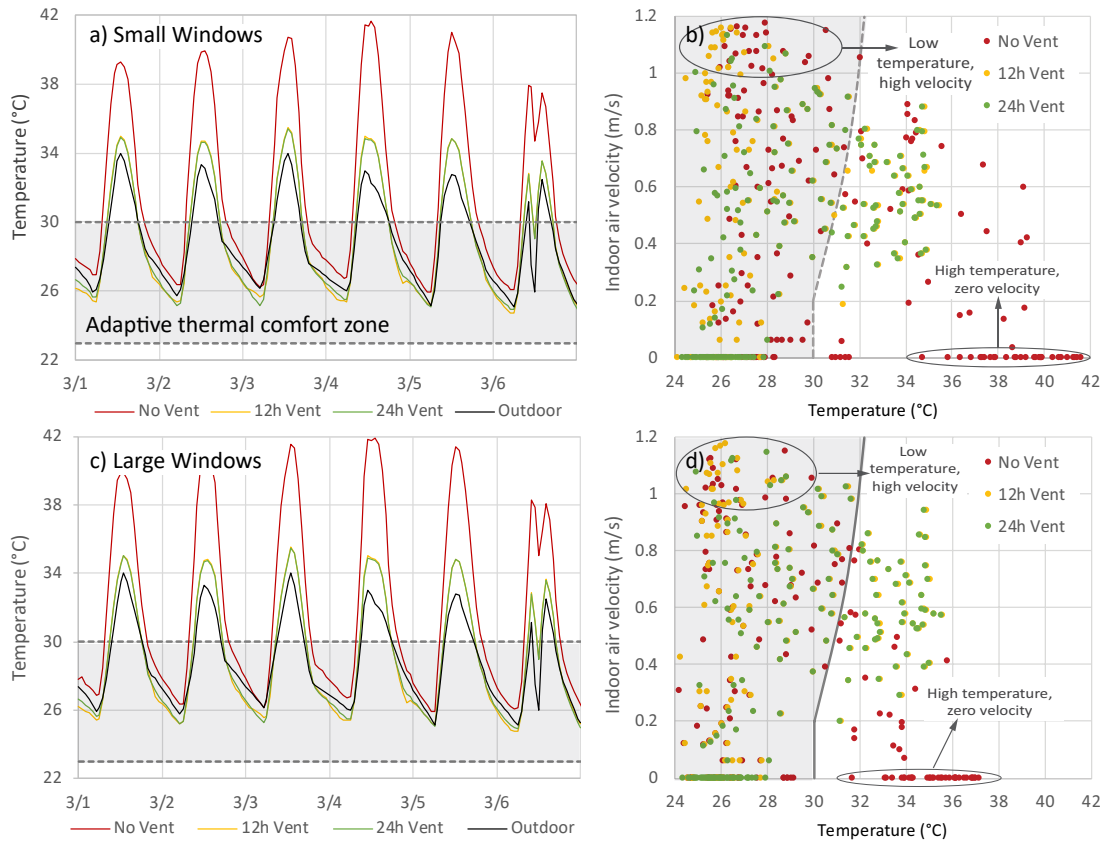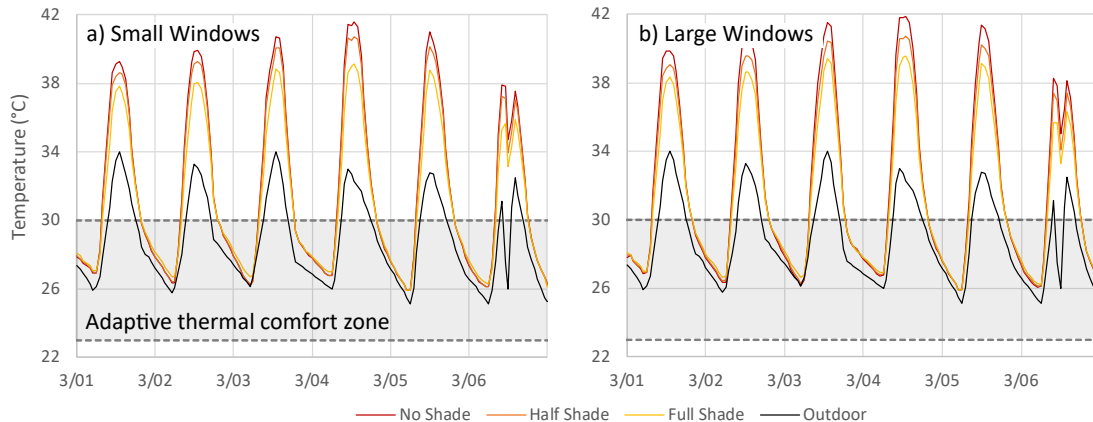
Figure 3. The predicted _____ natural ventilation alone on indoor operative temperatures and adaptive thermal comfort (shaded areas) over six representative March days in Accra, Ghana, for dwellings with small (a, b) and large (c, d) window _____ Vent":
"12h Vent": windows open 8am-8pm; "24h Vent": windows open at all times.

To reveal whether increased air velocity brought some of the warm hours into the velocity- expanded comfort zone (ASHRAE, 2017), air velocity was next plotted against operative temperature (Figs. 3b, d). "No Vent" models predicted considerable indoor air motion from infiltration; this was calculated as a function of pressure difference across each crack, which is a function of both temperature difference and wind pressure (USDOE, 2016), with the result that high indoor air temperatures drove considerable exfiltration (coinciding with calm indoor air, shown as pronounced rows of high-temperature, zero-velocity symbols (Fig. 3). Adding daytime ventilation ("12h Vent") replaced this hot-hour exfiltration with cooler air of considerably higher velocity, allowing thirteen hours with operative temperatures >30 °C to enter the velocity-expanded comfort zone over a six-day period, or ~2h per day. Adding all-day ventilation ("24h Vent") had little effect on daytime conditions, as expected, but diminished the bursts of infiltration-driven high air velocity that occurred during the coolest hours of the night in the previous two models, replacing them with steadier, lower-velocity air movement.

Shading. The cooling effect of shading alone was investigated by comparing a configuration with no shade at all ("No Shade") with two having external overhangs that shaded half or all of the south-facing wall at noon, including the entire south-facing window in both cases ("Half Shade" and "Full Shade", respectively). As expected, shading noticeably lowered indoor temperatures: while unshaded models reached peak operative temperatures of ~40°C on typical March days (Fig. 4), far beyond the thermal comfort range, half-shading reduced these peaks by 1-1.5°C, and full shading reduced them by 2-3°C, providing significant cooling given the un-

shaded, relatively conductive roof. Shading alone did not, however, bring additional hours into the adaptive comfort zone (Fig. 4), showing that further cooling measures would be necessary.

Figure 4. The predicted effect of shading alone (i.e. without natural ventilation, apart from infiltration) on indoor operative temperatures and adaptive thermal comfort (shaded areas) in six representative March days in Accra, Ghana, for dwellings with small (a) and large (b) window configurations. "No Shade": windows are unshaded at all times; "Half Shade": walls are half shaded at noon by exterior overhangs; "Full Shade": walls are fully shaded at noon by exterior overhangs.

Combinations. Since shading showed cooling ability independent of natural ventilation, combinations of "12h Vent" and "24h Vent" with "Half Shade" and "Full Shade" were next investigated. As expected, these out-performed each individual strategy, reducing peak operative temperatures by ~1°C each day in both small- and large-windowed models (Figs. 5a, c) and bringing them to within 1°C of the outside air temperature. They did not, however, cool additional hours below the 30°C threshold of the adaptive comfort zone; instead, additional cooling appeared confined to the warmest hours of the day. Furthermore, shading did not improve the ability of natural ventilation to bring additional hours into the comfort zone through air velocity; 12-14 warm hours were made comfortable by air movement regardless of shading level (Figs. 5b, d).

DISCUSSION

While building simulations are vulnerable to numerous sources of error, including algorithmic simplifications (USDOE, 2016), failure to capture occupant usage patterns accurately, etc., they are invaluable for revealing priorities for subsequent investigations. In this study, the modest effect of wall and window shading, combined with high heat gains through the roof, revealed the likely importance of ventilated attics that allow roofs to shade interior ceilings in such lightweight construction. Likewise, the ability of cross ventilation to expand the hours of adaptive comfort by two per day through increased air velocity suggests a valuable resource worthy of field investigation; thermal mass configurations were similarly shown to be in need of further study in this climate, with little diurnal temperature variation, given the nearly identical results generated by 12h and 24h ventilation patterns. Finally, any interdependence among intrinsic evaporative cooling, shading, and natural ventilation remains mysterious, although interaction is likely: a shaded wall is expected to evaporate less moisture, for example, while a naturally-ventilated interior might evaporate more.

CONCLUSIONS

Together, shading and natural ventilation, in the most effective combinations, lowered predicted indoor operative temperatures in the coconut-material study building from peak levels that exceeded outdoor temperatures by ~10°C to levels approximating outdoor temperatures.
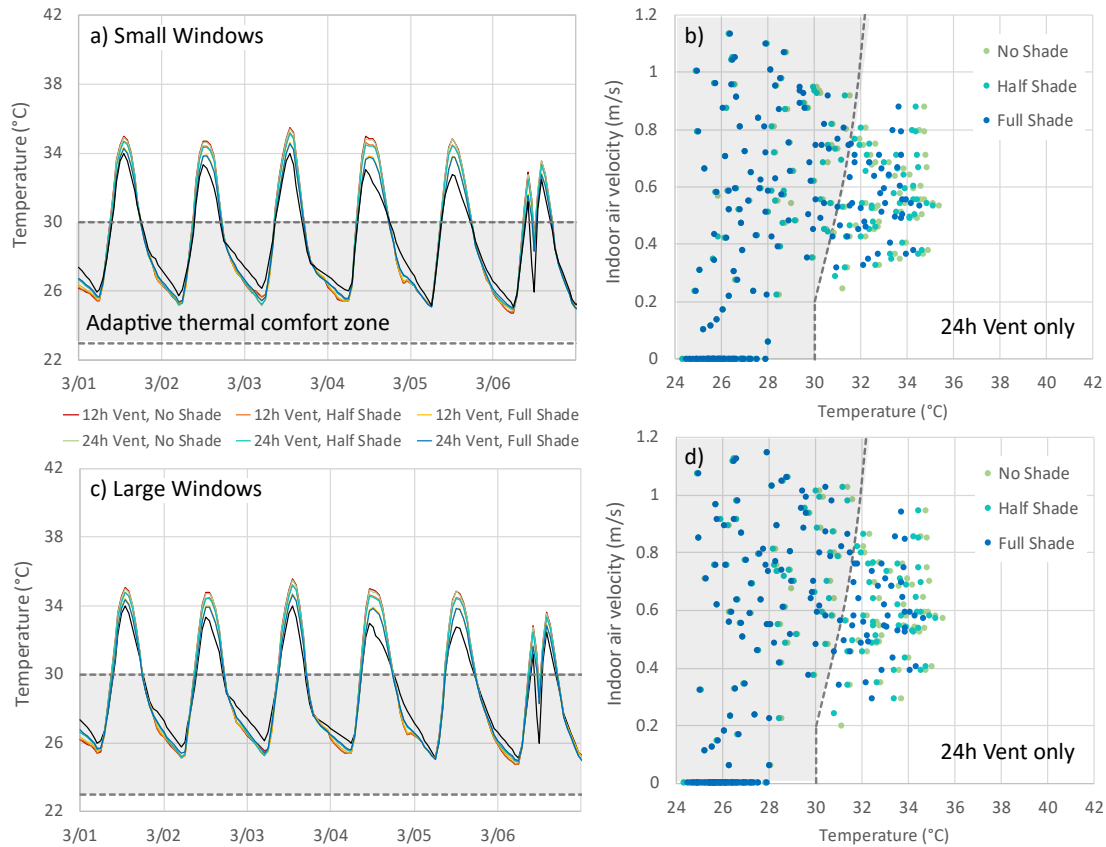
Figure 5. Predicted effects of combined shading and natural ventilation on adaptive thermal comfort (shaded) in March in Accra, Ghana, for dwellings with small (a, b) and large (c, d) window configurations. "No Shade": unshaded at all times; "Half Shade": walls half shaded at noon by exterior overhangs; "Full Shade": walls fully shaded at noon by exterior overhangs; "No Vent": infiltration only; "12h Vent": windows open 8am-8pm; "24h Vent": windows open at all times.

While further cooling is necessary for daytime comfort, this represents significant p rogress. The upcycling of local agricultural waste such as coconut husk into building materials has the potential to expand the economic value chain of coconut producers in tropical nations while producing low-embodied energy materials. Because of this, further investigations of their effective integration into buildings, allowing them to provide reliable thermal comfort without energy-intensive mechanical air conditioning, hold economic, environmental and social value.

REFERENCES

ASHRAE Standard 55. 2017. Thermal environmental conditions for human occupancy. Atlanta GA.

De Dear, R.J., Brager, G.S., Reardon, J. and Nicol, F., 1998. Developing an adaptive model of thermal comfort and preference/discussion. ASHRAE Transactions 104:145.

Lokko, M. 2016. Invention, design and performance of coconut agrowaste fiberboards for ecologically efficacious buildings (Ph.D. Thesis, Rensselaer Polytechnic Institute).

Rempel AR, Rempel AW. 2016. Intrinsic evaporative cooling by hygroscopic earth materials. Geosciences 6:1-38.

U.S. Dept. of Energy, 2016. EnergyPlus 8.7 Engineering Reference. Lawrence Berkeley National Laboratory.

Long term measurements and HAM modelling of an interior insulation solution for an office building in cold climate

Paul Klõšeiko[1,*], Targo Kalamees[1]

[1]Tallinn University of Technology, Estonia

[*]*Corresponding email: paul.kloseiko@ttu.ee*

ABSTRACT

Excessive mould damage was detected in an office building in Northern Europe and thus a renovation need was established. This paper studies a renovation solution using measurements and heat, air & moisture (HAM) modelling. Polyurethane (PUR) foam was used to fill the air gap in masonry while capillary active calcium silicate (CaSi) insulation was used on the interior surface at thermal bridges. During renovation works temperature and relative humidity (*t&RH*) and heat flux sensors were installed throughout the wall.

Nearly 3 years of measurements are presented. Average thermal transmittance (*U*) of the wall was reduced around 3 times. While the climate was probably not critical during the monitoring, the measured values stayed within hygrothermally safe limits.

The paper also compares the measurement data to 2D HAM modelling and discusses the discrepancies. Calibrated models were used to model the wall using real 42-year weather data and give a more thorough assessment of the hygrothermal performance. Although the original wall stayed fairly moist, no performance limits were exceeded and the interior surface became safer in terms of mould risk.

KEYWORDS
interior insulation, HAM modelling, capillary active, cold climate, case study

INTRODUCTION
Interior insulation has usually been disapproved in Northern Europe as a hygrothermally risky solution. However, "capillary active" insulation has gained ground in Central Europe and become a compelling choice by taking a different approach to mitigating the risks caused by insulation on the interior side (compared to traditional mineral wool + vapour barrier solution). This study took place on the last floor of an 8-storey office building (built in 1936; cultural heritage). Existing interior insulation (gypsum board, PE foil, min. wool) exhibited excessive mould damage and a renovation solution had to be found. Main challenges were: low surface temperatures, high thermal transmittance and avoidance of future biological decay. Preliminary HAM modelling showed that "closed cell" PUR foam injected into air cavities of the masonry and "capillary active" CaSi on the surface of the wall could perform well. This paper discusses the monitoring and modelling of the chosen solution.

METHODS
Measurement setup
Vertical and horizontal sections of the studied wall are given in Figure 1. The wall structure, renovation solution and sensor placement are also shown. Sensors and their positions were selected both to assess the hygrothermal situation after the insulation and to have enough reference points to calibrate the HAM models.

The following measurement devices were used: T&RH probes: Rotronic HygroClip HC2-C05 (accuracy ±0.3°C, ±1%RH); heat flux plates: Hukseflux HFP01 (accuracy ±5%); data logger Grant Squirrel SQ2020 1F8 (accuracy ±0.05% of readings ± 0.025% of range); temp. probes & logger: Onset Hobo UX120-006M & TMC6-HD (accuracy ±0.15°C); T&RH data loggers: Onset Hobo U12 and UX100 (accuracy ±0.21°C, ±2.5-3.5%RH). Measurement interval: 1h.
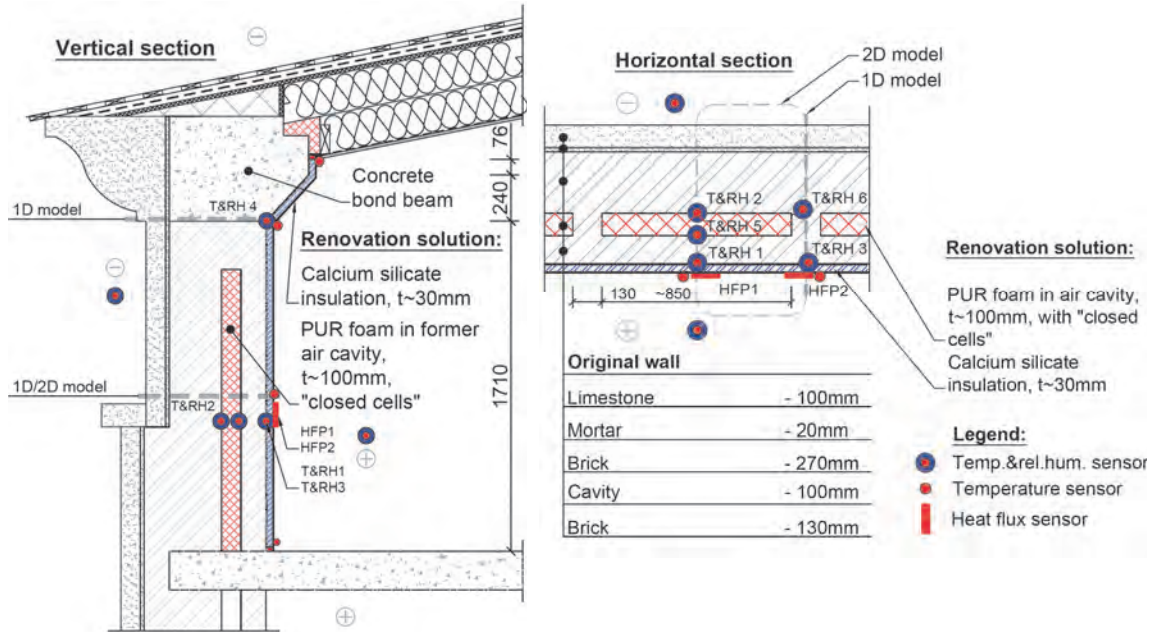

Figure 1. Vertical and horizontal sections of the wall showing sensor placement and wall layers.

Performance criteria
WTA Merkblatt 6-5 (Künzel et al. 2012) proposes to avoid frost and condensation in insulation and glue. Assessment according to saturation degree should be carried out – maximum of 30%$_{sat}$ is allowed to avoid frost damage. However, our previous research (Klõšeiko et al. 2017) showed that freeze-thaw cycling affected tensile strength of capillary active insulation material even though saturation degree stayed below the 30%$_{sat}$ limit. Therefore, slightly stricter limits of $RH_{crit.}$= 95 %$_{RH}$ and t_{crit} = -5 °C (Künzel 2011) are used in this study. Minimizing freeze-thaw cycles of the limestone cladding was not a criterion as conversion to ventilated façade is planned for the building.

Hygrothermal modelling
IBK Delphin 5.9.0 (Grunewald 1997; Nicolai et al. 2009) was used to model the hygrothermal performance of the exterior wall. Modelling consisted of 2 steps: 1) model calibration and 2) modelling with 42-year weather data. 1D and 2D models of the masonry section were created (while brickwork was treated as a homogenous material for both). Concrete bond beam was modelled as a 1D case. Model geometry is given in Figure 1.
During calibration, measured (t, RH (+ calculated vapour pressure), heat flux) and modelled data were compared. Then the HAM models were iteratively changed within plausible extents to achieve a better match between the two. Different bricks and concrete types from Delphin material database were tested (finally settling with ID 543 and 569 for brick and concrete respectively), PUR foam properties were fine-tuned according to limits given in its datasheet (based on ID 195; following changes were made: ρ = 39 kg/m³, μ = 39, λ = 0.022 W/(m·K)). Rest of the material IDs from Delphin database used in models were 464, 143, 424, 21, 230.

Boundary conditions for model calibration were: *t&RH* (measured on site); wind, rain (measured 10km away) and solar radiation (measured 165km away). 42-year weather data (*t*, *RH*, wind, rain, solar radiation; all measured 165km away) was used to assess the performance in more critical conditions. As the indoor humidity load in the test room was very low, more critical indoor *t* & moisture excess profiles were used for 42-year modelling (roughly moisture class 2 given in EN ISO 13788 Table/Figure A.2). They were based on an earlier study in a similar building (Klõšeiko & Kalamees 2016).

RESULTS & DISCUSSION
Measurement results
Temperatures behind CaSi (Figure 2 top, sensors TRH1, 3, 4) were closest to limits during the winter of the first year. At sensor TRH4 (concrete section) they fell to as low as -2.5°C, but not reaching the critical -5°C. In masonry section the temperatures were higher due to PUR insulation adding further thermal resistance. Consequently, sensors on the exterior side of PUR (TRH2 shown here) measured far lower temperatures than between CaSi and concrete bond beam. Figure 2 (bottom) gives the measured relative humidities. Dryout of the built-in moisture to stable levels took about 2.5…3 months. *RH* values between exterior brick leaf and PUR (sensor TRH2) were quite stable (fluctuating about 5%$_{RH}$ throughout the year) after the dryout of CaSi built-in moisture.
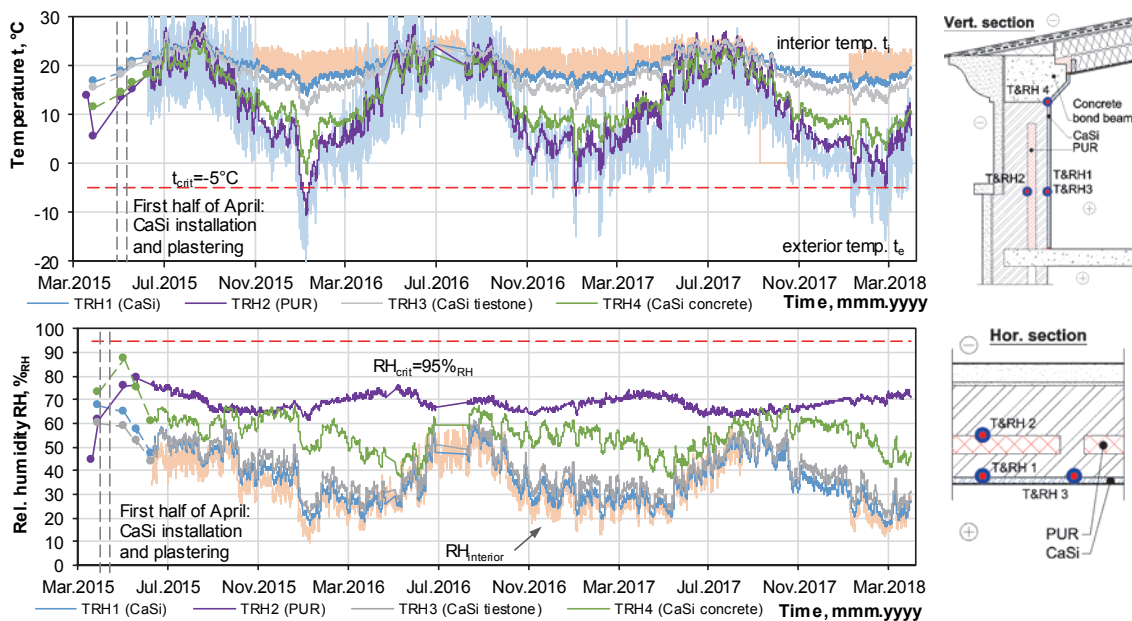
Figure 2. Measured temperatures (top) and relative humidities (bottom) throughout the monitoring period.

Moisture excess during the measurement period in the test room was very low (close to moisture class 1 according to EN-ISO 13788 A.2), as a well-functioning HVAC system was installed. Analysis of measured data hints that moisture contents of air in the pores of exterior masonry leaf are governed by outdoor climate while lagging about half a week. A ~ 4 g/m³ rise in moisture contents compared to indoor and outdoor air in autumn (mid-Aug...Oct.) is pronounced, possibly due to rain. However, moisture does not seem to be accumulating in the wall over time, which could be the case with vapour tight interior insulation and heavy wind

driven rain loads. Sensors behind CaSi insulation measured moisture contents quite close to that of the indoor air throughout the year. A lag of a couple of days was detected.

Temperature indexes (f_{Rsi}) were calculated from surface temperatures to assess mould and condensate risk on the wall surface. The worst situation was detected at wall-floor intersection (f_{Rsi} = 0.79) and at concrete bond beam (f_{Rsi} = 0.83). None of those results should indicate a risk, however, as indoor moisture load was low. f_{Rsi} values at the rest of the intersections were also considerably higher (i.e. safer).

Average heat flux and temperature data from 1. Nov. 2015... 29. Feb. 2016 was used to calculate the thermal transmittances (U) of the insulated wall (see Figure 1 for placement of the sensors). At tie bricks (HFP2) U = 0.52 W/(m²·K) was measured and between tie bricks (HFP1) the value was U = 0.31 W/(m²·K). 2D thermal transfer modelling of the insulated structure results in average thermal transmittance of U = 0.39 W/(m²·K), which is ~ 3-fold reduction compared to the uninsulated case (U = 1.14 W/(m²·K)).

Calibration of HAM models
Results from the models which achieved the best fit and positions that are most relevant to the assessment criteria are presented here. Figure 3 shows data from TRH2 (between CaSi and tie brick) and TRH4 (between CaSi concrete bond beam). Relative humidity is given as it integrates the errors in thermal and moisture calculations.

Agreement of calculated and measured temperatures (TRH3 2D model; TRH4 1D model) was within ±1°C for most of the year with overestimation of temperatures by 2…3°C taking place in summer (possibly due to deficiencies in solar modelling of the south facing wall). TRH3 1D model exhibits too low temperatures which results in higher than measured *RH*. Modelled *RH* values exhibit less fluctuation in all cases, however, that seems to be the characteristic of the Delphin program (Klõšeiko et al. 2015; Klõšeiko & Kalamees 2016; Klõšeiko et al. 2017). 24h avg. heat fluxes in masonry section achieved less than ±1 W/m² (~5…10%) difference for most of the heating period using 2D model; in case of 1D models, the errors were 4…8 times higher. Possible sources of errors could be: material data (limestone as location specific and inhomogeneous material; only basic parameters were measured for brick), unknowns concerning the actual wall structure, wind driven rain modelling, solar radiation modelling.
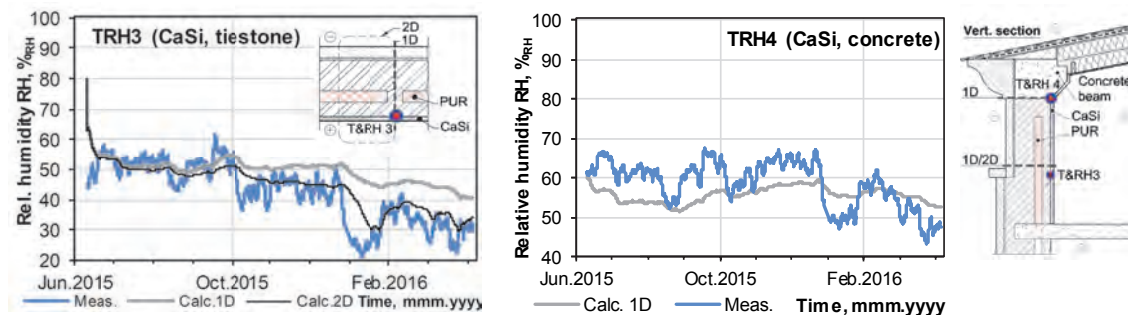

Figure 3. Comparison of measured and modelled relative humidities at TRH3 (between CaSi and tie brick; left) and TRH4 (CaSi insulation on top of concrete; right).

The correlation between measurements and modelling was deemed satisfactory. For performance assessment of CaSi insulation the 1D model of the masonry section might be good enough as the errors on that part were conservative. However, as wind driven rain could cause accumulation of moisture in the exterior masonry leaf, 2D model is also necessary.

Modelling with 42-year weather data

Due to limited space only the most critical point in the wall (TRH4 behind CaSi on concrete bond beam) is discussed here. Modelled $t\&RH$ values are given in Figure 4. Yearly minimum temperatures and maximum relative humidities are shown so the most critical year can be highlighted. In the case of TRH4, the 1986/1987 season was the harshest and is shown in Figure 4 (right). Yearly maximum relative humidities are much more stable than temperatures. "Flattening" the peaks of the RH graphs is possibly due to relatively high moisture capacity and redistribution of moisture in both concrete and CaSi.

Figure 4 also illustrates that 42-year modelled $t\&RH$ are far more critical than measured values. While lower t is largely the result of colder outdoor climate, the significantly higher modelled RH are caused by using higher indoor moisture load.

During 10 out of 42 years (~24%) t behind the insulation fell below critical -5°C. Still, RH was far below the 95%$_{RH}$ limit. Thus, according to the modelling data, frost damage in insulation system will not be a problem and the solution could be approved for use in the rest of the building. However, as previous research (Binder et al. 2013; Klõšeiko et al. 2017) has shown, the modelling results of "capillary active" materials can also be non-conservatively skewed, especially when higher moisture contents are concerned and values are closer to the performance limits. To overcome that, development of improved liquid and vapour conductivity curves for CaSi as well measurements of limestone and brick properties are in progress.
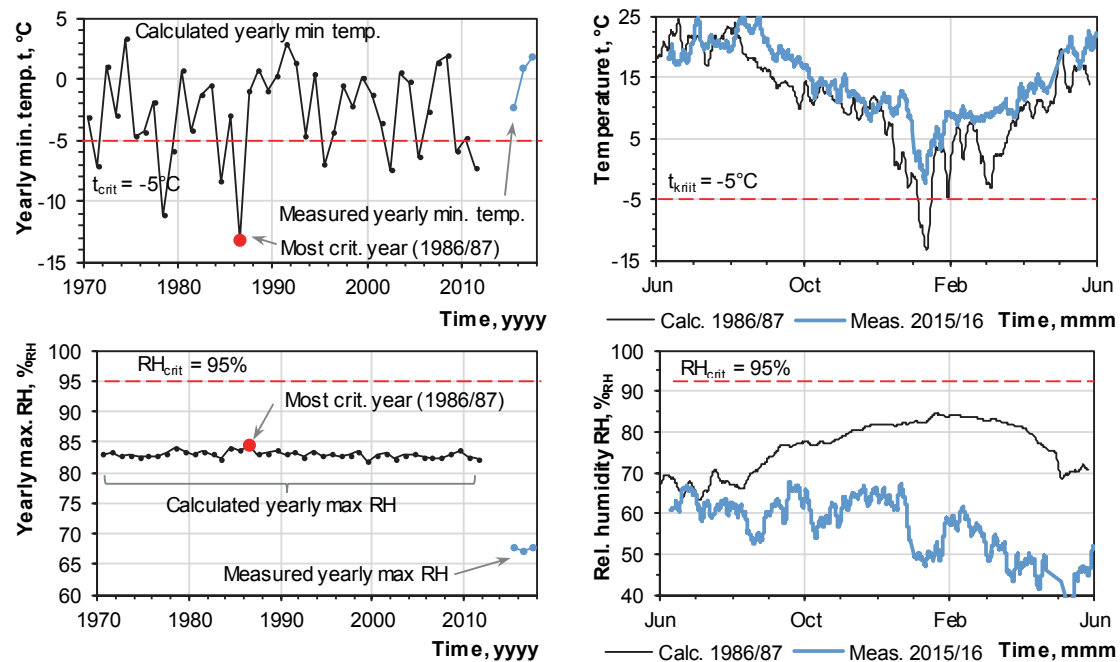

Figure 4. Most critical point in the wall (TRH4 – betw. CaSi insulation and concrete beam): yearly min. temperatures (top left) and max. rel. humidities (bottom left) of the 42-year HAM modelling and hourly values for the most critical year (right) compared to the measured values.

CONCLUSIONS

Measurements show that interior insulation can perform well at least if HVAC systems function nominally. Wind driven rain did not cause a notable accumulation of moisture on the exterior side of "vapour tight" PUR foam. Comparison of modelled and measured data shows that 2D modelling should be used for this type of structure. If interior insulation layers are thin, the HAM models can still fairly adequately portray the processes behind the insulation even if detailed material data for existing wall is unavailable.

Modelling results suggest that even in the case of increased moisture load, the CaSi boards are quite a robust solution and provide an extra layer of safety thanks to quite high moisture capacity and lack of biological decay. Modelling with long-term weather data gives an increased confidence in the results. For example, if test reference years are used, the principle of their selection might not always match that of the current modelling aim. Also, the measured data was far on non-conservative side compared to 42-year modelling results, partly due to current winters being quite mild. To test an experimental structure in more critical boundary conditions, modelling with historic data and calibrated model can be a viable option.

REFERENCES

Binder, A., Künzel, H.M. & Zirkelbach, D., 2013. A new approach to measure liquid transport in capillary active interior insulation. In *Proceedings of 2nd Central European Symposium on Building Physics*. Vienna.

Grunewald, J., 1997. *Diffusiver und konvektiver Stoff- und Energietransport in kapillarporösen Baustoffen*. TU Dresden.

Klõšeiko, P., Arumägi, E. & Kalamees, T., 2015. Hygrothermal performance of internally insulated brick wall in cold climate: A case study in a historical school building. *Journal of Building Physics*, 38(5), pp.444–464.

Klõšeiko, P. & Kalamees, T., 2016. Case study: In-situ testing and model calibration of interior insulation solution for an office building in cold climate. In *CESB 2016 - Central Europe Towards Sustainable Building 2016: Innovations for Sustainable Future*.

Klõšeiko, P., Varda, K. & Kalamees, T., 2017. Effect of freezing and thawing on the performance of "capillary active" insulation systems: a comparison of results from climate chamber study to HAM modelling. *Energy Procedia*, 132, pp.525–530.

Künzel, H. et al., 2012. Innendämmung nach WTA II: Nachweis von Innendämmsystemen mittels numerischer Berechnungsverfahren (Merkblatt 6-5).

Künzel, H.M., 2011. Bauphysik der Innendämmung und Bewertungsverfahren. In *1. Internationaler Innendämmkongress 2011*. Dresden: TU Dresden, pp. 9–16.

Nicolai, A. et al., 2009. An efficient numerical solution method and implementation for coupled heat, moisture and salt transport: The Delphin Simulation Program. In *Simulation of Time Dependent Degradation of Porous Materials*.

New Technology Creates New Lightscape

Jianzhen Qiu[1,2] and Shuoxian Wu[1,2]

[1]Dept. of Architecture,South China University of Technology.
[2]Key state Laboratory of Subtropical Building Sciences of China

[*]Corresponding email: jzqiu@scut.edu.cn

ABSTRACT

Light is a key element of our world's beauty. Chinese scholar Wu Shuoxian put forward the concept of "Lightscape", and proposed its research as a parallel discipline of the "Soundscape". As a special aspect of the visual-scape, lightscape can give us a comprehensive and multi-disciplinary perspective of living environment. Many traditional lightscape cases have always been remembered as the representations of specific regional cultures. This article presents several cases of modern lightscape created with new technologies and methods. Included in these cases are: outstanding lightscape and art installments created by artists using light as a key element and fulfilled with the help of new materials; preservation of nostalgia by transforming and flourishing the traditional lightscape; multidisciplinary cooperation where artists, scientists and engineers use digital technology and biology knowledge to create intriguing lightscape.

KEYWORDS
Lightscape Lighting technology creation

INTRODUCTION

The concept of lightscape, put forward by the Chinese scholar Wu Shuoxian as a special aspect of visual-scape, refers to the special visual-scape that utilizes light source, shadow and their transformations to form landscape and to invoke strong visual impression. We advocate it as a parallel discipline of "soundscape" and "smellscape", so that it can play an important role in inheriting human culture and creating a human habitation for a better living（Wu Shuoxian，2017）.

Since antiquity, the significance of light has gone beyond the practical level of delivering information. As a unique aspect of visual-spect, lightscape has specific records and meanings in various cultures. Historically, there was appreciation of the natural lightscape as well as the description of artificial light-based scenery. For instance, in China, the torch festival in minority areas is originated from primitive times ceremonies where the laboring people commemorated the harvest. The Lantern Festival, began at Han Dynasty, celebrates the first full moon night of the New Year. actually, the whole human-world has been creating wonderful lightscapes for thousands of years. This paper aims to tell that, with the help of new technology and its application, creative artificial lightscape will emerges constantly.

1. NEW LIGHTSCAPES AROUND THE WORLD
Human's beauty-love instinct is global. Civilization has been given new connotation by the developing science. Wonderful lightscape works supported by new technologies amaze people all over the world.

Fig.1 Light Show, Giza, Egypt
picture taken from：
http://www.nipic.com

1.1 Breathtaking light shows

There are light shows coming forward in well-known cities and famous scenic spots around the world. Compared to traditional performance, those emphasize more on the combination of light, shadow and other medias, with the addition of various means including music and installation art, to give a comprehensive sensory experience to live audiences.

Light and Sound Show of the Pyramids The Light and Sound Show in the Giza region, Egypt, uses dramatic narration means to present the tales of pyramids, the sphinx and influential persons. During the show, lasers are projected on the pyramids to form the shapes of inner structures, along with explanations. Accompanied by a mysterious voice that seems to come from ancient times, lights are cast on the pyramids making diversiform shadows. This hour-long show tells the story of ancient pharaohs in such a vivid way, that the audiences indulge in it as if they have taken an journey through the time.

Dame de C œur of Notre-Dame De Paris To mark the centenary of the end of the first world war, Notre-Dame De Paris dedicated the "Dame DE Coeur" 3D sound and light show directed by Bruno Seillier in November 11, 2017. In virtue of the touching story of a soldier and a nurse, history had a dialogue with art across the time. The magnificent and eye-dazzling 850-year-old Notre Dame cathedral was granted a full-bodied sense of technology. The frontal lines, the sculptures on the exterior wall and projections were fused with each other. Classic paintings joint performance of firework were all exhibited in 3D perspective.

Fig.2 light show, Notre-Dame De Paris,

Fig.3 Artwork, Guggenheim Museum Bilbao
picture taken from：
https://www.theguardian.com

Artwork of Guggenheim Museum Bilbao On October 2017, Guggenheim Museum Bilbao created a 20-minute public artwork for the 20th anniversary of Frank Gehry's architectural masterpiece in Spain. This artwork combining light, music and projection were played on a loop across four evenings. 59 Productions, the world leader in projection-mapping, was commissioned to produce a 20-minute public artwork called Reflections. This special anniversary program celebrated the role this museum has been playing in making Bilbao and the Basque region a thriving artistic centre.

1.2 Famous light festivals around the world

Lyon Festival of Lights The Lyon Festival of Lights, held on December and usually lasts for four days, is a centuries-old religious tradition where people use candlelight to express gratitude toward gods.

Today, the festival does still retain the art form of candlelight: every house still places candles along the outsides of all the windows to produce the spectacular ambience throughout the streets; a romantic candle show is held in Odeon of Lyon every year. On the other hand, it also integrates modern lightscape that sparkles in this old city: there are contemporary lighting artworks in the center and dozens of other places on the periphery, where sound, light, electricity, lasers and 3D special effects are widely used. The whole city is checkered with light and shades, attracting artists from France and all over the globe to show their talent here. Among pieces of

Fig.4 Lyon Festival of Lights
picture taken from：
http://www.sohu.com

art equipment, we can find some amazing works of traditional culture, such as the elegant colored drawing LUMIÈRE DE VERRE, Homer's epic Odysseus, were expressed using modern techniques. A astonishing and modern light and sound show is staged annually in the front of the gothic cathedral Saint-Jean Baptisete.

In Lyon, traditional and modern lightscape coexist ideally in harmony.

Vivid Sydney Light Festival Vivid Sydney light festival, started in 2009 as the smart light festival which promoted energy conservation , has become a famous stage for universal creativity competition. During the 3 weeks from May to mid-June every year, there are tens to hundreds of exhibitions and events, including lighting sculpture, multimedia interactive works, as well as the show of water, fog, light and shadow. Most astonishing among those are the projections of landmark, including the eye-catching super light show of Sydney Opera. In Vivid Sydney, the public are guided to communicate and have a discussion on art, where they have sufficient chances to interact with unique lighting technology.

Fig.5 light show, Sydney opera, Vivid Sydney
picture taken from：
http://www.poco.cn

So much unprecedented lightscape has been created thanks to technology development; in correspondence, unique lightscape also shortens the distance between those technologies and human.

2. NEW LIGHTSCAPES IN CHINA

As China grows in economy, science and technology, there have been many high-profile events held in China in recent years, including G20, Fortune Global Forum 2017 and other worldwide theme activities. Guangzhou International Light Festival has been held annually for 7 years, and in 2015 was selected to International Year of Light large-scale cultural event by UNESCO(United Nations Educational, Scientific and Cultural Organization), with a special recommendation on the website of International Year of Light.

2.1 Group of 20，2016，Hangzhou, China.

On October 2016, Hangzhou city undertook the G20 conference. Hangzhou, located in East China, is the most beautiful landscape city of China with the world-renowned west lake scenic spot. Zhang Yimou, the chief director of the opening ceremony of 2008 Beijing Olympic Games, directed a overwater artistic performance "Enduring Memories of Hangzhou" for G20, in which the application and effect of high-tech light and shadow was unprecedented. With the stage set 3cm under water, the traditional atmosphere "glistening wave and reflective water" of Chinese gardens was best portrayed. The show used the Pepper's ghost holographic projection technology to integrate images into the show harmoniously, where the performers were even able to interact with the lights. It was hard to tell the authenticity of bridges, lotus pond and pavilions in the view of natural lake, trees and mountain; the combination of light, music, scenery and performances brought audiences into the wonderland of Chinese classical landscape beauty.

Swan Lake ballet on water On the west lake, graceful dancers performed the classic ballet Swan Lake while shuttling through the milky way of an ancient bridge. This program uses holographic projection where real actors and virtual images interacted and completed the performance together. One of the most breath-taking scenes was: under the arched light bridge between landscape, a little swan appeared gracefully. After

Fig.6 Swan Lake ballet on water
picture taken from：
http://www.wekeywu.com

several challenging rotations, it split into 2 little swan, then 4, then 8... Suddenly, a group of swan girls magically appeared, and danced lightly, unanimously and gorgeously.

Piano playing 〝Clair de lune〞 Moonlight has always been an important part of the west lake scenery, evidenced by the natural lightscapes "Autumn Moon over the Calm Lake" and "Three Pools Mirroring the Moon". The performance combined the moonlight with the piano piece" Clair de lune",one of the most well-known works by French composer Debussy. When the smooth and stretched music was played craftily by the pianist, LED lights shaped the poetic hazy background atmosphere. The holographic projection of the moon entwined with the reflection of the moon in the water, coupled with the distant picturesque nightscape, composed a modern view of the west lake lunarscape.

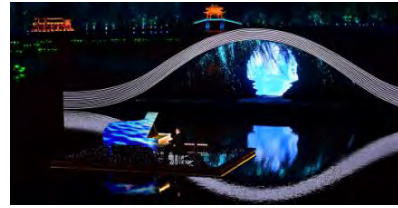Fig.7 Piano playing ”Clair de lune” picture taken from：http://www.xinhuanet.com

Play "A Beautiful Love Story" "The Butterfly Lovers" is one of the four folk love story in ancient China, which tells the tragedy of a pair of young lovers who fell in love with each other but could not stay together, and reputedly they turned into two concomitant butterflies in their deaths. The play "A Beautiful Love Story" is based on this myth. On the performance, when two dancers danced to the waves like two chromatic butterflies flying to the center of the stage, a huge fans was slowly unfolded from the surface of water. Then, patterns on the fan transforms continually between various elements of traditional Chinese realistic painting including peony, orchid, peacock, blue and white porcelain, landscape and human characters. As the story continues, the face rotated tridimensionally following the rhythm of music until the last note gradually faded away. Finally, the giant fan submerged into the water and the lake returned to calmness.

The fan is a traditional Chinese handicraft as well as a special local product in Hangzhou. This special mechanical folding fan, believed to govern a representative temperament of Hangzhou, measures up to 20m in diameter with a total weight of 20 tons. When spread out, the fan becomes a upright screen for well-designed 3D video to project on using 3D mapping. When it is furled, it is hidden underwater. The opening and closing of the fan have achieved precise synchronization with the live music, the video projection and dance tempo of the dancers in the performance.

Fig.8 play,"A Beautiful Love Story" picture taken from : http://www.wekeywu.com

2.2. Guangzhou International Lighting Festival

Guangzhou is a diversified southern metropolis. Over 2200 years of history blesses it with a deep traditional culture as well as opening, innovative and inclusive temper.

Beginning in 2011, at the end of every year, the Guangzhou International Lighting Festival is held at Flower City Square on the "new city axis of Guangzhou". The festival revolve around different themes each year and each has its own merits; for example, in 2015, representatives from Lyon, Sydney and Singapore were invited to communicate in present, and the 3D projection work "Illusion", which had shined on Vivid Sydney, was on display, while "People Screen" connected Perth in Australia with Guangzhou via internet.

The lighting festival has now become a tourist interest in Guangzhou. The 2017 Guangzhou Lighting Festival lasted for 24 day, had served more than 8 million people; moreover, the original artwork "Rain Beating Plantain" will visit Guangzhou's sister city Lyon for its lighting festival.

3D Print Work: Butterfly-changing Canton, 2016

The annotation of metamorphosis in Chinese represents a striking change towards perfection, similar to the rapid transformation of a pupa into an butterfly. At the main venue of 2016 Guangzhou International Light Festival, two gaudily-dressed "butterflies" perched on the side pool of Guangzhou Grand Theatre, contrasting with the streamlined main building of the very

Fig.9 The Butterfly-changing Canton, picture taken from：http://itbbs.pconline.com.cn

dynamic Theatre. To demonstrate the connotation of another butterfly-changing of Guangzhou city as the capital of commerce for thousands years. This work is actually an experiment in the field of architecture, as a bold attempt combining 3D printing technology and architectural digital design. The big "butterfly" span up to 6.6m and is 12 meters long, with only two supporting points, but the body part is only 3.8 cm thick. Its irregular hyperbolic form and texture are like the microscopic veins of the leaves. The entire set of the thin shell weighs 500 kg and was assembled from nearly a thousand units printed by 50 3D printers.

"Rain Beating Plantain", 2017 Canton music is one of the traditional Chinese local musics, and "Rain Beating Plantain" is the most representative and well known. Plantain, also known as Chinese banana, is a common native plant in Guangdong. 《The artistic lightscape installation "Rain Beating Plantain" involves environmental elements that frequently appear in Canton music such as plantain, moonlight, mini bridges, lotus leaves and colorful cloud, with the virtual rain scene to strengthen austral atmosphere, all created with light. The main artwork is formed with LED light source; the light outlines shape of plantain leaves and their venation. The moon in the background is made up of LED light pixels, which projects changeable clouds, and the luminance changes

following the rhythm of the background music. As a gesture of friendly communication, this lightscape artwork is going to attend the festival of Lyon. There will be interactive factors added at the time, making the production more interesting.
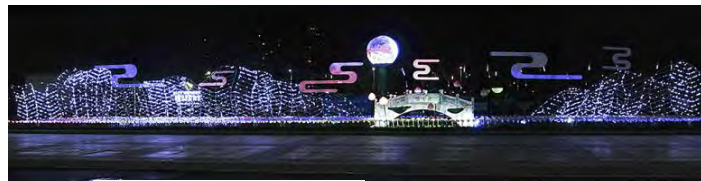

Fig.10 "Rain Beating Plantain" picture taken from：https://mp.weixin.qq.com

2.3 Fortune Global Forum 2017, Guangzhou, China.

 Fortune Global Forum is one of the most influential financial forums in the world, and the vibrant city Guangzhou was chosen to host it in 2017. More than 1000 business leaders, politician and economists attended.

Drone Formation Performance In the evening of December 7th, a welcome cocktail party was held in Canton Tower, while 1180 unmanned aerial vehicles flew over the Pearl River, performing a 8 minute technological dance. First, the drones formed the Chinese character "财富", which means "Fortune", and then changed to "FGF". Then, the formation transformed into different patterns, in the order of ship(Since Guangzhou is an old port city), the Chinese character "开放", "创新" which means correspondingly "open" and "innovation", English letters "I LOVE GZ", and last but not least the map of China, which marked the end of the show. Only 1 computer was needed to control the total of 1180 flying drones, and the error tolerance of precise positioning was 2cm. The lighting sets carried on the drones can create 60 thousand kinds of color, and change intensity as freely as

Fig.11 the drones formed the Chinese character "财富"
 picture taken from: http://gd.people.com.cn

breathing lights, which means designers can construct almost any pattern as they wish.

River Bank Animation Show Guangzhou is close to the South China Sea. It has been the departure port of Ancient Maritime Silk Road, and was the only port open to the oversea merchants in Qing dynasty. As the Pearl River flows from west to east across the urban area of the city, the beautiful scenery on both sides is an important tourist resource of this city with intriguing history and culture.

Fig.12 the map of China
picture taken
from：.http://news.sina.com.cn

During the 2017 Fortune Global Forum, guests took a cruise along the "Pearl River Night Tour" route to enjoy the lightscape animation that was shown on continuous facades of the 24 buildings on the north shore. The animation called "Stories of Guangzhou" is ten minutes long, divided into two parts. The first part, called "Southland Pearl, Thousand Years", depicts the prosperity of the ancient "Maritime Silk Road"; the second part, called "Amorous City of Lingnan" ,shows the traditional culture of porcelain, jade, tea culture, spices, embroidery, food culture, as well as characteristic Lingnan elements such as gardens, fruits, kapok, carp and lotus pond. This work utilized 210 thousand efficient LED lamps, which were coordinately controlled on the big data platform. The installation lasted for four months, involved the cooperation of as many as 1500 construction workers, including 500 steeplejacks.

Fig.13 carps play in the water
picture taken
from：http://s.dianping.com

EPILOGUE

This paper shows some light-works closely related to our life. Modern scientific and technological means can both create unprecedented lightscape and give traditional lightscape vitality, enabling its survival and further development. We wish, with the support of modern technology, designers would use more lightscape, soundscape, smellscape, and allow their combination with other forms of art, and more brilliant buildings, gardens and cities would turn up.

REFERENCES

Dame de Cœur. [EB/OL].

Fortune Global Forum 2017, Guangzhou. [EB/OL]. (in Chinese).

Guangzhou International Lighting Festival. [EB/OL]. (in Chinese).

Guggenheim Bilbao's 20th anniversary light show. [EB/OL].

Lyon's festival of lights. [EB/OL].

Qiu Jianzhen and Wu Shuoxian, Lightscape and Architecture, Architectural Journal, 2017, 09, No.588,115-118(in Chinese).

R. Murray Schafer. Our Sonic Environment and the Turning of the World: The Soundscape [M], Destiny Books Rochester Vemont, 1994.

Su Chaohao, Lin Kangqiang, Cui Yang, Sun Bin. "Butterfly-changing": A Visual Feast Combining Power and Beauty Presented by 3D Printing Technology[J].Southern Architecture,2018(02):120-125.

Vivid Sydney. [EB/OL].

Wang Xiaoyi. Deciphering the Performance for G20 by Zhang yimou: Tell the world some wonderful stories about China. (in Chinese). [EB/OL].

Wu Shuoxian, Main points of lightscape, South Architecture, 2017,03, No.179,4-6(in Chinese).

Optical Performance of Polycarbonate Multi-Wall Panels in the form of Transparent Insulation Based on Long-Term Outdoor Measurements

Miroslav Čekon [1, *]

[1]Brno University of Technology, Brno, Czechia

[*]*Corresponding email: cekon.m@fce.vutbr.cz*

ABSTRACT

Buildings are subject to strongly time variable solar radiation impacts, which are phenomena that typically occur at a characteristic timescale resolution. Recent technologies and advances which are currently being used to produce polycarbonate-based materials may be used in applications where it is useful to activate the solar transmittance functions of building envelopes. In general, systems utilizing polycarbonate as a type of transparent insulation material exhibit the thermal performance of standard glazing systems. This study is focused on the optical characterization of several polycarbonate panels for buildings that are based on different numbers of chambers and differing geometries. The optical performance was analyzed in order to monitor the long-term solar properties of polycarbonate panels, by means of outdoor measurements in order to demonstrate the impact of year-round aspects on solar transmittance. This represented a specific methodical approach incorporating real full-scale components. Finally, the solar transmittance is evaluated with regard to the various outdoor time scales (hourly/daily, monthly and year-round). The studied multi-wall polycarbonate panels indicate that they may have very specific characterization from the solar transmittance perspective regarding the solar radiation that penetrates throughout their internal structure. The solar transmittance of polycarbonates, to which the timescales of the outdoor conditions respond, may significantly vary. Overall, the differences in total solar transmittance for laboratory, declared and outdoor test methods are very obvious; they differ by tens of percent. The study provides an initial insight into the optical behaviour of polycarbonate multi-wall panels and a very large set of data in order to make careful use of these parameters concerning their specificity and time dependent characteristics in thermal analysis of building integration.

KEYWORDS

Transparent insulation, Polycarbonate system, Outdoor testing, Solar transmittance

INTRODUCTION

Transparent Insulation Materials (TIMs) (Kaushika and Sumathy 2003) have the potential to be predominantly used in current concepts that are being put forward in an attempt to replace conventional insulating materials. However, their involvement in the building envelope is specific and so their application in building practice is currently rather rare. Several early studies described the benefits, disadvantages and options for the application of TIMs in the 1990´s (e.g. Braun et al. 1992). Nevertheless, they are generally too expensive, though many cheaper materials have been diffusing such as polycarbonate sheets and panels. This represents one approach involving TIMs, which may be applied either directly as a transparent part of the building envelope, or as a part of potential solar façade concepts to obtain both transparency and thermal insulation. Various types have already been developed with different numbers of chambers and differing geometries. This development is specifically concerned with improvements from the thermal aspect. Furthermore, there could be potential in the development of polycarbonates regarding their optimal optical performance and

selective properties. Hence it is necessary to analyze in detail data for the materials which are already available, and their optical variation needs to be investigated from the spectral, angular and real outdoor perspectives. A variety of studies have been produced concerning different transparent glazing systems (e.g. Juráš et al. 2017), although some early studies aimed at measuring solar transmittance were performed on various honeycomb-type structures with an indoor solar simulator more than 25 years ago (Platzer 1992). In this relation, outdoor measurements using the sun as the source might be a good option. Overall, apart from Čekon et al (2017), there is a lack of information regarding real outdoor test in the literature dealing with solar transmittance measurements. Nevertheless, this may represent a very simple yet highly feasible way of measuring the total solar transmittance at a particular site, though Platzer (1992) pointed out that it is not an acceptable approach for Central European climates. Fundamental principles are already well implemented in the standard method of testing the solar transmittance of sheet materials using sunlight with detailed specification and procedures stated in ASTM (2015). In this relation, the key aim of this study is to investigate the optical performance of polycarbonate components that are primarily based upon multi-wall systems via real outdoor measurements. Based on the large quantity data obtained during long-term measurements, the aim of this study is to summarize these data with regard to their specificity and to provide time dependent characteristics.

MATERIALS AND METHODS

Three different polycarbonate systems were analyzed at the year-round scale. Table 1 shows all the measured components (PC10, PC25 and PC32) and their properties. The main difference between them lies in their overall thickness and the structure of their internal chambers. The analysis employs long-term measurements performed on vertical south-east (SE) oriented full-scale components located at the AdMaS centre operated by Brno University of Technology (Čekon et al. 2016) (longitude 16°34′, latitude 49°14′, altitude 297.23 m). Although there are many specific issues to take into account, such as inclined angular dependence, fluctuations of solar irradiation and overall solar distribution as well as cardinal point aspect, the estimation of solar transmittance via real outdoor measurements following ASTM (2015) principles was employed. This main objective is achieved via the analysis of optical performance studies carried out at different time-scale levels. The solar transmittance is then evaluated over various outdoor timescales (hourly/daily, monthly and year-round) and a comparison with values declared by the producers is provided as well.

Table 1. Description and key parameters of polycarbonate systems

	Type	Thickness [mm]	Declared T_{decl} [-]	τ_λ * ASTM G 173	Measured** ASTM E1084-86	Geometry
PC10	Clear 2walls	10	0.82	0.74	0.63	
PC10*	PC10 + prismatic glass	10+5	n/a	n/a	0.57	
PC25	Clear 3walls /diagonals	25	0.63	0.48	0.54	
PC32	Clear 6walls combined	32	0.53	0.43	0.53	

* obtained based on Čekon et al. (2017b); ** averaged values measured over 2017

Two photodiode elements were mounted in the air cavity behind each polycarbonate sample and a third additional element was left exposed to outdoor conditions. A commercial Star Pyranometer FLA 628 S was additionally used for photodiode comparison and accuracy correlations. Diode error depends on many factors and could not be directly determined. Based on the data obtained during diode circuit calibration procedures, the maximum error could be estimated at less than +/-10% of the measured value. However, a detailed analysis was conducted in relation to the measurement of solar radiant flux using a photodiode (Čekon et al 2016), its optimization and the estimation of its correction factor during measurements

(Slávik and Čekon, 2016). Finally, the ratio between the two solar intensity rates obtained by the silicon pin photodiodes represents the solar transmittance values.

RESULTS
As the focus on the long-term monitoring of real full-scale components is to demonstrate the annual progress of the total solar transmittance and passive solar gains of multi-wall panels, the fundamental principles of a standard test method an extraordinary mode was used. This section presents results from different timescales that depend for the purpose of evaluation on variables corresponding to hourly/daily, monthly and year-round progressions.

Hourly/daily-based timescale
The results presented in Figure 1 and 2 cover two different measurement days during which clear sunny and total cloud cover conditions prevailed. This corresponds to a combined hourly/diurnal time scale, where the detailed influence of polycarbonate structure can be observed. For the clear sunny period shown in Figure 1a, the results are strongly hourly sensitive due to the non-homogeneity of the tested polycarbonate systems and their internal structure (Figure 1b). This factor is demonstrated by the continuous variation in solar transmittance by several tens of percent resulting in a presence of multiple internal reflection of the incoming direct beam radiation distributed over a large-scale area towards the measurement sensor. The overall inhomogeneity and sun incident angle effect, occurring in both the parallel and perpendicular partitions over each tested structure, involve strong uniformly throughout the materials. On the other hand, very stable progressions are observed during overcast conditions (Figure 2a). For both test periods, the higher the maximum level of solar intensity, the higher the daily solar transmittance obtained.

a)   b)
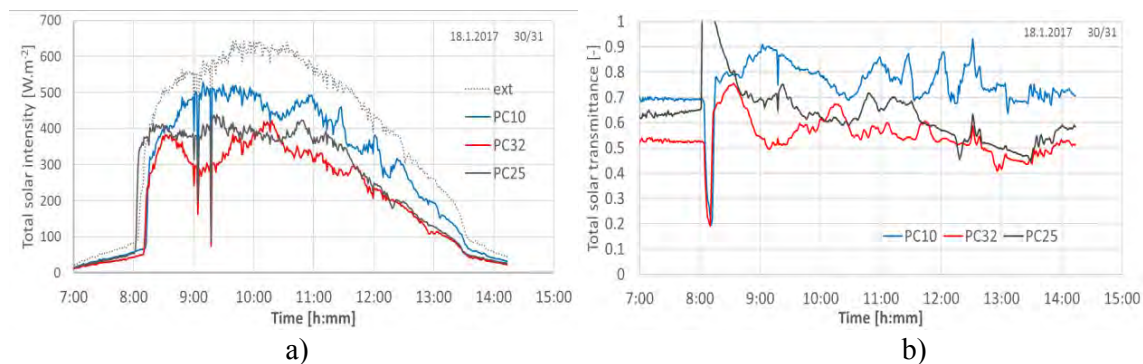
Figure 1. Measurements taken at an hourly/diurnal timescale under clear sky conditions; a) solar radiation rates measured; b) total solar transmittance derived.

a)   b)
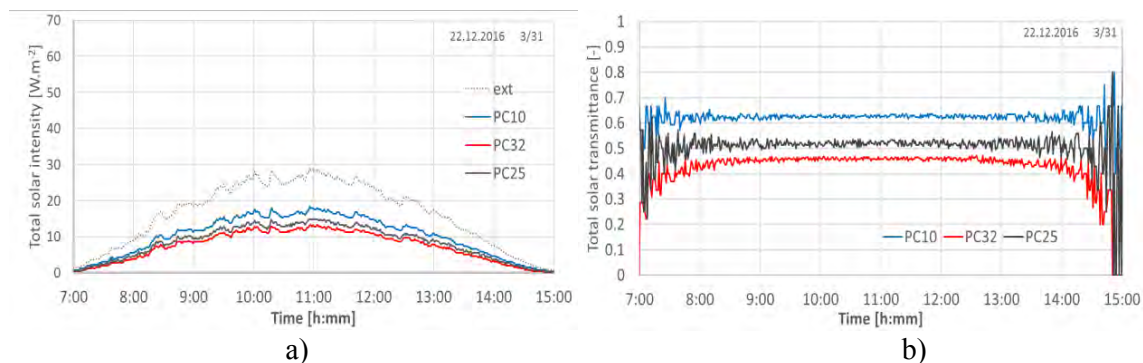
Figure 2. Measurements taken at an hourly diurnal timescale under total cloud cover; a) solar radiation rates measured; b) total solar transmittance derived.

Monthly-based timescale

The results shown in Figure 3 are an example of monthly-based result evaluation that is dependent on solar intensity rates and the relation with the angle of incidence of the sun above the horizon (altitude α). Outdoor solar intensities greater than $60W/m^2$ obtained at the vertical level of test samples are included starting at 135° from the north azimuth. The results are presented using point clouds. Linear tendencies are indicated so as to generalize these strongly time variable and numerous data. In this regard, resultant linear relation is derived, and the monthly dependencies shown in Table 2 are provided for each PC panel. It should be noted that the linear functions do not represent the measured values adequately as this is first preview gained from the analyzed data; in the case of this study it provides an initial insight.
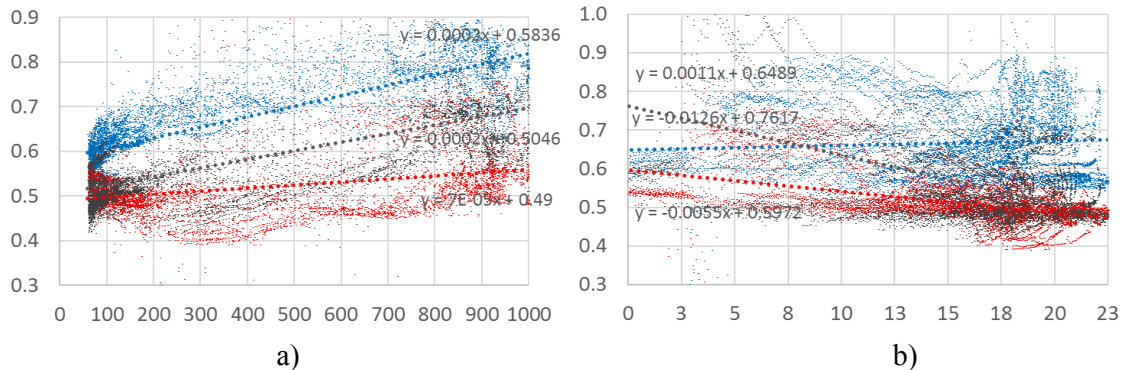

a)

b)

Figure 3. An example of measurements taken at a monthly-based timescale: a) the relation to the amount of total vertical solar radiation, b) the relation to the angle of incidence of the sun.

Table 2. Linear tendencies of monthly-based relations depending on solar intensity rates

2017	JANUARY	FEBRUARY	MARCH	APRIL	MAY	JUNE
max α	17° - 22°	22° - 31°	31° - 44°	44° - 54°	54° - 61°	61° - 64°
PC10	$2E\text{-}4{\cdot}I + 0.58$	$7E\text{-}5{\cdot}I + 0.60$	$7E\text{-}5{\cdot}I + 0.60$	$8E\text{-}5{\cdot}I + 0.61$	$9E\text{-}6{\cdot}I + 0.62$	$9E\text{-}5{\cdot}I + 0.51^*$
PC25	$2E\text{-}4{\cdot}I + 0.50$	$1E\text{-}4{\cdot}I + 0.50$	$1E\text{-}4{\cdot}I + 0.50$	$8E\text{-}5{\cdot}I + 0.54$	$-7E\text{-}6{\cdot}I + 0.56$	$-4E\text{-}5{\cdot}I + 0.55$
PC32	$7E\text{-}5{\cdot}I + 0.49$	$2E\text{-}5{\cdot}I + 0.50$	$2E\text{-}5{\cdot}I + 0.50$	$2E\text{-}5{\cdot}I + 0.50$	$-2E\text{-}5{\cdot}I + 0.51$	$-6E\text{-}5{\cdot}I + 0.53$
2017	JULY	AUGUST	SEPTEMBER	OCTOBER	NOVEMBER	DECEMBER
max α	64° - 59°	59° - 49°	49° - 37°	37° - 26°	26° - 18°	18° - 17°
PC10*	$9E\text{-}6{\cdot}I + 0.55^*$	$7E\text{-}5{\cdot}I + 0.55^*$	$7E\text{-}5{\cdot}I + 0.56^*$	$7E\text{-}5{\cdot}I + 0.55^*$	$2E\text{-}4{\cdot}I + 0.54^*$	$2E\text{-}4{\cdot}I + 0.54^*$
PC25	$-9E\text{-}5{\cdot}I + 0.57$	$-2E\text{-}5{\cdot}I + 0.56$	$4E\text{-}5{\cdot}I + 0.55$	$4E\text{-}5{\cdot}I + 0.57$	$1E\text{-}4{\cdot}I + 0.56$	$8E\text{-}5{\cdot}I + 0.57$
PC32	$-1E\text{-}4{\cdot}I + 0.57$	$-6E\text{-}5{\cdot}I + 0.56$	$-6E\text{-}5{\cdot}I + 0.57$	$-6E\text{-}5{\cdot}I + 0.56$	$-6E\text{-}5{\cdot}I + 0.58$	$-4E\text{-}5{\cdot}I + 0.57$

* Sample PC10 coupled with prismatic glass

Year-round time scale

Similarly, in Figure 4 and 5, year-round progressions are interpreted based on the same visualizations, and again linear relations are derived for each polycarbonate panel. The data obtained during year-round monitoring are divided into two presented periods. One corresponds to the first half of the year, and the other to the second half; during these two periods the maximum midday height of the sun above the horizon ranged from 17° to 61° and from 64° to 17°, respectively. In both periods, not surprisingly due to the angular aspects involved, the solar transmittance decreased with higher angles of incidence of the sun (see Figure 4). If Figure 5 is studied in detail, one can observe some angular selective functions of panel PC32 as well as PC10 combined with prismatic glass (PC10*). In contrast, the solar transmittance increases with increasing solar intensity rates, and vice versa, a trend that really corresponds to the height of the sun above the horizon during the whole year. This means that the differences in the behavior of the full-scale samples in relation to solar conditions become higher with increasing solar intensity, and vice versa.
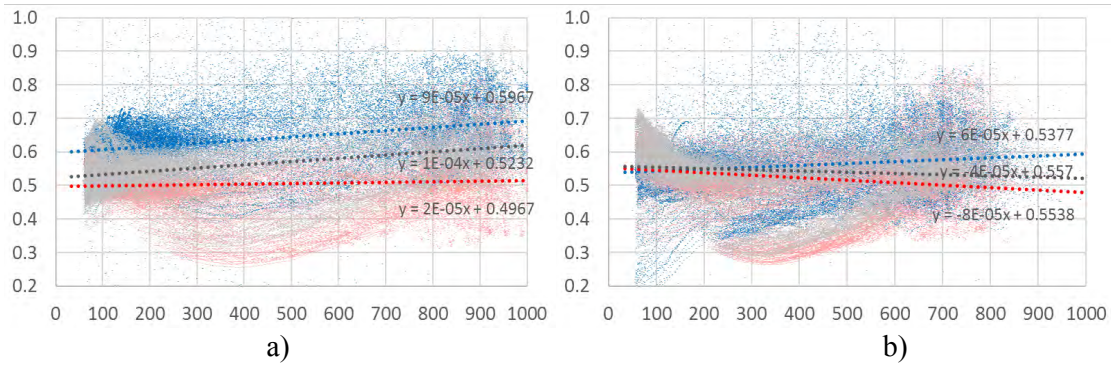
a)   b)

Figure 4. Measurements taken at the year-round timescale regarding the amount of total vertical solar radiation in a) the first half year before 1st June, b) the second after 1st June.
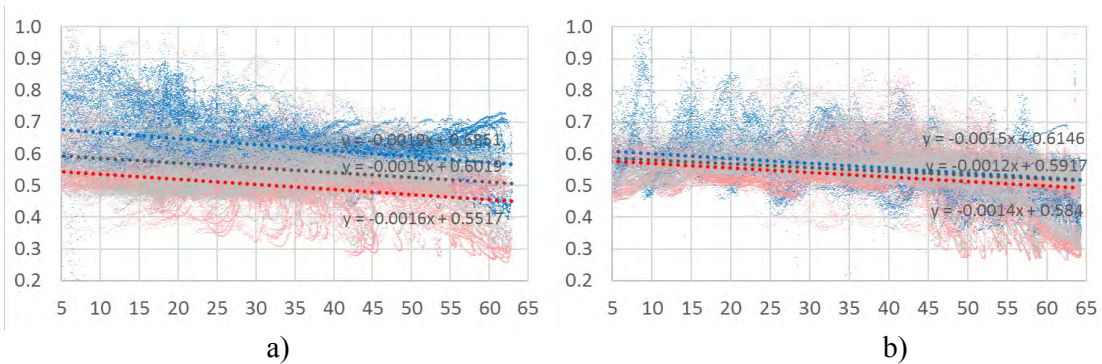

a)   b)

Figure 5. Measurements taken at the year-round timescale regarding the angle of incidence of the sun in a) the first half year before 1st June, b) the second half year after 1st June.

DISCUSSIONS

Based on the results presented, it can be observed that analyzed panels exhibit time-sensitive solar transmittance parameters. Looking at the hourly and/or daily scaled values, a continuous variation in solar transmittance of several tens of percent can be clearly detected. For the presented day with a clear sky, the obtained diurnal values are in the area of 0.79 (PC10), 0.53 (PC32) and 0.63 (PC25). This principally corresponds to the declared values (see Table 1). On the other hand, looking at the detailed hourly based progressions it can be seen that strong fluctuations occurred. This contrasts with overcast conditions, under which the average daily values are approximately 0.63 (PC10), 0.44 (PC32) and 0.52 (PC25). In this case the values correspond to those measured in the laboratory. Overall, the discrepancy in lab tests are that the incoming beam radiation is distributed disproportionately throughout the tested materials in range of approx. 15 nm diameter of spectrophotometer detector, while using outdoor tests, the transmittance is averaged over a large area. As regards the real outdoor measurements during longer timescale periods, the gained data concerning the influence of different solar intensity, angular and time dependent conditions on the solar transmittance is highly variable. The values obtained regarding solar intensity rates range from 0.50 to 0.55 (PC32), from 0.52 to 0.56 (PC25), from 0.60 to 0.67 (PC10) and from 0.54 to 0.60 (PC10*). Meanwhile, the values obtained regarding the angle of the sun above the horizon range from 0.59 to 0.49 (PC32), from 0.61 to 0.51 (PC25), from 0.68 to 0.57 (PC10) and from 0.61 to 0.52 (PC10*). However, the prevailing values show significant movement away from a linear tendency.

CONCLUSIONS

The paper presents the results of the long-term optical characterization of multi-wall panels utilizing co-extruded polycarbonate as a transparent insulation material (TIM). The study

evaluated the impacts of polycarbonates with different numbers of chambers and differing geometries. The experimental monitoring of full-scale components was focused on annual optical performance as a fundamental step towards understanding overall interactions influencing the solar transfer of the presented polycarbonate TIMs. Regarding the real outdoor in-situ measurements using the sun as the source, this study applied a specific methodical approach introduced by this research using long-term solar radiation rate monitoring and its evaluation with three different multi-wall panels. This indicates that the internal structures and geometry currently used to produce polycarbonate-based materials may affect the solar transmittance functions of such components. The analysis demonstrated that from this perspective, the presented panels employ selective aspects regarding the solar radiation that penetrates throughout their internal chambers. Overall, the differences in solar transmittance for all tested periods are strongly variable; they differ by tens of percent. Finally, these results may be considered in order to make careful use of the data in thermal calculation models. Further studies should be focused on the advanced statistical analysis of obtained data in order to describe their overall dependencies more adequately.

ACKNOWLEDGEMENT

REFERENCES

ASTM. 2015. *ASTM E1084-86* International Standard Test Method for Solar Transmittance (Terrestrial) of Sheet Materials Using Sunlight. ASTM International: West Conshohocken, PA, USA.

ASTM 2012. *ASTM G173-03*, Standard Tables for Reference Solar Spectral Irradiances: Direct Normal and Hemispherical on 37° Tilted Surface, ASTM International, West Conshohocken, PA, USA.

Braun P.O., Goetzberger A., Schmid J., Stahl W. 1992. Transparent insulation of building facades - Steps from research to commercial applications, *Solar Energy*, 49(5), 413-427.

Cekon M., Slavik R., Struhala K., and Formanek, M. 2016. Experimental Full- Scale Test Cell Optimizing for Research of Novel Concepts towards Climatically Active Solar Façade Design. *Applied Mechanics and Materials*, 861, 213-220.

Cekon M. and Slavik R. 2017. Total Solar Transmittance Quantifying of Transparent Insulation Building Materials Based on Real Climate Outdoor Measurements. *Energy Procedia*, 132, 243-248.

Cekon M., Slavik R. and Zach J. 2017. Experimental Analysis of Transparent Insulation Based on Poly-carbonate Multi-Wall Systems: Thermal and Optical Performance. *Energy Procedia*, 132, 502-507.

Cekon M., Slavik R. and Juras P. 2016 Obtainable Method of Measuring the Solar Radiant Flux Based on Silicone Photodiode Element. *Applied Mech. and Materials*, 824, 477-484.

Juras P., Staffenova D. and Durica P. 2017. Comparison of different windows for low-energy houses. *MATEC Web of Conferences,* 117

Kaushika N. D., Sumathy K. 2003. Solar transparent insulation materials: a review. *Renewable and Sustainable Energy Reviews*, 7(4), 317-351.

Slavik R. and Cekon M. 2016 Correction Factor Estimating of Silicon Pin Photodiode Derived from Outdoor Long-term Measurement. In Book of proceedings from ATF2016 4th International Conf. on Applied Technology, Leuven, Belgium, 262-266.

Platzer W.J. 1992. Directional-hemispherical solar transmittance data for plastic honeycomb-type structures. *Solar Energy*, 49 (5), 359-369.

Preliminary monitoring results of ventilated heavyweight building envelope from recycled aggregate

Marina Bagarić[1,*], Ivana Banjad Pečur[1] and Bojan Milovanović[1]

[1]University of Zagreb, Faculty of Civil Engineering, Department of Materials, Croatia

[*]*Corresponding email: mbagaric@grad.hr*

ABSTRACT

Potential of recycled aggregate concrete (RAC) has already been acknowledged by many researchers, but the focus was primarily on its mechanical and durability properties at material level. If the focus is shifted to element and whole building level, then the question can be raised; how building envelopes made from RAC behave when exposed to real environment? The present paper describes an experimental set up to monitor hygrothermal behaviour of one three-storey family house built with prefabricated ventilated sandwich wall panels made from recycled concrete and recycled brick aggregate. This type of building envelope can be classified as a heavyweight envelope. In ground-floor flat a wall in the living room facing south is analysed in terms of internal temperature evolution and humidity distribution. Conditions of indoor and outdoor environment were monitored as well. Time lag and decrement of temperature extremes were observed and these benefits can be attributed to the presence of thermal mass. Ventilation of air in cavity ensured acceptable humidity level in all characteristic layers of wall panel. Summer overheating occurred due to insufficiently shaded large transparent openings. Further step is validation of numerical model and assessing the suitability of presented envelope type to different climates. This paper indicates the great potential of RAC application in energy efficient and moisture safe building envelope design.

KEYWORDS

Recycled aggregate concrete, prefabricated ventilated sandwich panels, heavyweight building envelope, field monitoring, hygrothermal behaviour

INTRODUCTION

Recycled aggregate concrete (RAC) has been identified as sustainable alternative to conventional concrete. Its mechanical and durability behaviour has already been widely acknowledged by many researchers (Behera et al. 2014; Fraile-Garcia et al. 2017; Marco 2014). Contrary to that, its hygrothermal behaviour as an important aspect of overall performance, has only been scarcely investigated. There are fragmented research findings on thermal and hygric properties of different types of RAC at material level (Banjad Pečur et al. 2015; Fenollera et al. 2015; Zhu et al. 2015). Having in mind the influence that building envelope's hygrothermal behaviour has on buildings energy needs, service performance, indoor thermal comfort and air quality which is directly related to the health of occupants (Feng and Janssen 2016), obviously there is a strong need to predict hygrothermal behaviour of RAC at component and ultimately at entire building level. To establish trustworthy numerical model, experimental results are desirable for model validation. This paper investigates transient hygrothermal behaviour of ventilated heavyweight building envelope constructed with RAC prefabricated panels under real variable climate conditions and occupants' behaviour.

DESCRIPTION OF MONITORED BUILDING AND EXPERIMENTAL SET-UP

The subject of this study is a 3-storey family house (approx. 268 m^2) built within socially – supported housing program in City of Koprivnica, Republic of Croatia (Figure 1a) as very low energy (A+) standard.
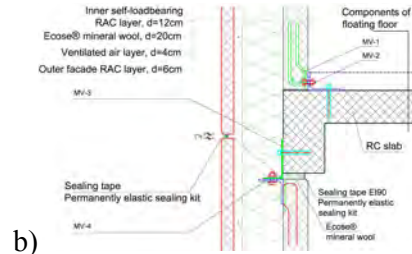

Figure 1. a) View of monitored building; b) Cross section of prefabricated ventilated RAC wall panel

Its building envelope consist of 42 cm thick prefabricated ventilated sandwich wall panels made from recycled aggregate. With surface mass of 458 kg/m^2, building constructed with this type of envelope system can be classified as a heavyweight building. Based on thorough research of mechanical and durability properties (Banjad Pečur et al. 2015), replacement ratio of 50 % natural aggregate with recycled one deemed as the most favourable. As shown in Figure 1b), observed panel consists of four characteristic layers: outer RAC facade layer (6 cm), ventilated air cavity (4 cm), thermal insulation (20 cm), and inner self-loadbearing RAC layer (12 cm). The thermal transmittance of panel is approx. 0.16 W/(m^{2}K).

For production of outer RAC façade layer (RAC-B), recycled brick from waste generated during manufacturing brick process was used, while recycled aggregate from demolition of old concrete structure was used for production of inner self-loadbearing RAC layer (RAC-C). Thermal insulation is formaldehyde-free glass wool with integrated wind barrier. Air cavity is placed between thermal insulation and outer façade layer, with aim to prevent possibility of water vapour condensation. The water-repellent coating was applied on outer façade surface. Main hygrothermal properties of target recycled aggregate concrete are shown in Table 1.

Table 1. Hygrothermal properties of RAC-C and RAC-B

	RAC-C	RAC-B
Dry density [kg/m^3]	2204.96	1948.22
Open porosity [%]	16.67	19.27
Thermal conductivity $\lambda_{dry,+10°C}$ [W/(mK)]	0.944	0.745
Water vapour resistance factor μ [-]	41	28

Conventional concrete made completely with natural aggregates with a density of 2300 kg/m^3 has λ-value of approximately 1.7 W/(mK). Replacement of 50% contributed to approx. 44% lower λ when concrete is used and approx. 56% when brick is used as recycled aggregate. It is suggested to use μ-value for normal concrete as a constant value of 150. From Table 1, it can be seen that μ-factors for RAC-C and RAC-B concrete are up to 80% lower compared to value suggested for normal concrete. This basic hygrothermal parameters indicate that more energy efficient building design can be achieved with RAC without compromising mechanical requirements – 43.3 MPa was mean cube compressive strength of RAC-C and 38.7 MPa of RAC-B, respectively.

In ground-floor flat a wall panel in the living room facing south (marked red in Figure 2a) is analyzed in terms of internal temperature evolution and humidity distribution. Panel is 128.5×297 cm, with the first set of sensors centrally positioned 86 cm from the panel's bottom and second set of sensors 100 cm, respectively.
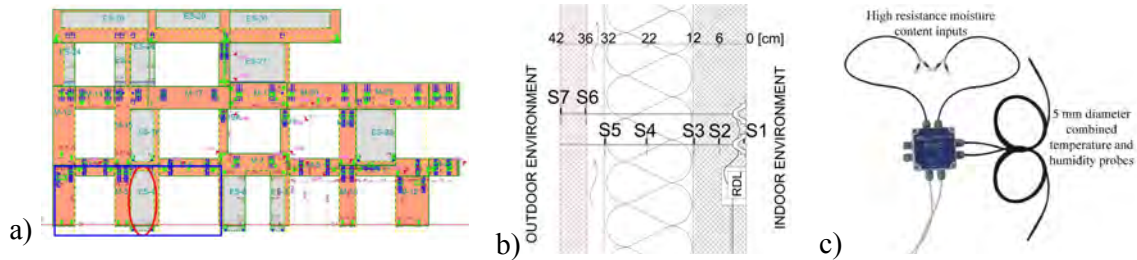
Figure 2. Measurement location: a) Position plan for southern façade; b) Arrangement of T-H sensors within panel layers; c) RDL Client-THR system

Temperature (T) and humidity (H) distribution was monitored in all four characteristic layers of presented wall panel, in total seven positions S1-S7 (Figure 2b), using the RDL Client-THR system from Caption Data Limited (Figure 2c). Installation of T-H sensors was carried out in precast factory during the moulding of panels (Figure 3). Presented monitoring system

Figure 3. Installation of T-H sensors

is a combination of wire-based and wireless measurement system. Sensors (S1-S7) at south measurement location are wired connected to the central measurement unit in building's entrance hall, where sensors readings are recorded every hour and then sent by Internet on a dedicated server. The data can be accessed via custom Brightcore computer system. Further analysis of measured data was performed with Microsoft Excel software. Boundary conditions in terms of indoor and outdoor environment were also monitored. Indoor climate is dependent on the occupants' behaviour – young couple with small child. TFA Klimalogg Pro Thermo-Hygro-Station data logger was used for monitoring and recording the air temperature and relative humidity in living room of the house every 15 minutes. Basic meteorological data were measured every 5 min at nearest available meteorological station Herešin. These data are taken as representative for the Cfb climate of City of Koprivnica (Köppen climate classification).

RESULTS AND DISCUSSIONS
Period of almost one year was monitored (March 9, 2017 – February 28, 2018). In winter months outside temperature was occasionally under 0°C with peak of -17.3°C at the end of February 2018. Five days in a row was the longest continuous period of temperature under 0°C with mean value of -6.6°C. Max value was 38.3°C in August 2017 and its average monthly value was 22.5°C. Inside air temperature (living room) was in range from 19.5 to 29.1°C. It needs to be noted that in this paper humidity distribution will be presented only in terms of relative humidity (RH). Used moisture content sensors are electrical resistance-based sensors with readings in [kohm] and establishment of correlation curves for both type of RAC is still in process. Those results will be published elsewhere. Figure 4a) and 4b) show the measured T and RH values within the panel. While the exterior surface T (S7) vary in a wide range (from -10.8 to 55.4°C) following the pattern of outdoor climate, T variations through inner RAC layer (S1 – S3) are more stable and limited from 17.18 to max 31°C. RH sensors at positions S1 – S3 (inner RAC layer) did not send any information (Figure 4b).

7
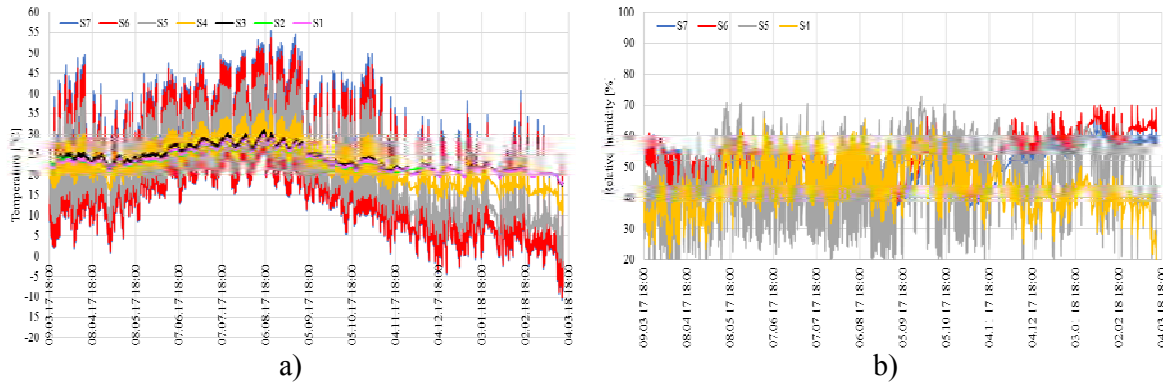
Fig 4. One-year monitoring data: a) Temperature b) Relative humidity

Figure 5 presents the measured RH in the mineral wool (MW) and RAC outer facade layer for period December 1, 2017 – February 28, 2018. MW is of big interest due to its thermal insulation function, while RAC outer façade layer presents the most humid area of the panel in winter by being directly submitted to wind driven rain. Despite high outdoor RH values (above 90%), for external surface of RAC façade layer RH oscillates mostly around 60%. This can probably be attributed to the water-repellent coating.
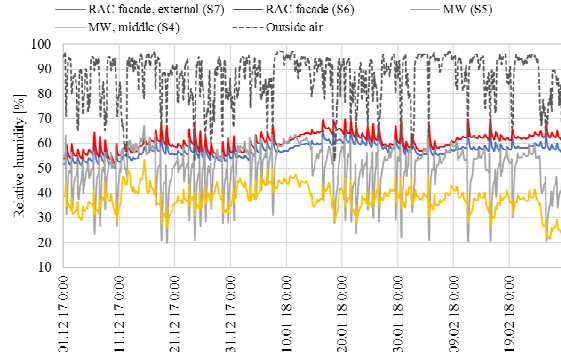
Figure 5. RH inside RAC outer façade and MW layer of monitored panel during winter

It appears that the RH is mostly, except the few occasional peaks, under 60 % at the surface of MW layer (S5). In the middle of MW (S4), RH is almost always under 50 % and mostly fluctuating around 40% which indicates the positive effect of air ventilation in cavity. To gain a deeper understanding of hygrothermal behaviour of observed south-facing panel, monitoring results are presented hereafter for the three coldest days of the winter period (February 26-28, 2018) and the three hottest days of the summer period (August 3-5, 2017), respectively.
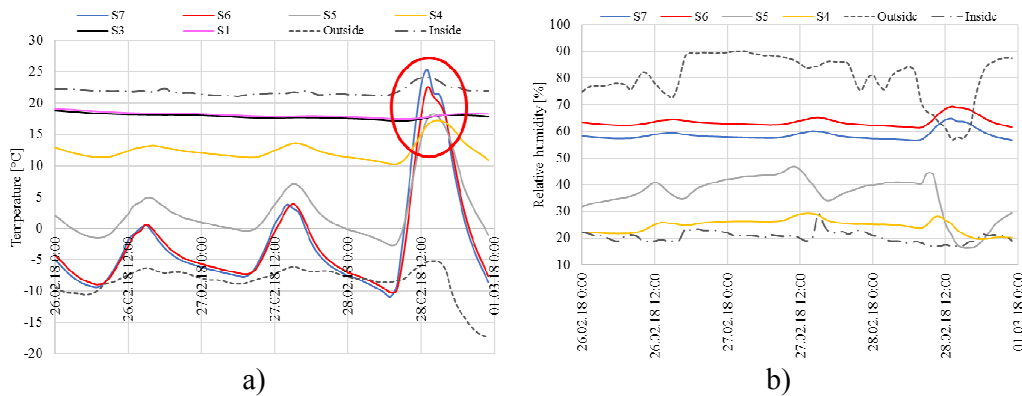
Figure 6. Hygrothermal responses within the panel for three coldest days: a) T; b) RH
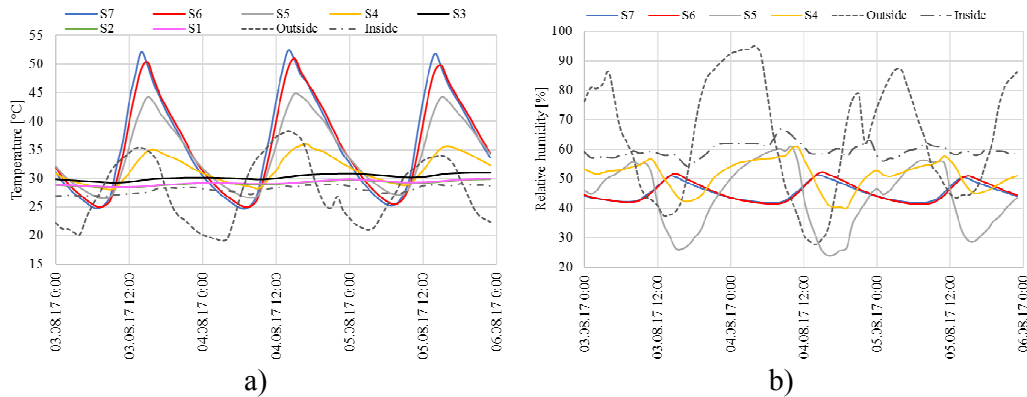
Figure 7. Hygrothermal responses within the panel for three hottest days: a) T; b) RH

In February 2018, indoor air temperature varies between 21.1 – 25.5°C with a mean of 22.9 °C. Values of RH vary between 41.3 – 17 % with a mean of 28.8 %. During August 2017, indoor air temperature varies in a wider range from 29.1 – 23.7°C, with a mean of 26.2°C, while values of RH vary between 69.3 – 37.3 % with a mean of 53.3 %. The fluctuations of indoor temperature are limited by heating system (mechanical ventilation with recuperation system and radiators as additional heating system in winter but without additional cooling system in summer). The exterior surface temperature (S7) of observed south-facing panel follows the pattern of behaviour of the outdoor temperature reaching a high peak at 14:00h in summer conditions due to the solar exposure. The same pattern is followed by S6 – S4 but with decreased amplitude. Further and more progressive attenuation of T amplitude is present in S3 – S1 (inner layer). In winter period, high peak occurs on February 28 reaching 25.3°C at panel's exterior surface at 13:00h. This specific peak is most likely induced by increased solar radiation at clear winter day compared to previous days (Figure 8). Unfortunately, there was occasional interruption of measurement and some hourly solar radiation data are missing.

Besides attenuation of T amplitude, a time shift between the peaks can be observed. These appearances are due to the thermal inertia of RAC panel. Thermal inertia is evaluated in terms of time lag and attenuation of heat wave amplitude while propagating from the outer surface to the inner surface. February 27, 2018 is analysed for winter conditions and August 4-5, 2017 for summer conditions, respectively. In summer conditions, between S7 – S1 a
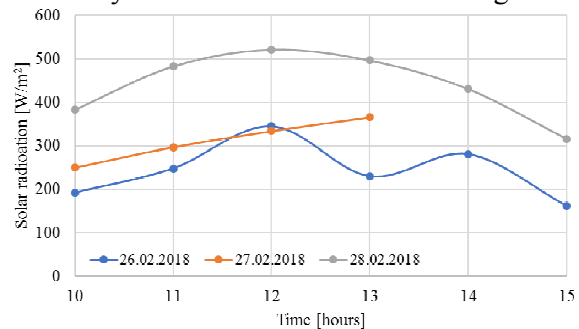
Figure 8. Solar radiation data in February 2018

damping of approx. 57 % is measured. The panel attenuates the temperature very well with a time lag of 10h over a period of 25 hours. These two observations indicate that the panel has a good thermal inertia. For completely opposite boundary conditions, i.e. winter conditions, the min exterior surface temperature (-7.7°C) and min interior surface temperature (17.8°C) are analysed. In this case, time lag is approximately 6h over a period of 24 hours. High façade surface temperatures (> 50°C) in the summer indicate there may be periods of overheating that potentially could compromise thermal comfort of occupants. Living room has large transparent openings (marked blue in Figure 2a) oriented to south which ensures considerable solar heat gains. In Figure 9 coincidence of the measured psychrometric data in living room and the summer comfort zone is presented for period of June 1 to September 1, 2018. Used summer comfort limits are the ones defined for living spaces in residential buildings, Category II (HZN 2008). During summer, T and RH were in the comfort zone 57.7% of time.

Actually, RH exceeds the upper threshold (60%) only 17.5% of the time, while T exhibited significant violation of upper threshold (26°C). This overheating is related to architectural design of building, where large transparent openings at south are not adequately shaded. To avoid installation of additional air-conditioning systems, application of adequate shading devices or/and external greenery should be considered. That would undoubtedly decrease operating temperatures in summer period.
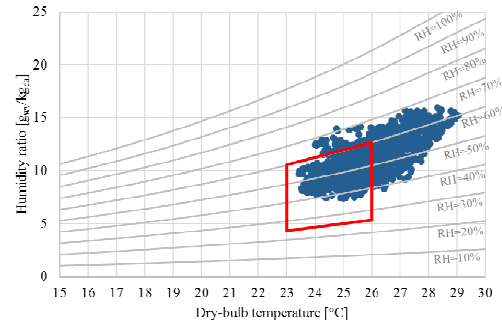
Figure 9. Internal psychometrics data vs. HRN EN 15251 summer comfort limits

CONCLUSIONS AND FURTHER RESEARCH ACTIVITIES

The first in-situ monitoring results of family house constructed with prefabricated ventilated sandwich wall panels from recycled aggregate concrete (RAC) were analysed. Hygrothermal behaviour under real variable climate conditions and real use of occupants was experimentally monitored during one year. The south-oriented RAC panel exhibited a good thermal inertia - high damping capacity (>50 %) and time shift up to 10 hours in summer period. Air ventilation maintained relative humidity levels in mineral insulation under 60 % during winter months. Even though these results are preliminary results, they can already confirm that it is possible to upscale RAC from laboratory material experiments to full-scale construction product implementation and design sustainable, energy efficient and moisture-safe buildings. Special attention should be on preventing summer overheating. Further research steps are: i) analysis of west- and north-oriented (more shady) facades and their comparison with presented south panel; ii) numerical simulation of panels and validation with experimental results (assessing the panel's suitability for different climates); iii) continue with monitoring for at least next two years – possibility to confirm pattern of RAC's hygrothermal behaviour.

ACKNOWLEDGEMENT

REFERENCES

Banjad Pečur, I., Štirmer, N., & Milovanović, B. 2015. Recycled aggregate concrete for nearly zero-energy buildings. *Magazine of Concrete Research*, *67*(11), 575–584.

Behera, M., Bhattacharyya, S. K., Minocha, A. K., Deoliya, R., & Maiti, S. 2014. Recycled aggregate from C&D waste & its use in concrete - A breakthrough towards sustainability in construction sector: A review. *Construction and Building Materials*, *68*, 501–516.

Feng, C., & Janssen, H. 2016. Hygric properties of porous building materials (II): Analysis of temperature influence. *Building and Environment*, *99*(Ii), 107–118.

Fenollera, M., Míguez, J., Goicoechea, I., & Lorenzo, J. 2015. Experimental Study on Thermal Conductivity of Self-Compacting Concrete with Recycled Aggregate. *Materials*, *8*(7), 4457–

Fraile-Garcia, E., Ferreiro-Cabello, J., López-Ochoa, L. M., & López-González, L. M. 2017. Study of the technical feasibility of increasing the amount of recycled concrete waste used in ready-mix concrete production. *Materials*, *10*(7).

HZN. 2008. *HRN EN 15251:2008 Indoor environmental input parameters for design and assessment of energy performance of buildings addressing indoor air quality, thermal environment, lighting and acoustics (EN 15251:2007)*, Zagreb: Croatian Standards Institute

Marco, P. 2014. A conceptual model to design recycled aggregate concrete for structural applications. *Ph.D. Thesis, Springer Theses*. Springer.

Zhu, L., Dai, J., Bai, G., & Zhang, F. 2015. Study on thermal properties of recycled aggregate concrete and recycled concrete blocks. *Construction and Building Materials*, *94*, 620–628.

Review of the sky temperature and solar decomposition, and their impact on thermal modeling

Farhad Hemmati[1,*], Fitsum Tariku[2]

[1&2]British Columbia Institute of Technology, Burnaby, BC, Canada

*Corresponding email: fhemmati@my.bcit.ca

ABSTRACT
Performing accurate hourly building energy modeling requires presence of reliable boundary conditions. The required data for energy simulation model entries are exterior air temperature, exterior air relative humidity, solar radiation, sky temperature, wind velocity and cloud cover. Unfortunately, most available measured solar energy data is in the form of global horizontal radiation. Moreover, measured night sky temperature is normally not available. Proper energy modeling of a full building requires to have accurate solar radiation intensity on angled building envelope assemblies as well as precise sky temperature data available.

In this study, among several available models, three hourly horizontal global solar radiation decomposition models, four hourly diffuse radiation on inclined surface models, and five sky temperature estimation models are studied for Vancouver climate. For solar radiation validation perspective, 2013 one-year measured total solar radiation on a south-east oriented wall located at BCIT Burnaby Campus is compared with the results from selected solar models. For both solar radiation and sky temperature models, impact of using different models on transient heat transfer results of light-weight and mass-type walls (two walls) are reviewed. Results reveal high impact of both solar and sky temperature models on hourly heat transfer simulation results.

KEYWORDS
Sky temperature, diffuse radiation on tilted surface, decomposition of global radiation, transient thermal simulation.

INTRODUCTION
From the total energy spent in 2013 within Canada, 17% was found in residential sector, and 10% in commercial and institutional sectors (Canada, 2016). Therefore, it is important to thoroughly understand the interaction between energy consuming elements within a building, which requires hourly energy simulation. Performing an accurate hourly energy simulation requires having correct input boundary conditions available. Two important boundary conditions that could highly impact the simulation results are solar radiation and sky temperature values.

Solar radiation
Most available climatic weather data only contains global value for solar radiation, while direct and diffuse components of solar radiation as well as diffuse radiation on inclined surfaces are not always available (Burlon, et al., 1991). These three components are ultimately required to calculate the total solar radiation on a tilted surface. Many decomposition models for calculation of diffuse solar radiation are developed based on the terminology first studied by Liu & Jordan (1960). Performance of several previous solar radiation models are reviewed in this study, and results are compared with the measured data for validation purposes.

Sky radiation

Measured sky radiation is not always available. Therefore, approximation models are being used to estimate the values.

There are several studies performed on sky radiation estimation. Most of the models are based on clear sky condition (Algarni & Nutter, 2015), while climates with high cloud coverage (i.e. Vancouver) require a certain correlation to account for sky condition. In this study, different models for cloudy sky temperature estimation are reviewed. Since no measured sky temperature values is available, only the impact of using different sky temperature models is reviewed on transient thermal modeling.

METHODS

In this study, total of three hourly horizontal global solar radiation decomposition models, four hourly diffuse radiation on inclined surface models, and five sky temperature estimation models are reviewed.

Solar radiation

The selected hourly horizontal global solar radiation decomposition models are Erbs, et al. (1982), Reindl, et al. (1990), and Orgill & Hollands (1977). Studied hourly diffuse radiation models on an inclined surface are Reindl, et al. (1990), Skartveit & Olseth (1986), Hay, (1979) and Perez, et al. (1990). These models are selected based on the climates that they have been developed based on, and extent of their use in energy modeling industry. Therefore, the combination of decomposition models and diffused radiation on tilted surface models would result in total of twelve models.

The above-mentioned models require extraterrestrial solar radiation, global solar radiation, cloud index, temperature and relatively humidity, and sun position as inputs. Model inputs are imported from Engineering Climate Datasets (Government of Canada, n.d.). The model results (total of twelve combined models) are compared with 2013 one-year measured total solar radiation on a south-east oriented wall located at BCIT Burnaby Campus. Global solar radiation (Government of Canada, n.d.) is decomposited into direct and diffuse components using the selected three models. Fraction of diffuse solar components on south-east wall is then calculated using the four selected models. Lastly, results for total tilted solar radiation on south-east orientation wall (twelve models) are compared with 2013 measured data from BCIT Burnaby Campus.

In order to review the impact of different solar radiation models on hourly thermal modeling, solar radiation from different models are used to simulate the transient heat transfer in one-dimensional light-weight and mass-type walls (total of two walls). Errors caused by utilizing different models are presented.

Sky temperature

In this study, selected sky emissivity models are Melchor (1982b), Clark & C. Allen (1978), Daguenet (1985) (both England and Sweden), and Aubinet (1994). All these models are developed according to climates with relatively high chance of rain; therefore, they would be potential candidates for climates such as Vancouver.

The above-mentioned models require relative humidity, ambient temperature, atmospheric pressure, site elevation, sky cover and clearness index as inputs. Model inputs are imported from Engineering Climate Datasets (Government of Canada website).

Since measured data was not available for sky temperature, only impact of using different sky temperature on hourly thermal modeling is reviewed. Sky temperature results from different models are used to simulate the transient heat transfer in one-dimensional light-weight and mass-type walls (total of two walls). 2005 hourly Vancouver International Airport weather data is used for the purpose of this simulation. Deviation of the results from the reference case of "no sky temperature" is reviewed for each model.

Simulation setup

For both solar radiation and sky temperature, light weight wall consists of ½" drywall, 5 ½" of batt insulation, ½" plywood sheathing, ½" air cavity and ½" hardie-siding, and mass-type wall consists of ½" drywall, 3" of XPS insulation and 8" concrete structural wall. Material properties are selected from 2013 ASHRAE Handbook – Fundamentals. Interior air film coefficient is assumed 8.33 W/m²K and exterior air film coefficient is assumed 33 W/m²K. No sky temperature radiation is considered for solar radiation simulation cases, and no solar radiation is considered for sky temperature simulation cases. Ground reflectivity is assumed to be 0.2 (dimensionless).

For all transient numerical simulations, COMSOL Multiphysics Modelling Software has been used. The software results are validated using the four benchmark cases from ISO 10211 (10211, 2007).

RESULTS

Solar radiation

Six days of hourly results for different solar radiation models on the south-east wall are provided in Figure 1. Discrepancy of results are calculated using seasonal and total Mean Absolute Error (MAE) for each model in Table 1. Figure 2 shows percentage of hourly solar radiation results corresponding to specified range of relative error, which reveals the reliability of each model.

Table 2 is provided to review the impact of different solar models on transient heat transfer simulation for light-weight and mass-type wall assemblies. This table contains seasonal and total heat transfer Normalized Mean Absolute Error (NMAE) compare with simulation results from measured solar values. The errors are normalized by dividing MAE by the average heat transfer results corresponding to measured values for the specified period of time.
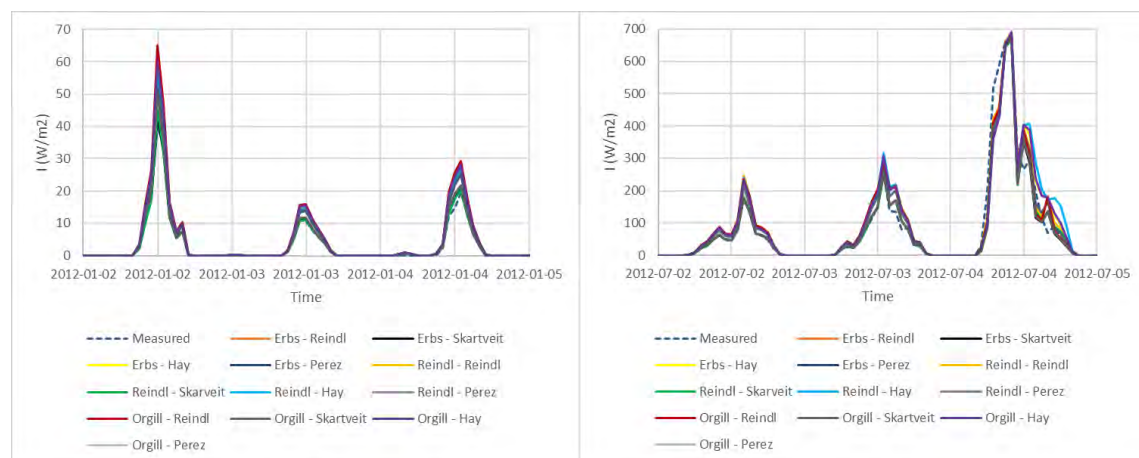

Figure 1. Solar radiation comparison for Jan 2nd-4th and July 2nd-4th.

Table 1. Solar radiation model comparison - MAE

Models	Winter	Spring	Summer	Fall	Total
Erbs - Reindl	32.7	37.8	49.6	33.4	39.6
Erbs - Skartveit	29.6	30.4	49.6	27.6	35.6
Erbs - Hay	33.5	38.5	50.0	34.7	40.3
Erbs - Perez	31.4	34.5	50.8	31.4	38.3
Reindl - Reindl	32.5	37.0	50.1	32.4	39.3
Reindl - Skartveit	29.6	29.8	48.4	26.2	34.7
Reindl - Hay	33.7	47.3	73.3	33.2	49.9
Reindl - Perez	31.4	34.4	50.8	31.5	38.3
Orgill - Reindl	33.5	38.5	50.0	34.7	40.3
Orgill - Skartveit	29.5	30.3	49.7	28.3	35.7
Orgill - Hay	34.3	44.8	66.3	35.8	47.6
Orgill - Perez	32.0	35.3	51.7	32.6	39.2
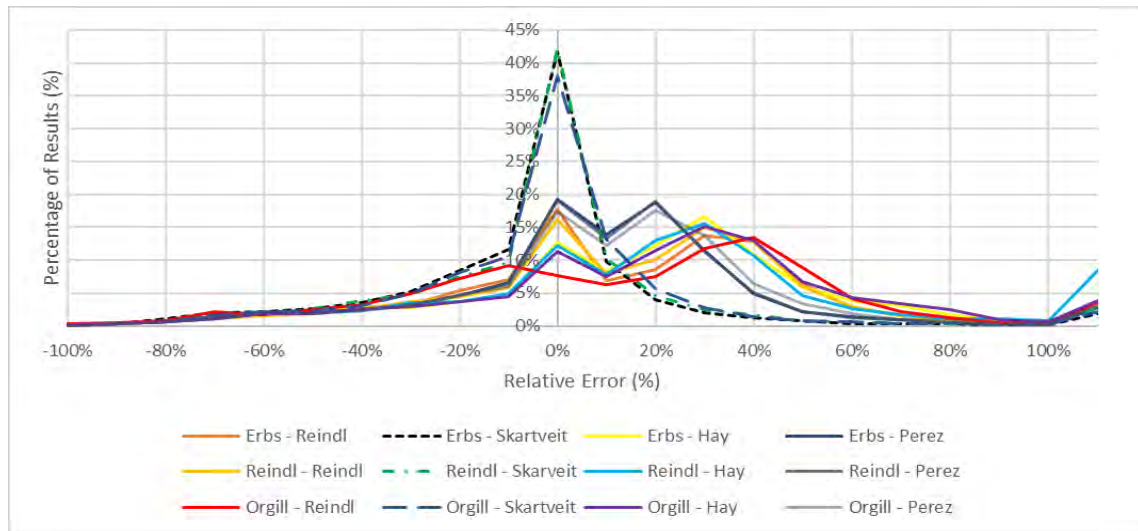
Figure 2. Percentage of results corresponding to selected range of relative error – solar model comparison

Table 2. Transient heat load comparison – Solar radiation – Light-weight and mass-type walls

Model	Light-Weight Wall					Mass-Type Wall				
	Winter	Spring	Summer	Fall	Total	Winter	Spring	Summer	Fall	Total
Erbs - Reindl	5.3%	7.2%	35.8%	2.8%	5.7%	4.3%	6.2%	30.3%	2.0%	4.6%
Erbs - Skartveit	4.8%	5.9%	36.3%	2.3%	5.2%	4.3%	5.5%	35.4%	1.5%	4.6%
Erbs - Hay	5.4%	7.3%	35.8%	2.9%	5.8%	4.4%	6.4%	30.3%	2.0%	4.7%
Erbs - Perez	5.2%	6.7%	37.1%	2.6%	5.6%	4.1%	5.4%	29.9%	1.7%	4.4%
Reindl - Reindl	5.2%	7.1%	36.2%	2.7%	5.7%	4.0%	5.7%	26.5%	1.9%	4.3%
Reindl - Skartveit	4.7%	5.7%	35.8%	2.1%	5.0%	4.0%	5.2%	31.0%	1.4%	4.3%
Reindl - Hay	6.6%	9.2%	53.7%	2.8%	7.3%	4.1%	5.8%	28.7%	1.8%	4.4%
Reindl - Perez	5.1%	6.7%	37.1%	2.5%	5.5%	4.0%	5.3%	29.3%	1.7%	4.3%
Orgill - Reindl	5.4%	7.3%	35.8%	2.9%	5.8%	4.4%	6.4%	30.3%	2.0%	4.7%
Orgill - Skartveit	4.9%	5.9%	36.5%	2.4%	5.2%	4.3%	5.5%	35.3%	1.6%	4.7%
Orgill - Hay	6.3%	8.8%	48.4%	2.9%	6.9%	4.2%	6.0%	27.9%	2.0%	4.5%
Orgill - Perez	5.3%	6.9%	37.9%	2.8%	5.7%	4.1%	5.5%	29.1%	1.9%	4.4%

Sky temperature

Fourteen days of hourly results for sky temperature are provided for each model in Figure 3. For both light-weight and mass-type walls, NMAE between calculated results from the

selected sky temperature models and reference model (no sky temperature) are shown in Table 3 in order to review the heat transfer deviation caused by different models.

Figure 3. Night sky temperature comparison for Jan 7th-14th and July 7th-14th

Table 3. Transient heat load comparison – Sky temperature – Light-weight and mass-type walls

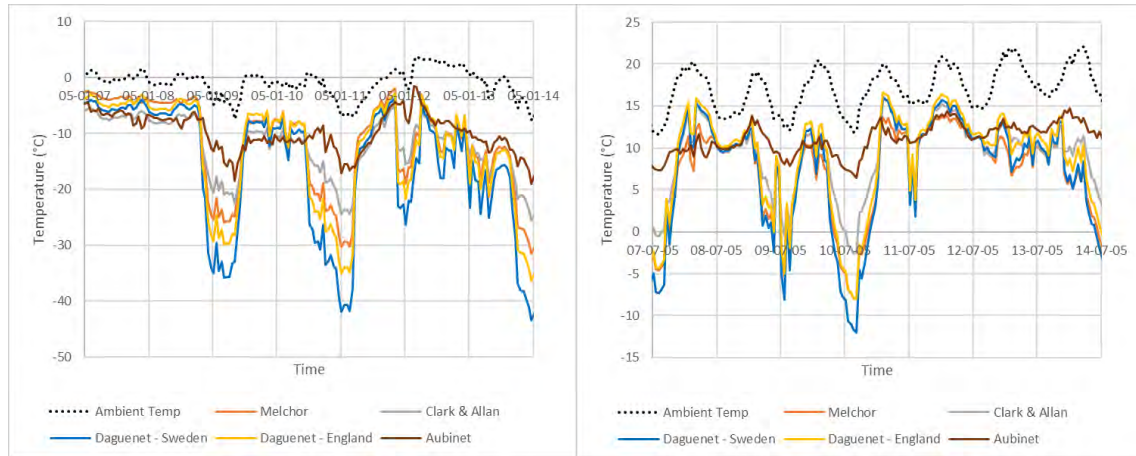| Model	Light-Weight Wall					Mass-Type Wall				
	Winter	Spring	Summer	Fall	Total	Winter	Spring	Summer	Fall	Total
Melchor	3.6%	7.0%	19.1%	3.4%	6.5%	7.4%	11.2%	25.0%	6.8%	10.6%
Clarke	2.7%	5.5%	14.5%	2.6%	5.0%	7.0%	10.0%	19.9%	6.9%	9.5%
England	5.3%	10.2%	15.2%	8.4%	8.8%	8.9%	14.9%	20.0%	12.8%	13.0%
Sweden	6.5%	12.6%	17.9%	10.4%	10.7%	10.5%	17.5%	23.0%	15.1%	15.3%
Aubinet	1.4%	3.1%	7.3%	1.5%	2.7%	4.4%	7.0%	11.9%	4.3%	6.0%

DISCUSSIONS
Solar radiation
Table 1 and Figure 2 reveal that Erbs - Skartveit, Reindl - Skartveit and Orgill - Skartveit models result in the closest solar radiation values to measured data. Among these three models, Reindl - Skartveit model has the best performance with 42% of the results within ±10% relative error, and has the lowest seasonal and total MAE (35.78 W/m2). This model also shows the least seasonal fluctuation in MAE values, which proves the stability.

Table 2 confirms the fact that Reindl - Skartveit model also results in the lowest seasonal and total NMAE (5.09% for light-weight and 4.31% for mass-type) hourly heat transfer for both light-weight and mass-type walls. Different solar models could result up to 2.26% additional discrepancy in total NMAE for the light-weight wall and 0.47% additional discrepancy in total NMAE for the mass-type wall. Similar pattern could be found for seasonal NMAE results.

Sky temperature
Significant variation between sky temperature models' results is revealed in Figure 3, which mostly occurs during days with clear sky. Using different night sky models could result in total deviation (Table 3) in the range of 2.71% to 10.77% for light-weight wall and 6.09% to 15.33% for mass-type wall from the reference case (no sky radiation). Significant seasonal deviation is also shown in Table 3 for both light-weight and mass-type walls. This shows the great impact of utilizing different sky temperature models on transient heat transfer simulations.

CONCLUSIONS

Several different horizontal global solar radiation decomposition models, hourly diffuse radiation on inclined surface models, and sky temperature estimation models are reviewed in this study. Solar radiation models' results are compared with one-year measured data from BCIT campus. With respect to solar radiation, combination of Reindl, et al. (1990) and Skartveit & Olseth (1986) models revealed the best result compare with measured values. Impact of using different solar radiation model on transient heat transfer modelling was reviewed, and 2.26% additional discrepancy on the light-weight wall and 0.47% on the mass-type wall were found. Using different sky radiation models could result in additional deviation of 8% in light-weight wall and 9.3% in mass-type wall compare with reference results.

Transient thermal simulation results reveal the fact that sky temperature models' estimation have more impact on total transient heat transfer compare to solar radiation models. Overall, in order to conduct an accurate building energy simulation, it is critical to diligently select the proper estimation model for both solar radiation and sky temperature if the measured values are not available.

REFERENCES

10211, I. 2007. Thermal bridges in building construction – Heat flows and surface temperatures – Detailed calculations.

Algarni, S., & Nutter, D. 2015. Survey of sky effective temperature models applicable to building envelope radiant heat transfer. *ASHRAE Transactions, 121*, p.351.

Aubinet, M. 1994. Longwave sky radiation parametrizations. *Solar energy, 53(2)*, pp.147-154.

Burlon, R., Bivona, S., & Leone, C. 1991. Instantaneous hourly and daily radiation on tilted surfaces. *Solar Energy*, 47(2), pp.83-89.

Canada, N. R. 2016. *EFFICIENCY, N. R. C. S. O. O. E. Energy Efficiency Trends in Canada 1990 to 2013.* .

Clark, G., & C. Allen. 1978. The estimation of atmospheric radiation for clear and cloudy skies. *Proceedings of 2nd National Passive Solar Conference (AS/ISES)*, 2:675–8.

Daguenet, M. 1985. Les séchoirs solaires: théorie et pratique. *Paris: United Nations Educational, Scientific and Cultural Organization*.

Erbs, D., Klein, S., & Duffie, J. 1982. Estimation of the diffuse radiation fraction for hourly, daily and monthly-average global radiation. *Solar energy, 28(4)*, pp.293-302.

Government of Canada. (n.d.). Retrieved from http://climate.weather.gc.ca/historical_data/search_historic_data_e.html

Hay, J. 1979. Calculation of monthly mean solar radiation for horizontal and inclined surfaces. *Solar energy, 23(4)*, pp.301-307.

Liu, B., & Jordan, R. 1960. The interrelationship and characteristic distribution of direct, diffuse and total solar radiation. *Solar energy*, pp.1-19.

Melchor, C. 1982b. New formula for the equivalent night sky emissivity. (model B). *Solar Energy, 28(6)*, 489–98.

Orgill, J., & Hollands, K. 1977. Correlation equation for hourly diffuse radiation on a horizontal surface. *Solar energy, 19(4)*, pp.357-359.

Perez, R., Ineichen, P., Seals , R., & Michalsky, J. 1990. Modeling daylight availability and irradiance components from direct and global irradiance. *Solar energy, 44(5)*, pp.271-289.

Reindl, D., Beckman, W., & Duffie, J. 1990. Diffuse fraction correlations. *Solar energy, 45(1)*, pp.1-7.

Reindl, D., Beckman, W., & Duffie, J. 1990. Evaluation of hourly tilted surface radiation models. *Solar energy, 45(1)*, pp.9-17.

Skartveit, A., & Olseth, J. 1986. Modelling slope irradiance at high latitudes. *Solar energy, 36(4)*, pp.333-344.

Roof Windows for Passive Houses – What Can Be Improved?

Jan Tywoniak[1,*], Kamil Staněk[1] and Vítězslav Calta[1]

[1]Czech Technical University in Prague, Czech Republic

Corresponding email: tywoniak@fsv.cvut.cz

ABSTRACT
In general, skylights and roof windows in pitched roofs can be described as the critical components of buildings concerning heat losses, risk of surface condensation, increased risk of overheating of rooms behind etc. This is very sensible task especially for passive house solutions. The paper informs about studies analyzing the importance of these relatively small areas in the building envelope and more detailed in pitched roof of a passive house. One of the key problems is the position of roof window within the pitched roof construction.
Second part of the paper comments results of detailed analysis of thermal performance for different combination of frame type and glazing. These studies are performed hand in hand with development works. It is documented that such approach can lead to promising results, reducing the thermal transmittance of roof window to $0.7 - 0.5$ W/(m^{2}K). If we consider the real roof window quality including the thermal couplings due to window installation such thermal transmittance stays safely bellow 0.9 W/(m^{2}K).

KEYWORDS
roof window, pitched roof, thermal transmittance, passive house

INTRODUCTION
It is known that roof windows are the weakest components of building envelope. Therefore they are quite unpopular by passive house designers. Nevertheless, they have to be used in some cases and the resulting increased heat transmission must be compensated in order to achieve the passive house criteria. The database of components certified for passive houses (PHI, 2018a) contains only 2 products (for comparison: there are 218 products of passive house suitable vertical windows in this database). The problem with roof window quality is rather complex and starts with the non-optimal position of such window in the pitched roof: Perimeters of window frames are more or less exposed to outdoor condition (Fig.1). Typically for passive houses, no heating body bellow the window is placed there. This can be a critical issue for avoiding the risk of surface condensation in some details. Even if the heating body would be used its temperature is controlled according to heating demand which does not guarantee the presence of warm air movement near to window surface. From both mentioned reasons only the very best roof windows should be used, carefully checked for very low thermal transmittance and for high enough surface temperature.
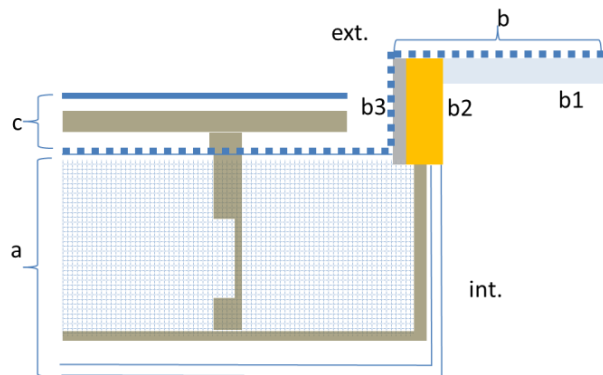
Figure 1. Schematic horizontal cross section of a typical position of roof window in a pitched roof. Dotted line represents the surfaces exposed to the exterior temperatures.
(a typical pitched roof assembly (from interior): indoor gypsum board lining, OSB boards, mineral wool thermal insulation, protective membrane open to water vapor diffusion), b roof window (simplified): b1 glazing unit, b2 frame and sash, b3 possible additional thermal insulating shield), c roof covering)

THERMAL TRANSMITTANCE

Thermal transmittance of the roof window installed in a pitched roof can be described in an extended way as follows (in accordance with PHI, 2018b):

$$U_{w,inst.} = \frac{A_g \cdot U_g + A_f \cdot U_f + \Sigma(\psi_g \cdot l_g) + \Sigma(\psi_w \cdot l_w)}{A_g + A_f}$$

where the $\Sigma(\psi_w \cdot l_w)$ describes the effects of installation. It is illustrated in Fig.2 for hypothetical window of excellent quality: Assumed thermal transmittance of glazing 0.60 W/(m²K), frame U_f 0,60 W/(m²K), thermal bridges of glazing edge expressed by linear thermal transmittance ψ_g 0,03 W/(mK), thermal bridge due to installation in the roof (ψ_w 0,05 W/(mK), considering the reference window size 1.14 m x 1.40 m. It can be seen that for improvements of roof windows all parts are of a high importance: glazing, frame and installation method and overall geometry.
.
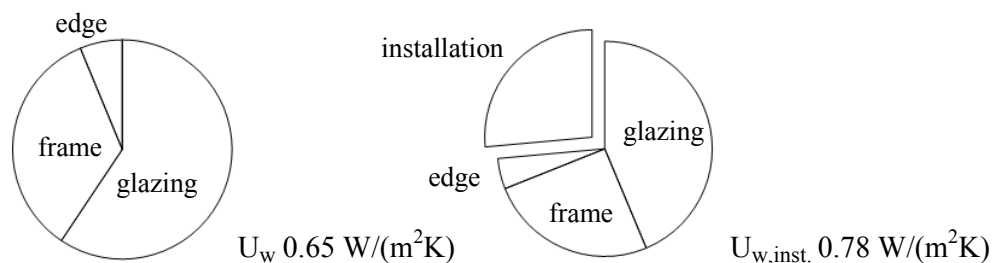
Figure 2. Result of a study for excellent roof window in typical position in pitched roof (see Fig.1). Heat transfer of window (left), heat transfer of window including installation in the pitched roof (right) based on 2D calculations for all relevant cross sections.

IMPORTANCE OF ROOF WINDOWS IN HEAT LOSS OF BUILDING ENVELOPE
Two studies were performed to show the influence of roof window in the overall transmission heat loss of a building envelope for simple single family house. Thermal transmittances used here are based on standard requirements (CSN 73 0540-2, 2011) as well as on recommendations for passive buildings published there. First study (Fig.3, Tab.1) deals with the whole building envelope. The second one (Tab.2) is focused to pitched roof only – with or without windows, considering different thermal qualities. At the pitched roof of 140 m^2 for a passive house is the opaque part responsible for 77 % and the roof windows (6 pcs a 1 m^2) for 23 % of heat losses respectively. This corresponds to and ¼ increase of heat losses compared to the roof without windows.
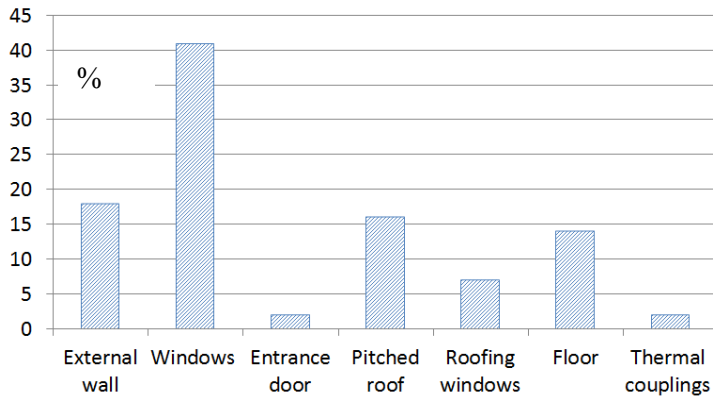
Figure 3. Distribution (%) of transmission heat loss for simple single family house with typical values needed for reaching passive house level.

Table 1. Data for case study – Effect of 6 roof windows in the building envelope.

	Thermal transmittance [W/(m^{2}K)]	Area [m^2]
External walls	0.15	120
Windows in walls	0.8	46
Doors	1.0	2
Pitched roof	0.10	134
Roof windows (6pcs a 1m^2)	0.8	6
Floor	0.25	100
Overall effect of thermal couplings between building components	+2 %	--

Table 2. Distribution of transmittance heat loss for a pitched roof of the family house with 6 roof windows. Alternative **A** corresponds to traditional solution around year 2000, alternative **B** for passive house quality roof with traditional roof windows, alternative **C** for passive house quality with high performing windows.

	Thermal transmittance	Heat transfer coefficient			Overall increase [%] (100 % = no windows)
		[W/K]	[%]		
A					
Roof	0.3 W/(m²K)	40.2	69	69	
Roof windows	1.8 W/(m²K)	10.8	19		
Thermal coupling by installation	0.3 W/(mK)	7.2	12	} 31	
Total		58.2	100		139
B					
Roof	0.1 W/(m²K)	13.4	49	49	
Roof windows	1.5 W/(m²K)	9.0	33		
Thermal coupling by installation	0.2 W/(mK)	4.8	18	} 51	
Total		27.2	100		194
C					
Roof	0.1 W/(m²K)	13.4	77	77	
Roof windows	0.6 W/(m²K)	3.6	21		
Thermal coupling by installation	0.02 W/(mK)	0.5	2	} 23	
Total		17.5	100		125

DETAILED STUDY

A roof window in typical geometry, usual opening system (horizontal pivot casement) and typical installation in the roof was the subject of thermal analysis during our real development process (UCEEB, 2017) (Figure 5). Frame combining wood (assumed thermal conductivity 0.12 W/(mK)) and hard polymer parts (0.04 W/(mK)) together with two types of glazing (U_g 0.30 and 0.50 W/(m²K)) units were used. Installation is assumed to be carried out using thermal insulating installation frame in the roof (demonstrated here by block of extruded polystyrene thickness 100 mm) or traditionally without such additional frame. Two geometries of interior side lining are assumed: perpendicular to the window or symmetrically slanted (opened) to the interior with an angle of 45°. All data are based on 2D calculations of heat conduction for 4 typical cross sections of windows and related to the reference size 1.14 m x 1.40 m. The thermal transmittance of respective frames and linear thermal transmittance of glazing edges were calculated according to EN ISO 10 077-2. Adiabatic boundary layer was set according to EN ISO 12 567-2. The ratio of glazed area to full projected area of the window is 0.63.
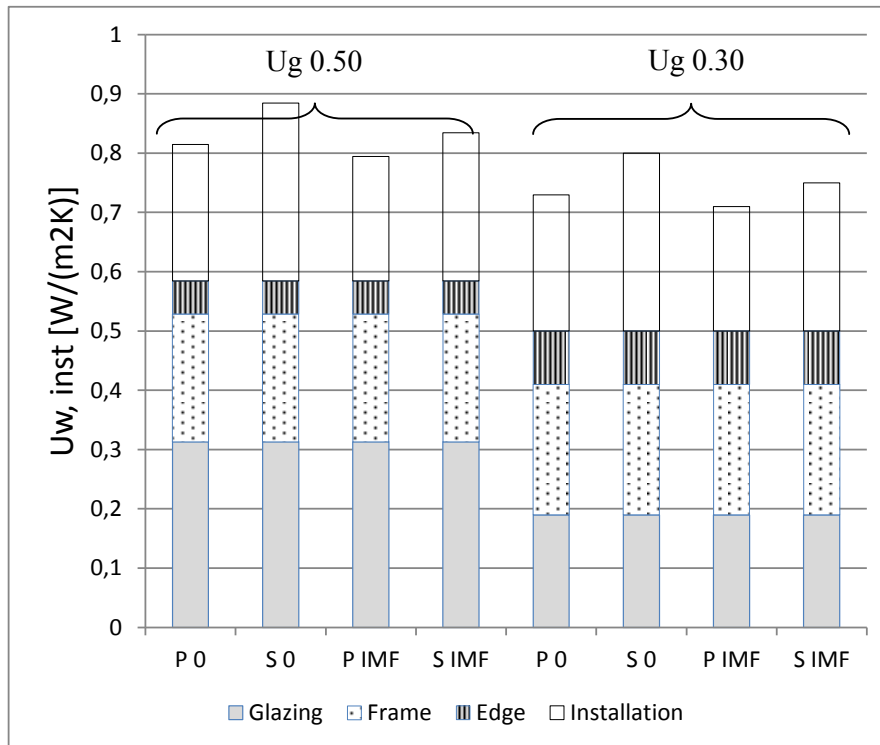
Figure 5. Thermal transmittance of roof windows with the newly developed frame (U_f 0.59 W/(m^{2}K)) and two types of glazing (Ug 0.30 and Ug 0.50 W/(m^{2}K) respectively). (P for perpendicular, S for slanted side lining, IMF for insulating mounted frame)

The results presented in Fig. 5 can be summarized as follows: Even with the (still un-usual) best glazing unit (U_g = 0.30 W/(m^{2}K)) and optimized window frame (U_f = 0.59 W/(m^{2}K)), the U-value of the window installed in typical configuration (P 0) is 0.72 W/(m^{2}K). With a standard triple-glazed unit (U_g = 0.50 W/(m^{2}K)) the overall U-value rises to 0.88 W/(m^{2}K).

The thermal coupling due to installation, which can be hardly avoided, plays a significant role in both cases ($\psi_w \cdot l_w$ = 0.23 W/(m^{2}K)).

The additional thermal insulating frame (IMF) has effect only in combination with slanted interior lining (S), where it lowers the thermal transmittance of about 0.05 W/(m^{2}K). The installation with slanted interior lining (S 0) has higher thermal transmittance of about 0.05 W/(m^{2}K) compared to perpendicular case (P 0). However, this solution may still be preferable due to better distribution of daylight.

RESULTS
The relative high influence of roof window for overall thermal transmittance was identified. In order to reach the passive house criteria the increased thermal loss even by the best possible roof windows has to be compensated. It is advantageous to combine the best glazing with a frame having the thermal transmittance in the same range. Best option seems to be the use of a high performing insulation material directly in the frame. In order to reduce the negative impact of the installation in the roof additional installation components (mounting frames) can be used or (better) the window frame itself should contain corresponding continuing thermal insulation material on its perimeter.

1453

The geometry of side lining (widening to interior) has no significant negative influence on heat loss due to limited amount of thermal insulation there (UCEEB, 2017).

CONCLUSION AND OUTLOOK
Consistent and complex application of building physic instruments can effectively accompany ongoing development works. All parts of future roof window should be optimized in order to achieve plausible results: Of critical importance is the frame in terms of material choice and shape. The form of installation has a big influence on the final result as well.

Based on these findings our research will continue in following directions:
a) Developing and testing of a real solution together with industrial partner according to already performed theoretical and experimental studies (not published here). It is expected that the frames will be alternatively made of hard polymer with appropriate surface layer (high pressure laminate. veneer lumber etc.) or made of high quality wood profiles combined with hard polymer.
b) Continuation in theoretical and experimental research concerning heat transfer at surfaces of windows in order to guarantee no condensation risk there, especially for situations without possible positive effects of heating bodies placed bellow.
c) Continuation (UCEEB, 2017) in day-lighting experimental studies for optimum size and installation. The side lining widened to interior can support better distribution of daylight. In general, such measure can lead to sufficient daylight with smaller window areas which has an additional energy saving effect.
d) Studies about optimum shading and estimation of overheating risks.

ACKNOWLEDGEMENT

References

EN ISO 10 077-2. Thermal performance of windows, doors and shutters - Calculation of thermal transmittance - Part 2: Numerical method for frames
EN ISO 12 567-2. Thermal performance of windows and doors - Determination of thermal transmittance by hot box method - Part 2: Roof windows and other projecting windows
PHI, 2018a: https://database.passivehouse.com/de/components/list/roof_window. 25.2.2018
PHI, 2018b: http://www.passiv.de/downloads/03_zertifizierungskriterien_transparente_bau-teile.pdf
UCEEB, 2017. Project TH01021120 Interim report, not public.
CSN 73 0540-2, 2011 Thermal protection of buildings. Part 2 -Requirements, UNMZ 2011

Nomenclature
U thermal transmittance $W/(m^2 K)$
A area m^2
l length m
ψ linear thermal transmittance $W/(m.K)$

indexes
g glazing, f frame, w window, inst installed

Sensitivity Analysis Using the SWMM LID Control for an Extensive Green Roof in Syracuse, NY

Lucie L. Worthen[1,*]and Cliff I. Davidson[1,2]

[1]Department of Civil and Environmental Engineering, Syracuse University, 151 Link Hall, Syracuse, NY 13210
[2]Center of Excellence in Environmental and Energy Systems, Syracuse University, Syracuse, NY 13210

[*]*Corresponding email: llworthe@syr.edu*

ABSTRACT

Green roofs are a popular form of sustainable drainage infrastructure. They provide many environmental benefits, such as reducing peak urban stormwater runoff by enabling retention and evapotranspiration similar to natural conditions. Each green roof has unique hydrologic behavior based on physical properties of its growth medium, types of vegetation, structural design, and climate. To improve the application of green roof technology at a site, there is a need to predict stormwater mitigation for several designs before commencing green roof construction. The Storm Water Management Model (SWMM) includes a low impact development control module which makes it possible to model the hydrologic performance of a green roof by directly defining the physical characteristics of its layers. In this study we compare the outputs of the SWMM model with hydrologic performance data from a large extensive green roof in Syracuse, NY from April 2017 to October 2017. Our objectives are to evaluate the performance of SWMM as a long-term modeling software appropriate for predicting the hydrologic performance of a green roof, and to explore changing parameters that might improve hydrologic performance when designing future green roofs. It is expected that this work will help designers of green roofs in climates similar to those of Central NY. In the future, more extensive hydrologic data will be obtained to enable better assessment of SWMM as a tool to help design green roofs.

KEYWORDS
Green roof, SWMM, Green roof modelling, Stormwater management, Green infrastructure

INTRODUCTION
Urbanization contributes to an increase in impervious surfaces and a decrease in land area covered by soil and vegetation. This reduces ecosystem services such as infiltration and evapotranspiration, leading to an increase in urban stormwater runoff. Green infrastructure (GI), which is an important component of low impact development (LID), is being used in urban settings to restore ecosystem services. Green roofs, a form of GI, can restore ecosystem services by retaining and detaining stormwater runoff (Carson et al. 2013; Li and Babcock, 2014) and increasing urban biodiversity (Baumann, 2006; Francis and Lormier, 2011).

Monitoring studies have been conducted to understand the hydrologic performance of green roofs (Peng and Stovin, 2017). Since green roofs vary in configuration, they can range in retention and detention rates (Carson et al. 2013). Though many studies have aided in understanding green roof performance (Heusinger et al. 2018), this indicates the need for engineers to accurately forecast green roof performance through the application of modelling whenever a new green roof is built. The Storm Water Management Model (SWMM) is the most

commonly used commercial hydrologic and hydraulic model and provides a quick assessment tool for quantifying the hydrologic performance of GI (Li and Babcock 2014).

The first objective of this study is to assess the SWMM model as a tool for predicting hydrologic performance of a green roof by comparing model outputs with monitoring data from a full-scale, extensive green roof located in Syracuse, NY. The second objective is to perform a sensitivity analysis which will lead to future adjustment of the model parameters and verification. This research is still in an early phase.

METHODS
Green Roof Test Site
The study site is a 5550 sq. meter green roof located on the roof of the Nicholas J. Pirro Convention Center (the OnCenter) in downtown Syracuse, New York (43.04368N, 76.14824W). See Squier-Babcock and Davidson (2018) for a detailed description of the site, drainage design, and monitoring equipment.

Precipitation, runoff, and temperature data have been collected between 4/1/17 and 10/31/17 at 5-minute intervals. Common retention and detention metrics are used to quantify performance. Retention is calculated cumulatively for the entire monitoring period. For the purposes of comparison, rainfall and runoff are expressed as equivalent depth in mm.

EPA SWMM Model
The EPA Storm Water Management Model (SWMM version 5.1.012) is a dynamic hydrology, hydraulic, and water quality simulation model that can be used for both single-event or continuous simulation (Rossman, 2015). The LID controls in SWMM are designed to specifically model GI, such as green roofs. The LID controls work by performing and tracking moisture balances between different vertical layers that are defined by parameters in the graphical user interface.

To model restoration of retention capacity, SWMM has five methods for calculating Potential ET (PET). In this study, following the methods of Peng and Stovin (2017), monthly PET values are calculated using the Hargreaves equation (Marasco et al. 2015) which is standard in SWMM. Note that SWMM models ET strictly as a constant proportion of PET and does not automatically account for the reduction in actual ET (AET) that occurs during moisture limited periods. The proportion can generally be used to account for crop variability or moisture limited months (Peng and Stovin, 2017). For this analysis, the proportion was initially set to 1.

The green roof is modelled in SWMM as a subcatchment that is 100% occupied by the green roof and has an outlet. The dimensions of the subcatchment are 111 m width by 50 m length since the water flow path is perpendicular to the width, which represents the actual flow path of the OnCenter roof. To test the accuracy of the ET component of the model for predicting long-term retention, SWMM is used to generate runoff for the period of 4/1/17 to 10/31/17 at an hourly temporal resolution, avoiding periods of freezing.

The long-term simulation used observed precipitation from the OnCenter green roof site. Monthly PET values were calculated with monthly temperature minimums, maximums, averages, and the geospatial location of the OnCenter. The initial green roof parameter values were estimated from field measurements by Squier and Davidson (2016), Yang and Davidson (2017), and CH2M who performed the initial modelling studies of the OnCenter green roof, and SWMM default values. The values and sources for each parameter utilized in the SWMM Bioretention Module are presented in Table 1.

Table 1. SWMM Parameters and Initial Values for Uncalibrated Simulations

Parameter	Initial Value	Data Source
Subcatchment		
ET coefficient	1	Default
Area	5600 m^2	Squier and Davidson (2016)
Width	110.8 m	Squier and Davidson (2016)
Surface Layer		
Berm Height	0	CH2M Estimate
Vegetation Volume	0	CH2M Estimate
Surface Roughness	0.4	CH2M Estimate
Surface slope	1%	Squier and Davidson (2016)
Soil (substrate)		
Thickness	7.6 cm	Squier and Davidson (2016)
Porosity	0.5	Yang and Davidson (2017)
Field capacity	0.2	CH2M Estimate
Wilting point	0.1	CH2M Estimate
Conductivity	32,400 mm/hr	Yang and Davidson (2017)
Conductivity slope	10	CH2M Estimate
Suction head	41.7 mm	CH2M Estimate
Storage		
Thickness	304.8 mm	CH2M Estimate
Void ratio	0.02	CH2M Estimate
Seepage Rate	0	CH2M Estimate
Clogging Factor	0	CH2M Estimate
Drain		
Flow coefficient	0.075	CH2M Estimate
Flow exponent	0.5	CH2M Estimate
Offset Height	0	CH2M Estimate

Sensitivity Analysis

To determine the parameters that would most effectively minimize the difference between observed and simulated results, a sensitivity analysis was performed using the long-term simulation results. The method suggested by Rosa et al. (2015) and Peng and Stovin (2017) was followed, where each single parameter is adjusted over a range of plus or minus 10 and 50 percent of its original value while holding the other parameter values constant. The difference in annual retention and annual runoff volume were determined for the long-term simulation. Sensitivity was calculated using Eq. (1) (Rosa et al. 2015; Peng and Stovin, 2017):

$$Sensitivity = \left(\frac{\delta R}{\delta P}\right)\left(\frac{P}{R}\right) \tag{1}$$

Where δR = the difference between the original and the new model output; δP = the difference between the original and the adjusted parameter value; R = the original model output; and P = the original value of the parameter.

Validation

The Nash-Sutcliffe model efficiency (NSME) coefficient in Eq. 2 (Nash and Sutcliffe, 1970) was used to reflect the accuracy of the model results as compared to the collected data. An NSME value equal to 1 indicates that the model predicted the performance of the green roof

perfectly, while an NSME value greater than 0.5 is still an indication of acceptable model performance (Rosa et al. 2015, Peng and Stovin, 2017). The long-term simulation hourly results were compared in this study to determine an NSME value.

$$NSME = 1 - \left[\frac{\Sigma_1^N (Q_m - Q_p)^2}{\Sigma_1^N (Q_m - Q_{Am})^2} \right] \tag{2}$$

where N = number of samples; Q_m = runoff observed; Q_P = modeled runoff; and Q_{Am} = mean observed runoff.

In the future continuation of this work, single events will be modelled and evaluated with NSME. The subsequent NSME values from this study and future studies will lead to evaluation of the model.

RESULTS
Uncalibrated Long-Term Simulations
Long-term simulations run with these initial parameter values show less than ideal agreement. The cumulative runoff predicted by SWMM totaled 345 mm while the cumulative runoff collected from the green roof totaled 451 mm, or about 100 mm difference. As Figure 1 shows, the model consistently underestimates the amount of runoff compared with the observations. The value of NSME is -0.07. One possible cause of the disagreement is that SWMM may be overestimating ET; work is underway to explore the reasons for the difference. These are the very first results using SWMM with this green roof, and we expect results will improve as we continue to measure roof characteristics rather than using default values and estimates.

Sensitivity Analysis
The results of the sensitivity analysis are presented in Table 2. The negative sensitivity values indicate a decrease in corresponding runoff volume or annual retention, while positive values indicate an increase. The total runoff volume and annual retention were found to be influenced by the ET coefficient, the soil field capacity, and the soil wilting point. The surface slope, soil porosity, soil conductivity, conductivity slope, suction head, storage void ratio, drain flow coefficient, and drain flow exponent were found to have less impact on the model results. For one run, the values were not valid because porosity cannot be smaller than field capacity. Both the annual retention and the total annual runoff were most sensitive to a change in the soil field capacity, followed by the wilting point, and then the ET coefficient. Field capacity influences the retention capacity; wilting point and ET influence retention recovery. Both retention capacity and recovery are essential contributors to annual retention performance. The importance of both ET and field capacity in green roof performance have been cited in many studies (Peng and Stovin, 2017; Cipolla et al. 2016; Stovin et al. 2013).

DISCUSSION
The SWMM bioretention module for a green roof with a drain has the potential to be an accurate model representation. However, the initial results of consistently underestimating runoff points to the way that a green roof's storage capacity is restored – ET. The sensitivity analysis identifies the importance of ET in green roof retention, which is well supported by many studies (Stovin et al. 2013; Peng and Stovin, 2017). The use of the Hargreaves equation, a temperature-based model for ET, and the standard option in SWMM, could contribute to overestimate ET during moisture limited conditions. Further examination of alternative options for ET modeling will be explored, specifically related to energy-based models and PET verses AET, in pursuit of model simulation and observed agreement with data.

Table 2. Sensitivity of Annual Retention and Annual Runoff Volume to SWMM Bioretention Parameters Adjusted ±10% and ±50%

| Parameter	-50%		-10%		10%		50%	
	Annual Retention	Runoff Volume	Annual Retention	Runoff Volume	Annual Retention	Runoff Volume	Annual Retention	Runoff Volume
ET coefficient	-0.343	0.369	-0.277	0.292	0.229	-0.247	0.187	-0.202
Surface slope	0	0	0	0	0	0	0	0
Soil porosity	-0.0004	0.0004	0	0	0	0	0	0
Soil field capacity	-	-	-1.045	1.127	0.936	-1.010	0.667	-0.720
Soil wilting point	0.414	-0.447	0.471	-0.508	-0.508	0.547	-0.583	0.629
Soil conductivity	0	0	0	0	0	0	0	0
Conductivity slope	0	0	0	0	0	0	0	0
Suction head	0	0	0	0	0	0	0	0
Storage void ratio	0.003	-0.004	0.005	-0.005	0	0	0	0
Drain flow coefficient	0.001	-0.002	0	0	0	0	0	0
Drain flow exponent	0.001	-0.002	0	0	0	0	0	0
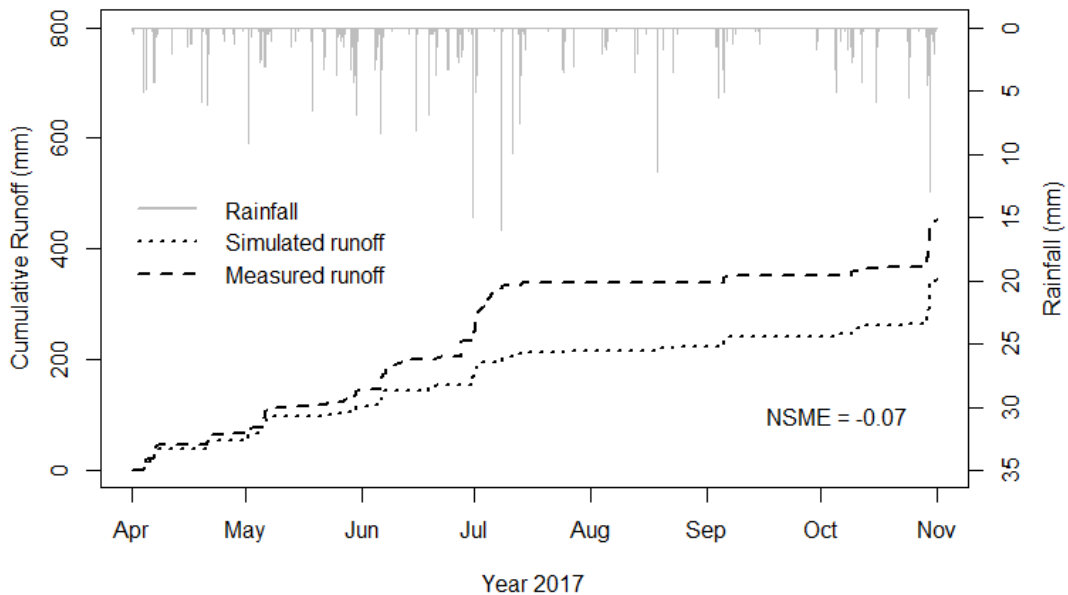
Figure 1. Uncalibrated long-term simulation. NSME calculated from hourly runoff. The rainfall is given in mm for each 1 hr timestep. The runoff is given as cumulative depth in mm.

CONCLUSIONS

The initial comparison of the results obtained from the OnCenter green roof and the SWMM bioretention module needs further investigation before concluding that the model can represent the hydrology of a green roof. The concepts of accurate PET verses AET and antecedent dry weather period are important for green roof model representation. This study is merely a first step in validating SWMM as an accurate model for a green roof in Syracuse, NY.

ACKNOWLEDGMENTS

REFERENCES TO BE UPDATED

Baumann, N. (2006). "Ground-nesting birds on green roofs in Switzerland: Preliminary observations." Urban Habitats, 4(1), 37–50.

Carson, T. B., Marasco, D. E., Culligan, P. J., and McGillis, W. R. (2013). "Hydrological performance of extensive green roofs in New York City: observations and multi-year modeling of three full-scale systems." Environmental Research Letters, 8(2), 024036.

Cipolla, S. S., Maglionico, M., & Stojkov, I. (2016). A long-term hydrological modelling of an extensive green roof by means of SWMM. Ecological Engineering, 95, 876–887.

Francis, R.A. and Lorimer, J., 2011. "Urban reconciliation ecology: the potential of living roofs and walls." Journal of Environmental Management, 92, 1429–1437.

Heusinger, J., Sailor, D. J., & Weber, S. (2018). "Modeling the reduction of urban excess heat by green roofs with respect to different irrigation scenarios." Building and Environment, 131, 174–183.

Li, Y. and Babcock, R.W., 2014. "Green roof hydrologic performance and modeling: a review." Water Science and Technology, 69, 727–738.

Marasco, D. E., Culligan, P. J., & Mcgillis, W. R. (2015). "Evaluation of common evapotranspiration models based on measurements from two extensive green roofs in New York City." Ecological Engineering, 84, 451–462.

Nash, J. E., and Sutcliffe, J. V. (1970). "River flow forecasting through conceptual models. Part I: A discussion of principles." J. Hydrol. (Amsterdam, Neth.), 10(3), 282–290.

Peng, Z., & Stovin, V. (2017). Independent Validation of the SWMM Green Roof Module. Journal of Hydrologic Engineering, 22(9), 1–12.

Rossman, L., 2015. Storm Water Management Model Reference Manual Volume I-Hydrology.

Squier, M. and C. I. Davidson (2016), "Heat flux and seasonal thermal performance of an extensive green roof." Building and Environment, 107 235-44.

Squier-Babcock, M and C. I. Davidson (2018), "Hydrologic performance of an extensive green roof system in Syracuse, NY." Manuscript in preparation.

Stovin, V., Poë, S., & Berretta, C. (2013). "A modelling study of long term green roof retention performance." Journal of Environmental Management, 131, 206–215.

Yang, Y. and C. I. Davidson (2017), "Green roof performance influenced by growth medium characteristics", Poster Presentation, 15th Annual New York State Green Building Conference, Syracuse, NY, March 30-31, 2017.

Simulation of Building Physics for Beginning Design Students

Alexander Timmer[1]

[1]University of Wisconsin – Milwaukee, Milwaukee

*Corresponding email: timmer@uwm.edu

ABSTRACT
Concepts such as heat transfer, stack effect, natural ventilation, and other problems related to building physics are taught to beginning design students through architectural examples, deterministic diagrams, and rules of thumb. Unlike the approach to teaching form, which involves exploration and iteration within a studio environment, often suspending disbelief to allow exploration, these exercises see architecture through the lenses of optimization, equilibrium, and objective outcomes. They are taught as steady state concepts. Instead of leaning on teaching techniques derived from an engineering standpoint, often technocratic and deterministic, it would serve beginning design students well to explore these concepts through experimentation and scaled built models that demonstrate the intended atmosphere effect. Can we ask the students to think compositionally about an architectural atmosphere in the way we ask them to think about form, proportion, sequence, and hierarchy? The goal then is to have students learn to think about atmosphere and energy from a design standpoint. As Kiel Moe notes, this point of view comes from an understanding of architecture and energy as one of magnificence and not of management. (Moe, 2017) With the help of students at the University of Wisconsin – Milwaukee, this research looks to explore reciprocal design techniques that allow students to iterate within an open system of their design. This ongoing investigation looks to grow the rigor and accessibility of scaled physical simulation of atmosphere and energy in buildings within a beginning design student studio.

KEYWORDS
Buoyancy Ventilation, Simulation, Physical Models, Early Design Education, Design Process

INTRODUCTION
This research is focused on the physical simulation of building physics. This ongoing research attempts to balance a desire for the visual representation of building physics for use in the architectural design studio with a repeatable and measurable outcome. While the primary purpose of the model is not measurement, the various inputs of heat and matter are scaled appropriately. Using the concept of similitude, this model is scaled to allow for the building of a representational section, which can then be heated to demonstrate the flow of fluid through the section. While focusing primarily on the simulation of buoyancy ventilation in two dimensions, this project develops a working methodology that encourages iteration. Students design parts within Rhino 3D, print them with a 3D printer, test them in the rheoscopic fluid bath, document them with a long exposure camera, evaluate the results and then repeat the process. This work was completed as part of an exhibition and workshop at the University of Wisconsin – Milwaukee.

METHODS
This design exercise asked students to work through a fixed loop. Students design a section within Rhino 3D, print them with a 3D printer, test them in a rheoscopic fluid bath, document them with a long exposure camera, evaluate the results and then repeat the process. The first

step is the design of an initial section in Rhino 3D, a NURBS modelling software. Students are asked to produce sectional models in which the wall thickness is fixed at .8mm. While the first section is a guess on the student's part, the next model made will be informed by the process to come. The second step is the printing of the student's design. Students print their sections 6mm thick out of PLA plastic. For the third step students place their prints into a heated bath. The parts are pinched between a piece of glass and the milled aluminium back which heats that fluid. The medium of the bath is a rheoscopic fluid that makes the flow visible. (Figure 3) A heating element is mounted to the back of the aluminium half of the tank. After this, students document the sections with a camera, make changes to their design and repeat the process. The models where scaled using similitude and the Galileo Number. (Etheridge, 2011)

RESULTS
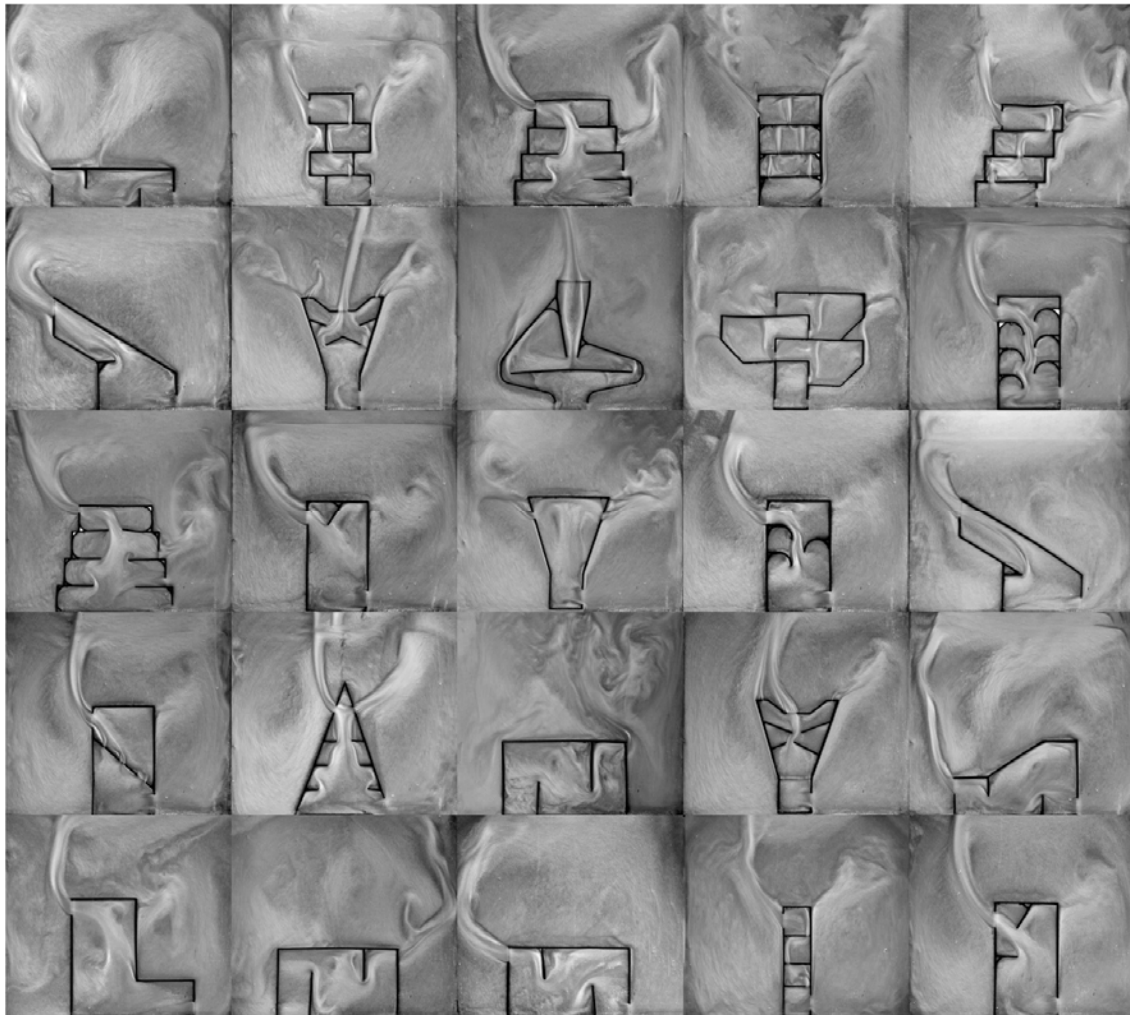
Figure 1. Iterations produced by the students.

The students produced a wide range of examples. (Figure 1,2) The studies often led to a series of variations in which each student explored the role of shape, form, and proportion in the flow of fluid by buoyancy ventilation. The more successful explorations used simple forms to better understand the effects of their design decisions. While the models are essentially two dimensional, they offer a way into the process of natural ventilation from the point of view of

a designer. The work was exhibited and functioned as a workshop to introduce the students to the concept of buoyancy ventilation. (Figure 4, 5, 6)
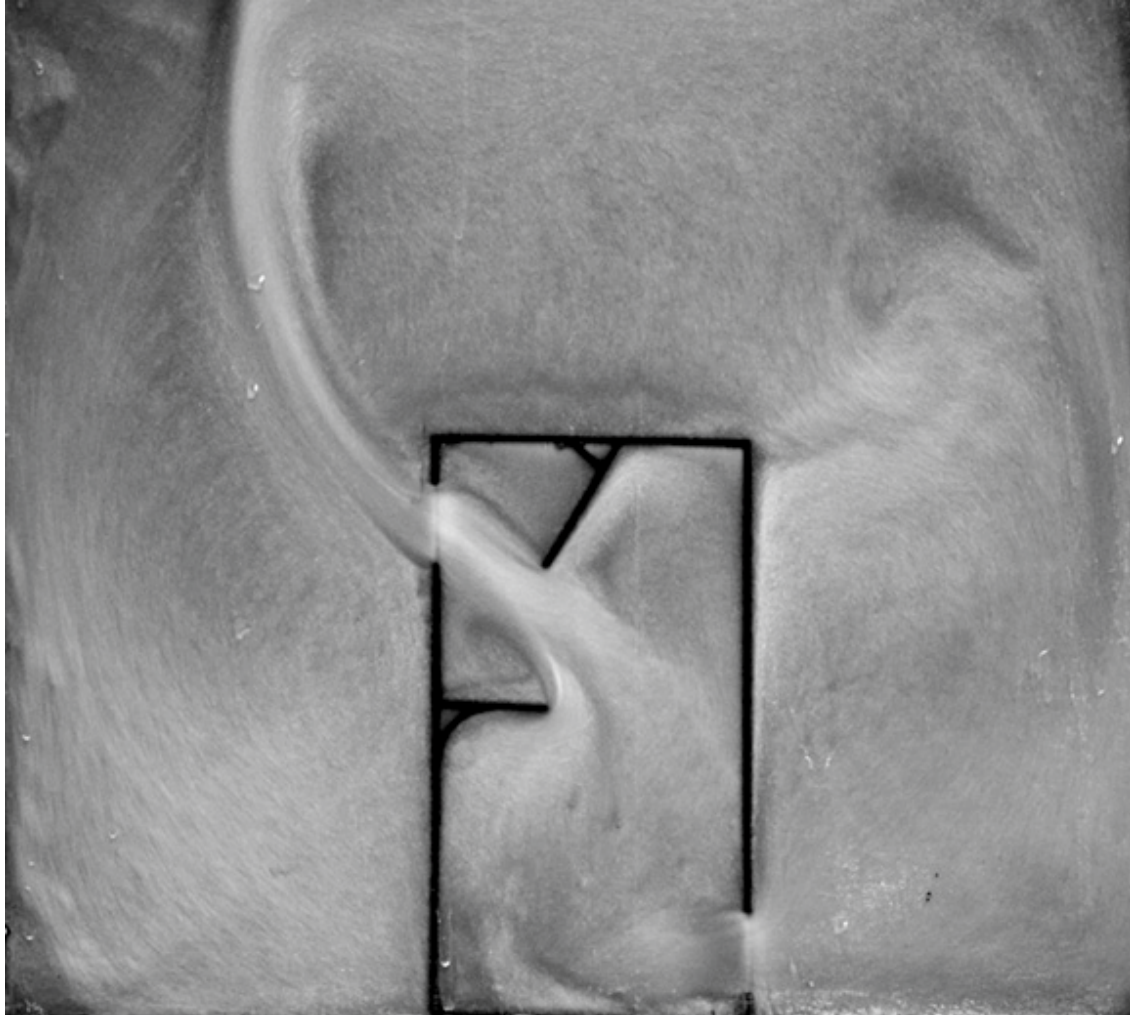
Figure 2. Long exposure documentation of rheoscopic fluid.

Figure 3. Rheoscopic fluid tank with section.

Figure 4. Exhibition and workshop.

Figure 5. Exhibition and workshop.

Equations

$$Ga_M \equiv \left[\frac{\Delta T_0}{T_0}\right]_P \left[\frac{\Delta T_0}{T_0}\right]_M Ga_P \tag{1}$$

Using dimensionless analysis similarity between the model and prototype can be achieved by increasing the ΔT_0 in the model. This equation assumes a simple single cell enclosure in which ventilation is achieved with buoyancy only. (Etheridge, 2011)

Names and units

Ga   Galileo Number
T   Temperature, C°

DISCUSSIONS
The most problematic aspect of these models is the lack of three dimensionality. While the two-dimensional model allows students to understand some of the basic concepts of buoyancy ventilation, it lacks the complex reality of a three-dimensional model. The appropriate application of this pedagogy to the design of a building, not merely proto architectural objects, requires more research. In general, though the next steps in this research will require a transition to three dimensions. Additionally, while this modeling technique allows for the visual approximation of heat driven flows, it does not at this time allow for the measurement of the rate of flow. Although, the appropriate scaling of the model and its heat input should allow for a measurable rate of flow through the openings by mathematical means. As mentioned before, the intended goal of this exercise is the development of a pedagogy that encourages design students to explore building physics as an opportunity for design and spatial innovation.

CONCLUSIONS
When we think of architectural models, we think of them as objects, representational at best, a stand-in for a larger construct. While this has not always been the case historically, new digital measures seek to reduce the physical model further to merely the output of a printer: a stereotomic afterthought. Renaissance model makers, for example, used the model as a stand-in for construction documents that were intended to assist the builders with complex geometry, calculating structural loads, and testing the quality of light. These models participated in the construction of buildings. At the Bauhaus, making was integral to the introductory design exercises, asking students to fold the paper and imagine the spatial and sculptural qualities. The paper though was not a stand-in for another material but the material of study itself. With the advent of the digital model, and more recently the BIM model, the physical artifact has been pushed out. In its transformation, it has lost its material intelligence and its active role in the design process. It has been reduced to a representational artifact and an imperfect imitation of its digital doppelganger. What then is the role of the contemporary physical model, what could its role be in contemporary design practice?

These new operative artifacts find themselves between a study model and a finished representational model. They hang ambiguously between these two states. They are far from pristine, but they are highly rigorous and intensely participatory. They are objects that both represent a complete thought and speak to a possible future. These objects develop out of an understanding of design as an open system, a series of inputs and outputs, in which the model is understood as an active participant in the design process rather than passive byproduct.

ACKNOWLEDGEMENT

REFERENCES

Etheridge, D. (2011). Natural ventilation of buildings: theory, measurement and design. Retrieved from https://ebookcentral.proquest.com

Moe, K. (2017). Magnificence: On the Appearance of the Baths of Caracalla, Journal of Architectural Education, 71:2, 241-246

Study on multivariate regression model of indoor and outdoor particulate pollution in severe cold area of China

Yang Lv[1,*], Haifeng Wang[1], Yuwei Zhou[1], Tongke Zhao[1], Bin Chen[1], Lei Zhang[2], Qi Zhao[2]

[1]Dalian University of Technology, Dalian
[2]Northeast Petroleum University, Daqing

*Corresponding email: *lvyang@dlut.edu.cn*

ABSTRACT

At present, the widespread existence of haze phenomenon has a serious impact on indoor air quality. Indoor particulate pollution has been paid more and more attention by the society. However, the correlation and diffusion mechanism of indoor and outdoor particulate matter are still controversial. In order to explore the correlation between indoor and outdoor particulate matter of different building types in heating season and non-heating season, the indoor and outdoor particulate concentrations and meteorological parameters of 110 stations in severe cold area of China were monitored by experiments. The analysis shows that indoor and outdoor temperature, humidity, air velocity, wind direction and atmospheric pressure are the main factors affecting indoor and outdoor particulate concentration. And based on these factors, it can model the indoor predicted particulate concentrations by multivariate regression. It also shows a significant difference in the relationship between the concentration of particulate matter and factors of indoor and outdoor particulate matter. Therefore, this study provides a good premise for exploring the health risks and control measures of particulate matter.

KEYWORDS
Particulate Matter, Severe Cold Area, Correlation Analysis, Regression Model

INTRODUCTION
Human inhalable particulate matter (PM_{10}, $PM_{2.5}$) is the primary pollutant in most cities in China, especially for fine particulate matter ($PM_{2.5}$). More and more epidemiologists show that there is a positive correlation between human morbidity, mortality and mass concentration of particulate matter (Dockery et al. 1993; Zhao et al. 2015; Tseng et al. 2015; Cohen et al. 2017; Klemm R J et al. 1996). People spend 90% of their time indoors, so indoor air quality plays an important role in human health. The study showed that the outdoor pollution components can enter into the indoor air through natural ventilation, mechanical ventilation and infiltration ventilation. There is a significant correlation between the indoor and outdoor particles. The proportion of indoor $PM_{2.5}$ from outdoor is 30~75% (Dockery and Spengler, 1981; Koutrakis et al., 1992; Ozkaynak et al. 1995; Xiong et al. 2004).

The situation of indoor and outdoor particulate matter in severe cold area of China is different from that in other regions because of geographical location, climatic condition and building type. This paper will via the long-term monitoring of indoor and outdoor particulate concentrations to analyze the correlation between indoor particles concentrations and indoor and outdoor influencing factors of different building types in Daqing, which will provide parameters and basis for indoor particulate matter exposure assessment.

METHODS

Selection of measured objects and sampling points

The sampling points were located in five districts of Daqing which were total of 110 sampling points, including 30 classrooms, 30 offices and 50 residences, among which were divided into urban and rural residences. To get the seasonal variations of particulate pollution, we collected data of summer and winter from November 2016 to April 2017 and June to August 2016, respectively. A sampling point was sited in and out of each room, measured simultaneously. Each point was collected seven days of valid data. To analyze more accurately, the hourly average value of each sampling point was calculated. The measuring instrument includes QT50 particulate online monitor ($\pm 1\mu g/m^3$). The measurements contents include indoor and outdoor temperature, relative humidity and $PM_{2.5}$ mass concentration. The monitoring time was set to start every 15 minutes, and the data were collected for 5 minutes each time.

Data analysis and processing method

In this paper, the analysis data is mainly based on the hourly average of each parameter. With the SPSS software, the statistical analysis of sampling data was completed, and finished the multiple analysis such as bivariate correlation analysis and multiple linear regression.

Bivariate correlation analysis is an important method to evaluate the relationship between two of variables. Pearson coefficient (r) could measure the extent of correlations, which could be expressed as:

$$r = \frac{\sum (X - \bar{X})(Y - \bar{Y})}{\sqrt{(X - \bar{X})^2 (Y - \bar{Y})^2}} \quad\quad (1)$$

Where X and Y - variables, $\bar{X}$ and $\bar{Y}$ - the averages of variables. In this part, Pearson coefficient (r) is used to express the relationship between indoor particulate concentration and indoor and outdoor influencing factors (such as outdoor particulate concentration, temperature and humidity, etc.).

Multivariate linear regression is a regression with one dependent variable and two or more independent variables, each of which is a single term. It is one of the most commonly used statistical methods in the measurement of microenvironment or exposure of particulate matter. The mathematical model of multivariate linear regression can be expressed as follows:

$$y = a + b_1 x_1 + b_2 x_2 + \cdots + b_n x_n \quad\quad (2)$$

Where, y is a dependent variable; x_1, x_2 ... x_n are independent variables; b_1, b_2 ... b_n are coefficients of independence variables; a is a constant term. To ensure the accuracy of the regression model, the errors between the observed and predicted values of five performance

indexes are used in this paper: the normalized absolute error (NAE), the root mean square error (RMSE), the prediction accuracy (PA), the determinant coefficient (R^2) and the index of agreement (IA).

RESULTS AND DISCUSSIONS

Correlation Analysis between Indoor $PM_{2.5}$ concentration and factors

There are many factors affecting indoor particulate concentration, such as indoor particulate source strength, settling rate, air exchanges rate, penetration coefficient, building types and meteorological conditions. The results show that there is a certain relationship between indoor particulate concentration and them above, while little attention has been paid to this aspect in the present researches. By the method of bivariate analysis, Pearson correlation coefficient (r) was used to express the extent of the linear correlation between the indoor particulate concentration and these factors. The probability distribution value ($P < 0.05$) was considered to be statistically significant.

Table 1. The correlation analysis between indoor $PM_{2.5}$ concentration and affecting factors

Building type			T_{in}	RH_{in}	$PM_{2.5}$(Out)	T_{out}	RH_{out}	P	WD	WS
Office	Summer	r	0.027	0.289	0.734	0.030	0.126	-0.048	-0.183	0.092
		P	0.392	0.000	0.000	0.341	0.000	0.126	0.000	0.003
		N	1041	1041	1041	1041	1041	1041	1041	1032
	Winter	r	0.001	0.007	0.903	0.206	-0.063	-0.296	-0.036	0.198
		P	0.978	0.846	0.000	0.000	0.075	0.000	0.305	0.000
		N	806	806	806	806	806	806	806	806
Classroom	Summer	r	0.199	0.245	0.745	0.143	0.118	-0.083	-0.176	0.052
		P	0.000	0.000	0.000	0.000	0.000	0.008	0.000	0.038
		N	1032	1032	1032	1032	1032	1032	1032	1032
	Winter	r	-0.006	0.349	0.809	0.227	0.071	-0.076	-0.101	0.000
		P	0.862	0.000	0.000	0.000	0.034	0.024	0.003	0.990
		N	886	886	886	886	886	886	886	886
Urban residence	Summer	r	0.071	0.497	0.837	0.21	0.067	-0.235	0.038	0.112
		P	0.006	0.000	0.000	0.000	0.009	0.000	0.146	0.000
		N	1485	1485	1485	1485	1485	1485	1485	1485
	Winter	r	0.008	0.045	0.604	-0.111	0.144	0.027	-0.04	0.033
		P	0.797	0.152	0.000	0.000	0.000	0.392	0.195	0.291
		N	1028	1028	1028	1028	1028	1028	1028	1028
Rural residence	Summer	r	0.159	0.336	0.848	0.205	0.02	-0.217	0.129	0.13
		P	0.010	0.000	0.000	0.001	0.750	0.000	0.037	0.035
		N	263	263	263	263	263	263	263	263
	Winter	r	0.284	0.123	0.862	0.105	-0.034	-0.02	-0.089	0.092
		P	0.000	0.123	0.000	0.190	0.669	0.802	0.267	0.248
		N	158	158	158	158	158	158	158	158

Note: r-Correlation , P- Significance, N- Sampling times, T - Temperature, RH - Relative humidity, P - Atmospheric pressure, WD- Wind direction, WS- Wind speed

Table 1 compares the correlation analysis between indoor $PM_{2.5}$ concentration and indoor and outdoor factors of four building types in summer and winter, statistics of which have significant correlation has been bold. On the whole, it can be found that outdoor $PM_{2.5}$ concentration has the strongest correlation with indoor $PM_{2.5}$ whether it is summer or winter. Indoor $PM_{2.5}$ concentration is positively correlated with indoor and outdoor temperature, humidity and outdoor wind speed, negatively correlated with outdoor atmospheric pressure, and both positively and negatively correlated with outdoor wind direction. However, all these factors are significantly related to indoor particulate concentration for summer. For winter, the main factor of indoor $PM_{2.5}$ concentration is outdoor particulate concentration, the influence of other factors is relatively little. The primary explanation is that the main ventilation mode of the measured buildings is natural ventilation during summer, outdoor particulate matter can enter into the indoor environment which is vulnerable to wind pressure and hot pressure. Outdoor wind speed and atmospheric pressure will affect the indoor and outdoor air exchange rate and the concentration of indoor particulate matter. For the season of winter, the indoor temperature is constant due to the use of heating equipments, which has little effect on the diffusion and transfer of particulate matter. At the meanwhile, doors and windows are always closed and the impermeability of enclosure structure is well, the change of outdoor atmospheric pressure has little effect on the permeation process of indoor particulate matter.

Multivariate regression model fitting
According to the correlation analysis above, it found that all the factors mentioned could affect indoor particulate concentration. Based on these factors, a multivariate linear regression model of indoor $PM_{2.5}$ concentration prediction was proposed. In order to ensure the reliability of the results, the data is divided into two groups, one composed of 70% of the original data for regression, and the other 30% is used to verify the regression model. Table 2 shows the regression model between indoor particulate concentration and factors of four building types in summer and winter. The simulation results are standardized to ensure the comparability among the model parameters, which can be found that the range of determining coefficient R^2 obtained by calculation of four building types in summer and winter is 0.57 ~ 0.85, indicating that the model has a strong fitting.

Table 2. The regression model between indoor particulate concentrations

	Season	R^2	model
Office	Summer	0.57	$y=0.15x_1+0.28x_2+0.62x_3+0.09x_4+0.04x_5-0.05x_6-0.10x_7-0.05x_8$
	Winter	0.85	$y=0.02x_1-0.03x_2+0.94x_3-0.01x_4+0.01x_5+0.06x_6+0.06x_7+0.04x_8$
Classroom	Summer	0.67	$y=0.09x_1+0.14x_2+0.77x_3+0.02x_4+0.04x_5+0.14x_6-0.03x_7+0.02x_8$
	Winter	0.69	$y=-0.03x_1+0.15x_2+0.80x_3-0.10x_4-0.05x_5+0.01x_6+0.02x_7-0.03x_8$
Urban residence	Summer	0.67	$y=0.09x_1+0.23x_2+0.76x_3-0.02x_4-0.02x_5+0.02x_6-0.03x_7-0.05\ x_8$
	Winter	0.69	$y=0.08x_1+0.07x_2+0.65x_3-0.04x_4+0.02x_5+0.01x_6+0.01x_7+0.02x_8$
Rural residence	Summer	0.67	$y=0.22x_1+0.14x_2+0.73x_3-0.06x_4-0.11x_5-0.05x_6+0.05x_7+0.03x_8$
	Winter	0.69	$y=0.20x_1+0.06x_2+0.83x_3-0.03x_4-0.09x_5+0.11x_6-0.05x_7-0.02x_8$

Note: x_1- Indoor temperature; x_2-Indoor humidity; x_3-Outdoor $PM_{2.5}$ concentration; x_4-Outdoor temperature ; x_5-Outdoor humidity; x_6-Outdoor atmospheric pressure; x_7-Outdoor Wind Direction; x_8-Outdoor air velocity

Table 3. The results analysis of performance indicators

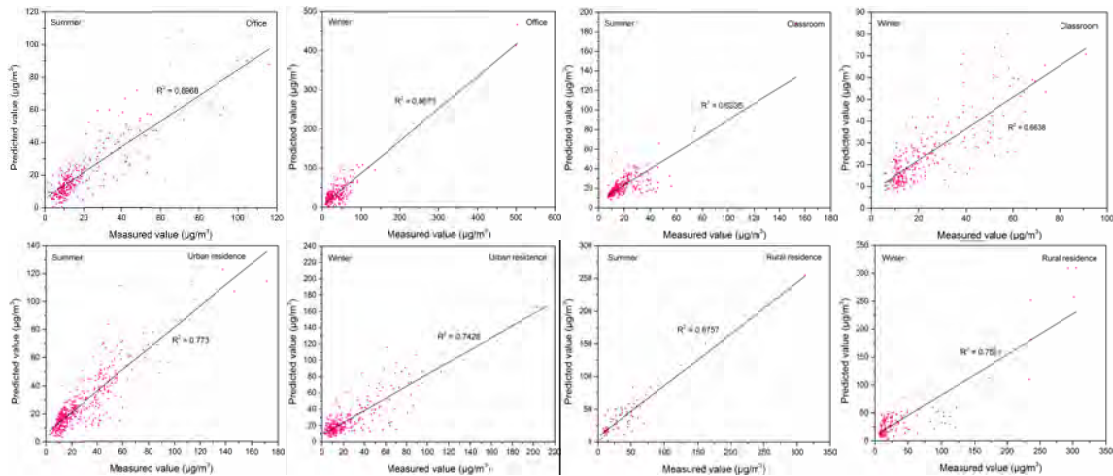|	Office		Classroom		Urban residence		Rural residence	
	Summer	Winter	Summer	Winter	Summer	Winter	Summer	Winter
NAE	0.290	0.344	0.341	0.306	0.271	0.385	0.269	0.527
RMSE	10.250	20.540	8.420	9.710	10.730	14.510	16.890	32.230
R^2	0.740	0.868	0.684	0.664	0.773	0.743	0.876	0.756
PA	0.537	0.834	0.820	0.630	0.122	0.661	0.405	0.628
AI	0.719	0.680	0.724	0.682	0.699	0.997	0.700	0.556

Figure 1. The comparison between predicted and measured values of regression model

According to the results of regression model in Table 2, the predicted value of the model is compared with the measured by 30% test data. Figure 1 is the result of comparison of each model. It can be found that there is a strong correlation between the measured and predicted values of indoor PM$_{2.5}$ concentration. Table 3 shows the analysis results of the errors between the measured values and the predicted values of five performance indexes, the values of NAE, RMSE are relatively small and R^2, PA and IA are close to 1, which indicates that the prediction model and the method are practical to some extent.

Comparative analysis of model parameters
Table 2 shows the regression results of the model parameters standardization. According to the comparative analysis , it can be found that the outdoor PM$_{2.5}$ concentration plays a leading role in the model, whether it is summer or winter, air velocity and wind direction are relatively weak, while the other parameters have their diversities respectively. For heating season, the influence of indoor temperature and humidity account for a large proportion of the model, while small in the non-heating season. Therefore, the correlation between indoor particulate concentration and all the parameters has significant seasonal differences, while no for different building types.

CONCLUSIONS

In this paper, the indoor and outdoor particulate concentrations of four building types were monitored to analyze the correlation and factors of indoor and outdoor particulate concentrations and establish the prediction model of indoor particulate concentration. Specific conclusions are as followed:

(1) Outdoor temperature and humidity, air velocity, wind direction and atmospheric pressure are the main factors affecting indoor particulate concentration. According to the results, indoor $PM_{2.5}$ concentration is positively correlated with indoor and outdoor temperature and humidity as well as outdoor air velocity, negatively with outdoor atmospheric pressure and both positively and negatively with outdoor wind direction.

(2) Based on these factors, the study uses multivariate linear regression to establish the indoor $PM_{2.5}$ concentration prediction model. No matter in summer and winter season, outdoor $PM_{2.5}$ concentration plays a leading role in the model, the outdoor air velocity and wind directions are relatively weak, while the other parameters have their diversities respectively.

ACKNOWLEDGEMENT

REFERENCES

Dockery D W, Pope C A, Xu X P, et al. 1993. An association between air pollution and morality in six United-States cities. *New England Journal of Medicine*, 329(24), 753-759.

Zhao J, Bo L, Gong C, et al.2015. Preliminary study to explore gene-PM2. 5 interactive effects on respiratory system in traffic policemen. *International journal of occupational medicine and environmental health*, 28(6), 971-983.

Tseng E, Ho W C, Lin M H, et al. 2015.Chronic exposure to particulate matter and risk of cardiovascular mortality: cohort study from Taiwan. *BMC public health*, 15(1), 936.

Cohen A J, Brauer M, Burnett R, et al. 2017.Estimates and 25-year trends of the global burden of disease attributable to ambient air pollution: an analysis of data from the Global Burden of Diseases Study 2015. *The Lance*.

Klemm R J, Mason R M, Heilig C M, et al. 1996.Is daily mortality associated specifically with fine particles? *Journel of the Air&Waste Management Association*, 46(10), 927-965.

Dockery D W, Spengler J D. 1981. Indoor-outdoor relationships of respirable sulfates and particles. *Atmospheric Environment (1967)*, 15(3), 335-343.

Koutrakis P, Briggs S L K, Leaderer B P. 1992. Source apportionment of indoor aerosols in Suffolk and Onondaga Counties, New York. *Environmental Science & Technology*, 26(3), 521-527.

Ozkaynak H, Xue J, Spengler J, et al.1995. Personal exposure to airborne particles and metals: results from the Particle TEAM study in Riverside, California. *Journal of Exposure Analysis and Environmental Epidemiology*, 6(1), 57-78.

Xiong ZM, Zhang GQ, Peng JQ, et al. 2004. The research status of indoor inhalable particulate matter pollution. *HVAC*, 34 (4), 32-36.

The Design, Construction and Commissioning of a Small Scale Dynamic Calibrated Hot Box (CHB)

Timothy P. O'Leary[1,*], Aidan Duffy[2]

[1]Dublin Institute of Technology, Ireland
[2]Dublin Institute of Technology, Ireland

*Timothy.oleary@dit.ie

ABSTRACT

Sustainable construction and in particular the sustainability of materials is a global issue with legislation on material properties and product performance at the forefront. In traditional constructed buildings however, it can be extremely challenging to get accurate data on performance. The variability of building materials design, manufacture and construction from different eras is substantial, even within local areas due to the vernacular nature of construction from these periods. Material properties testing can be expensive and is not always readily available when required and is therefore often ignored, particularly in the retrofitting of historic buildings. This can have major adverse effects on the building fabric and for its inhabitant's health if the appropriate material interventions are not chosen. An inexpensive environmental chamber for testing such materials has been designed and built at the Dublin Institute of Technology, (DIT) Ireland, adopting comparable standards from EN ISO 8990 and ASTM C1363. This paper describes the design requirements for the construction of an affordable and mobile calibrated hot box (CHB) for the testing of historic materials. A characterisation panel has been used to carry out early calibration testing and the results of this are discussed. Improvements and tweaking of the first test are also discussed.

KEYWORDS
Calibrated hot box, Historic materials, Characterisation panel, Data acquisition.

INTRODUCTION
Buildings' energy consumption accounts for approximately 40% of total energy use in developed countries. The legislation on energy efficiency in buildings, such as the EU Directive 2010/31 has tried to raise minimum energy efficiency standards, for both the single components and the entire building. The building fabric plays a fundamental role in its energy balance, particularly the thermal properties when exposed to moisture and often generic values are used in ideal situations when modelling. In solid walled structures these values are, expensive and difficult to accurately ascertain due to the inconsistency of materials.

To establish accurate and reliable data on structures with different materials used in the one homogenous unit requires different approaches such as numerical simulation, but this is only as accurate as the accuracy of the inputs which often tend not to be validated. Hot boxes have been used to establish accurate properties with guarded hot boxes used mainly for commercial use and calibrated hot boxes used in laboratory work, where often it is necessary for greater levels of refinement and accuracy be achieved. The design of the hot box produced at the DIT was motivated by the need for such testing of small building elements from historic buildings primarily. These material dimensions influenced the design and construction of the whole apparatus and in particular the dimensions of the panel which hosts the sample.

Hot boxes require two closed rooms kept at constant, individual temperatures: a metering chamber, which is warm and the environmental chamber that is cold. A test wall typically containing the specimen under test, divides the two chambers. The overall thermal resistance

is evaluated from the heat flux between the two chambers including that of the internal and external air resistances. This research paper looks at the design, build and calibration of a calibrated hot box (CHB) constructed in the Dublin Institute of Technology, incorporating guidelines from EN ISO 8990 and ASTM C1363-05 with the primary aim of designing and constructing an affordable dynamic environmental test chamber. The construction of the facility was carried out in the Dublin Institute of Technology (DIT) workshops and Labs.

Objectives

a) Design and construct a dynamic environmental hot box to meet the input requirements for a later hygrothermal simulation, establishing thermodynamic properties b) Calibrate a small-scale, affordable apparatus for thermal testing of non-conventional materials using a characterisation panel of known thermal conductivity and c) Analyse and compare measured versus theoretical data to establish % error.

Literature review

Typical thermal testing of multilayer wall systems is conducted using a hot box apparatus according to standards comparable to ASTM C1363 [2] and EN ISO 8990 [4]. The properties of non- conventional materials can create challenges when conducting thermal tests using apparatus designed for conventional materials. For example, past tests conducted on historic brick varied in reliability due to poor fit inside conventional testing frames (Baker, 2011). EN ISO 6990 & ASTM Standard C1363-11 details the requirements for design and operation of a test apparatus for evaluating thermal performance of building materials and envelope assemblies by means of a hot box apparatus. The sensors measure the surface-to-surface heat transfer rather than the overall thermal resistance, and the initial performance is evaluated using heat transfer calculations.

Ulgen (2002) measured the time lag and decrement factor using wall compositions of opaque materials in a hot box simulation. Sala et al., (2008) conducted dynamic testing of insulated brick walls using a calibrated guarded hot box. The two types commonly used are the: Guarded hot box : In the guarded hot box, the metering box is surrounded by a guard box in which the environment is controlled to minimize lateral heat flow in the specimen. The total heat flow through the specimen will then be equal to the heat input to the metering box. In practice, there will be a limit in detecting imbalance in each test. (EN ISO 8990) [4]

Calibrated hot box : The calibrated hot box is surrounded by a temperature-controlled space not necessarily at the same air temperature as inside the metering box. The heat losses through the box walls are kept low by using a construction of high thermal resistance. The power input shall be corrected for the wall and flanking losses. The correction for chamber and flanking losses are determined by tests on specimens of known thermal resistance. For flanking loss calibration, the calibration specimens should cover the same thickness and conductivity range as the specimens to be measured and the temperature range of intended use. (EN ISO 8990)

Schumacher, et,. al,.(2013) constructed a hot box and concluded that the thermal performance of wall assemblies is complex and heavily influenced by factors such as insulation level, air leakage, thermal bridging, operating conditions, moisture content and installation defects and argue that simple R value calculation is not sufficient to address the above factors. They contend that more sophisticated testing is required before a new metric for testing is established. They used finite element programme analysis for the flanking losses.

International Standards lays down the principles for the design of the apparatus and minimum requirement that shall be met. It does not, however, specify a particular design since requirements vary, particularly in terms of size, and also to a lesser extent in terms of operating conditions. This International Standard describes also the apparatus, measurement technique and necessary data reporting.

The air exchange rate (AER) is not often measured in hot box construction and three methods using tracer gases exist for its determination. These are the concentration decay method, the constant injection method, and the constant concentration method (Laussman e t .. a l . 2011). The primary function being to establish additional heat losses at junction interfaces.

METHODOLOGY
All thermal bridge calculations were carried out according to EN ISO 10211. Numerical simulations were performed using the 2D and 3D finite element program Psi Therm. The U-value of the metering chamber was calculated according to EN ISO 6946:2007

Design for construction
Concept: It was determined that a calibrated hot box would be the most suitable for the testing requirements within the DIT. The limiting factors in design and dimensioning of the apparatus were the size of the door openings in different buildings as it was constructed in the Bolton street campus, 4-5 Km away. Transportation also determined the overall weight and mobility of the unit and had to be factored into the design and construction. The maximum specimen area achieved was 715mm (L) by 715 mm (H) by 200mm (T). 200mm was chosen as being capable of testing a panel of representative material to achieve accurate results. Bricks from a historic building have been prepared to a test standard size of 180 x 80 x 55mm for testing in the chamber. The following items were addressed: Identification of experiments to be carried out, Comply with standards, Capable of testing historic elements, Self-contained unit, Logging capabilities/ dynamic, Humidifier capacity and location, Highly insulated, Thermal bridge free or as low as practicably possible, Constructible in DIT and mobile, Good compactness ratio, Robust but adaptable specimen holder panel, Cost effective, Compliance and Practical implications re; budget, size, mobility.

Construction of CHB
The hot box, shown in Figure 1 was constructed using a 45 mm medium density fibreboard (mdf) outer structural layer, with one layer of 200mm EPS insulation glued to the inside surfaces with PVA glue. Air leakage was prevented by using a brush-on waterproof tanking layer, this also ensuring that the insulation and mdf thermal properties do not change due to moisture uptake from within. A 100mm wide mdf strip was glued on internally to provide fixings for the heaters/fans thus ensuring no fixings penetrated the eps. Heating is produced by a single 60W resistance heater located as far as is practicably possible away from the specimen. Cooling is provided by the environmental chamber on the other half of the apparatus, -a insulated box identical in size and construction to the metering box. The cooling is provided by a chiller unit placed on top of the unit with the evaporator connected internally. The identical dimensioning of the hot box ensures that air circulation and velocity across the sample face should be almost identical as they are placed in the same position in both boxes. Both boxes were designed to accommodate a 6mm mdf baffle painted matt black, installed 200mm from the face of the test specimen. Air circulation is provided by 2 computer fans per box placed behind the baffles in identical positions. Each specimen prepared for testing, is fitted with insulation plugs around its perimeter, identical to the layers insulating the hot box.

Four castors per box allow for easy opening and closing of the units. External threaded bars are used to tighten the two chambers together during testing, minimising air leakage. A humidifier has been fixed to the outside of the chamber and each chamber is equipped with a humidity probe and 8 thermocouples. All data is acquired and managed by the use of a single National Instruments cRio datalogger using Labview programming.

Calibration: The accuracy of each individual apparatus shall be estimated with reference to homogeneous specimens of thermal conductance extending over a range of temperatures, close to what the final testing conditions are likely to be. The metering chamber was set up to keep steady-state conditions: the set point was 30 °C, with an air flow rate of 3.8 m/s measured and RH that ranges in average between 30% - 47% with the environmental (cold) chamber value 'set point' changing at $5\ ^{0}C$ intervals from 25, 20, 15, 10, and $0\ ^{0}C$, until steady state environment was reached at each.
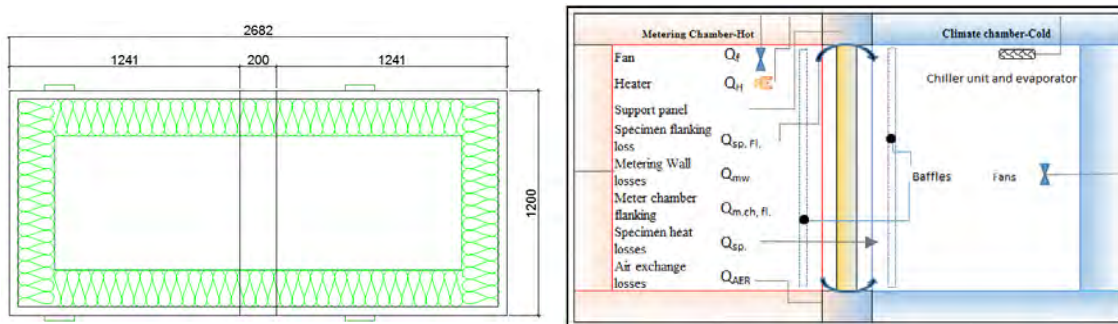

Figure 1.Horizontal section through apparatus. Figure 2. Components and Heat Pathways

Air Exchange Rate (AER)
The air change rate (ACR) through the box as a whole was determined through standard tracer gas measurement. After CO_2 was released into the chamber, its concentration decays exponentially, if no further CO_2 supply occurs and if the driving forces for air exchange remain constant. After introduction of the CO_2 into the sealed enclosure, the concentration of the gas decreased as air entered and exited. Plotting the natural logarithm of this exponential decay curve against time normally result in a straight line, the slope of which is the (AER) air changes per unit time The mass balance equation is used to describe the relationship between the concentrations of gas in a space as a function of time. The general form of the equation for calculating air exchange per unit time is given as follows:

$$N = [\ln(C_{int}\ t\ 0 - C_{ext}) - \ln(C_{int}\ t\ 1 - C_{ext})]/(t1 - t0) \qquad (1)$$

where N= number of air changes, $C_{int}\ t\ 0$ = internal concentration of tracer gas in enclosure at start, C_{ext} = external concentration of tracer gas in room, $C_{int}\ t\ 1$ = internal concentration of tracer gas in enclosure at end, t 0 =time at start (days), t 1 = time at end (days) and ln = natural logarithm.

CHARACTERISATION AND ESTIMATION OF LOSSES
A characterization panel of known thermal resistance (wood fibre board λ 0.04 W/mK) is used in a number of tests, over the expected operating temperature range. Each test determines the difference between the measured heat input to the metering chamber and the heat transfer through the characterization specimen, calculated from the measured temperature drop across it and its known resistance.
Calculations: A significant difference in temperature across the specimen is suggested. The air velocity on both sides was held constant and the heat flow across the sample was measured.

EN ISO 8990 and ASTM C1363-05 requires the following heat balance equation be verified. A schematic showing the heat transfer pathways is given in Figure 2.

$Q_{\text{Source}} = Q_{\text{Heater}} + Q_{\text{Fans}}$, Specimen $= U_{\text{Specimen}}$ x A_{Specimen} x ΔT and
$Q_{\text{metering chamber losses}} = U_{\text{Chamber}}$ x A_{Chamber} x $\Delta T + Vcp\rho\Delta T + Q_{\text{flanking}}(W)$ (2)

Where: A_{Specimen} = Sample area (m^2), Q_{Heaters} = Heat input from heaters (W), Q_{Fans} = Heat input from fans (W), $Q_{\text{m ch}}$= Heat transfer rate through metering walls, floor and ceiling (W), Q_{flanking} = Heat transfer rate at junction of specimen to frame (W), U_{chamber} = Thermal conductivity of the chamber (W/m^2.K), A_{chamber} = Area of chamber walls where losses occur (m^2), $\dot{V}$ = Air exfiltration rate m^3/s, c_p = A Specific Heat Capacity of 1007 J/kg.K at 30 ^{0}C is used, ρ = Air density between 1.16 – 1.27 kg/m^3 used, ΔT_{air}=Inside to outside temperature difference (^{0}C), $\Delta T_{surfaces}$= Temperature difference between hot and cold surfaces (^{0}C), U_{Specimen} = Thermal conductivity of the sample (W/m^2.K)

RESULTS
The results of the CO_2 analysis are shown in Figure 3, where the air exchange rate equals the slope of the line at 0.087 ach and this is multiplied by the chamber volume to get a volume per second time of 1.313E-05 to be used in the heat balance equation. The test was conducted at ambient temperature only and accounted for less than 2% of the overall energy input, however further tests at different temperatures should further verify this figure.
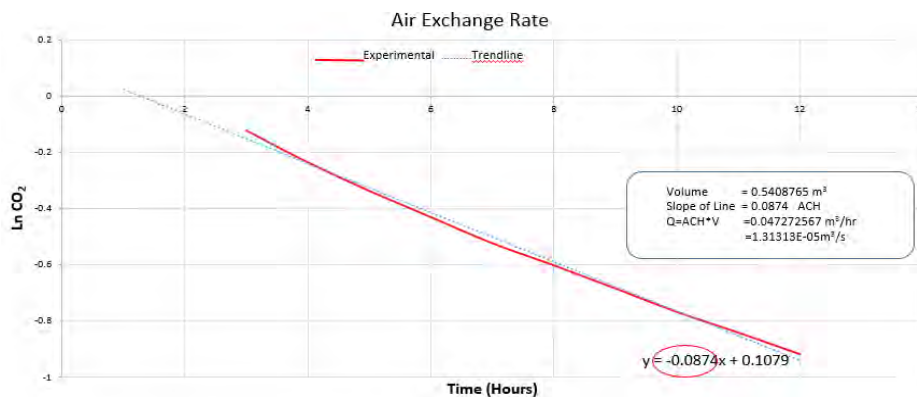

Figure 3. CO_2 results for air leakage of the chambers.

Table 1. Measured and calculated results over delta T of 5, 10, 15, 20 &25 ^{0}C

Delta T	30_25	30_20	30_15	30_10	30_05	30_00
Q_{fl}	1.28	1.21	1.22	0.93	0.86	1.14
$U_{ch}*A_{ch}*dT_{surf}$	3.85	3.70	3.71	3.23	3.01	3.45
$V*Cp*p*dTair$	0.13	0.12	0.12	0.10	0.09	0.11
Q_{fl} sample	0.18	0.40	0.62	0.85	1.08	1.14
$U*A*dT_{specimen}$	0.99	2.21	3.47	4.73	6.06	6.35
Q_{H+F}	6.76	7.94	9.04	10.26	11.39	12.55
Balance equation	*0.33*	*0.29*	*-0.10*	*0.42*	*0.29*	*0.37*
$Q_{AER}+Q_{fl}+Q_{fl}+Q_{mw}$	6.43	7.64	9.14	9.83	11.10	12.18
% Error	4.83	3.69	-1.09	4.14	2.55	2.94

Characterisation results
Table 1 shows the inputs for the heat balance equation measured over five delta T's during the testing of an 80mm woodfibre board. The stated manufacturer's lambda value for this panel is 0.04 W/mK and is used in the U value component (Table 1) of the U*A*dTspecimen. As the balance equation should read 0, the percentage error shown in the last row is just under 5%. The theoretical and experimental results are plotted in Figure 3 and can be seen to have good correlation with the distance between the lines representing the gap to be identified.
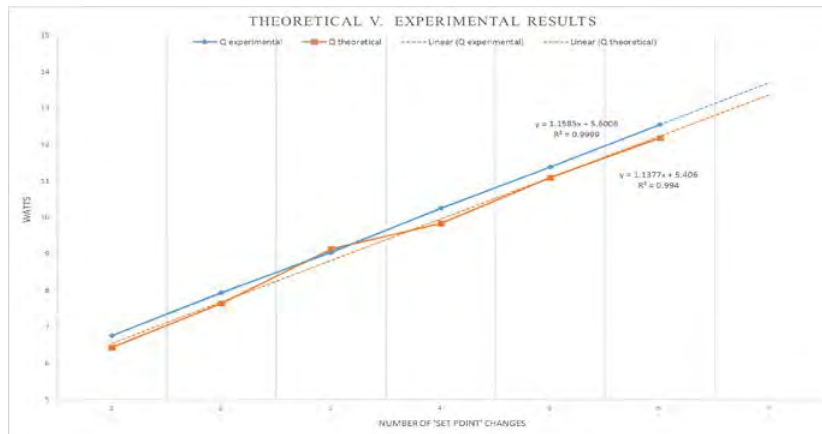
Figure 3. Theoretical versus Experimental losses of wood fibre board over 5 ΔT's

ANALYSIS AND DISCUSSION
The limitations of this CHB are its relatively small size and also the fine levels of accuracy of some of the equipment but these have been counteracted by the extra care taken in the construction and calibration process. The maximum size of 715mm by 715mm sample area size requires that the thermal bridge calculation needs to be extremely accurately identified.
The advantages of reduced dimensions over more traditional hot box systems however, provides a reduced mass and, thus, reduced thermal inertia of the overall system. First tests on a wood fibre board of an accepted conductivity (0.04 W/mK) shows very close relationship between theoretical and experimental data. The percentages of error varies by approximately 5%. The average temperatures in both chambers were steady throughout the testing period. Investigation is required to establish the cause of the slight non-linearity at delta T, of 15 ^{0}C.
Finally the CHB built in the DIT set out to design and build an affordable testing chamber for establishing the material properties of historic building materials with the first step of calibrating a panel thickness of 80mm of known thermal conductivity. This was satisfactorily achieved and the percentages error of approximately 5% is acceptable for this apparatus The next steps of testing historic building materials from a case study building is currently underway, with the results being inputted to a hygrothermal simulation.

REFERENCES
Asdrubali, F., Baldinelli, G., 2011. Thermal Transmittance measurements with the hot box method; Energy Build.
ASTM C1363-11. 2005. Standard Test Method for Thermal Performance of Building Materials and Envelope Assemblies by Means of a Hot Box Apparatus.
Baker P. H., 2011; U-values and Traditional Buildings: Historic Scotland Technical Paper 10; Edinburgh: Historic Scotland;
EN ISO 8990:1996. Thermal insulation –Determination of steady state thermal transmission properties –Calibrated and guarded hot box.
Laussmann, D, & Helm, D, 2011. Air Change Measurements Using Tracer Gases: Methods and Results. Significance of air change for indoor air quality. DOI. 10.5772/18600
Sala, J.M., Urresti, A., Martin, K, Flores, I., Apaolaza, 2008. A., Static and dynamic thermal characterisation of hollow brick wall: Tests and numerical analysis, Energy and Buildings.
Schumacher, C.J. et al., 2013. Development of a New Hot Box Apparatus to Measure Building Enclosure Thermal Performance. Proceedings of Building XII.
Ulgen K., 2002. Experimental and theoretical investigation of effects of wall's thermophysical properties on time lag and decrement factor, Energy Build.

The Effect of Human Walking on Distribution Characteristics of Indoor Particulate Matter

Yang Lv[1,*], Haifeng Wang[1], Hiroshi Yoshino[2], Hiroshi Yonekura[2], Rie Takaki[3], and Genta Kurihara[4]

[1]School of Civil Engineering, Dalian University of Technology, China
[2]Department of Architecture & Building Science, Tohoku University, Japan
[3]Tohoku Institute of Technology, Japan
[4]Kajima Construction, Japan

[*]*Corresponding email: lvyang@dlut.edu.cn*

ABSTRACT

In modern society, house dust particulate matters pollution had become serious. Ventilation is an important method for removing house dust particulate matters and it is very important to explore the removal efficiency of house dust particulate matters under different ventilation modes. This study analyses the removal effect of house dust particulate matters under the two typical ventilation modes called ceiling exhaust and slit exhaust strategy through experiments and date analysis. In the process of experiments, riboflavin particles were used as the house dust particulate matters, instantaneous microbial detection (IMD) was used to measure the house dust particulate matters. Walking test was carried on after the ventilation system running for some time, which aimed to explore the influence of human behaviour on the house dust particulate matters distribution under two different ventilation modes. It is concluded that larger size particles had larger sedimentation velocity and sedimentation velocity of particles would be faster significantly after the ventilation system working. After walking experiment, particles concentration returned to background concentrations due to the effect of the ventilation system. Particles concentration in slit exhaust strategy was lower than ceiling exhaust so that the effect of slit exhaust strategy is superior to the ceiling exhaust.

KEYWORDS
Ventilation strategy; House dust particulate matters; Experiment; Concentration distribution; Walking test

INTRODUCTION
In modern society, people spend 80% of the time in indoor environment (Peggy et al., 1992; Robinson and Nelson, 1995), thus indoor air quality is particularly important. With the worsening of atmosphere particle pollution, indoor particle pollution has become increasingly severe due to the infiltration by building exterior and other reasons. US Environmental Protection Agency had conducted an investigation for 5 years, which found that indoor pollution was serious in residential and public building (Zhu, 2002). Due to the limitations of various factors in China, indoor air environment can't build a more comprehensive monitoring network, resulting to indoor air quality is even more worrying.
Epidemiological studies showed that short or long-term exposure to dust particle would lead to widespread adverse effects on human multiple systems. "Global Environment Outlook" published UNEP pointed out that nearly 2 million premature deaths were related with particulate matter pollution. There was a positive correlation between the particle mass concentration with human mortality and morbidity, even the concentration lower than the

national limits standards (Yang, 2014). Dockery (1993) conducted a prospective study in six cities, and it found that particle pollution was related with cardiovascular diseases. With the increase of the annual average concentration of particulate matter, all-cause mortality, cardiovascular mortality and lung cancer mortality was significantly increased after controlling confounding factors (Pope et al., 2002). Under the same concentration, house dust particulate matters pollution was more harmful to the human body (Dockery et al., 1993; Pope et al., 2002; Guo et al., 2010; Tinker and Roberts, 1999). House dust particulate matters can enter the lungs to made greater harm to human body (Wang et al., 2013; Wang et al., 2007; Nikasinovic et al., 2006; Neas et al., 1994; Delfino et al., 2006; Zhu et al., 2015).

A growing number of epidemiological studies had shown that population incidence and mortality were associated with the particle mass concentration, especially significantly the indoor particulate matter concentrations (Yang, 2014; Dockery et al., 1993; Pope et al., 2002; Guo et al., 2010; Tinker and Roberts, 1999; Wang et al., 2013; Wang et al., 2007). Thus, the distribution characteristics of indoor particles and the health risks have been common concern in environmental science and engineering. Zhang and Chen (2006) studied particle transportation and distribution in ventilation chamber using experimental and numerical methods, who found that different ventilation forms had a great impact on indoor particle concentration distribution. Munat (2001) investigated and analysed the influence of different airflow forms on particle suspension, and the results showed that displacement ventilation system had small resuspension harm. Zhao B (2004) compared the diffusion characteristics of indoor particulate matter in displacement ventilation and mixing ventilation using numerical simulation method.

Many indoor air environment-related research study have been carried out, but it's not clear how indoor human behaviour affects indoor particle distribution under different ventilation. To solve this problem, the study made a research to figure out the effect of indoor human behaviours' influence to house dust particle distribution under different airflow. It will improve the prevention and control level of indoor air pollution and provide scientific basis of human health.

METHODS
Selection of particles
In the experimental study of house dust particulate matters, Japan used JIS-11 as experimental particles (Liu et al., 1996). JIS-11 test powder is non-biological particles produced by volcanic ash. The concentration of non-biological particles was high in the air, and its impact on the health is not clear, so in this study, riboflavin particles were used as the test particles because it is harmless for biological particles (Kurihara et al., 2010). Riboflavin is a special kind of biological particles which can emit fluoresce when it is exposed to light sources with certain specific wavelength. And it can be detected by particle detector (IMD) based on optical sensors and fluorescence detection techniques as biological particles. Studies have shown that value of riboflavin powder is low in the air, so it doesn't affect experimental results (Kurihara et al., 2010).

Ventilation systems and experiment process
Figure 1 shows experimental room (L×W×H=5.37m×2.74m×2.25m) and ventilation systems. The window is sheltered by aluminum foil corrugated board to prevent solar radiation, and the walls are insulated by expanded polystyrene board. This study analyses the effect of the human walk activity on indoor particles distribution under two typical ventilation modes including ceiling exhaust and slit exhaust. Ceiling exhaust is the traditional ventilation way. For the slit exhaust strategy, delivery outlet was located in the center of the ceiling (In this study, delivery outlet of two ventilation system was same), the exhaust port is located at

the junction of walls and floors. Delivery outlet size of two ventilation systems were 0.05m × 0.10m. The exhaust port size in ceiling exhaust was 0.05m × 0.10m. As for the slit exhaust system, exhaust port size in the east was 4.2m×0.005m, 4.53m×0.005m in the west. Figure 2 shows ceiling exhaust and slit exhaust system. Ventilation time was 0.75 times/h during the experiment
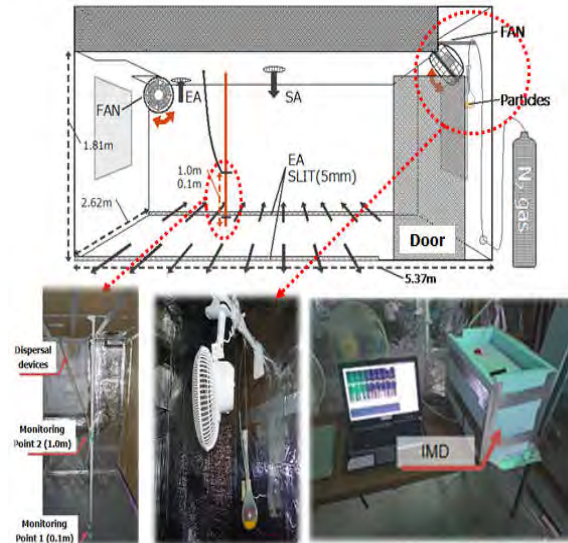

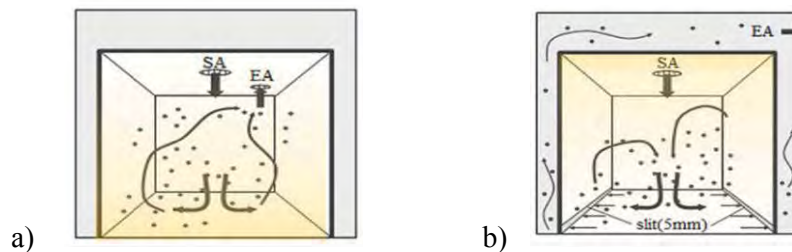
Figure 1. Experimental room and ventilation systems.

Figure 2. Two ventilation system. a) ceiling exhaust, b) slit exhaust

Indoor particles distribution was shown in Figure 1. The house dust particles were put in a measuring flask, which was fixed at the corner near the ceiling of the room. Nitrogen gas was blown into the measuring flask to disperse the house dust particles. Nitrogen gas flow rate was set as 10 L/min. To make the distribution of house dust particles as evenly as possible in the room, the house dust particles were mixed by an electric fan which was fixed close to the flask. Taking into the account of the height of the child, the position of the monitoring point was set at 0.1m and 1.0m. IMD (instantaneous microbial detection; IMD-A 200-1, BioVigilant Systems) was used to measure the particles, which is based on optical fluorescence sensor technology and is capable of detecting the size of biological or non-biological particles in the environmental air. Particle sizes were classified as the following six levels: 0.5-1.0 μm, 1.0-3.0 μm, 3.0-5.0 μm, 5.0-7.0 μm, 7.0-10.0 μm, and 10.0-15.0 μm.

Experimental procedure (total 42 hours): the first hour - indoor particles spreading; 2 to 9 hours – indoor particles free settling; 10 to 42 hours - the ventilation system running. Indoor people started walking test from 27th hours. The purpose of the walking test was to explore the impact of walking behaviour to indoor particle concentration distribution under two different ventilation modes. Research was determined according to Liu Yu's experimental

methods from Japan's National Public Health Institute (Lu et al., 1982). In the study, male experimenter entered to room doing walk test, and walked in the room for 10min according to designated route (60 steps/ minute, 60 cm/step, a total of 600 steps). Figure 3 shows the walk test details.
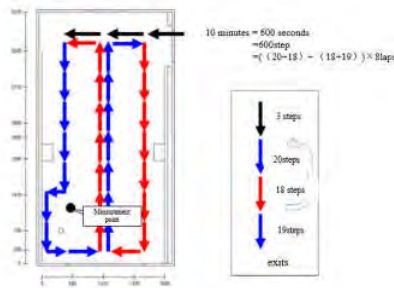

Figure 3. The walk test details

RESULTS AND DISCUSSIONS
The results in the ceiling exhaust strategy
Figure 4 shows the variation of particles concentration(0.5-1.0 μm, 1.0-3.0 μm, 3.0-5.0 μm) in two different measuring points (from the ground 0.1 meters and 1.0 meters)in the ceiling exhaust strategy. It shows that: ①Before spreading powder (-6-0h), all size particles' background concentration was low in air (about 10P/L). ②When powders walked for 1 hour (0-1h), indoor particles concentration increased rapidly; After 8hours(1-9h), different size particles (0.5-1.0 μm, 1.0-3.0 μm, 3.0-5.0 μm) exhibited different settlement curve because of gravity; The larger particle size, the faster fall velocity. ③After running the ventilation system (9h ~), all size particles accelerated subsidence(settlement curve sudden steep in figure 6); When did walk test(27h-) , particles concentration increased significantly, which may be due to suspended caused by disturbance of human walking; After the walk test, particles concentration returned to background concentration under the action of the ventilation system running continuously. Two measuring points showed above trend.
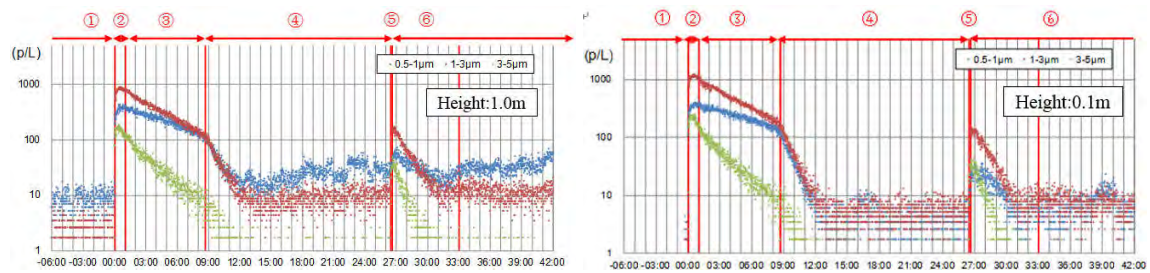
Remarks: ①background values;②powder spreading;③free settling;④ventilation;⑤walk test;⑥ventilation
Figure 4. Variation of particle concentration inthe ceiling exhaust strategy
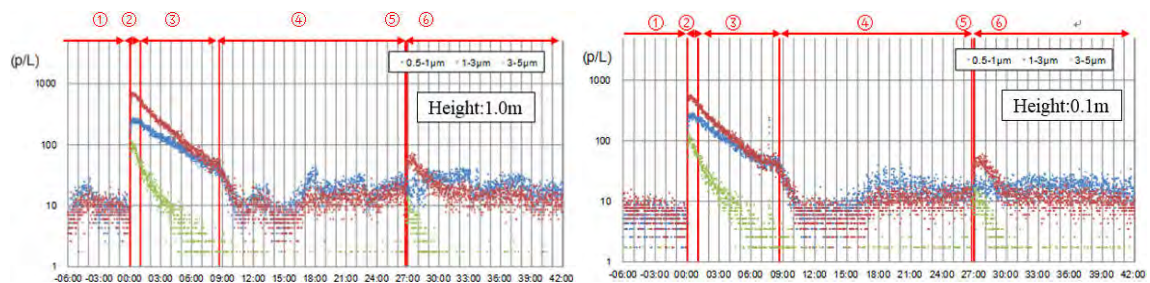
Remarks: ①background values;②powder spreading;③free settling;④ventilation;⑤walk test;⑥ventilation
Figure 5. Variation of particle concentration in the slit exhaust strategy

The results in the slit exhaust strategy
Figure 5 shows the particles concentration variation of two different measuring points (from the ground 0.1 m and 1.0 m) in the slit exhaust strategy. The variation trend of particles concentration in two measurement point was basically same with Figure 4, but there were some differences in concentration distribution.

Comparison of indoor particles concentration distribution in both ventilation systems
Figure 6 shows the different size particles concentration after ventilation system running (9h-) under two ventilation modes. Figure 6a shows the results in the height of 1.0m, and Figure 6b shows the results in the height of 0.1m. The results indicate that particles concentration in slit exhaust was lower than that of ceiling exhaust in the two measurement points. The lower the height, the more obvious of the effect for slit exhaust. The exhaust outlet was located at the junction of walls and floors for the slit exhaust, thus indoor particle gathered in the corner and excluded.
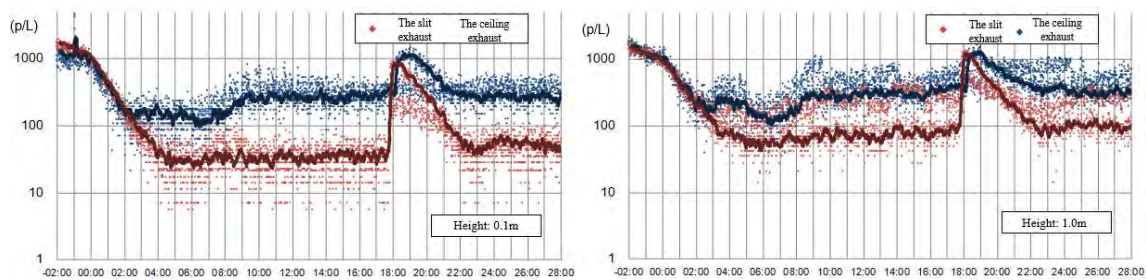

Figure 6. Particles concentration after ventilation system running in two ventilation systems.

CONCLUSIONS
This paper clarifies the effect of human walk behaviours on house dust particle distribution under different ventilation modes (including ceiling exhaust and slit exhaust). The following conclusions have been drawn:
1) Riboflavin was used to indoor house dust particles and IMD was used to measure the riboflavin particles concentration.
2) Larger size particles had larger sedimentation velocity and sedimentation velocity of particles accelerated significantly after the ventilation system working. Comparison of the number of particle in experimental monitoring point shows that the number of house dust particles in the ceiling exhaust was higher than that of the slit exhaust after house dust particles decreased as same level as background.
3) At the beginning of walking test, particles concentration increased significantly. After the walking test, particles concentration returned to background concentration under the action of the ventilation system running continuously.
4) Particles concentration in slit exhaust strategy was lower than that of the ceiling exhaust, thus the effect of slit exhaust is superior to the ceiling exhaust.

REFERENCES

Peggy L. Jenkins, Phillips Thomas J., Mulberg Elliot J., et al. 1992. Activity patterns of californians: use of and proximity to indoor pollutant sources. *Atmospheric Environment Part A General Topics*, 26(12), 2141-2148.

Robinson J, Nelson W.C. 1995. National human activity pattern survey data base. *US EPA, Research Triangle Park*.

Zhu LT. 2002. Indoor air pollution control .BeiJing: Chemical Industry Press.

Yang L. 2014. Communication and control of indoor air pollution. *BeiJing: Machinery Industry Press*.

Dockery D W, Pope C A, Xu X P, et al. 1993. An association between air pollution and morality in six United-States cities. *New England Journal of Medicine*, 329(24), 753-759.

Pope C A, Burnett R T, Thun M J, et al. 2002. Lung cancer, cardiopulmonary mortality, and long-term exposure to fine particulate air pollution．*Journal of the American Medical Association*, 287(9), 1132-1141．

Guo Q B, Cheng X F, Hou h, et al. 2010. Pollution characteristics and morphology analysis of PM10 and PM2.5 in winter. *Environmental Monitoring in China*, 26(4), 55-58.

Tinker J. A. , D. Roberts. 1999. Modeling air quality and bacteria levels in an operating theatre. *In Proceedings of Indoor Air' 99*, Edinburgh, 4, 731

Wang WF, Yu J, Xu DD, et al. 2013. Pollution characteristics of particles and its main components in ningbo urban atmosphere. *Environmental Monitoring in China*, 29(5), 43-44.

Wang YX, Niu JP, Ding GW, Noordin MM, Chen XY. 2007. Effects of air pollution on juvenile lung function in Lanzhou. *J Environ Health*, 24(6), 415-418.

Nikasinovic L, Just J, Sahraoui F, et al. (2006). Nasal inflammation and personal exposure to fine particles PM2.5 in asthmatic children. *J Allergy Clin Immunol*, 117(6), 1382-1388.

Neas LM, Dockery DW, Ware JH, et al. 1994. Concentration of indoor particulate matter as a determinant of respiratory health in Children. *Am J Epidemiol*, 139(11), 1088-1099.

Delfino RJ, Staimer N, Gillen D, et al. 2006. Personal and ambient air pollution is associated with increased exhaled nitric oxide in children with asthma. *Environ Health Perspect*, 114(11), 1736-1743.

Zhu SW, Wei Cai, Hiroshi Yoshino, et al. 2015. Primary pollutants in schoolchildren's homes in Wuhan, China. *Building and Environment*, 2015, 1-13.

Zhang Z, Chen Q. 2006. Experimental measurements and numerical simulations of particle transport and distribution in ventilated rooms. *Atmospherie Environment*, 40(18), 3396-3408

Mundt E. 2001. Non-buoyant pollutant sources and particles in displaeement ventilation. Building and Environment, 36(7), 829-836.

Zhao B, Zhang Y, et al. 2004. Comparison of Indoor Aerosol particle Concentration and Deposition in Different ventilated Rooms by Numerieal Method. *Building and Environment*, 39(1), l-8.

Liu Yu, Ikeda Kouichi, Irie Tatehisa, Hiraoka Kenji. 1996. Characterization of re-dispersion of settled particulates into the space with raised floor and conventional ceiling HVAC system. *Journal of architecture, planning and environmental engineering*, (483), 49-54.

Kurihara Genta, Yoshino Hiroshi, Yonekura Hiroshi, Takaki Rie, Lu Yang. 2010. Experimental method for determining removal efficiency of house dust by mechanical ventilation. *31st conference of the Air Infiltration and Ventilation Centre (AIVC2010)*, Korea, 78-92.

Yang Lu, Jing Liu, Hiroshi Yoshino, et al. 2015. Study on Distribution and Deposition of House Dust by Different Ventilation Systems in a Full-scale Residential Room. *International Journal of Ventilation*, 13(4), 417-426.

Thermal performance analysis of traditional housing in Albania

Rudina Belba[1, *] and Sokol Dervishi[1, 2]

[1] Epoka University, Faculty of Architecture, Tirana/Albania
[2] Vienna University of Technology, Institute of Architecture Science, Vienna/ Austria

[*] *rbelba12@epoka.edu.al*

ABSTRACT

This paper introduces the results of a one-year research, to gather and analyse data on the traditional housing buildings in Kukes region, Albania. The energy performance and the thermal comfort conditions in five different buildings were examined. The Design Builder Energy simulation software was used to analyse the thermal performance of the selected typologies. Detailed construction activity and weather information was applied in modelling the houses. Simulation results showed that these buildings require only heating during the winter. As for the first villa, seven improvement scenarios were applied and examined. The same scenarios incorporate the use of thermal insulation of the walls and the roof as well as the use of double glazing. The results suggest that improvements and insulations in building fabrics could reduce the annual energy consumption up to 35 %.

KEYWORDS
Thermal performance, Traditional building, Parametric simulation, Design Builder

INTRODUCTION
Adaptive reuse contributes to the sustainability of the urban generation, as it extends the life cycle of the buildings, avoids demolition waste, encourages energy efficient solutions, and provides significant social and economic benefits to the society (Resuli and Dervishi, 2015). Due to the difficulty of finding maintained buildings, very few researches analyze the energy efficiency of traditional buildings in Albania (Rexhepi and Mahdavi, 2010). Previous studies have identified effective ways for the energy conservation in the existing buildings (Kaleci and Dervishi, 2014). The renovation of the existing buildings is one of them, consisting of interventions on improving the functionality and sustainability of traditional buildings. This study consists of five traditional buildings located in Lume village, in the Region of Kukes, Albania, on which, records on thermal conditions and the energy use were gathered over a period of one year.

This paper is specifically related to five case studies of traditional houses in the villages of Kukës and identifying their sustainable potentials. The selected houses have been historically exploited as a shelter for the locals, guests, and foreigners. Nowadays their conditions have deteriorated and a large amount of energy is used for heating. Increase of energy consumption is caused by the low temperatures of this area, and the absence of insulations in old buildings, specifically the wall insulation, roof insulation, and double glazing. In most case studies, the building design does not consider orientation, glazing ratio, shading devices, or thermal mass. The sustainable environment is achieved using natural resources (sun, wind, temperature variation) in sustainable approaches, which directly affect the quality of the inner space (comfort, energy efficiency, and lighting) (Rashani and Mahdavi, 2015), and hence, this study is concerned with the following objectives: i) analyzing the energy consumption and

how it affects thermal conditions; ii) evaluating the thermal performance; iii) analyzing the comfort of inner spaces; and iv) developing strategies towards improvement.

METHODS
The five selected buildings diverge in terms of construction period, location, orientation and occupancy. Table 1 summarizes general information regarding the concerned houses such as area, function, construction year, presence of Kulla, and the materials used.

Table 1. Overview of the selected houses (year of construction, area, interventions, material used).

	H 1	H 2	H 3	H 4	H 5
Approximate year of construction	1930	1920	1915	1965	1940
Occupancy	full	non	non	full	partial
Interventions	*				*
Two story house	*	*	*		*
Warehouse and livestock		*	*		
Both inner and outer stairs					*
Presence of wood in main façade	*	*	*		*
Materials: Clay, Stone, Wood	*			*	*
Presence of inner wall	*	*	*	*	*

Indoor thermal Condition and Energy Used
Indoor climate parameters (indoor air temperature and relative humidity) and the energy use were simulated for all houses (living room and in the entire building over a period of one year (Jan 1st- Dec 31th). In order to evaluate the existing indoor thermal conditions, the ratios of air temperature and relative humidity are diagrammed in psychometric charts. Based on the questionaries' and gathered information, building performance simulation models were generated and secondarily used to test various improvement scenarios by means of parametric simulation software [Design Builder 2013], (see Table 2).

Table 2. Questionnaire output (thermal insulation, heating equipment, cooling equipment, lamps, thermal comfort)

Questions	H1-Results	H2-Results	H3-Results	H4-results	H5-Results
Thermo insulation	No	No	No	No	No
Heating Equipment	Mineral wood	-	-	Mineral wood	Mineral wood
Cooling Equipment	No	No	No	No	No
Lamps	Economical fluorescent lighting	-	-	Economical fluorescent lighting	Economical fluorescent lighting
Energy used for cooking	Mineral wood	-	-	Mineral wood	Electric
Thermal Comfort (Summer)	Hot-Ground floor Hot-First floor	Neutral-Ground floor Neutral-First floor	Neutral-Ground floor Neutral-First floor	Hot	Neutral-Ground floor Hot-First floor
Thermal Comfort (Winter)	Neutral	Cold	Cold	Neutral	Neutral

Simulation study
Five buildings, respectively H1, H2, H3, H4, and H5 were simulated over a period of one year. The gathered geometry and the construction records were used to generate the base case simulation models. Assumptions were made based on in situ observations, historical documents, and questionnaires'. Simulation assumptions regarding actual construction data

are summarized in Table 3. To run the simulations, weather files were generated based Meteonorm (2007) software platform.

Table 3. Base case construction materials and respective U values for all houses (H1-H5).

Code	Scenario	U-Values	Description
BC 1	Base case- H1	U_{Walls}= 1.31 $W.m^{-2}.K^{-1}$	Wall- 60 cm stone wall
		U_{roof}= 1.95 $W.m^{-2}.K^{-1}$	Roof- Uninsulated pitched roof, Heavy weight
	Base case- H2	Uwindow = 2.6 $W.m^{-2}.K^{-1}$	Window- Double glazing, Clear, Argon filled
BC 2		U_{Walls}= 1.46 $W.m^{-2}.K^{-1}$	Wall- 60 cm stone wall
		U_{roof}= 2.11 $W.m^{-2}.K^{-1}$	Roof- Uninsulated pitched roof, Medium weight
	Base case- H3	Uwindow = 5.5 $W.m^{-2}.K^{-1}$	Window- 4 mm Single glazing, Clear
BC 3		U_{Walls}= 1.61 $W.m^{-2}.K^{-1}$	Wall- 50 cm stone wall
		U_{roof}= 2.11 $W.m^{-2}.K^{-1}$	Roof- Uninsulated pitched roof, Medium weight
	Base case- H4	Uwindow = 5.5 $W.m^{-2}.K^{-1}$	Window- 4 mm Single glazing, Clear
BC 4		U_{Walls}= 1.22 $W.m^{-2}.K^{-1}$	Wall- 60 cm stone wall
		U_{roof}= 1.95 $W.m^{-2}.K^{-1}$	Roof- Uninsulated pitched roof, Heavy weight
	Base case- H5	Uwindow = 2.6 $W.m^{-2}.K^{-1}$	Window- Double glazing, Clear, Argon filled
		U_{Walls}= 1.38 $W.m^{-2}.K^{-1}$	Wall- 70 cm stone wall
BC 5		U_{roof}= 1.95 $W.m^{-2}.K^{-1}$	Roof- Uninsulated pitched roof, Medium
		Uwindow = 2.6$W.m^{-2}.K^{-1}$	Window- 6 mm Single glazing, Clear

Improvement scenarios

To demonstrate thermal improvement possibilities a number of seven improvement scenarios (S1-S7) were introduced only for the first typology (H1) for parametric simulations in a 2 day interval (1st and 2nd of July). The first scenario (S1) explores the impact of the thermal insulation on the external walls. The second scenario (S2) involves the thermal insulation of the roof. The third scenario (S3) involves the use of double glazing as a replacement for of single glazing. The fourth, fifth, sixth, and seventh scenarios (S4-S7) comprise the combination of the aforementioned scenarios. The purpose is to achieve a more stable temperature in the indoor environment and to reduce energy consumption. Table 4 summarizes improvement scenarios for one selected representative house.

Table 4. Improved scenarios for H1 (WI, RI, DG, WI+RI, WI+DG, RI+DG, WI+RI+DG)

| Code	Scenario	U-Values	Description
WI	Wall Insulation	U_{Walls}= 0.26 $W.m^{-2}.K^{-1}$	Inner Insulation PVC= 12 cm
RI	Roof insulation	U_{roof}= 0.151 $W.m^{-2}.K^{-1}$	Glass Wool 8 cm
DG	Double glazing	Uwindow = 1.07 $W.m^{-2}.K^{-1}$	Replacement of Single Glazing with Double Glazing
WI+RI			
WI+DG			
RI+DG			
WI+RI+DG			

RESULTS AND DISCUSSION

Figure 1 shows an indication of the existing thermal performance only in the first house (H1) based on the simulation results in a course of a 2 day interval (1st and 2nd of July 2017). Taking into account the weather conditions in Kukes, no cooling took place during simulation, and ventilation was considered during day and night hours with altered recesses (see Table 5). Figure 2a shows the assessment of indoor temperatures of all selected houses, compared with the outdoor temperature for a 2 day interval measurements (1st and 2nd of July 2017). As indicated in the relevant figures, the indoor temperature is more constant during day and night, compared to the outdoor temperature. Owing to that stone is the material that

was used in outer walls its conductivity directly brings about a stable room temperature. A considerable difference is shown between indoor temperatures of occupied houses (H1, H4, and H5) and unoccupied houses (H2 and H3), as the absence of activity affects the sustainability of internal temperatures in H2 and H3. Figure 2b compares the humidity measurements of all houses in the 2 day interval (1st and 2nd of July 2017). Based on the results, the amount of humidity is lower in the occupied houses (H1, H4, and H5) because the unoccupied houses (H2 and H3) are unventilated. Additionally, Figure 3a shows the comparison of energy between five houses in one year interval, while Figure 3b,c shows the ratio of indoor temperatures and relative humidity for one month (July 2017) for H1 (occupied) and H2 (unoccupied) represented by psychometric charts. As it is shown in the charts, the houses are positioned differently related to the comfort zone. The first typology (H1) is the most comfortable one, since its construction belongs to more recent years whilst the second typology (H2) is out of the comfort zone, since it is unoccupied and the amount of humidity is bigger. Figure 4a,b and shows that energy and temperature are changed based on improvement scenarios for the first typology (H1). As shown in the figure 4b the lowest value consists the first typology (H1) due to its recent interventions and insulation system. The second lowest value consists of the fifth typology (H5) which has the same material as the fourth typology (H4) but its activity takes place only during the summer period. For the unoccupied houses (H2 and H3) the results show relatively low performance. The implementation of all scenarios together reduces the amount of energy consumption (yearly) and decreases the indoor temperature in the 2 day interval (1st and 2nd of July). As expected, interventions in the external wall, roof and windows affect directly the indoor temperature and energy consumption. The combinations of the all scenarios (WI + RI + DG) decrease the average of the indoor temperature from 25°C to 22°C during summer period and reduce the annual amount of energy consumption from 74 kWhY.m-2 to 45 kWhY.m-2.

Table 5. Ventilation schedule for all houses (H1-H5)

	H1		H2		H3		H4		H5	
	Day	Night	Day	Night	Day	Night	Day	Night	Day	Night
Ventilation hours	09:00-17:00	22:00-01:00	-	-	-	-	09:00-17:00	22:00-01:00	09:00-17:00	22:00-01:00
% of opening	80 %	20 %	-	-	-	-	80 %	20 %	80 %	20 %

a)   b)
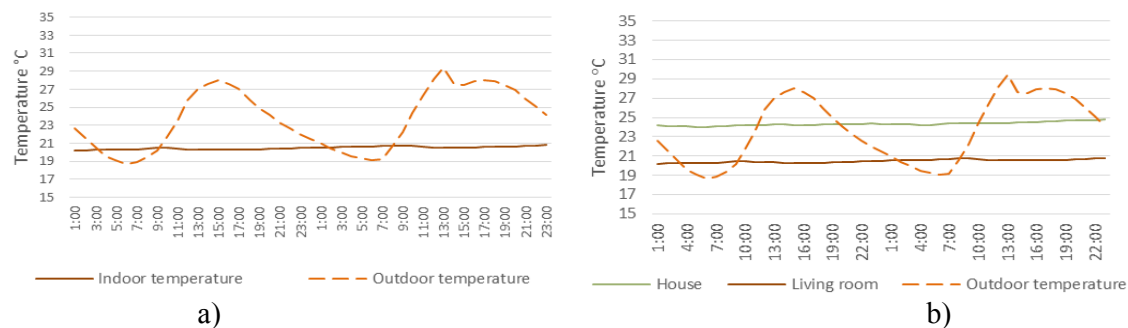
Figure 1. a) Base case temperature (living room of H1), b) Symptoms. Base case temperature (living room and H1) in a 2 day interval (1st and 2nd of July 2017).
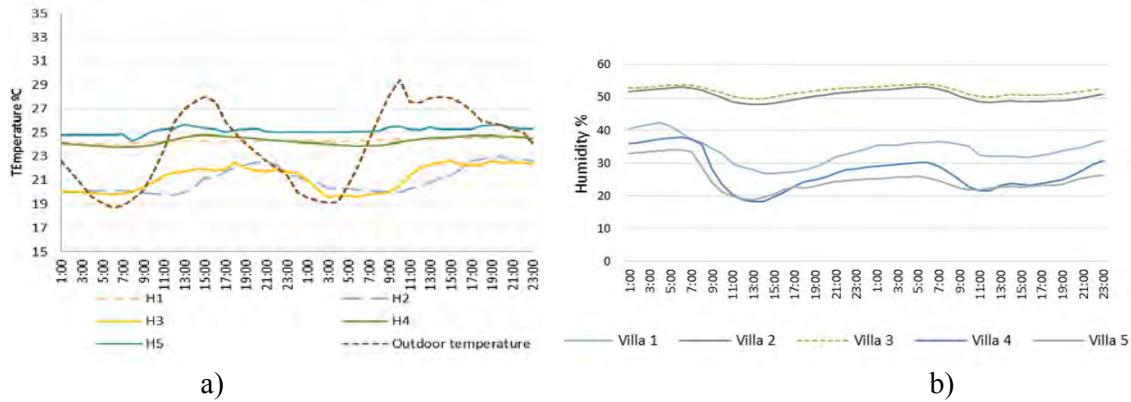
a)   b)

Figure 2. a) Comparisons of BC temperatures (H1-H5), b) Comparisons of BC humidity's (H1-H5).

a)   b)   c)
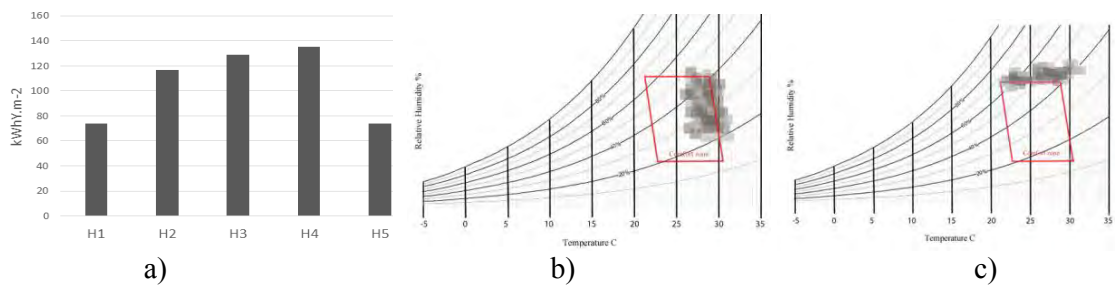
Figure 3. a) Simulated heating loads/yearly (H1-H5), b) Hourly temperature and relative humidity H1, c) Hourly temperature and relative humidity H2.

a)   b)
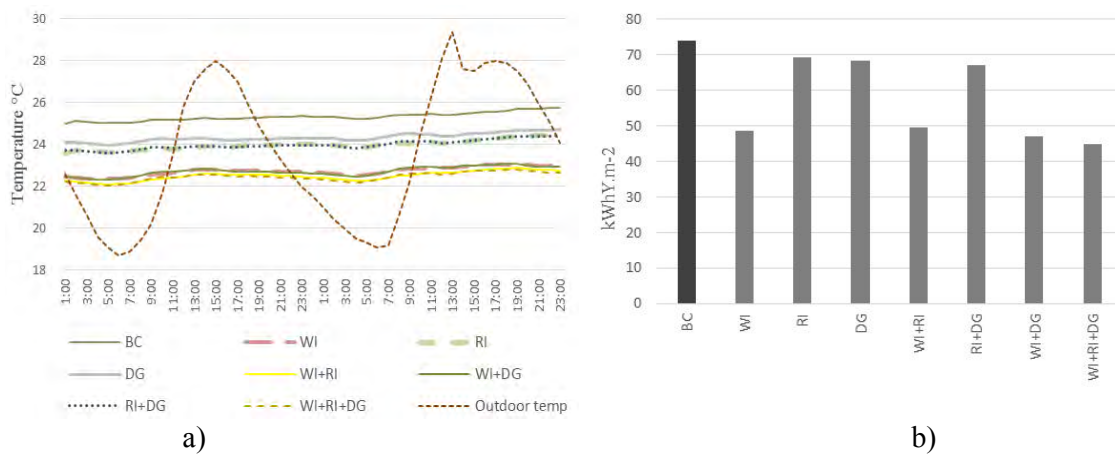
Figure 4. a) Comparison of BC and Scenario Temperatures (H1-H5), b) Scenarios heating loads (H1).

CONCLUSIONS

The paper is about a study conducted on the comfort and energy consumption of five traditional housing conditions in Northern Albania, using one year simulation measurements. Given the climatic conditions in Kukes, traditional houses require only heating during the winter and no cooling in summer. The simulation results establish that thermal comfort is

directly connected to the climate conditions, manufacture fabrics, dwelling shape, and occupants' activity. Altered involvements to the building's fabrics can bring about better performance. Certain combinations of improvement measures (such as insulations in walls, roof, and double glazing) have the ability to recover the thermal performance of the buildings in the climatic context of Kukes, Albania. Wall insulation and other related arrangements have significantly increased the temperatures and condensed the energy consumption, compared with the other scenarios (30 to 35%). Replacement of glazing and roof insulation affects less the thermal comfort (2 to10%). Future studies may address the impact of the change of the structure and activity on the energy consumption of the building.

REFERENCES

Rashani M. and Mahdavi A. 2015. Energy performance assessment of existing multi-family apartment buildings in Kosovo. In: *Proceedings of the 6th International Building Physics Conference the* IBPC 2015, Torino, pp. 782-787.

Resuli P., Dervishi S. 2015. Thermal performance of cultural heritage italian housing in Albania. In: *Proceedings of* the *6th International Building Physics Conference*, IBPC 2015, Torino, pp. 753-758.

Mahdavi A. and Orehouning K. et al. 2007, Analyzing Traditional Buildings Empirically Calibrated Building Performance Models. In: *Proceedings of the 10th International Building Performance Simulation Association Conference and Exhibition* IBSA 2007, Beijing, (China), pp. 75-78.

Marino C. and Minichiello F. 2015. Existing buildings and HVAC systems: incidence of innovative surface finishes on the energy requirements. In: *Proceedings of the 70th Conference of the Engineering Association* ATI 2015, Roma, pp 499-505.

Zhang H. and Lei S L. 2012. An Assessment Framework for the Renovation of Existing Residential Buildings regarding Environmental Efficiency. In: *Proceedings of the Pacific International Conference on Environment-Behaviour Studies* AicE-Bs 2012, Cairo, pp. 549-563.

Kaleci E. and Dervishi S. 2014. Implementation Challenges to the Adaptive Reuse of a Heritage Building in Tirana, Albania. In: *Proceedings of the 2nd International Conference in Architecture and Urban Design Epoka University* ICAUD 2014, Tirana, Albania, pp. 1-10.

Giombini M. and Pinchi E. M. 2015. Energy functional retrofitting of historic residential buildings: the case study of the historic center of Perugia. In: *Proceedings of the 70th Conference of the Engineering Association* ATI 2015, Roma, pp 1009-1016.

Vieites E. and Vassileva I. et al. 2015. Europian initiatives towards improving the energy efficiency in existing and historic buildings. In: *Proceedings of the 3rd International Conference on Advanced Electromaterials* ICAE 2015, ICC Jeju, Korea, pp 1679-1685.

Akande O. K. and Odeleye D. et al. 2016. Performance evaluation of operational energy use in refurbishment, reuse, and conservation of heritage buildings for optimum sustainability. In: *Proceedings of the Foundation for Auditing Research* FAR 2016, pp. 371-382.

Rexhepi A. and Mahdavi A. 2010. Emprical and computational study of the Thermal Performance of a traditional housing type in Kosovo. In: *Proceedings of the 3rd German-Austrian IBPCA Conference*, IBPCA 2010, Vienna, Austria, pp. 1-6.

Uncertainty in Building Energy Performance Characterization: Impact of Gas Consumption Decomposition on Estimated Heat Loss Coefficient

Marieline Senave[1,2,3,*], Glenn Reynders[1,3], Behzad Sodagar[4] and Dirk Saelens[1,3]

[1]KU Leuven, Department of Civil Engineering, Building Physics Section, Belgium
[2]VITO, Smart Energy and Built Environment Unit, Belgium
[3]EnergyVille, Cities in Transition Section, Belgium
[4]University of Lincoln, School of Architecture and the Built Environment, United Kingdom

[*]*Corresponding email: marieline.senave@kuleuven.be*

ABSTRACT

Characterization of building energy performance indicators such as the Heat Loss Coefficient (HLC) based on in-situ measurement data calls for thorough building physical insight, a well-designed measurement set-up to collect sufficient, qualitative data and adequate data analysis methods. On-board monitoring may be an alternative for dedicated experiments to perform the data collection task. This paper analyses the sensitivity of the end-result of the characterization, the HLC estimate, to flaws in the monitoring data set. More specifically, the impact of not installing submeters to disentangle the gas consumption for space heating and the production of domestic hot water is evaluated. Hereto, multiple gas decomposition methods are applied on a case study monitoring data set, after which the HLC is assessed. The results show deviations up to 33% for the mean estimate and non-overlapping 95% confidence intervals.

KEYWORDS
Characterization, Heat Loss Coefficient, On-board Monitoring,
Gas Consumption Decomposition, Sensitivity Analysis.

INTRODUCTION
Building energy performance (BEP) characterization based on in-situ measurements has recently been gaining much attention in the framework of IEA EBC Annex projects 58 and 71. Furthermore, Bauwens (2015), Deconinck (2017) and Farmer et al. (2017) demonstrate how the thermal resistance of building elements and the HLC of building envelopes can be estimated through application of statistical modelling techniques on data collected in on-site steady-state an dynamical measurement experiments. The HLC hereby describes the amount of heating power needed to maintain a temperature difference of 1 degree Kelvin over the entire building envelope [W/K]. The case studies investigated to date, however, mainly focus on mock-ups or unoccupied dwellings. Not only because the measurement conditions can be better controlled, but also because the measurement set-up can be perceived as intrusive and costly.
On-board monitoring, using sensors to collect data of an occupied, in-use building, is put forward as a solution to the issues of cost and intrusiveness (Saelens and Reynders, 2016). However, much uncertainty still exists about the optimal sensor set-up, the way disturbances induced by occupants should be handled, etc.

The present paper aims to address a particular data related challenge that researchers, aspiring to estimate the HLC, might have to face; namely that the same type of fuel has been used for both space heating (SH) and the production of domestic hot water (DHW), and that no submeters can or have been installed to differentiate between both end uses.
The dynamic heat balance for a single zone (Eq.1), which forms the framework for both the

monitoring campaign and the data analysis model, stipulates that the HLC at each timestep t depends on the effective heat capacity C_i [J/K] of the zone, the difference between the interior and exterior temperature (T_i and T_e resp. in [K]), the heat flow rates due to mechanical ventilation with heat recovery, internal and solar gains ($\varphi_{vent,hr}$, φ_{int} and φ_{sol} resp.), and the net power supplied by the heating system φ_H [W]. This final term not only implies that the gross fuel consumption has to be conversed in net energy use on the basis of the system efficiency, but also that the energy use for SH should be separated from that for DHW production and that the latter should be eliminated from the analysis for as far that it does not induce internal gains.

$$C_i \cdot \frac{dT_i}{dt} = HLC \cdot \left(T_{i;t} - T_{e;t}\right) + \varphi_{vent,hr;t} + \varphi_{int;t} + \varphi_{sol;t} + \varphi_{H;t} \qquad (1)$$

Not decomposing the fuel consumption results in an overestimate of the HLC. However, disentangling it incorrectly might just as much lead to an erroneous estimate. This paper will therefore evaluate the sensitivity of the HLC estimate to the approach used to determine the not-monitored fuel (gas) consumption for space heating.

The first part of the methodology section describes the case study dwelling and on-board monitoring campaign used to this end. Next, three different ways to decompose the gas consumption and thus approach φ_H are discussed. In the final part of the methodology section, the data analysis procedure used to estimate the HLC is delineated. In the results section, differences between the decomposition outcomes are shown, and, more importantly, their impact on the characterization of HLC is demonstrated. Finally, conclusions are drawn on the present study and recommendations are given for future research.

METHODOLOGY
Case study dwelling and on-board monitoring campaign
The object of this study is a semi-detached, two-story house built in 2012 in Gainsborough, UK. A theoretical HLC of 47 W/K is calculated based on the target U-values and surface areas of the building envelope parts, the average result of three blowerdoor tests, and the assumption that the efficiency of the mechanical ventilation heat recovery unit equals 100 %. SH and DHW are provided by a gas fired combi boiler. Together with the other dwellings in its terrace, the house has been the subject of a monitoring campaign conducted from October 2012 until November 2015. During this period, the dwelling was inhabited by three persons. The interior temperature of the living room and bedroom (both from the studied and neighbouring dwelling), the exterior temperature, the gas, water and electricity consumption and the PV production were monitored with a 5 min sample frequency. Hourly averaged values of the global horizontal solar irradiance (GHR) were obtained from a RAF weather station located 30 km from the site. A detailed description of the dwelling and performed monitoring campaign can be found in (Sodagar and Starkey, 2016), in which the dwelling is referred to as 'House 1'.

Gas consumption decomposition methods (DMs)
Classifying all gas consumption for the production of DHW as internal gains and thus assessing HLC based on the total gas consumption ('No decomposition') is incorrect since the hot tap water directly leaves the dwelling through the sewage system.

A first decomposition method to disentangle both end uses ('DM1') could therefore be the application of a default distribution. In this case study there will be opted for a 76/24 distribution for the end uses SH/DHW, as reported by Menkveld (2009). A major drawback of this method is that it does not take the actual consumption, SH demand or occupant behavior into account.

The second decomposition method ('DM2') is fully based on the assumptions that (1) in the case of the combi boiler, the production of DHW and SH do not occur at the same time and (2)

the gas consumption for DHW production perfectly coincides with the DHW consumption. It involves the implementation of two rules on the 5min-interval monitoring data. The first rule stipulates that the gas consumption for DHW production must be set to 0 when mains water consumption is 0, else gas consumption for the production of DHW must be set equal to the total monitored gas consumption. The second rule states that the gas consumption for SH must be set to 0 when mains water is consumed, else gas consumption for SH must be set equal to the total monitored gas consumption.

This DM is straightforward and easy to implement. However, a number of potential flaws can be identified. First, the assumptions imply that all cold water tappings occurring while gas is used for SH are classified as DHW usage. The fact that grey water is used to flush the toilets though makes this assumption more reasonable. Secondly, the hot water tappings could be significantly shorter than the 5 min sampling time. Yet, from the moment water consumption is observed, however small, the full gas consumption for that 5 min period is allocated to DHW production. Higher frequency logging could solve this issue. Thirdly, small time delays between starting and stopping of water and gas consumption will create some error.

The third approach, 'DM3', which was demonstrated by Bacher et al (2016), uses a robust, zero order, Gaussian kernel smoother to estimate the 'gas consumption for SH'-profile underlying the noisy 5 min gas consumption data. Next, all spikes of the total gas consumption significantly above this kernel (smoother) estimate are classified as DHW heating spikes and their values are obtained by subtraction of the kernel estimate. Finally, subtraction of the estimated heat load for the production of DHW from the total heat load gives an estimate for the heat load for SH. The parameters of the kernel smoother procedure were tuned with an eye on limiting the gas consumption classified as 'gas used for space heating' during the summer months. The final model parameter values are as follows: kernel window: 1 h, bandwidth: 0.5 h, threshold for bisquare robust estimation γ: 7 MJ/h, separation threshold q_{tres}: 1.1.

Just like DM2, this decomposition method has not been verified on a case study were the total gas consumption and the consumption for the production of DHW and SH were measured separately. In contrast with the previously described approach, this method assumes that gas consumption for both end uses can occur simultaneously. It should furthermore be noted that all peaks are classified as DHW heating, although the start-up of the space heating might also result in a similar peak in the fuel consumption.

Determination of HLC

For the characterization exercise, four periods were selected from the entire data set: a relatively long model training period, extending from the 1st of October 2014 till the 31st of March 2015, and three different shorter model validation periods, in January, February and March 2014. With the heat balance equation (Eq.1) in mind, the following variables were selected from the monitoring data; the exterior temperature T_e, the interior temperature of the dwelling itself and the neighbouring dwelling (T_i and T_n, resp). Both T_i and T_n are approximately determined as the arithmetic mean of the sensor data collected in the living room and bedroom. In the absence of data on the incident radiation on the different facades, the GHR will be used to represent I_{sol}. After adaptation with the calorific values published by National Grid (2017) and decomposition through one of the above-mentioned decomposition methods, the gas consumption data will be used as φ_H. The system efficiency is thus assumed to be equal to 100 %. Although this value is uncertain and in reality not even constant, this will not pose an issue for this study, which focuses on the relative differences caused by DMs used for gas consumption. The same holds for the other assumptions made. Finally, the internal gains φ_{int} are neglected in a first run ('φ_{int} = 0') and assumed to equal the total electricity consumption in a second run ('$\varphi_{int} > 0$'). The latter variable is hereby approximated as the mains electricity consumption plus half of the PV

production to account for the not-submetered electricity that is directly fed to the grid. Next, an Auto-regressive with eXogenous input (ARX) model is fitted on the selected time series data, utilizing the 'lm' function in R-Studio:

$$\varphi_i(B) \cdot \boldsymbol{T_{i;t}} = \omega_e(B) \cdot \boldsymbol{T_{e;t}} + \omega_n(B) \cdot \boldsymbol{T_{n;t}} + \omega_{sol}(B) \cdot \boldsymbol{I_{sol;t}} +$$
$$\omega_H(B) \cdot \left(\boldsymbol{\varphi_{H;t}} + \boldsymbol{\varphi_{int;t}}\right) + Int + \varepsilon_t \qquad (4)$$

with $T_i, T_e, T_n, I_{sol}, \varphi_H$ and φ_{int} the previously determined variables, resampled to hourly values, and $\varphi_i(B)$ an input polynomial of order p_i in the backshift operator B. Likewise, the $\omega_x(B)$'s are output polynomials of order p_x. Int is a constant intercept term and ε_t the residual (error) (Madsen, 2016).

To decide on the model order, a backward elimination procedure is followed, starting from a model including 24 lags for each of the considered polynomials. After every run, the significance of the fitted model coefficients is verified using a t-test (threshold of $p < 0.05$), starting with the highest available order. When coefficients of a certain order prove insignificant, their variables are eliminated from the model description and the model is refitted. The iterative process ends when all model coefficients present are significant.

To validate the developed models, it is verified whether their residuals resemble white-noise in plots of the autocorrelation function (ACF) and cumulated periodogram (CP). By comparing the normalized RMSE (nRMSE) [%] between the measured interior temperature and its one-step-ahead prediction for both the training and a validation period, it is checked whether the model is not overfitted.

If the model is accepted, HLC is calculated as the quotient of steady-state gains $\omega_e(1)/\omega_H(1)$. Finally, the models are compared based on (1) their score for the Akaike Information Criterion (AIC) and (2) the nRMSE between the observed and simulated interior temperature for the cross-validation periods. For both criteria, a lower value indicates a better model.

RESULTS ANALYSIS AND DISCUSSION
Differences between the gas consumption for SH estimated by the DMs
Table 1 compares the decomposition of gas consumption for SH and DHW production obtained through the different approaches. The default method (DM1) almost always results in a higher gas consumption for SH than DM2 and DM3. The method with the robust kernel smoother (DM3) uses a certain threshold instead of selectively classifying the gas consumption as either gas consumption for SH or production of DHW as DM2 does. This way it appears to systematically obtain a lower gas consumption for SH.

Table 1: Total gas consumption [kWh] and the gas consumption for SH as estimated by the four approaches [expressed as a percentage of the total gas consumption], per month.

	Oct 2014	Nov 2014	Dec 2014	Jan 2015	Feb 2015	Mar 2015
Total gas consumption	188 kWh	286 kWh	486 kWh	526 kWh	428 kWh	267 kWh
No decomposition	100 %	100 %	100 %	100 %	100 %	100 %
DM 1	76 %	76 %	76 %	76 %	76 %	76 %
DM 2	58 %	69 %	74 %	77 %	74 %	59 %
DM 3	44 %	55 %	62 %	63 %	59 %	45 %

Validation of developed ARX models
Given the applied model selection procedure, all finally included parameters of the 8 models (4 variants for φ_H times 2 scenarios for φ_{int}) are significant. Except for the models with φ_H based on DM2 or DM3 and φ_{int} =0, the interior temperature of the neighboring dwelling appeared to be an insignificant model input, probably because of a nearly constant profile of T_n. For the

other validation tests, the results were positive for all models: the nRMSE did only increase with about 1 % for the one-step-ahead cross-validation test, and the ACF and CP plots indicated white noise residuals. All models thus appear to be statistically valid.

Comparison of resulting HLC

Figure 1 shows the impact of the applied gas decomposition method on the HLC estimate, and this for the two different φ_{int} scenarios. The models appear to yield fairly different results, with 95 % confidence intervals that do not all overlap. In the case of $\varphi_{int} = 0$ the mean estimates range from 47 to 71 W/K, which is a difference of 33 %. The assumption that the internal gains equal the (approximated) total electricity consumption not only slightly reduces the uncertainty on the outcomes, but also lowers the impact of the choice for a certain DM (maximal difference of 25 % between the means). Nonetheless, the mean outcomes for DM2 and DM3 still differ with 14 %. Notably, the observed deviances are dwelling and occupant specific. In the case of a less-insulated dwelling with a lower DHW consumption and higher setpoint temperature of the heating system, the sensitivity of the characterization result to the applied DM may be lower.

The majority of the estimates fall above the calculated reference value, suggesting that the actual HLC is higher. As neither DM2 nor DM3 has yet been validated and the information available on the boiler is limited, it is impossible to claim that one of the HLC outcomes
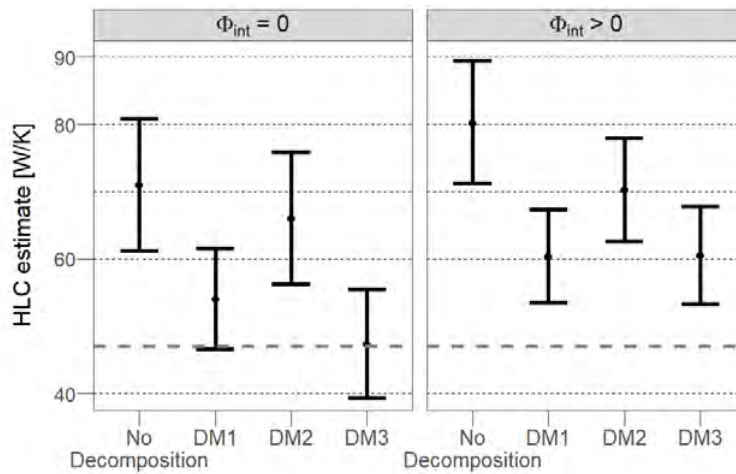

Figure 1: Overview of the HLC estimates and their related 95 % confidence intervals for the different models. The dashed line indicates the theoretically calculated reference value.

Table 2: Comparison of the different models based on the AIC and nRMSE between the measured (T_i) and simulated ($\hat{T}_i$) interior temperature.

	AIC	nRMSE(T_i, $\hat{T}_i$) [%] for validation periods in:		
	Training period	Jan '14	Jan-Feb '14	Feb-Mar '14
$\varphi_{int} = 0$				
No decomposition	-4319.60	24.52	18.59	33.62
DM 1	-4316.53	24.51	18.62	33.69
DM 2	-4585.14	14.07	10.13	14.72
DM 3	-4515.00	18.10	17.25	16.76
$\varphi_{int} > 0$				
No decomposition	-3415.77	35.74	28.44	43.49
DM 1	-3390.58	43.01	34.22	48.54
DM 2	-3558.96	22.05	16.04	23.96
DM 3	-3548.66	26.94	26.75	30.34

is correct. However, some conclusions can be drawn from a statistical point of view. When comparing the models' AIC and their nRMSEs for the simulation validation periods (Table 2), we see that the models with $\varphi_{int} = 0$, and the models where DM2 (and DM3) are applied, are better capable of predicting the interior temperature. The more accurate predictions on cross-validation data may indicate more correct input data and a more accurate model structure, and are therefore argued to be a reason for favoring the outcome of those models.

CONCLUSION

The present paper explored how the HLC of a building envelope can be characterized based on on-board monitoring data. The focus was on the sensitivity of the characterization outcome to the preciseness of the knowledge on the supplied net heating power. This way the paper aimed to address the common problem that the two end-uses of gas (SH and DHW) are not submetered. By means of a case study, diverse approaches to approximate the unknown gas consumption for SH were illustrated. It was uncovered how, depending on the approach used, the HLC outcome can be 33 % apart. Uncertainty regarding other variables involved, e.g. the internal gains, furthermore influences this result. Since the applied gas decomposition methods have not yet been validated, the 'correct' characterization outcome could not be identified. However, based on statistical model comparison tests, suggestions on the trustworthiness of the outcomes were given. Submetering the gas consumption would, however, clear all doubts and increase the accuracy of the outcome. In next steps the applied decomposition techniques should be validated and the sensitivity of the HLC estimate towards assumptions on other variables (e.g. the system efficiency, interior temperature, incident solar radiation) should be explored.

ACKNOWLEDGEMENT

REFERENCES

Bacher P., de Saint-Aubain P.A., Christiansen L.E., and Madsen H. 2016. Non-parametric method for separating domestic hot water heating spikes and space heating. *Energy and Buildings,* 130, 107-112.

Bauwens G. 2015. In situ testing of a building's overall heat loss coefficient. *Ph.D. Thesis*, KU Leuven (Belgium), 200 pages.

Deconinck A.H. 2017. Reliable thermal resistance estimation of building components from on-site measurements. *Ph.D. Thesis*, KU Leuven (Belgium), 224 pages.

Farmer D., Gorse C., Swan W., Fitton R., Brooke-Peat M., Miles-Shenton D., and Johnston D. 2017. Measuring thermal performance in steady-state conditions at each stage of a full fabric retrofit to a solid wall dwelling. *Energy and Buildings*, 156, 404-414.

Madsen H., Bacher P., Bauwens G., Deconinck A., Reynders G., Roels S., … Lethé G. 2016. IEA EBC Annex 58: Report of Subtask 3, part 2: Thermal performance characterisation using time series data - statistical guidelines. KU Leuven (Belgium), 83 pages.

Menkveld M. 2009. Kentallen warmtevraag woningen. Final Report for RVO. ECN, 7 pages.

National Grid UK. 2017. Calorific Value (CV): CV Data: Data Item Explorer. National Grid UK: https://www.nationalgrid.com/uk/gas/market-operations-and-data/calorific-value-c, consulted October 6, 2017.

Saelens D., and Reynders G. 2016. IEA EBC Annex 58: Report of Subtask 4b: Towards a characterisation of buildings based on in situ testing and smart meter readings and potential for applications in smart grids. KU Leuven (Belgium), 25 pages.

Sodagar B., and Starkey D. 2016. The monitored performance of four social houses certified to the Code for Sustainable Homes Level 5. *Energy and Buildings*, 110, 245-256.

Ventilation Potential Assessments for Residential Building Arrangements Based on Exceedance Probability Analysis

Wei You[1], Lian Tang[1] and Wowo Ding[1,*]

[1] School of Architecture and Urban Planning, Nanjing University, Nanjing 210093, China

[*]*Corresponding email: dww@nju.edu.cn*

ABSTRACT

In this study, the building ventilation potentials were assessed at building group level. Exceedance probability analysis was applied to estimate the uncertainties associated with the influence of climate on wind environment. The criterion was proposed based on building facade pressures. Two typical residential building arrangements were investigated. Simulation results show that facade pressure based exceedance probability are efficient in assessing the natural ventilation potentials of building groups and building height variations are important for improving building natural ventilation potentials.

KEYWORDS

Residential buildings, Ventilation potential, Exceedance probability, Facade wind pressure.

INTRODUCTION

Natural ventilation is a common adopted passive building design strategy. It can improve indoor thermal comfort and air quality by removing excess heat and airborne contaminants. Optimizing building natural ventilation design is not only related to building façade opening size and location, but also refers to the arrangements of buildings. Thus, the assessments of natural ventilation potentials require an investigation at building group level.

For building natural ventilation, wind pressure distribution of building facade is an important boundary condition, as wind is the driving force. Many studies had investigated the indoor natural ventilation in terms of wind pressures for building groups. Tsutsumi et al. (1992) experimentally studied the wind pressure on a building surrounded by a group of buildings. The relations between average wind pressure coefficients and various layouts of buildings are discussed under different wind conditions. Similar studies were also carried out by Kim et al. (2012) and Shirzadi et al. (2018). In addition, Asfour (2010) investigated the effect of building layout patterns on ventilation potential of these buildings. Six hypothetical arrangements of buildings were assessed by calculating wind pressure difference. Bady et al. (2011) carried out wind tunnel experiments to study wind pressure characteristics on groups of buildings located within high density building arrays. The results all show that buildings configuration and wind direction are important factors in determining urban ventilation. However, most studies had investigated single building under typical wind directions.

For wind environment evaluation considering the uncertain upper wind parameters, some researches introduced the probability analysis into wind performance studies. This method estimates the probability of ventilation performance satisfying certain criteria. In past researches, probability analysis had most been applied in investigation of pedestrian-level wind environment, generally focusing on wind comfort/safety issues (Blocken and Persoon, 2009; Du et al. 2017). Recently, several researchers had introduced the probability concept into other wind performance area. Pietrzyk (2008) developed a probabilistic model and

studied the problem of air infiltration in low-rise buildings. Bu et al. (2009) analyzed the exceedance probability of local air change rate and local kinetic energy for investigating the ventilation performance and thermal comfort within urban street canyons.

This study attempted to introduce probability concept into wind-driven natural ventilation area for valuating natural ventilation potentials of building groups. Exceedance probability was calculated in terms of wind pressure on building facades. Two typical residential building arrangements, namely multi-story buildings and high-rise buildings, were adopted as the evaluation objects. The cases were located at a typical southeast monsoon wind city - Nanjing. And residential building units were investigated for natural ventilation potentials. To calculate building facade pressures, computational fluid dynamics (CFD) method with ANSYS-Fluent was adopted. The exceedance probabilities were post-processed by MATLAB and ArcGIS.

RESIDENTIAL BUILDING GROUP CONFIGURATION

A 3 x 3 building group were built for building arrangement analysis. The central group (CG) was the analysis unit, and surrounding units (SG) were arranged around the studied area as environmental conditions, as shown by Figure 1a. Road widths (Sr1, Sr2) were determined as 30m according to design code. Two residential building types were established for case comparison (Figure 1b-c). Case A was multi-storey building group (building height H=18m), and Case B was high-rise building group (H=36m). Building widths L and depth D were determined as 72 and 12m, respectively. Lateral spacing S were 12m, and north-south spacing was 24m and 48m for multi-storey and high-rise building group. Figure 1d shows the data extracted zones for probability calculation and comparison. W1-W6 numbered the south and north facade of living units. W0 and W7 numbered the east and west facade of living units. For vertical partition, multi-storey building was divide into three part, which represent the living unit at low, middle and high levels, and high-rise building was divide into six levels.
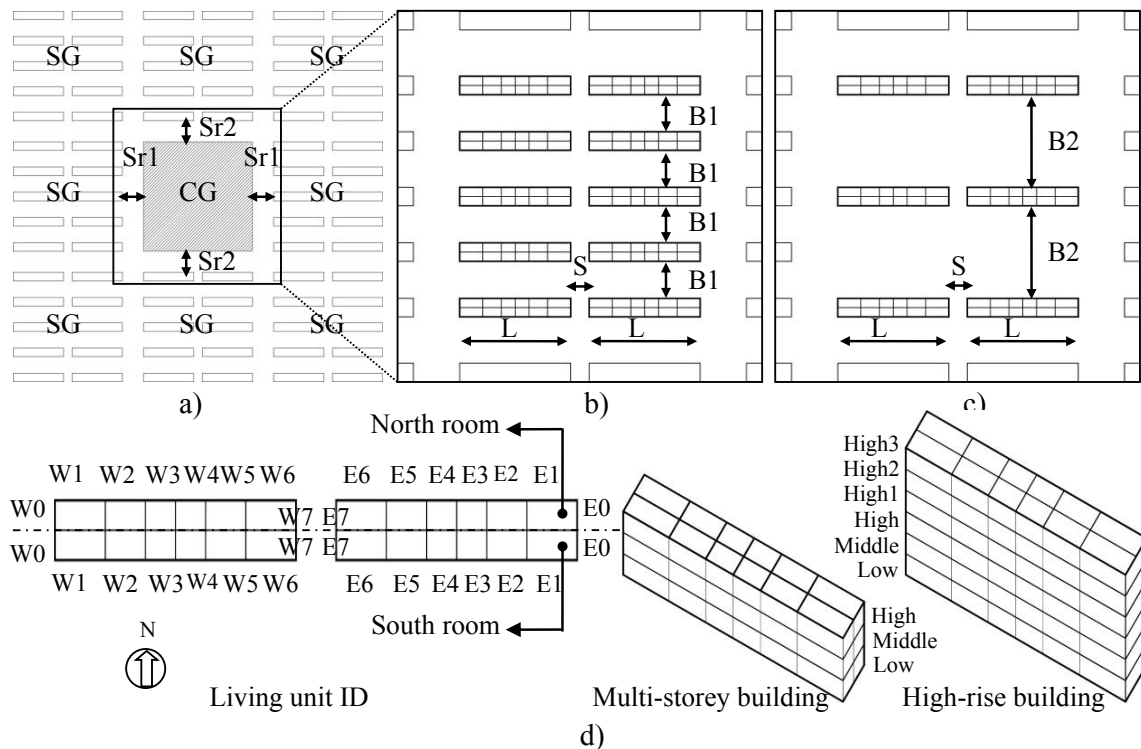

Figure 1. a) Building groups setting, b) Case A, c) Case B, d) Data extracted zones

EXCEEDANCE PROBABILITY CALCULATION FOR VENTIALION POTENTIALS
The exceedance probability based building ventilation assessment consisted of three parts, as shown in Figure 2. The first part was the base data collection, which include weather data, building geometry data and wind flow data. The second part was MATLAB based data processing. In this step, wind data and façade pressure data were extract from the weather file and simulation results. Exceedance probability for each building façade were calculated by processing façade pressure data. At last, building façade geometry and the corresponding probability data were linked and by ArcGIS's spatial join tool for further ventilation potential analysis. The probability distributions were also visualized for each studied surface.
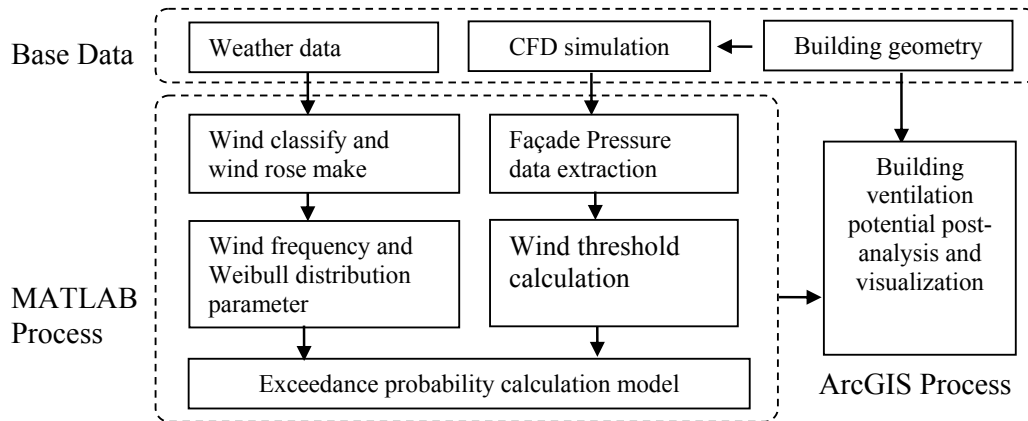

Figure 2. Flow chart of exceedance probability calculation

Base data obtaining
The wind climate of Nanjing was obtained from calibrating the hourly wind data of the solar and Wind Energy Resource Assessment (SWERA) weather file, which were download from EnergyPlus Weather Data (EPW) website. Building façade pressure data were obtained from CFD simulation results. The study referred to the AIJ (Architectural Institute of Japan) guidelines (Tominaga et al. 2008). For turbulence model selection, the Reynolds-Averaged Navier-Stokes (RANS) approach with standard k-ε model was adopted in this study due to its less time consumption and less complexity in boundary condition setting.

Exceedance probability calculation
The pressure based exceedance probability (P_g-EP) at each point above building facade was assumed to follow a two-parameter Weibull distribution in this study. And the P_g-EP for 12 azimuths was calculated as follow:

$$P(P_g > P_g^*) = \sum_{i=1}^{12} A(i) \exp\left[-\left(\frac{\sqrt{P_g^*}}{R \cdot C(i)} \cdot \left(\frac{H_{met}}{\delta_{met}} \right)^{\alpha_{met}} \right)^{k(i)} \right] \tag{3}$$

$$R = \frac{\sqrt{abs(P_g)}}{V_{ref}} \cdot \left(\frac{H}{\delta} \right)^{\alpha} \tag{2}$$

Where $P(P_g > P_g^*)$ is the probability of exceeding the specified P_g^*. i is the wind direction number, and $A(i)$ is the occurrence frequency, and $K(i)$, $C(i)$ are two parameters of Weibull distribution. P_g is the façade pressure extracted from CFD simulation results. V_{ref} is the

reference up wind speed at the height H. α, α_{met}, δ and δ_{met} are the wind speed profile exponent and boundary layer thickness of the studied building located terrain and the weather station located terrain. H_{met} is the wind measured height at the the weather station.

RESULTS AND DISCUSSION

Figure 3 showed the distributions of exceedance probability percentage (P_g-EP) on building facade for multi-story and high-rise buildings. In subplot (a)-(b), the facade P_g-EP distribution were viewed from southeast and in subplot (c)-(d), the P_g-EP distribution were viewed from northeast. The natural ventilation potentials of the building groups were clearly revealed by the P_g-EP distribution on each building facades. High-rise buildings obviously improved the building natural ventilation potentials, comparing with that of multi-story buildings. The variation range of P_g-EP was between 30% and 70% for high-rise buildings, while between 20% and 60% for multi-story buildings. For high-rise building group, the more ventilation living units were located at the first (south) and third (north) row, which the P_g-EPs of first row building's south facade (Figure 3b) and the third row building's north facade (Figure 3d) were almost above 60%. It was because the surrounding buildings were multi-story buildings, which wind can directly reach the up part of the high-rise building facades. For the multi-story building group (Figure 3a) and the middle row high-rise buildings (Figure 3b), the more ventilation living units were located at the building's eastside. It was due to effect of southeast monsoon in summer. Due to the recirculation flow phenomenon, the middle level P_g-EPs of the multi-story buildings' north facade increase (Figure 3c). It revealed the ventilation potentials of north living units at the third and fourth storey building are improved.
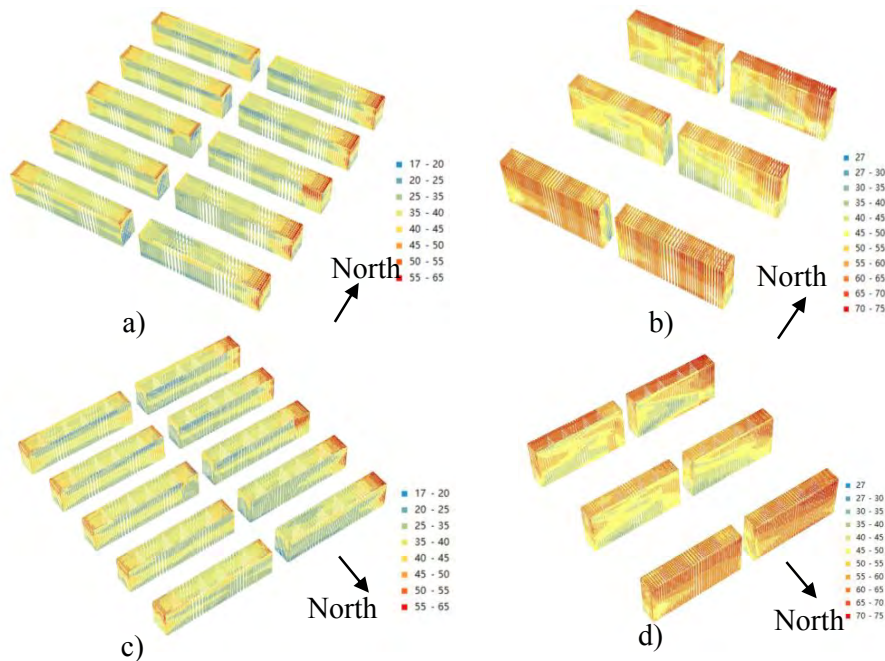

Figure 3. Distributions of the exceedance probability percentage on building facades.

More detailed quantitative analysis of natural ventilation potentials of the building groups was shown in Figure 4 and Figure 5. Figure 4 were the P_g-EP compassion of different height level residential units for multi-story and high-rise buildings. From the figure, it can be found that for the multi-story building group, the P_g-EPs were all below 50% (Figure 4a). And the natural ventilation potentials of low, middle and high levels of high-rise building units all increased, with P_g-EP around 50% (Figure 4b). It was due to the strengthen of air flow by the

upper facade of the high-rise building. The natural ventilation potentials of higher levels (high1 high2 and high3) of high-rise buildings were improved greatly due to the less effect of surrounding buildings. The P_g-EPs of these areas were all generally above 50% (Figure 4c). In terms of the positions of residential units at one storey, ventilation potentials of side units are better than that of middle units, and ventilation potentials of east side units are better than that of west side units. It is more obviously reflected within the multi-story building group. Figure 5 shows the P_g-EPs of south and north units for multi-story and high-rise buildings. The simulation results showed that P_g-EPs of north units were slightly better than that of south room for multi-story building. It was due to the turbulence flow, which acted on the north facade of the multi-story residential building, which discussed above.
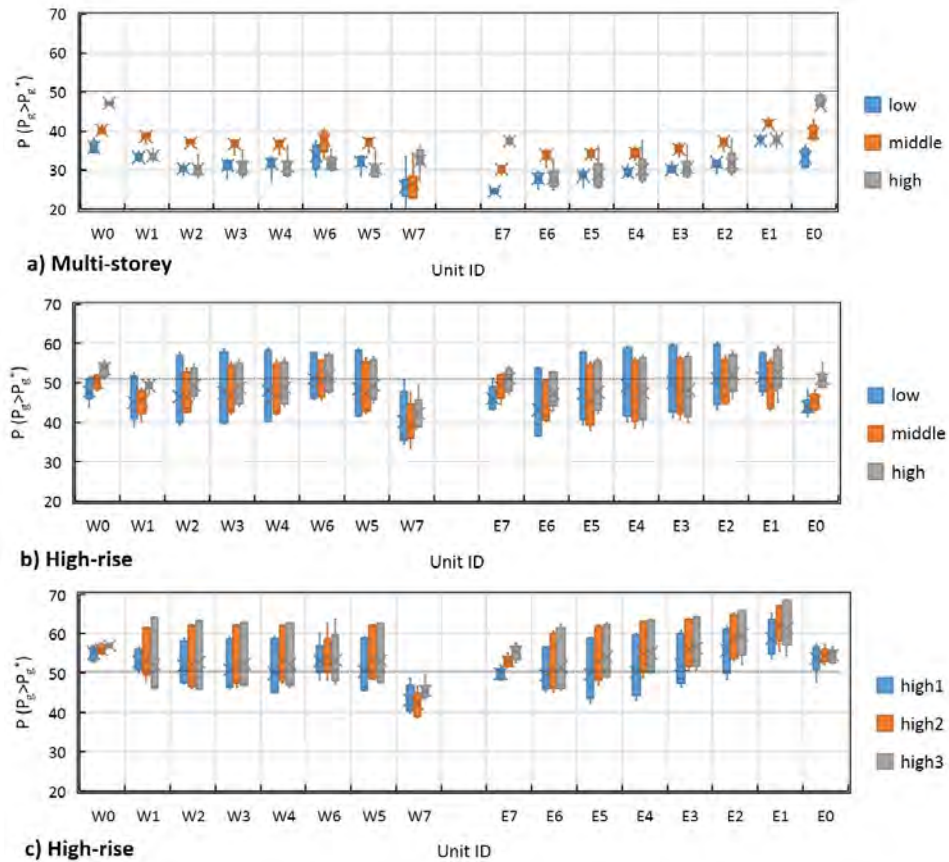

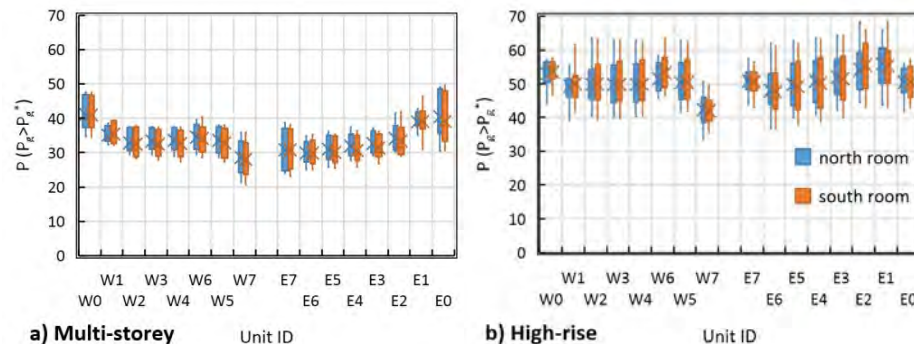Figure 4. Comparison of different living-unit levels for multi-story and high-rise buildings.

Figure 5. Comparison of living-unit facade directions for multi-story and high-rise buildings.

CONCLUSIONS

This paper provided a simple method to assess building group's natural ventilation potentials considering the effect of local wind climate. The cases studies show that, by calculation the exceedance probability of wind pressure on building facades, the natural ventilation potentials of building group can be revealed for each living units. Two typical residential building arrangements were investigated using the façade pressure based exceedance probability. Simulation results show that high-rise buildings could obviously improve the building's natural ventilation potentials by increasing P_g-Eps of around 20%, comparing to that of the same levels (1-6 storey) of multi-story buildings. In southeast monsoon regions, the ventilation potentials of eastside living units is indeed improved especially for multi-story buildings. The P_g-Eps could increase by about 10%. And the ventilation of north façade living units could also be beneficial by the turbulence flows.

This study is a preliminary test of using façade pressure based exceedance probability as an indicator for assessing of building natural ventilation potentials. Only two typical residential building groups were investigated. In the following study, more building arrangement cases will be evaluated to provide design strategies for architects.

ACKNOWLEDGEMENT

REFERENCES

Blocken B. and Persoon J. 2009. Pedestrian wind comfort around a large football stadium in an urban environment: CFD simulation, validation and application of the new Dutch wind nuisance standard. *Journal of Wind Engineering and Industrial Aerodynamics*, 97, 255-270

Du Y.X, Mak C.M, Kwok K, Tse K-T, Lee T-C, Ai Z.T, Liu J.L, and Niu J.L. 2017. New criteria for assessing low wind environment at pedestrian level in Hong Kong. *Building and Environment*, 123, 23-36

Bady M, Kato S, Takahashi T, and Huang H. 2011. Experimental investigations of the indoor natural ventilation for different building configurations and incidences. *Building and Environment,* 46, 65-74

Shirzadi M, Naghashzadegan M, and Mirzaei P.A. 2018. Improving the CFD modelling of cross-ventilation in highly-packed urban areas. *Sustainable Cities and Society*, 37, 451–465

Asfour, O.S. 2010. Prediction of wind environment in different grouping patterns of housing blocks. *Energy and Buildings*, 42, 2061–2069.

Tsutsumi J, Katayama T, and Nishida M. 1992. Wind tunnel tests of wind pressure on regularly aligned buildings. *Journal of Wind Engineering and Industrial Aerodynamics,* 43, 1799-1810

Kim Y.C, Yoshida A, and Tamur Y. 2012. Characteristics of surface wind pressures on low-rise building located among large group of surrounding buildings. *Engineering Structures*, 35,18-28.

Pietrzyk K, Hagentoft C-E. 2008. Probabilistic analysis of air infiltration in low-rise buildings. *Building and Environment,* 43(4), 537–49.

Bu Z, Kato S, Ishida Y, and Huang H. New criteria for assessing local wind environment at pedestrian level based on exceedance probability analysis. *Building and Environment,* 44, 1501-1508

Tominaga, Y.; Mochida, A.; Yoshie, R.; Kataoka, H.; Nozue, H.; Yoshikawa, M.; Shirasawa, T. 2008. AIJ guidelines for practical applications of CFD to pedestrian wind environment around buildings. *Journal of Wind Engineering and Industrial Aerodynamics,* 96, 1749-1761